



UNIVERSITY OF CAMPINAS
School of Mechanical Engineering

DIRCEU SOARES JÚNIOR

**Iterative method of identifying
Multiple-Input-Multiple-Output systems in
state-space**

**Método iterativo de Identificação de Sistemas de
múltiplas entradas e saídas no espaço de estados**

Campinas

2022

DIRCEU SOARES JÚNIOR

**Iterative method of identifying
Multiple-Input-Multiple-Output systems in
state-space**

Thesis presented to the School of Mechanical Engineering of the University of Campinas in partial fulfillment of the requirements for the degree of Doctor in Mechanical Engineering, in the area of Solid Mechanics and Mechanical Design.

Tese apresentada à Faculdade de Engenharia Mecânica da Universidade Estadual de Campinas como parte dos requisitos exigidos para a obtenção do título de Doutor em Engenharia Mecânica, na área de Mecânica dos Sólidos e Projeto Mecânico.

Orientador: Prof. Dr. Alberto Luiz Serpa

ESTE TRABALHO CORRESPONDE À VERSÃO FINAL DA TESE DE DOUTORADO DEFENDIDA PELO ALUNO DIRCEU SOARES JÚNIOR, E ORIENTADA PELO PROF. DR. ALBERTO LUIZ SERPA.

Campinas

2022

Ficha catalográfica
Universidade Estadual de Campinas
Biblioteca da Área de Engenharia e Arquitetura
Elizangela Aparecida dos Santos Souza - CRB 8/8098

So11i Soares Júnior, Dirceu, 1969-
Iterative method of identifying Multiple-Input-Multiple-Output systems in state-space / Dirceu Soares Júnior. – Campinas, SP : [s.n.], 2022.

Orientador: Alberto Luiz Serpa.
Tese (doutorado) – Universidade Estadual de Campinas, Faculdade de Engenharia Mecânica.

1. Identificação de sistemas. 2. Sistemas MIMO. 3. Métodos de espaço de estados. 4. Correlação de dados. 5. Ruído - Medição. I. Serpa, Alberto Luiz, 1967-. II. Universidade Estadual de Campinas. Faculdade de Engenharia Mecânica. III. Título.

Informações para Biblioteca Digital

Título em outro idioma: Método iterativo de Identificação de Sistemas de múltiplas entradas e saídas no espaço de estados

Palavras-chave em inglês:

System identification

MIMO system

State-Space methods

Data correlation

Measurement noise

Área de concentração: Mecânica dos Sólidos e Projeto Mecânico

Titulação: Doutor em Engenharia Mecânica

Banca examinadora:

Alberto Luiz Serpa [Orientador]

Janito Vaqueiro Ferreira

Matheus Souza

Samuel da Silva

Sérgio Junichi Idehara

Data de defesa: 23-06-2022

Programa de Pós-Graduação: Engenharia Mecânica

Identificação e informações acadêmicas do(a) aluno(a)

- ORCID do autor: <https://orcid.org/0000-0002-0876-634>

- Currículo Lattes do autor: <http://lattes.cnpq.br/5471356042256233>

**UNIVERSITY OF CAMPINAS
SCHOOL OF MECHANICAL ENGINEERING**

THESIS

**Iterative method of identifying
Multiple-Input-Multiple-Output systems in
state-space**

Autor: Dirceu Soares Júnior

Orientador: Prof. Dr. Alberto Luiz Serpa

A Banca Examinadora composta pelos membros abaixo aprovou esta Tese:

**Prof. Dr. Alberto Luiz Serpa
FEM/UNICAMP**

**Prof. Dr. Janito Vaqueiro Ferreira
FEM/UNICAMP**

**Prof. Dr. Matheus Souza
FEEC/UNICAMP**

**Prof. Dr. Samuel da Silva
FEIS/UNESP**

**Prof. Dr. Sérgio Junichi Idehara
CTJ/UFSC**

A Ata de Defesa com as respectivas assinaturas dos membros encontra-se no SIGA/Sistema de Fluxo de Dissertação/Tese e na Secretaria do Programa da Unidade.

Campinas, 23 de junho de 2022

ACKNOWLEDGEMENTS

First of all, I bow to God to thank and glorify for my life, especially in the face of this challenge that He has provided me over the last five years.

I thank my love wife, Cibele, and my sons, Guilherme and Daniel, for their patience and understanding when sometimes I could not be really with them. I desire this doctoral degree can work as an inspiration for them to keep forward in the endless search for knowledge.

I thank my mother and my father (in memory) for all the love that guided my human and educational formation.

I thank my doctoral supervisor, Prof. Dr. Alberto Serpa, for the experiences and lessons I learned along the journey, which I will take with me for the research activities and for the life.

I thank the School of Mechanical Engineering (FEM) of the University of Campinas (UNICAMP) for the welcome every time I had the pleasure of staying present.

I thank the Federal Institute of Espirito Santo (IFES) for the incentive and have allowed me to withdraw from the teaching activities during the doctoral degree program.

This study was financed in part by the Coordenação de Aperfeiçoamento de Pessoal de Nível Superior Brasil (CAPES) Finance Code 001.

I thank the CAPES for the financial support and for making this DINTER project possible under the grant number AUX-PE-DINTER 2343/2015.

RESUMO

Este trabalho abrange objetivos relacionados ao aprimoramento de algoritmos de realização no espaço de estados (State-Space Realization Algorithm) SSRA, baseados no tradicional algoritmo de realização de autosistemas (Eigensystem Realization Algorithm) ERA, que surge de oportunidades comparando o método com outras técnicas de Identificação de Sistemas de múltiplas entradas e múltiplas saídas (Multi-Input-Multiple-Output) MIMO. O objetivo principal deste trabalho é introduzir uma nova abordagem considerando a forma iterativa do método SSRA com correlação de dados (State-Space Realization Algorithm with Data Correlation) SSRA-DC. Esta perspectiva visa melhorar a eficácia de identificação do algoritmo quando o sistema possui ruído de medição. O método proposto é composto por iterações do SSRA-DC por meio da retroalimentação da matriz de parâmetros de Markov. Um fator de ganho é aplicado na retroalimentação para atualização dos parâmetros de Markov a cada iteração. Ao longo do trabalho, sinais de sequência binária pseudo aleatória (Pseudo Random Binary Sequence) PRBS, sinais de varredura senoidal (Sine Sweep signal) CHIRP, e sinais de ruído branco gaussiano (Gaussian White-Noise) GWN são empregados como excitação de entrada nas simulações de modelos massa-mola-amortecedor com 5, 50 e 100 graus de liberdade, para verificar o desempenho dos algoritmos. Adicionalmente a esses sistemas lineares, um sistema não-linear com Pêndulo sobre estrutura móvel (Cart-Pendulum) C-PEN é também submetido às simulações dos algoritmos. Vários resultados foram concebidos com base em uma análise estatística de 100 simulações para cada configuração dos algoritmos. Por fim, uma análise comparativa entre o método iterativo SSRA-DC-iCL com as técnicas mais conhecidas do "SI toolbox" do Matlab evidencia a eficácia do novo método. Para os sistemas lineares massa-mola-amortecedor com 50 e 100 graus de liberdade, a precisão de identificação foi um pouco melhor no algoritmo N4SID do que no SSRA-DC-iCL, embora o tempo de processamento computacional (CPT) tenha sido muito menor com o novo método. Para o sistema não linear C-PEN de 2 graus de liberdade, os resultados se inverteram ao comparar os métodos SSRA-DC-iCL e N4SID, no entanto, para este sistema o método ARMAX foi o que apresentou melhor eficácia na identificação.

Palavras-chave: Identificação de sistemas, Algoritmo de realização no espaço de estados, Sistemas de múltiplas entradas e saídas, Correlação de dados, Sequência binária pseudo-aleatória (PRBS), Ruído branco gaussiano (GWN), Ruído de medição, Parâmetros de Markov.

ABSTRACT

This work encompasses objectives related to improvements of State-Space Realization Algorithms (SSRA) based on the traditional Eigensystem Realization Algorithm (ERA), which arise from opportunities comparing the method with other identification techniques of MIMO systems. The main objective of this work is to introduce a new approach considering the iterative form of SSRA with Data Correlation (SSRA-DC) method. This perspective wants to improve the identification algorithm effectiveness when the plant has measurement noise. The proposed method is composed of SSRA-DC iterations with the feedback of the Markov parameters matrix. A gain factor is applied in the feedback for updating the Markov parameters at each iteration. Throughout the work, Pseudo Random Binary Sequence (PRBS) signals, CHIRP signals, and Gaussian White-Noise (GWN) signals are employed as input excitation in the simulations of mass-spring-damper models with 5, 50, and 100 degrees of freedom to verify the performance of the algorithms. Additionally to these linear systems, a nonlinear Cart-Pendulum system is also submitted to the algorithms simulations. Several results were performed based on a statistical analysis of 100 simulations for each configuration of the algorithms. Finally, a comparative analysis between the iterative method SSRA-DC-iCL with the most well-known techniques from the "SI Toolbox" of Matlab evinces the novel method's effectiveness. For the linear mass-spring-damper systems with 50 and 100 degrees of freedom, the identification accuracy was a tiny better in the N4SID algorithm than the SSRA-DC-iCL, even though the computational processing time (CPT) was much smaller with the new method. For the nonlinear Cart-Pendulum system of 2 degrees of freedom, the results were inverted when comparing the SSRA-DC-iCL and N4SID methods; however, for this system, the ARMAX method showed the best identification effectiveness.

Keywords: System Identification, State-Space Realization Algorithm, MIMO systems, Data correlation, Pseudo Random Binary Sequence (PRBS), Gaussian White-Noise (GWN), Measurement noise, Markov parameters.

LIST OF FIGURES

Figure 1.1 – SI Fundamental concept: an unknown system to attain a parametric model through an identification method.	26
Figure 2.1 – Linear system $G(z)$, excited by input $u(k)$ with output $y(k)$ and additive measurement noise $v(k)$. $G(z)$ is an abuse of notation where it intends only to work as shift operators for the discrete-time regressive terms.	37
Figure 3.1 – Prediction Error Method (PEM)	46
Figure 3.2 – Squematic representation of ARMAX	49
Figure 3.3 – Squematic representation of BOX and JENKINS	50
Figure 3.4 – Subspace and Classical Methods of SI	54
Figure 4.1 – Main steps of the classical State-space Realization Algorithm.	68
Figure 4.2 – Block diagram of SSRA-DC-iCL	77
Figure 5.1 – Circuit of m bits shift register to generate the PRBS	86
Figure 5.2 – PRBS generation steps yielding 500 samples; from top to bottom, the steps of the signal: white zero mean Gaussian noise, 5th order Butterworth filter in the pass band $1 \leq \omega \leq 2$ (rad/s), PRBS generated signal.	87
Figure 5.3 – PRBS signal for 500 samples in the range [0,1] with 0.1 s sampling time, and with $\mathcal{C}_{\mathcal{F}} = 14.88$ rad/s (left) and $\mathcal{C}_{\mathcal{F}} = 1.52$ rad/s (right).	87
Figure 5.4 – CHIRP signals with $f_{min} = 0.2$ Hz, and $f_{max} = 7$ Hz (on the left graph) and $f_{max} = 14$ Hz (on the right graph).	89
Figure 5.5 – GWN signal with unit-variance	91
Figure 5.6 – Schematic 5 degree of freedom model (M5DOF), where m_i :masses, k_i :stiffnesses and d_i :dampings. Friction not considered.	94
Figure 5.7 – Schematic 100 degree of freedom model (M100DOF), where m_i :masses, k_i :stiffnesses and d_i :dampings. Friction not considered.	95
Figure 5.8 – Schematic 50 degree of freedom model with accelerometers in y_i (M50DOF-a), where m_i :masses, k_i :stiffnesses and d_i :dampings. Friction not considered.	96
Figure 5.9 – Schematic representation of the C-PEN. Friction not considered on the rolls.	97
Figure 5.10 – Free body diagrams of cart (left) and pendulum rod (right).	97

Figure 5.11 – Computational steps of systems simulations to make available the algorithm data set.	101
Figure 6.1 – Singular values from Hankel matrix for: M5DOF, $d_t = 0.5$ s, $q = 100$, $p = 20$, noises of 0% and 1%.	106
Figure 6.2 – Original (red) and identified (blue) systems: outputs y_1 (left) and y_2 (right) for $d_t = 0.5$ s, $q = 100$, $p = 20$, $n = 13$	110
Figure 6.3 – Original (red) and identified (blue) systems: outputs y_1 (left) and y_2 (right) for $d_t = 0.5$ s, $q = 400$, $p = 80$, $n = 10$	110
Figure 6.4 – Original (red) and identified (blue) systems: outputs y_1 (left) and y_2 (right) for $d_t = 0.1$ s, $q = 500$, $p = 100$, $n = 13$	110
Figure 6.5 – Original (red) and identified (blue) systems: outputs y_1 (left) and y_2 (right) for $d_t = 0.1$ s, $q = 2000$, $p = 400$, $n = 10$	111
Figure 6.6 – Original (red) and identified (blue) systems: outputs y_1 (left) and y_2 (right) for $d_t = 0.1$ s, $q = 2000$, $p = 400$, $n = 8$	111
Figure 6.7 – Original (red) and identified (blue) systems: outputs y_1 (left) and y_2 (right) for $d_t = 0.1$ s, $q = 2000$, $p = 400$, $n = 8$, $\mathcal{C}_{\mathcal{F}} = 1.47$ rad/s.	111
Figure 6.8 – Original (red) and identified (blue) systems: outputs y_1 (left) and y_2 (right) for $d_t = 0.02$ s, $q = 2500$, $p = 500$, $n = 13$	112
Figure 6.9 – Original (red) and identified (blue) systems: outputs y_1 (left) and y_2 (right) for $d_t = 0.02$ s, $q = 10000$, $p = 2000$, $n = 10$	112
Figure 6.10 – Original (red) and identified (blue) systems: MSV diagram for $d_t = 0.5$ s, $q = 400$, $p = 80$, $n = 10$	114
Figure 6.11 – Original (red) and identified (blue) systems: MSV diagram for $d_t = 0.1$ s, $q = 2000$, $p = 400$, $n = 10$	115
Figure 6.12 – Original (red) and identified (blue) systems: MSV diagram for $d_t = 0.02$ s, $q = 10000$, $p = 2000$, $n = 10$	115
Figure 6.13 – Original (red) and identified (blue) systems: $d_t = 0.02$ s, $q = 5000$, $p = 1000$, $n = 10$, PRBS excitation, and 1% of additive measurement noise. . .	118
Figure 6.14 – Original (red) and identified (blue) systems: $d_t = 0.02$ s, $q = 10000$, $p = 1000$, $n = 10$, GWN excitation, and 1% of additive measurement noise. . .	118
Figure 6.15 – Boxplot of 200 simulations of M100DOF system, PRBS excitation: $d_t = 0.03$ s, $q = 9000$, $S_N = 1\%$	120

Figure 6.16 – Boxplot of 200 simulations of M100DOF system, CHIRP excitation: $d_t =$ 0.03 s, $q = 9000$, $S_N = 1\%$	120
Figure 6.17 – Boxplot of 200 simulations of M100DOF system, GWN excitation: $d_t =$ 0.03 s, $q = 9000$, $S_N = 1\%$	120
Figure 6.18 – Boxplot of 200 simulations of M100DOF system, PRBS excitation: $d_t =$ 0.03 s, $q = 9000$, $S_N = 3\%$	121
Figure 6.19 – Boxplot of 200 simulations of M100DOF system, CHIRP excitation: $d_t =$ 0.03 s, $q = 9000$, $S_N = 3\%$	121
Figure 6.20 – Boxplot of 200 simulations of M100DOF system, GWN excitation: $d_t =$ 0.03 s, $q = 9000$, $S_N = 3\%$	121
Figure 7.1 – Maximum Singular Values of continuous-time system (red) and discrete- time system (blue) for M50DOF (left) and M100DOF (right).	126
Figure 7.2 – Maximum and Median $\overline{\text{VFR}}$ throughout the reductions of q in the SSRA- DC simulations for M50DOF.	127
Figure 7.3 – Maximum and Median $\overline{\text{VFR}}$ throughout the reductions of q in the SSRA- DC simulations for M100DOF.	128
Figure 7.4 – $\overline{\text{FR}}(\%)$ evolution of SSRA-DC-iCL for M50DOF with $d_t = 0.02$ s, $q =$ 1500, $p = 600$, and $S_N = 0.3\%$ (left), $S_N = 1\%$ (right).	129
Figure 7.5 – K_{p_j} gain (left) and the FR_j (right) from SSRA-DC-iCL for M50DOF with $d_t = 0.02$ s, $q = 1500$, $p = 600$, and $S_N = 0.3\%$, in the simulation of BFR=98.98%.	130
Figure 7.6 – K_{p_j} gain (left) and the FR_j (right) from SSRA-DC-iCL for M50DOF with $d_t = 0.02$ s, $q = 1500$, $p = 600$, and $S_N = 0.3\%$, in the simulation of BFR=96.81%.	130
Figure 7.7 – $\overline{\text{FR}}(\%)$ evolution of SSRA-DC-iCL for M100DOF with $d_t = 0.03$ s, $q =$ 3000, $p = 500$, and $S_N = 0.3\%$ (left), $S_N = 1\%$ (right).	131
Figure 7.8 – Boxplot with outliers of 100 simulations at the M50DOF system applying SSRA-DC (left) and SSRA-DC-iCL (right) algorithms. Parameters: $d_t =$ 0.02 s, $q = 1500$, $p = 600$, $\xi = 2$, $\gamma = 2$, and $S_N = 1\%$	133
Figure 7.9 – Boxplot without outliers of 100 simulations at the M50DOF system ap- plying SSRA-DC (left) and SSRA-DC-iCL (right) algorithms. Parameters: $d_t = 0.02$ s, $q = 1500$, $p = 600$, $\xi = 2$, $\gamma = 2$, and $S_N = 1\%$	134

Figure 7.10 – Boxplot with outliers of 100 simulations at the M100DOF system applying SSRA-DC (left) and SSRA-DC-iCL (right) algorithms. Parameters: $d_t = 0.03$ s, $q = 3000$, $p = 500$, $\xi = 2$, $\gamma = 0$, and $S_N = 1\%$	134
Figure 7.11 – Boxplot without outliers of 100 simulations at the M100DOF system applying SSRA-DC (left) and SSRA-DC-iCL (right) algorithms. Parameters: $d_t = 0.03$ s, $q = 3000$, $p = 500$, $\xi = 2$, $\gamma = 0$, and $S_N = 1\%$	135
Figure 7.12 – $\overline{\text{FR}}(\%)$ evolution of SSRA-DC-iCL for M50DOF-a with $d_t = 0.02$ s, $q = 1500$, $p = 600$, and $S_N = 0.3\%$ (left), $S_N = 1\%$ (right).	138
Figure 7.13 – Boxplot with outliers of 100 simulations at the M50DOF-a system applying SSRA-DC (left) and SSRA-DC-iCL (right) algorithms. Parameters: $d_t = 0.02$ s, $q = 1500$, $p = 600$, $\xi = 1$, $\gamma = 1$, $\ell = 0.0005$, and $S_N = 1\%$	138
Figure 7.14 – Boxplot without outliers of 100 simulations at the M50DOF-a system applying SSRA-DC (left) and SSRA-DC-iCL (right) algorithms. Parameters: $d_t = 0.02$ s, $q = 1500$, $p = 600$, $\xi = 1$, $\gamma = 1$, $\ell = 0.0005$, and $S_N = 1\%$	139
Figure 7.15 – Theoretical linear curves of the relation between added noise S_N and attained $\overline{\text{VFR}}$ for M50DOF and M100DOF	139
Figure 7.16 – Boxplot of 1000 simulations of validation at identified systems from the original M100DOF system. Parameters: $d_t = 0.03$ s, $q = 3000$, $S_N = 0.3\%$ (left), $S_N = 1\%$ (right).	141
Figure 7.17 – MSV of original system (red) and identified system (blue) from M100DOF model with $\overline{\text{VFR}} = 99.04\%$ (left) and $\overline{\text{VFR}} = 96.52\%$ (right).	141
Figure 7.18 – Comparative view ($\overline{\text{VFR}}$) of methods with best results for M50DOF and M100DOF systems.	149
Figure 7.19 – Comparative view (CPT) of methods with best results for M50DOF and M100DOF systems.	149
Figure 7.20 – $\overline{\text{FR}}(\%)$ evolution of SSRA-DC-iCL for C-PEN with $d_t = 0.01$ s, $q = 1600$, $p = 800$, $S_N = 0.3\%$, and $\ell = 0.02$ (left), $K_p = 0.05$ (right).	152
Figure 7.21 – $\overline{\text{FR}}(\%)$ evolution of SSRA-DC-iCL for C-PEN with $d_t = 0.01$ s, $q = 1600$, $p = 800$, $S_N = 1\%$, and $\ell = 0.02$ (left), $K_p = 0.05$ (right).	152
Figure 7.22 – $\overline{\text{FR}}(\%)$ evolution of SSRA-DC-iCL for C-PEN with $d_t = 0.02$ s, $q = 2000$, $p = 500$, $K_p = 0.05$, and $S_N = 0.3\%$ (left), $S_N = 1\%$ (right).	153

Figure 7.23 – Outputs y_x (left) and y_θ (right) from OS (red) and IS (blue) for: $d_t =$ 0.02 s , $q = 2000$, $p = 500$, $K_p = 0.05$, and $S_N = 0.3\%$	154
Figure 7.24 – Boxplot with outliers of C-PEN system simulations.	157
Figure 7.25 – Comparative view (\overline{VFR}) of methods for C-PEN system.	158
Figure 7.26 – Comparative view (CPT) of methods for C-PEN system.	158
Figure 7.27 – MSV of the OS (red) and the IS (blue), comparing the best (left) and worst (right) results of \overline{VFR}	160
Figure 7.28 – Step Response graphs from the OS (red) and IS (blue) when $\overline{VFR} =$ 98.62% for both outputs of the C-PEN system ($d_t = 0.01\text{ s}$).	160
Figure 7.29 – Step Response graphs from the OS (red) and IS (blue) when $\overline{VFR} =$ 95.84% for both outputs of the C-PEN system ($d_t = 0.02\text{ s}$).	161

LIST OF TABLES

Table 1.1 – Main contributions summary	32
Table 3.1 – Schematic representation of ARX, FIR, and OE models, comparatively. . .	47
Table 3.2 – Polynomial sizes and orders	51
Table 5.1 – Displacements measured and excitation forces in the M50DOF and M100DOF models	95
Table 5.2 – Mass and stiffness values from the elements of the M50DOF and M100DOF models	95
Table 6.1 – Time response results	108
Table 6.2 – Natural frequencies [rad/s] of the continuous-time and discretized system . .	113
Table 6.3 – Comparison of Fit Rate index for PRBS and GWN excitations	116
Table 6.4 – Time response results with 1% of measurement noise added into the system	118
Table 6.5 – Maximum Frequency (f_{max}) of the simulated CHIRP signals.	122
Table 6.6 – Comparative results of the excitation signals for the M100DOF system with: $d_t = 0.03$ s, $q = 9000$, and $p = 900$	123
Table 7.1 – Limits of sampling frequency (ω_s) and sampling time (d_t) for the discretized systems	125
Table 7.2 – SSRA-DC-iCL and SSRA-DC comparative results for M50DOF system: $d_t = 0.02$ s, $q = 1500$, $p = 600$, $\xi = 2$, $\gamma = 2$	133
Table 7.3 – SSRA-DC-iCL and SSRA-DC comparative results for M100DOF system: $d_t = 0.03$ s, $q = 3000$, $p = 500$, $\xi = 2$	135
Table 7.4 – SSRA-DC-iCL and SSRA-DC comparative results for M50DOF-a system: $d_t = 0.02$ s, $q = 1500$, $p = 600$, $\xi = 1$, $\gamma = 1$, $\ell = 0.0005$	137
Table 7.5 – Validation of 1000 simulations for identified systems from the original M100DOF at $d_t = 0.03$ s and $q = 3000$	140
Table 7.6 – Comparative results for: M50DOF, $dt = 0.02$ s, $q = 1500$, $S_N = 0.3\%$. . .	145
Table 7.7 – Comparative results for: M50DOF, $dt = 0.02$ s, $q = 1500$, $S_N = 1\%$. . .	145
Table 7.8 – Comparative results for: M100DOF, $dt = 0.03$ s, $q = 3000$, $S_N = 0.3\%$. .	146
Table 7.9 – Comparative results for: M100DOF, $dt = 0.03$ s, $q = 3000$, $S_N = 1\%$. . .	147
Table 7.10 – Comparative results for C-PEN system: $d_t = 0.01$ s, $q = 1600$, $p = 800$. . .	155

Table 7.11 – Comparative results for C-PEN system: $d_t = 0.02$ s, $q = 2000$, $p = 500$. . . 156

Table 7.12 – Comparative results of C-PEN system under nonlinear OS and linearized OS .164

LIST OF ABBREVIATIONS AND ACRONYMS

ARX	AutoRegressive with External input
ARMAX	AutoRegressive Moving Average with External input
BFR	Best Fit Rate
BJ	Box-Jenkins model structure
C-PEN	Cart-Pendulum system
CG	Center of gravity of the pendulum rod
CHIRP	Sine Sweep signal
CPT	Computational processing time
CVA	Canonical Variate Analysis
ERA	Eigensystem Realization Algorithm
ERA-DC	Eigensystem Realization Algorithm with Data Correlation
FIR	Finite Impulse Response model
FR	Fit Rate index
GWN	Gaussian White-Noise signal
IS	Identified system
LS	Least-Squares method
LTI	Linear time-invariant system
M5DOF	Mass-spring-damper system of 5 degrees of freedom
M50DOF	Mass-spring-damper system of 50 degrees of freedom
M50DOF-a	Mass-spring-damper system of 50 degrees of freedom with accelerometers
M100DOF	Mass-spring-damper system of 100 degrees of freedom

MIMO	Multiple-Input-Multiple-Output
MOESP	Multivariable Output Error State-Space
MSV	Maximum Singular Values
N4SID	Numerical Subspace State Space System Identification
OE	Output Error model
<i>OS</i>	Original system
PEM	Prediction Error Method
PRBS	Pseudo Random Binary Sequence signal
RK4	Runge Kutta 4 th order numerical method
SI	System Identification
SIM	Subspace Identification Method
SIMO	Single-Input-Multiple-Output
SISO	Single-Input-Single-Output
SSRA	State-Space Realization Algorithm
SSRA-DC	State-Space Realization Algorithm with Data Correlation
SSRA-DC-iCL	State-Space Realization Algorithm with Data Correlation in iterative Closed-Loop
SVD	Singular Value Decomposition
VFR	Validated Fit Rate index

LIST OF SYMBOLS

A, B, C, D	State-space model matrices
$\mathcal{A}, \mathcal{B}, \mathcal{C}, \mathcal{D}, \mathcal{F}$	Polynomials from the autoregressive model structure
$\mathcal{C}_{\mathcal{F}}$	PRBS clock frequency
C_r	Crest Factor of a signal
d_t	Sampling time
e	White-noise source or sequence of independent random variables
f_s	Sampling frequency in Hz
f_{min}	Minimum frequency from the CHIRP signal configuration in Hz
f_{max}	Maximum frequency from the CHIRP signal configuration in Hz
F_H, F_V	Horizontal and Vertical component forces from the free body diagrams
FR_j	Fit Rate index from output j of the identified system
\overline{FR}	Average FR_j from all outputs of the identified system
\mathcal{G}	Process transfer function (from input to output)
\mathcal{H}	Noise transfer function (from white-noise to output)
H	Markov parameters matrix
H_v	Markov parameters block matrices of H
$H_{(i)}$	Markov parameters matrix at the i th iteration
H_h	Hankel matrix
H_{sh}	Shifted Hankel matrix
H_k	Hankel matrix with generalized discrete-time shifting samplings
\mathcal{H}_k	Block correlation Hankel matrix

i, j, m	Integers for overall use
I	Moment of inertia
k	Discrete-time sample indicator
\mathbf{K}_p	Proportional gain matrix
K_{p_j}	Proportional gain value (diagonal element of \mathbf{K}_p)
ℓ	Weighting factor of the proportional gain K_{p_j}
L	Half of the pendulum rod length
m_i, d_i, k_i	i th element of mass, damping and stiffness from multi degree of freedom model
$\mathcal{M}, \mathcal{D}, \mathcal{K}$	Mass, damping, stiffness matrices
n	State-space order of the realization
n_m	Orders of the polynomials $\{\mathcal{A}, \mathcal{B}, \mathcal{C}, \mathcal{D}, \mathcal{F}\}$ with $m = \{a, b, c, d, f\}$
\mathbf{O}, \mathbf{W}	Observability and controllability matrices
p	Determines the Hankel matrix order
q	Number of samples
r_u	Autocorrelation function of the variable u
r_{uy}	Cross-correlation function between the variables u and y
\mathbf{R}_u	Autocorrelation matrix of the vector \mathbf{u}
\mathbf{R}_{uy}	Cross-correlation matrix between the vectors \mathbf{u} and \mathbf{y}
$\mathcal{R}h_k$	Data correlation matrix
S_N	Set-point value of measurement noise
t	Time
T	Period of a signal

$\mathbf{u}(k)$	Discrete-time input vector at instant k
$u_j(k)$	j th input element of $\mathbf{u}(k)$
\mathbf{U}	Input matrix of MIMO system
\mathbf{U}_s	Input matrix of SISO system
\mathbf{U}_V	Input matrix of MIMO system from validation data
\mathbf{U}, \mathbf{V}	Orthonormal matrices from singular value decomposition (SVD)
\mathbf{v}	Measurement noise vector
\mathbf{V}	Measurement noise matrix
\mathbf{V}_V	Measurement noise matrix to the validation stage
VFR_j	Validated Fit Rate index from output j of the identified system
$\overline{\text{VFR}}$	Average VFR_j from all outputs of the identified system
\mathbf{V}_n	Cost function to be minimized
\mathbf{w}	Process noise (or input noise) vector
\mathbf{x}	State vector
$\mathbf{x}^d, \mathbf{x}^s$	State vectors from deterministic and stochastic subsystems
\mathbf{X}	State vector (Laplace domain)
$\hat{\mathbf{y}}$	Estimated output (vector with q samples)
$\mathbf{y}(k)$	Discrete-time output vector at instant k
$\hat{y}(k)$	Estimated output element from $\hat{\mathbf{y}}$
$\mathbf{y}^d, \mathbf{y}^s$	Output from deterministic and stochastic subsystems
$y_j(k)$	Element of $\mathbf{y}(k)$ related to the output j
\mathbf{y}_x	Cart displacement output from the Cart-Pendulum system
\mathbf{y}_θ	Pendulum angle output from the Cart-Pendulum system

\mathbf{Y}	Output matrix of MIMO system
\mathbf{Y}_j	j th output (row) of \mathbf{Y} matrix
\mathbf{Y}_s	Output matrix of SISO system
\mathbf{Y}_V	Output matrix of MIMO system from validation data
z, z^{-1}	Forward and backward shift operators
α, β	Integers for overall use
γ	Determines the number of columns of the matrix \mathcal{H}
$\Delta \overline{\text{VFR}}$	Improvement gain of the $\overline{\text{VFR}}$
ε	Residual matrix of Markov parameters
ζ_i	i th damping ratio
θ	Unknown parameters to be estimated
ν	Predictor error vector
ξ	Determines the number of rows of the matrix \mathcal{H}
σ_i	i th singular value
σ_m^2	Variance of the variable m
Σ_i	Singular value matrix from SVD of order higher than n
Σ_n	Singular value matrix from SVD of order equal to n
Φ	Covariance of the residual matrix ε
$\psi(k-1)$	Regression vector one step back prediction
Ψ	Regression matrix
$\omega_{d_{max}}$	Maximum damped frequency in rad/s
ω_{max}	Maximum frequency in rad/s
ω_{min}	Minimum frequency in rad/s

ω_{n_i}	i th natural frequency in rad/s
ω_s	Sampling frequency in rad/s
$\omega_{s_{min}}$	Minimum sampling frequency in rad/s
$\omega_{s_{max}}$	Maximum sampling frequency in rad/s
$E(\cdot)$	Statistical expected value operator or mathematical expectation
$\frac{d}{dt}(\cdot), (\dot{\cdot})$	First order derivatives
$\frac{d^2}{dt^2}(\cdot), (\ddot{\cdot})$	Second order derivatives
$(\cdot)^\dagger$	Moore-Penrose pseudoinverse of a matrix
$(\bar{\cdot})$	Average value of a variable
$(\hat{\cdot})$	Estimated value of a variable
$(\cdot)_{(i)}$	i th iteration of a variable
$\ (\cdot)\ $	Frobenius norm of a matrix

CONTENTS

1	Introduction	25
1.1	A view of System Identification	25
1.2	Thesis Subjects and Research Scope	29
1.3	Objectives and Original Contributions of the Thesis	31
1.4	Thesis structure	32
2	Literature overview	34
2.1	Overview of first researches	34
2.2	Identification of linear systems	36
2.3	State-Space Realization Algorithm	38
2.4	Input excitation signals	40
2.5	Challenges and trends in System Identification	42
3	Identification methods for comparative analysis	44
3.1	Introduction	44
3.2	FIR, ARX and OE	47
3.3	ARMAX	49
3.4	Box and Jenkins	50
3.5	Polynomials sizes and orders for MIMO systems	51
3.6	N4SID	53
3.7	Some considerations	58
4	The novel SSRA-DC-iCL method and its background	59
4.1	Introduction	59
4.2	SSRA concepts and formulation	60
4.2.1	SSRA for Single-Input-Single-Output (SISO) systems	60
4.2.2	SSRA for Multiple-Input-Multiple-Output (MIMO) systems	63
4.2.3	The Least-Squares in Markov matrix computing	68
4.3	SSRA-DC concepts and formulation	69
4.3.1	Fundamentals concepts	69
4.3.2	SSRA-DC basic formulation	72
4.4	The novel method SSRA-DC-iCL	75

4.4.1	Condition of small samples set available	76
4.4.2	The proposed method	76
4.4.3	Markov matrix updating	80
4.4.4	The algorithm of SSRA-DC-iCL	83
5	Systems and Models configuration	84
5.1	Introduction	84
5.2	Excitation signals	84
5.2.1	Pseudo Random Binary Sequence (PRBS)	85
5.2.2	Sine Sweep (CHIRP)	88
5.2.3	Gaussian White-Noise (GWN)	90
5.3	Measurement noise	91
5.4	Mass-Spring-Damper models	92
5.5	Cart-Pendulum model	96
5.6	Procedure of data supply to the algorithms	101
5.7	Systems discretization	101
5.7.1	For the Mass-Spring-Damper system	102
5.7.2	For the Cart-Pendulum system	103
6	Analysis of the settings influence on SSRA	104
6.1	Specific settings and system configurations for the SSRA simulations	104
6.2	Time response analysis to the M5DOF system	107
6.3	Frequency response analysis to the M5DOF system	112
6.4	Analysis for white-noise excitation and measurement noise in the M5DOF . . .	116
6.5	SSRA performance comparison for the 3 excitation signals in the M100DOF .	119
7	Results and discussion of the SSRA-DC-iCL method	124
7.1	Introduction	124
7.2	Specific settings and system configurations for the SSRA-DC-iCL simulations .	124
7.3	Analysis of the number of samples reduction in the SSRA-DC simulations . . .	126
7.4	SSRA-DC-iCL algorithm performance	128
7.5	Statistical analysis of the SSRA-DC and SSRA-DC-iCL methods	131
7.5.1	Simulations analysis of the M50DOF system	132
7.5.2	Simulations analysis of the M100DOF system	134
7.5.3	Simulations analysis of the M50DOF-a system (with accelerometers) .	136

7.5.4	Influence of the noise levels on the results	138
7.6	Validation aspects to ratify the results	140
7.7	Frequency response analysis to attest the previous results	141
7.8	Comparative statistical analysis with reference identification methods	142
7.8.1	Comparison for the M50DOF system	144
7.8.2	Comparison for the M100DOF system	146
7.8.3	Overview of the comparative analysis	148
7.9	Cart-Pendulum system simulations results	150
7.9.1	Specific settings for simulations with the C-PEN system	150
7.9.2	SSRA-DC-iCL simulation results and analysis	151
7.9.3	Comparative statistical analysis with reference identification methods	153
7.9.4	Comparative analysis between nonlinear and linearized C-PEN systems	159
8	Highlights and concluding remarks	165
8.1	Overview of the thesis	165
8.2	Highlights from the results	166
8.3	Concluding remarks	168
8.4	Possible future works	170
Bibliography		172
APPENDIX A Mathematical development of the SSRA with Data Correlation		181

1 INTRODUCTION

1.1 A view of System Identification

Representing a system and physical phenomena through mathematical models has always been a significant challenge in many knowledge areas. Since ancient times, men have been searching for ways to mathematically express what is observed and experimented with within their continuous creative process. Despite the development of new modeling techniques, the old challenge of reproducing a physical system with a mathematical analog remains the same. The growing necessity to construct models from observed data rather than mathematical equations, considering the increase of system complexity, and the technological advancements with the rise of computational processing capacity, made it appear the procedure known as empirical modeling, or better known nowadays System Identification (SI) ([Aguirre, 2015](#)).

System identification is the science field that applies the technology of building mathematical models of a dynamical system from observed input-output data. Or as defined by Juang in ([Juang, 1994](#)): “Identification is the process of developing or improving a mathematical model of a physical system using experimental data to describe the input, output and noise relationship.” SI techniques search for having a better-identified system in terms of more straightforward to use and more accurate ([Ljung, 2010a](#)). System identification is a recognized sub-area of Automatic Control with over 60 years of history of methods and algorithms development, comprehending industrial applications and software packages as the Matlab System Identification Toolbox ([Ljung, Lennart, 2014](#)). For the standard Automatic Control view, SI can be considered an inverse problem, given that usually, the output is the result of a convolution between the input and the system’s response. Thus, SI is a deconvolution problem ([Pillonetto et al., 2014](#)).

The fundamental concept of system identification is summarized through the diagrams presented in Figure 1.1. Figure 1.1(a) represents the unknown system to be identified once consisting of measured outputs \mathbf{Y} attained accordingly the inputs \mathbf{U} that excite the system subject to unmeasurable perturbations \mathbf{V}_x . Figure 1.1(b) shows the identified system obtained that can be represented by a parametric model providing the state-space matrices \mathbf{A} , \mathbf{B} , \mathbf{C} , \mathbf{D} . The system output $\hat{\mathbf{Y}}$ becomes an estimated output as stated by the obtained model. Figure 1.1(c) synthesizes the SI process where a set of inputs \mathbf{U} and outputs \mathbf{Y} are employed as in-

puts to an identification method that is executed to generate a state-space model, for instance (Aguirre, 2007).

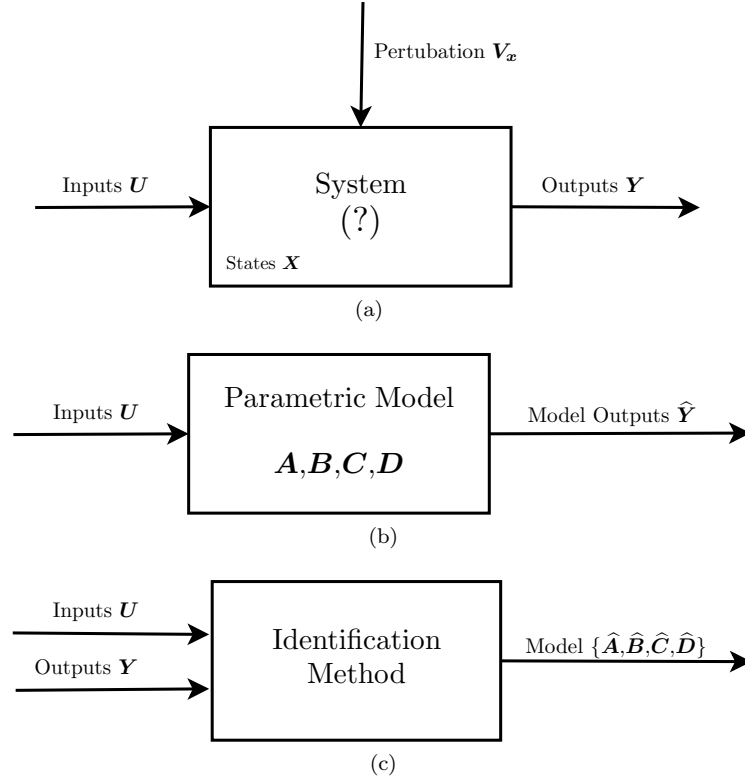


Figure 1.1 – SI Fundamental concept: an unknown system to attain a parametric model through an identification method.

SI modeling techniques count on three classification forms: white-box modeling, black-box modeling, and gray-box modeling. The white-box modeling requires a good knowledge of the system under study to provide the physical laws needed for describing the system thoroughly. For this reason, this modeling is also called modeling by physics or conceptual modeling. SI is the area that explores alternatives solutions to the white-box modeling when there is no need for previous knowledge of the process, or no information can be taken. The methods related to this environment are encompassed by the black-box modeling (Giordano; Sjöberg, 2018), which is the subject of the present work. The gray-box modeling technique is of considerable challenge in SI. According to the system's initial conditions, in this case, additional information can be added to modeling a process that would be considered a typical black-box (Aguirre, 2015).

Some concepts about System Identification subjects shall be introduced here as the basis of the knowledge applied all over the work. As is usual in SI, a discrete-time representation of equations will be used in the context rather than continuous-time characterization.

Experimental data from measurement devices are recorded in digital format of numbers as a basis of system identification, being discrete by nature (Juang, 1994). Model parametrization based on the physical characterization of the process is inherently more appropriate to employ continuous-time models in SI once the physical laws are mathematically determined with differential equations (Soderstrom; Stoica, 1989). In this case, the identification comes closer to a white-box modeling.

In this work, the identified systems will be considered and conceptually built as linear time-invariant (LTI). Most of the application models here are assumed from a linear structural system with the input-output experimental data coming from simulations. Accordingly to Chen in (Chen, 1984), a system is called a linear system if, for every initial time t_0 and any two state-input-output pairs

$$\left. \begin{array}{l} \mathbf{x}_i(t_0) \\ \mathbf{u}_i(t), t \geq t_0 \end{array} \right\} \rightarrow \mathbf{y}_i(t), t \geq t_0, \quad (1.1)$$

where, for $i = 1, 2$, following the superposition property, yields:

$$\left. \begin{array}{l} \alpha_1 \mathbf{x}_1(t_0) + \alpha_2 \mathbf{x}_2(t_0) \\ \alpha_1 \mathbf{u}_1(t) + \alpha_2 \mathbf{u}_2(t), t \geq t_0 \end{array} \right\} \rightarrow \alpha_1 \mathbf{y}_1(t) + \alpha_2 \mathbf{y}_2(t), t \geq t_0, \quad (1.2)$$

for any real constant α_i , where $\mathbf{y}_i, \mathbf{u}_i$, and \mathbf{x}_i are outputs, inputs and states of the system, respectively.

The respective linear system is also stated as time-invariant if, for every state-input-output pair as in Equation (1.1), and any period T , the following is worthy:

$$\left. \begin{array}{l} \mathbf{x}(t_0 + T) \\ \mathbf{u}(t - T), t \geq t_0 + T \end{array} \right\} \rightarrow \mathbf{y}(t - T), t \geq t_0 + T. \quad (1.3)$$

Accordingly to Chen, Equation (1.3) shows that “if the initial state t_0 is shifted to time $t_0 + T$ and the same input waveform is applied from $t_0 + T$ instead of from t_0 , then the output waveform will be the same except that it starts to appear from time $t_0 + T$ ”. For a LTI system, it can be assumed, without loss of generality that $t_0 = 0$. From Equation (1.3), it is realized that if the initial state and input do not change each other over time, no matter at what time they are applied, the output values will always not change either (Chen, 1984). The time-shifting aspect takes part in the time-invariant characteristic of a system. However, it can not be misunderstood with the dynamics of a system that does not change itself in the period in which the system is considered. A LTI system with a scalar output signal $y(t)$ and a scalar input signal $u(t)$ was

synthetically defined by Ljung in (Ljung, 1999): “The system is said to be time invariant if its response to a certain input signal does not depend on absolute time. It is said to be linear if its output response to a linear combination of inputs is the same linear combination of the output responses of the individual inputs”.

Additionally to the application models coming from simulations of typical linear systems, as previously conceptualized, this research extends the foreseen scope to also compose the input-output data as from simulations of a nonlinear dynamical system. This nonlinear system will be presented in full in Chapter 5, together with the definitions and characteristics of the linear systems.

Throughout the work, mostly in Chapter 5, the steps and procedures for providing the way how the System Identification process should attain the results are presented and discussed in more detail. For now, the objective here is to describe a synthesis of the overall stages involved in the SI process, as following (Ljung, 1999; Aguirre, 2015):

1. Dynamical tests and data record: the input-output data are determined during an identification experiment that can be obtained on-line while the SI algorithm is working (recursive algorithms) or off-line, which is more usual, where the data are stored previously to the posterior algorithm processing. This step is crucial to the algorithm’s effectiveness, where fundamental concerns such as excitation signals choosing and eventual constraints should be well planned in the experiment.
2. Select the model structure and/or the SI method: choose a set of candidate models first. A priori knowledge of the system characteristics and engineering intuition can help to define a specific model to be tested. This SI stage is considered one of the most difficult choices with a significant impact on the identification performance.
3. The setting of the algorithm parameters: this step refers to the adjustments of the parameters required to the method’s functioning. This task can be straightforward and brief depending on the SI algorithm chosen. On the other hand, even when only a few parameters are necessary, such as the systems’ order, this can be challenging if the method’s characteristics and application knowledge is poor. In this step, the parameter setting can also require systems’ information.
4. Model estimation: this refers to the own SI algorithm processing, where the estimated parameters of the identified system are obtained. In some methods and software tools,

the model estimation provides the functionality of determining the best model based on how the models perform when they try to reproduce the data. Assessing this result is essential to avoid inconsistencies as the loss of identified system poles. This functionality is performed before processing the SI algorithm.

5. Model validation: after achieving a particular identified system composed of the complete model with its estimated parameters, it is time to evaluate if that system is good enough to incorporate the characteristics of interest from the original system. For this appraisal task, applying an index to measure the adherence of the identified system related to the original system is desired. In this work, a Fit Rate indicator will be used to support this test of identified system confidence.

The previous steps describe a natural and logical flow in the SI process. However, it may be necessary to go back and revise some of the steps accomplished if the result is not the expected, indicating that the model used for the identified system attained can be deficient for that identification purpose.

Lastly, it should be pointed out that the terms **model** and **method** can be applied to the same representation. Both terms will then refer to a straight mathematical representation or an algorithm structure all along with this work, mainly for the autoregressive models, which will be discussed in Chapter 3.

1.2 Thesis Subjects and Research Scope

This thesis aims to study and propose alternatives to tackle some drawbacks of the traditional State-Space Realization Algorithm (SSRA) method regarding the identification effectiveness of large MIMO (Multiple-Input-Multiple-Output) systems under measurement noise conditions. For that, developing a new SI method based on the SSRA arises as a challenge, improving the correlated methods by introducing features related to the iterative algorithms. The typical scenario of this contribution considers the algorithm applied to MIMO systems with additive measurement noise and a reduced number of samples acquired from the process.

A remark of this developed research regarding MIMO systems should be mentioned when compared to multivariable systems submitted to identification methods that work with SISO (Single-Input-Single-Output) systems. In this concept, an identification method configured to work with only SISO systems needs to generate $r \times s$ state-space models to depict the

dynamic of a multivariable system of r outputs and s inputs. The SI methods approached in this work provide an identification solution with a single state-space model that sufficiently depicts the dynamic of the multivariable system in an integrated way.

The new approach represents an evolution taken from the SSRA with data correlation (SSRA-DC), especially under noisy systems conditions. The methods here called SSRA and SSRA-DC stem from the traditional Eigensystem Realization Algorithm (ERA) (Juang; Pappa, 1985), and ERA with Data Correlation (ERA-DC) (Juang *et al.*, 1988), respectively. These methods add some functionalities such as the attainment of eigenvectors, eigenvalues, natural frequencies, and modal damping, which are not considered in the SSRA and SSRA-DC algorithms, the basis of this work. SSRA and SSRA-DC are developed starting from the input and output data set until the identified system is obtained through the state-space realization. The novel method developed in this research stems from the SSRA-DC by applying the iterative concept to the input-output data set that has its representation in charge of the Markov parameters matrix. The data correlation treatment as an even resource in the SSRA-DC to minimize the noise effects starts to receive the features from an iterative algorithm to add more effectiveness to the identification method.

Another purpose of the present work is to introduce a State-Space Realization Algorithm for generalized multi-input signals, similar to the General Realization Algorithm implementation (De Callafon *et al.*, 2008). However, analyzing here the algorithm settings in terms of the influence of input excitation and parameter adjustments in the results of the simulation tests. Rather than an impulsive signal employed in the traditional ERA, the excitation comes from an arbitrary Pseudo Random Binary Sequence (PRBS) signal in the first phase of the work.

The research scope considered applying the methods employing only simulated experiments to compose the input-output data set. The concern of the systems' excitation to the SI performance contributed to the research applying Pseudo Random Binary Sequence (PRBS) as a novelty in terms of excitation signal to the SSRA. The PRBS signal was also submitted to a comparative outlook with CHIRP signals and Gaussian White-Noise (GWN) signals. Nevertheless, the research steps encompassing the novel method had only the GWN as input excitation following the traditional application of the White-Noise in the structural identification.

An index was thought to be a quality tool aiming to measure the identified system's effectiveness for the SI developments. Applying a well-known and established indicator in the identification area was crucial, making it feasible to use one of the main indexes applied

at Matlab's SI Toolbox (Ljung, Lennart, 2014). The Fit Rate index (FR) employment as an indicator for the SSRA and its derived algorithms served as a standard evaluation criterion for comparison purposes all over the work.

1.3 Objectives and Original Contributions of the Thesis

The initial work planning relied on developing a broad study and looking over System Identification methods with application analysis for some conditions that could distinguish the systems to be identified by their complexity. The complex systems would be characterized as of considerable size in the length of the system matrix (system's order), with MIMO variables, and working in the noise presence. The diversification of these conditions for several types of methods would support research focusing on the contribution in terms of a broad data survey of SI performance. Therefore, this would be considered some original contributions of the thesis.

Considering some difficulties in the SSRA configuration settings, the research project had a starting objective of studying algorithm parameters influencing the method performance entrusted to the results measured by the Fit Rate index (FR). This study led to the assessment of the relationship between algorithm parameters influencing the SI results.

In the sequel, considering the takeaways from the initial developments, the main objective of this work relies on minimizing effectiveness problems that occur with the increase of MIMO system size and is motivated by the searching for SSRA improvements. The algorithm enhancement provided a novelty contribution of the SSRA to tackle the possible measurement noise in the systems. The implemented concept of an iterative algorithm in a closed-loop with Markov parameters' in the feedback condition supported the technique's application to the SSRA Data Correlation (SSRA-DC) method. This method further improved its situation in the face of exposure to the noisy system condition since the SSRA-DC was already designed to become better than the traditional SSRA in those circumstances of noise.

Some specific objectives complementary to the previously described primary purpose shall be mentioned here. A comparative analysis between the most well-known SI methods is performed, incorporating the new iterative SSRA-DC-iCL algorithm, thus, leading to an even more significant contribution to this work. Also, the new iterative method was submitted to simulations of a nonlinear system to compose the input-output data set. In this condition, a Single-Input-Multiple-Output (SIMO) system with only two outputs but with nonlinear dynam-

ical characteristics was tested similarly to the linear systems to evaluate the novel method's effectiveness under nonlinearities conditions straightly coming from the original dynamics of the system.

A brief view of the thesis parts (chapter or section), where each contribution phase of the research takes part as the main subject, is presented in Table 1.1.

Table 1.1 – Main contributions summary

Contribution	Chapter(C) or Section(S)
Phase 1: Influence of SSRA settings in SI effectiveness	S:4.2; C:6
Phase 2: New iterative SSRA-DC-iCL method	S:4.3; S:4.4; S:7.4; S:7.5
Phase 3: Comparison between iterative SSRA-DC-iCL and reference methods	C:3; S:4.4; S:7.8
Phase 4: Evaluation of the methods for a nonlinear system simulated	S:5.5; S:7.9

1.4 Thesis structure

In this section it is presented a summary of the research topics and the main subjects discussed throughout the chapters and sections, depicting how the text was organized:

- **Chapter 2 - Literature overview:** Relevant publications available in the literature related to the research subjects are described, composing a historical view of the researches in the thesis correlated area, and more recent challenges.
- **Chapter 3 - Identification methods for comparative analysis:** The most well-known SI methods designed for linear systems are presented, introducing a summed up review of its main characteristics and features.
- **Chapter 4 - The novel SSRA-DC-iCL method and its background:** A complete background with mathematical formulations of the traditional State-space Realization Algorithm is presented as well as the theory to support the following approach. The SSRA Data Correlation (SSRA-DC) is also described as an algorithm version derived from SSRA to attend systems under noise conditions and as the fundamental basis to the new method. The research's main contribution is reported, presenting the SSRA-DC-iCL characteristics for systems with measurement noise. A block diagram is introduced to represent the iterative method implemented. The new algorithm is shown in detail.

- **Chapter 5 - Systems and Models configuration:** Presents supporting conditions established in the research to provide the input data through simulations, describing the configuration and characteristics of input excitation signals, the simulations procedure, the mass-spring-damper models, the nonlinear Cart-Pendulum model, the systems discretization, and the measurement noise applied.
- **Chapter 6 - Analysis of the settings influence on SSRA:** The traditional state-space realization algorithm based on the ERA method is tested with several algorithm settings showing the relation between the parameters configurations and the correspondent results, taking the Fit Rate index as a guide for better algorithm configuration searching.
- **Chapter 7 - Results and discussion of the SSRA-DC-iCL method:** The results from numerical experiments carried out through several data set simulations are presented and discussed. Firstly, it contemplates the results regarding the second phase of the research accomplished with the SSRA-DC-iCL algorithm for some systems' configurations. For the third research phase, the chapter introduces a broad comparison between the SI methods approached in Chapter 3 and the iterative SSRA-DC-iCL method (Section 4.4). In the fourth phase, the nonlinear system presented in Section 5.5 has its results detailed in Section 7.9. The comparative analysis also considers the computational processing time (CPT). Hence, the overall performance of the methods is taken in this analysis.
- **Chapter 8 - Highlights and concluding remarks:** The conclusions and central topics of the research are presented, pointing out the more relevant discussion items and gaps to motivate future works.
- **Appendix A - Mathematical development of the SSRA with Data Correlation:** Presents the mathematical steps with the corresponding equations of the method SSRA-DC until the attainment of the identified system in the state-space representation.

2 LITERATURE OVERVIEW

2.1 Overview of first researches¹

The term Identification attributed to determining input-output relationships in a black-box system was pioneered introduced by Zadeh in (Zadeh, 1956). More than four decades before that, Fisher already proposed the Maximum Likelihood estimate method (Fisher, 1912), which has turned into one of the most important developments in statistics in the last century. This method of probability estimate maximizes the likelihood of the input data. Fischer's theory led to a huge impact, influencing the development and evolution of System Identification since that time. More than a century before the Maximum Likelihood method, in 1809, Gauss introduced the basic principles of least-squares (Stigler, 1981), which determined the most modern SI methods' theories.

The work of Eykhoff in 1968 (Eykhoff, 1968), stated that “The Markov and least-squares estimate had been derived from the Maximum Likelihood estimate under the assumption of Gaussian noise.” Eykhoff comparatively clarified the different estimates methods existing until that time: Maximum likelihood, least-squares, Markov, and Bayes. Concomitantly, Balakrishnan and Peterka have written about estimation methods applied to linear, nonlinear, dynamical, and noise systems, concluding that despite significant progress in system identification had been accomplished, many problems remain (Balakrishnan; Peterka, 1969).

Based on estimation theory like the well-known least-squares and Maximum Likelihood, the basic SI methods were developed in 1960 and 1970 when computers became available to process the respective calculations stem from the algorithms. A record number of researches regarding these developments were written in these decades, including releasing many books. In 1971, Åström and Eykhoff made a relevant contribution with a broad survey paper that given an overview and prospect of System Identification (Åström; Eykhoff, 1971). The classification of SI methods is a challenging task considering the many aspects characterizing the methods. The works of Eykhoff (Eykhoff, 1968), and Balakrishnan and Peterka (Balakrishnan; Peterka, 1969) had already introduced this subject, but Åström and Eykhoff (Åström; Eykhoff, 1971) consolidated this concept summarized as follows:

¹ Some parts presented in this chapter were published in the papers (Soares Jr; Serpa, 2021; Soares Jr; Serpa, 2022).

- The class of models: parametric or nonparametric models. In this thesis, all the approached models are parametric, as it is used nowadays for modern system identification methods. The nonparametric models relate to models represented by transfer functions, impulse response, spectral densities, and other forms different from mathematical equations containing parameters. The parametric models are related to the models established by parameters, which are numbers, coefficients, characterizing them. In other words, when there is information a priori about the system as the ones from physical laws to describe the system, it can be represented by a parametric model ([Aguirre, 2015](#)).
- The class of input signals: determined by the type of input signals (impulse functions, step functions, colored or white-noise, sinusoidal, PRBS, etc). This work employed the PRBS, the CHIRP, and the GWN signals in the simulations. Considering these signals are similar in characteristics regarding being persistently exciting, which is sufficient to provide consistent estimates of least-squares and maximum likelihood ([Åström; Eykhoff, 1971](#)), this classification item do not differentiate the signals applied in the present research.
- The error criterion: refers on how the model handles error concepts. The options are output error, input error or generalized error. The first one is the type adopted in this work, which occurs when the white-noise errors in the output measurement is the only disturbance acting.
- Computational aspects: type of the iterative minimization in the optimization problem to find the parameters that lead to lower errors. The possible techniques are the gradient method, the steepest descent method, Newton's method, the conjugate gradient method, etc. For the developed iterative method based on SSRA, the previously mentioned minimization techniques are not applicable. This classification criterion is not suitable for the iterative methods presented in Chapter 3, as the respective methods employed from Matlab's SI Toolbox provide an automatic mode to choose the best minimization method.

Considering several characteristics in common between the models that make it difficult to separate through classification, it will be following applied some SI research subjects to discriminate the most relevant literature references, which are straightforwardly engaged with this work's contents.

2.2 Identification of linear systems

As seen in the section before, the firsts theoretical basis of System Identification came up from more than a century. Issues related to the state-space realization and minimal realization of linear systems appeared in a pioneering investigation as in the works of Tether in 1970 (Tether, 1970), and Silverman in 1971 (Silverman, 1971). Some years earlier, in 1968, Åström introduced the simple equation error model which later came to be known as ARX (Autoregressive with Exogenous input) model (Åström, 1968), as follows:

$$y(k) + a_1y(k-1) + \dots + a_ny(k-n) = b_1u(k-1) + \dots + b_nu(k-n) + e(k), \quad (2.1)$$

in a discrete-time SISO system where k is the discrete-time sample indicator.

A state-space representation of a linear system in continuous-time, can be written as (Silverman, 1971):

$$\begin{aligned} \dot{\mathbf{x}}(t) &= \mathbf{A}\mathbf{x}(t) + \mathbf{B}\mathbf{u}(t), \\ \mathbf{y}(t) &= \mathbf{C}\mathbf{x}(t), \end{aligned} \quad (2.2)$$

where $\mathbf{y}(t) \in \mathbb{R}^r$, $\mathbf{u}(t) \in \mathbb{R}^s$, and $\mathbf{x}(t) \in \mathbb{R}^n$ are the output, input and state vectors, respectively. The system is assumed to be represented by the triple $(\mathbf{A}, \mathbf{B}, \mathbf{C})$, where these matrices have sizes compatible with the respective vectors in the continuous-time system. The output equation can consider a more general case when a direct transmission matrix is present, i.e., $\mathbf{y}(t) = \mathbf{C}\mathbf{x}(t) + \mathbf{D}\mathbf{u}(t)$.

The SI representations depicted by Equations (2.1) and (2.2), related to autoregressive and in state-space forms, respectively, are primary representation types that will be seen all over this work. However, they will be presented in the discrete-time form, as was mentioned in Section 1.1.

The work of Gopinath in 1969 should be held as the first method known for System Identification of linear time-invariant systems from MIMO data (Gopinath, 1969). In 1980, Kailath presented detailed algebraic aspects of multivariable linear systems, introducing some properties related to polynomial matrices (Kailath, 1980). A pioneering publication about linear-regression models in a general framework with Single-Input-Single-Output (SISO) systems was released by Ljung and Soderstrom in 1983 (Ljung and Soderstrom, 1983).

The Prediction Error Method (PEM), which will be conceptualized in the Chapter 3, was introduced by Ljung in 1976 (Ljung, 1976). PEM is one of the most well-known SI methods that works iteratively supported by the least-squares method. The method is employed

by many of the autoregressive/polynomials models and even basic state-space models. PEM is available integrated to the models of the SI Toolbox from Matlab.

Research works interested in estimating transfer functions of linear systems have arisen as relevant contributions for SI evolution. For instance, these models' frameworks are mainly linear-regression forms like a Finite Impulse Response model (FIR). The present work focuses on methods based on the state-space realization model, which is part of a classical SI approach. Whatever the theory and model type involved, in the SI black box concept, input-output data characteristics are the core of the overall process. Commonly, in the first SI researches, the data were used to be attained from impulse response, as originally happened with the traditional Eigensystem Realization Algorithm.

A SISO linear system structure in the discrete-time can be defined by the following expressions for an FIR (Finite Impulse Response) model (Figure 2.1):

$$Y(z) = G(z)U(z) + V(z), \quad (2.3)$$

$$G(z) = \sum_{m=1}^q g_m z^{-m},$$

where $Y(z)$, $U(z)$, and $V(z)$ are the z-transform of $y(k)$, $u(k)$, and $v(k)$, respectively, and $k = 1, 2, \dots, q$ is the sampling index, z is the shift operator, i.e., $zu(k) = u(k+1)$, $v(k)$ is the measurement noise independent of the input $u(k)$, $y(k)$ is the system output and $G(z)$ is the transfer function of the linear system with the coefficients g_m , $m = 1, 2, \dots, q$ (Chen *et al.*, 2012a; Chen *et al.*, 2012b; Ljung, 1999).

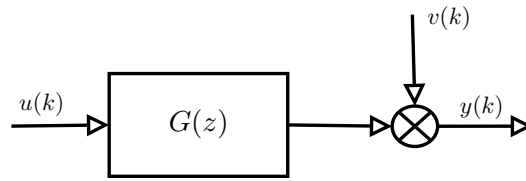


Figure 2.1 – Linear system $G(z)$, excited by input $u(k)$ with output $y(k)$ and additive measurement noise $v(k)$. $G(z)$ is an abuse of notation where it intends only to work as shift operators for the discrete-time regressive terms.

Figure 2.1 and Equation (2.3) are typical representations of linear-regression models. Analogously to the transfer function $G(z)$ in the regression model, the SSRA, that provides a state-space realization like the one shown with Equation (2.2), is based on the Markov parameters working as a numerical transfer function. The Markov parameters matrix is originated from the input-output data attained at the onset of a black box SI process.

2.3 State-Space Realization Algorithm

The ERA was introduced by Juang and Pappa in 1985 (Juang; Pappa, 1985) as a method for modal parameter realization and model reduction in identification of dynamical structures. The results from the algorithm yield a model with the smallest state-space dimension among systems that should have the same transfer function within a specified degree of accuracy. It should be mentioned the relevant contribution in 1978 from Kung (Kung, 1978), where a similar approach based on the singular value decomposition technique and equivalent state-space identification concepts were developed. Juang and Pappa in (Juang; Pappa, 1986) developed some emerging tools to minimize the noise effects, such as the singular values of the data matrix and modal amplitude coherence. Since these tools provide quantitative indicators to discriminate the noise effect in the identified system, the noisy system can have its order closer to the order of the true system, which will depict a system less corrupted by the noise effect.

Later, the researches regarding the ERA were refined to handle the effects of noise and nonlinearities. The improvement of state-space identification from the ERA with jointed techniques to tackle the effect of measurement noise in the SI process is the main objective of this work. Juang et al. developed some additional methods based on ERA to reduce the effect of system noise on algorithm effectiveness (Juang *et al.*, 1988). In this cited work, a new method (ERA-DC) was presented concerning data correlation in the Markov parameters matrix and hence in the Hankel matrix to reduce bias errors due to noise effect without the need for the model overestimation. Afterwards, Juang et al. (Juang *et al.*, 1993) yielded a method, known as the Observer/Kalman filter identification (OKID) method, to characterize and handle system uncertainties, from plant disturbance or measurement noise, using the Kalman filter equation to implement the Markov parameters. A new version of OKID was developed by Vicario et al. in 2016 (Vicario *et al.*, 2017), where the approach transforms a stochastic identification problem into a deterministic subspace identification. In 2018, Alenany et al. (Alenany *et al.*, 2019) proposed another OKID method improvement using the least-squares method twice to minimize residuals from the Kalman filter and Markov parameters where a comparative of the formulation and results between the three OKID methods is performed.

Although most of these prior mentioned methods are powerful in system identification of dynamical models, they are based only on impulse response. To cope with this restriction in the Eigensystem Realization Algorithm, in 2008, Callafon et al. (De Callafon *et al.*, 2008) developed the General Realization Algorithm, a new version of the ERA, working with arbitrary

input signal instead of using the impulsive signal, as it happens in many practical situations in a dynamical structure.

More recently, Kramer and Gugercin ([Kramer; Gugercin, 2016](#)) proposed a new ERA method, called Tangential interpolation-based ERA (TERA), which uses a tangential interpolation tool to minimize the computational effort mainly when the number of inputs and outputs is high, thus handling with a large scale dense Hankel matrix computing. In 2018, with a similar objective, Kramer and Gorodetsky ([Kramer; Gorodetsky, 2018](#)) developed an algorithm looking for computational efficiency, based on the reduction of Hankel matrix size using the CUR decomposition rather than the traditional Singular Value Decomposition (SVD). In 2019, Moaveni and Masoumi ([Moaveni; Masoumi, 2019](#)) presented operational improvements to the ERA concerning selecting a more appropriate sampling frequency and defining a more proper fitting order of the system to be identified. These algorithms were called the modified ERA (mERA) and the modified fast ERA (mfERA).

A recursive algorithm works by processing input data piecewise while this data is measured and made available sequentially. A recursive ERA was developed by Longman and Juang ([Longman; Juang, 1989](#)) in 1989 with the resource to determine the appropriate realization order gradually, starting with a lower Hankel matrix to optimize storage and computational time, but not expecting the same advantage regarding accuracy. In this thesis, the algorithms will operate in batch mode, when all the input data are previously collected and jointly used once in the algorithm processing. Eigensystem Realization Algorithm involving systems working in closed-loop, where the algorithm concepts are established for a system plant with an existing feedback controller, are present in the works of Juang and Phan ([Juang, 1994](#)), and Phan et al. ([Phan et al., 1994](#)).

Several modal identification methods were released for mechanical structures undergoing ambient excitation. The techniques are usually known nowadays as output-only identification methods. In 1995, the ERA with Natural Excitation Technique (NExT) was developed by James et al. ([James et al., 1995](#)). Mohanty and Rixen proposed a modified ERA in 2004 ([Mohanty; Rixen, 2006](#)), following the concept of the Operational Modal Analysis (OMA) method, including the effects of harmonic vibrations, and considering that structural vibration is not a purely white-noise excitation. Sometime later, the works of Caicedo et al., related to contributions of ERA-NExT, emerged ([Caicedo et al., 2004](#); [Caicedo, 2011](#)). In 2013, Chang et al. presented the ERA-NExT-AVG as another improvement of the ERA-NExT method

(Chang; Pakzad, 2013). State-Space Realization Algorithms (SSRA) improvements as derived techniques, or even relevant applications of the method, can have several works mentioned as references (Chiang *et al.*, 2010; Chiang; Lin, 2010; Li *et al.*, 2011; Narazaki *et al.*, 2018; Li *et al.*, 2020).

The Subspace Identification Method (SIM) stems from the classical state-space methods, which had the first influence relied on the realization theory that has arisen in Ho and Kalmans work in 1966 (Ho; Kalman, 1966), and indeed from the works already mentioned of Tether and Silverman. A review article stated the minimum realizations and system modeling (Rossen; Lapidus, 1972), consolidating the subject also crucial for SIM. The Kung's paper (Kung, 1978) relevantly contributed to the state-space realization theories in the joint concept of Markov parameters, Hankel matrix, and SVD. Even so, although several related works have come after that time, the great advance and consolidation of SIM theories occurred with the contributions of Overschee and De Moor in 1994 and 1996 (Van Overschee; De Moor, 1994; Van Overschee; De Moor, 1996), where the Numerical Subspace State-Space System Identification (N4SID) is the principal and most well-known Subspace identification method. From this time, many works of Subspace Identification took a prominent place in SI area developments.

In addition to state-space identification methods and subspace methods, several works as (Kerschen *et al.*, 2007; McNeill; Zimmerman, 2008; Hazra, B., A. J. Roffel, S. Narasimhan; Pandey, 2009; Yang; Nagarajaiah, 2013; Yao *et al.*, 2018; Yi *et al.*, 2019b; Yi *et al.*, 2019a) currently developed output-only identification methods, or general applications of structural engineering based on the Blind Source Separation (BSS) technique (Amari; Cichocki, 1998). Recently, BSS has spread widely in many applications areas as biomedical engineering, signal processing, besides structural engineering.

2.4 Input excitation signals

Systems inputs play a central role in the System identification process. The excitation signal choice represents the initial and fundamental problem of SI. As pointed out by Juang in (Juang, 1994): "The challenge of system identification is to correctly infer from the measured data the characteristic of each of the individual, contributing modes. The accuracy with which this inference can be performed depends on many factors, including the characteristics of the data and the sophistication algorithm being used."

In 1965, in the paper of Åström *et al.* (Åström; Torsten, 1965), the definition of a

persistently exciting signal took place, where they have already defined this signal as a virtuous excitation for the SI process, being one of the conditions to the system be better identifiable. In 1971, Ljung ([Ljung, 1971](#)) has written a further analysis regarding persistently exciting signals.

Since at least 1955, the Pseudo-Random Binary Sequence (PRBS) theories started to be developed. Many papers had been published since this time. In 1968, Nikiforuk and Gupta's work showed a bibliographic survey from this period, mentioning many different denominations related to PRBS that arise from that survey, as follows: shift-register-sequences (name adopted by the own authors), pseudo-random shift registers sequence, pseudo-random sequence, pseudo-random signals, pseudo-random binary signals, chain codes, discrete-interval binary noise ([Nikiforuk; Gupta, 1969](#)). These first researches about PRBS signals were in applications of areas correlated to communication, with an enormous emphasis as a noise signal (pseudo-noise), becoming an option to the use of white-noise. However, soon, the PRBS encountered employment in the identification and optimization areas.

The basic PRBS concepts were encompassed to multi-variable systems application in the work of Briggs and Godfrey (1966). The cross-correlation and autocorrelation aspects of the PRBS inputs were discussed, with the signal sequences composed in two amplitude levels (-1 and $+1$) or three levels (-1 , 0 , and $+1$) ([Briggs; Godfrey, 1966](#)). In 1976, other relevant work detailed the numerical aspects and properties regarding several types of shift-register sequences and the concept of the m-sequence that will be presented in Section 5.2.1 of this work ([MacWilliams; Sloane, 1976](#)).

While the PRBS arises as a novel excitation for identification with SSRA method and structural applications, the signal is broadly used as excitation in several engineering application references, many of them in the identification of electrical and thermal systems areas ([To; David, 1996](#); [Miao *et al.*, 2005](#); [Gabano *et al.*, 2011](#); [Fairweather *et al.*, 2012](#); [Boghani *et al.*, 2013](#)). The PRBS is also found in some application references encompassing mechanical excitation devices like piezoelectric actuators in beams ([Choi; Kim, 1996](#); [Butcher *et al.*, 2016](#); [Vuojolainen *et al.*, 2017](#)).

As with the PRBS signal, the first theories related to the CHIRP signals started to be developed in the decades of 60 and 70, most of them driven to attend signal processing objectives and communication areas. For instance, in 1970, Bluestein's work discussed the CHIRP's application as a filter in a linear filter processing, introducing that the CHIRP filtering a waveform functions close to a Discrete Fourier Transform (DFT) ([Bluestein, 1970](#)). The work of Roy

and Lowenschuss, in 1974, described two methods to generate CHIRP waveforms through the use of a small number of digital samples, which had applications to linear frequency-modulated sweep (FM) waveforms very used in radars at that times (Roy; Lowenschuss, 1974). The concepts based on time-bandwidth adjustments for CHIRP signals, presented in Roy's work, remain with the same principles to generate the system identification process signals. The practical application of the CHIRP signals in mechanical systems came some time later, as in the work of McConnell and Cappa in 2000, where the CHIRP was employed in a typical problem acting as a vibration exciter of a beam structure. It was compared the frequency response function (FRF) between the CHIRP, the random excitation, and the impulse excitation, with the CHIRP showing the best overall coherence in the presented results (McConnell; Cappa, 2000).

The SSRA technique approached in this work and the overall Subspace methods are based on arbitrary excitation signals. Many of these methods applied to structural identification traditionally use the impulse response of a dynamical system. The white-noise excitation signal has come to tackle the difficulty to estimate existing structures with the impulse response as pointed out by Chang and Pakzad (Chang; Pakzad, 2013).

Some excitation signals in structural engineering always motivated the improvement and searching for more appropriate identification methods since the application characteristics are determined mainly through the environment vibration data. Therefore, since then, the Gaussian white-noise takes place in many vibration-based modal identification methods. Usually, the estimation of modal parameters from vibration data is attained in the structure's typical working conditions. All the output-only system identification methods, in fact, are supposed that its excitation is white-noise (Garrido *et al.*, 2017; Yin *et al.*, 2012).

2.5 Challenges and trends in System Identification

This section aims to provide a general view of the challenges encompassing the system identification area in the last years and even the trends toward the main concerns about this theme evolution.

In 2009, the work of Ninness (Ninness, 2009) discussed three key challenges that could be considered as remaining in the identification area: estimation of general nonlinear models, estimation of systems with high dimensions, and deliver accurate results even with "short" data lengths. More recently, another work also talking over about challenges, but now focused on the nonlinear system identification (Schoukens; Noël, 2017), specified in more de-

tail the first topic formerly mentioned by Ninness. The issues related to Schoukens work are: dynamical nonlinearities as hysteresis that are categorically not measurable from input or output devices, absence of a more realistic representation of noise framework, and the short data records, which was also an item pointed out in the prior research.

More recently, regarding the estimation of nonlinear models and hence the attainment of accurate identification methods, some works were in charge of applying Design of Experiments (DoE) as a crucial step in the SI process. In these works ([Schrangl *et al.*, 2020](#); [Karimshoushtari; Novara, 2020](#)), the Design of an Experiment gives the maximum information about the system dynamics of the process of interest, optimizing the input data applied to the identification algorithm. DoE technique combined with SI is more advised to be used in data-driven models when the data reproduces the input-output system behavior correctly without trying to describe its physics accurately. Thus, in data-driven, the relationship between the system state variables is sufficient independently of the knowledge of the system's physics.

Several works have been applied techniques that use the data-driven concept together with System Identification models. The correlated techniques based on data-driven objectifies the SI algorithms can “learn” from the data, which is a characteristic of Machine Learning, Deep Learning, Reinforcement Learning, etc. The work of Fuentes *et al.* applies Machine Learning for SI in nonlinear structural dynamics via Bayesian approach on sparse linear regression for combined model selection and parameter estimation ([Fuentes *et al.*, 2021](#)). In the work of Masti and Bemporad ([Masti; Bemporad, 2021](#)), Machine Learning techniques based on autoencoders and neural networks were applied from input/output data in the SI of nonlinear state-space models. Ljung *et al.* ([Ljung *et al.*, 2020a](#)) approached the employment of Deep Learning for estimating dynamical systems and highlighting the strong links of the technique with system identification practice, concluding: “the workflow in deep learning and system identification has many similarities; the power of deep nets also for standard system identification has been demonstrated.” Many recent researches can be cited as examples of this trend, some of them, for instance, employing Bayesian theory in system identification ([Chen *et al.*, 2020](#); [Liu *et al.*, 2021](#)).

3 IDENTIFICATION METHODS FOR COMPARATIVE ANALYSIS

3.1 Introduction

This chapter aims to present an overview of well-known SI methods, broadly used and available in the System Identification Toolbox of Matlab. These methods were used for comparison with the new technique developed in this research. The results from this comparison are reported in Section 7.8 and Section 7.9.3. For simplicity, especially in terms of notation, most of the concepts and mathematical expressions presented in this chapter were developed for SISO systems. However, the simulations were performed for the MIMO systems whose characteristics are introduced in Chapter 5.

The SSRA methods are based on state-space systems structure. The linear-regression or polynomials models have a specific framework for systems identification, determining the composition of the several methods introduced in this chapter, to know: Output Error (OE), Finite Impulse Response (FIR), AutoRegressive with External input (ARX), AutoRegressive Moving Average with External input (ARMAX), and Box-Jenkins (BJ). It is widespread in the identification literature to refer to these algorithms only as autoregressive models or linear prediction model. The same happens with the Subspace State-Space model incorporating different algorithms terms, just called N4SID, Multivariable Output Error State-Space (MOESP), and Canonical Variate Analysis (CVA) models.

Most of the linear-regression methods working as iterative algorithms are based on the Prediction Error Method (PEM). And the non-iterative methods, such as the ARX, FIR, and even the N4SID that is part of the subspace models set, rely on the traditional Least-Squares method (LS). In practice, the PEM can be considered the LS method for iterative algorithms, both shown in the next.

The fundamental LS equations that briefly introduce the method concepts can be stated by the following sequence:

$$\mathbf{y}(k) = \hat{\mathbf{y}}(k) + \boldsymbol{\nu}(k), \quad \hat{\mathbf{y}}(k) = \boldsymbol{\psi}^T(k)\boldsymbol{\theta}, \quad (3.1)$$

$$\mathbf{V}_n(\boldsymbol{\theta}) = \frac{1}{n} \sum_{k=1}^n (\boldsymbol{\nu}(k))^2 = \frac{1}{n} \sum_{k=1}^n (\mathbf{y}(k) - \hat{\mathbf{y}}(k))^2, \quad (3.2)$$

$$\hat{\boldsymbol{\theta}}_n^{LS} = \arg \min_{\boldsymbol{\theta}} \mathbf{V}_n(\boldsymbol{\theta}) , \quad (3.3)$$

where $\boldsymbol{\psi}$, $\boldsymbol{\theta}$, and $\boldsymbol{\nu}$ are the regression vector, the unknown parameters to be estimated, and the predictor error vector, respectively. The Least-Squares concept here presented consists of minimizing the mean square error between the actual (true) output \mathbf{y} and the estimated output $\hat{\mathbf{y}}$ for the attainment of the parameters $\boldsymbol{\theta}$. $\mathbf{V}_n(\boldsymbol{\theta})$ is the cost function to be minimized.

To obtain the $\hat{\boldsymbol{\theta}}_n^{LS}$ it suffices by setting the first derivative of \mathbf{V}_n equal to zero:

$$\frac{d}{d\boldsymbol{\theta}} \left(\mathbf{V}_n(\boldsymbol{\theta}) \right) = 0 , \quad (3.4)$$

$$\frac{d}{d\boldsymbol{\theta}} \left(\frac{1}{n} \sum_{k=1}^n (\mathbf{y}(k) - \boldsymbol{\psi}^T(k)\boldsymbol{\theta})^2 \right) = \frac{-2}{n} \sum_{k=1}^n \boldsymbol{\psi}(k)(\mathbf{y}(k) - \boldsymbol{\psi}^T(k)\boldsymbol{\theta}) = 0 , \quad (3.5)$$

$$\left(\frac{1}{n} \sum_{k=1}^n \boldsymbol{\psi}(k)\boldsymbol{\psi}^T(k) \right) \boldsymbol{\theta} = \frac{1}{n} \sum_{k=1}^n \boldsymbol{\psi}(k)\mathbf{y}(k) , \quad (3.6)$$

$$\hat{\boldsymbol{\theta}}_n^{LS} = \left(\frac{1}{n} \sum_{k=1}^n \boldsymbol{\psi}(k)\boldsymbol{\psi}^T(k) \right)^{-1} \left(\frac{1}{n} \sum_{k=1}^n \boldsymbol{\psi}(k)\mathbf{y}(k) \right) , \quad (3.7)$$

where Equation (3.7) (Soderstrom; Stoica, 1989) represents the LS method applied to the system defined by Equation (3.1), and the parameters $\boldsymbol{\theta}$ are the variables to be computed by the method.

The Prediction Error Method (PEM) (Figure 3.1), also called Prediction Error Minimization in the Matlab SI Toolbox, is predominantly formed by an LS method (from Equation (3.1) to Equation (3.7)) in iterative processing for several types of model structures like the AR-MAX and the Box and Jenkins, for instance. The decision to stop the minimization of the cost function $\mathbf{V}_n(\boldsymbol{\theta})$, which is shown in the schematic diagram of the PEM (Figure 3.1), depends on the performance criterion of any selected iterative descent method. However, this numerical optimization process can get stuck in local minima (Katayama, 2005). Additionally, a PEM filter can be configured to damp imperfections on measured data, awaiting for the predictor error $\boldsymbol{\nu}$ to provide minor variance as possible.

For linear systems, a general model structure can be defined to attend the algorithm methods described in this chapter as follows:

$$Y(z) = \mathcal{G}(z, \theta)U(z) + \mathcal{H}(z, \theta)\mathcal{E}(z) , \quad (3.8)$$

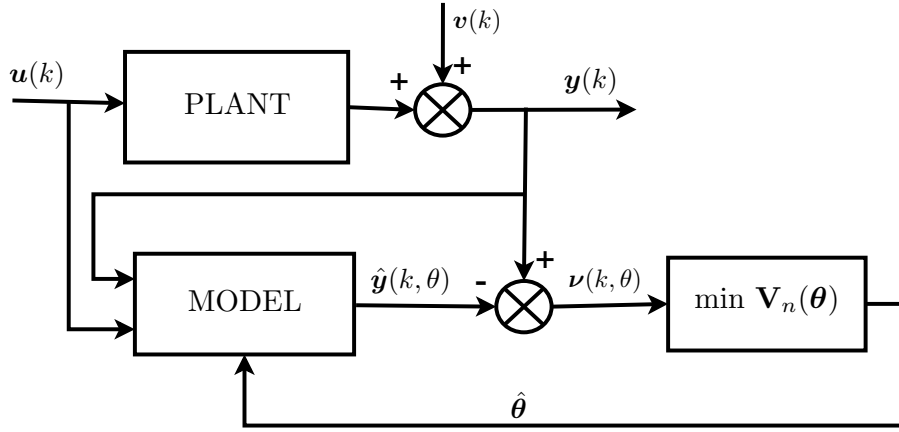


Figure 3.1 – Prediction Error Method (PEM)

where $Y(z)$, $U(z)$, and $\mathcal{E}(z)$ are the z -transform of $y(k)$, $u(k)$, and $e(k)$ (white-noise source), respectively, with

$$\mathcal{G}(z, \theta) = \sum_{k=1}^{\infty} g(k)z^{-k}, \quad \mathcal{H}(z, \theta) = 1 + \sum_{k=1}^{\infty} h(k)z^{-k}, \quad (3.9)$$

where z denotes the shift operator $z^{-1}u(k) = u(k-1)$. $\mathcal{G}(z)$ and $\mathcal{H}(z)$ are commonly referred as process transfer function and noise transfer function, respectively. The expression of \mathcal{H} in Equation (3.9) shows the expansion starting with a unity, i.e., $\mathcal{H}(z)$ is monic.

The general model structure's parametrization continues with \mathcal{G} and \mathcal{H} deployment to be rational in the shift operator:

$$\mathcal{G}(z, \theta) = \frac{\mathcal{B}(z)}{\mathcal{F}(z)}, \quad \mathcal{H}(z, \theta) = \frac{\mathcal{C}(z)}{\mathcal{D}(z)}, \quad (3.10)$$

and when $\mathcal{F} = \mathcal{D} \neq 1$, the polynomials in the denominators of \mathcal{G} and \mathcal{H} are renominated as polynomial \mathcal{A} .

The respective polynomials from Equation (3.10) are defined as following:

$$\begin{aligned} \mathcal{A}(z) &= 1 + a_1z^{-1} + a_2z^{-2} + \dots + a_{na}z^{-na}, \\ \mathcal{B}(z) &= b_1z^{-1} + b_2z^{-2} + \dots + b_{nb}z^{-nb}, \\ \mathcal{C}(z) &= 1 + c_1z^{-1} + c_2z^{-2} + \dots + c_{nc}z^{-nc}, \\ \mathcal{D}(z) &= 1 + d_1z^{-1} + d_2z^{-2} + \dots + d_{nd}z^{-nd}, \\ \mathcal{F}(z) &= 1 + f_1z^{-1} + f_2z^{-2} + \dots + f_{nf}z^{-nf}, \end{aligned} \quad (3.11)$$

where na , nb , nc , nd and nf are integers that represent the respective orders of the polynomials \mathcal{A} , \mathcal{B} , \mathcal{C} , \mathcal{D} , and \mathcal{F} , respectively.

As can be seen from Equation (3.11), the polynomials are monic, except the polynomial \mathcal{B} (Ljung, 2019). Once the general model structure was outlined, the autoregressive algorithms that employ these polynomials models should be presented next.

3.2 FIR, ARX and OE

FIR (Finite Impulse Response), ARX (Autoregressive with External input), and OE (Output Error) are algorithm models close to each other due to their model structure similarity. Since these methods have the polynomial $\mathcal{C} = 1$, the structure does not allow to describe the properties of the white-noise source e , which is possible when the polynomial \mathcal{C} provides and makes available the conditions of the disturbance term some steps before the last instant of the output-input data.

The schematic representation of the three models that are determined following each polynomial condition stated at Equations (3.10) and (3.11) is suitable to attain the respective linear-regression equations easily (Table 3.1). The ARX schematic representation should be enhanced, which was attained after handling the block $\frac{1}{\mathcal{A}}$ since it changes position from before to after the sum operator. Moreover, this ARX configuration clarifies the independence of the white-noise e related to the regression samplings. Hence, the ARX model structure is less able to consider noisy systems because the polynomial \mathcal{A} must account for both the system dynamics and the noise.

The FIR model can be considered a composite structure from ARX and OE in terms of having the dynamic transfer function equivalent to the ARX regarding the input regressors and having the noise transfer function identical to OE, which provides partial features of both models. On the other hand, the order n should be large to be well close to the true system, therefore demanding more parameters for the estimation process (Ljung, 1999).

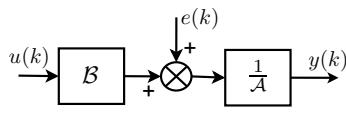
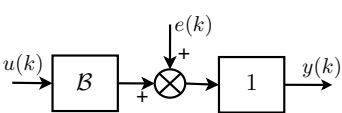
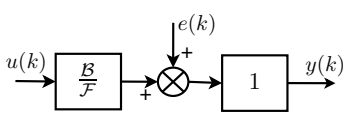
ARX	FIR	OE
$\mathcal{F} = \mathcal{D} = \mathcal{A}, \mathcal{C} = 1$ 	$\mathcal{F} = \mathcal{C} = \mathcal{D} = 1$ 	$\mathcal{C} = \mathcal{D} = 1$ 

Table 3.1 – Schematic representation of ARX, FIR, and OE models, comparatively.

Considering the models structures definition provided in Table 3.1, a linear-regression model of the ARX method can be performed from Equation (3.1) in this respect (Ljung, 2010b):

$$\mathbf{y}(k) = \boldsymbol{\psi}^T(k)\boldsymbol{\theta} + \boldsymbol{\nu}(k) , \quad (3.12)$$

with the ARX model structure composed as follows:

$$y(k) + a_1y(k-1) + \dots + a_{na}y(k-na) = b_1u(k-1) + \dots + b_{nb}u(k-nb) + e(k) , \quad (3.13)$$

by taking

$$\begin{aligned} \hat{\boldsymbol{\theta}} &= \begin{bmatrix} a_1 & \dots & a_{na} & b_1 & \dots & b_{nb} \end{bmatrix}^T , \\ \boldsymbol{\psi}(k) &= \begin{bmatrix} -y(k-1) \dots -y(k-na) & u(k-1) \dots u(k-nb) \end{bmatrix}^T , \end{aligned} \quad (3.14)$$

where the predictor error vector $\boldsymbol{\nu}(k)$ is characterized here as a white-noise source $e(k)$.

It suffices to take out the regressive elements of $y(k)$ and the respective parameter elements a_{na} from the ARX linear-regression model for attaining the FIR linear-regression model. For the OE linear-regression model, the following equations applies:

$$\mathcal{F}(z)(y(k) - e(k)) = \mathcal{B}(z)u(k) , \quad (3.15)$$

representing a mathematical equation not in a formal agreement since the polynomials in z-transform only intend to work as shift operators for the discrete-time regressive terms, which yields

$$\begin{aligned} y(k) + f_1(y(k-1) - e(k-1)) + \dots + f_{nf}(y(k-nf) - e(k-nf)) \\ = b_1u(k-1) + \dots + b_{nb}u(k-nb) + e(k) , \end{aligned} \quad (3.16)$$

$$\begin{aligned} \hat{\boldsymbol{\theta}} &= \begin{bmatrix} f_1 & \dots & f_{nf} & b_1 & \dots & b_{nb} & f_1 & \dots & f_{nf} \end{bmatrix}^T , \\ \boldsymbol{\psi}(k) &= \begin{bmatrix} -y(k-1) \dots -y(k-nf) & u(k-1) \dots u(k-nb) & e(k-1) \dots e(k-nf) \end{bmatrix}^T . \end{aligned} \quad (3.17)$$

From Equation (3.17), the OE model can infer similarity with the ARMAX model at first glance, as will be seen in Section 3.3. However, the disturbance parameters (f_{nf}) from the OE model are the same as the output parameters. The correct issue is that the OE model is prompted to parameterize dynamics and is not able to estimate noise parameters as in the ARMAX model, which is supported by the fact that the noise transfer function \mathcal{H} is unitary in

the OE model. At that point, the OE linear-regression model should be formed according to the estimated output $\hat{y}(k)$ as follows:

$$\hat{y}(k) = \psi^T(k)\theta, \quad \hat{y}(k) = y(k) - e(k). \quad (3.18)$$

Based on what was seen, any one of the models previously presented is inappropriate to deal with noise considering the models' structures verified. As will be seen next, it is proper to apply the ARMAX or the Box-Jenkins model structure, where different polynomials model the dynamics term and the noise term.

3.3 ARMAX

The Autoregressive Moving Average with External input (ARMAX) is a SI method working as an extension of ARX to provide more flexibility with the inclusion of noise in the model, now considering $\mathcal{H} \neq 1$. ARMAX adds to the ARX model the moving average function of the polynomial $\mathcal{C}(z)$, maintaining the premiss $\mathcal{F} = \mathcal{D} = \mathcal{A}$. It leads the noise to enter as the input to the algorithm. The schematic representation of the ARMAX assumes the following form:

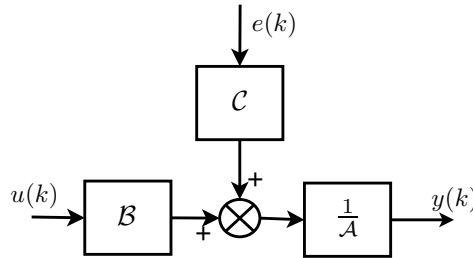


Figure 3.2 – Squematic representation of ARMAX

The linear-regression model of the ARMAX method can be directly determined from the schematic representation in Figure 3.2, and from Equation (3.11) and Equation (3.12) as follows (Ljung, 1999):

$$\mathcal{A}(z)y(k) = \mathcal{B}(z)u(k) + \mathcal{C}(z)e(k), \quad (3.19)$$

where it is worthy the same remark made in Equation (3.15) related to not obey a formal mathematical representation, which yields

$$\begin{aligned} & y(k) + a_1y(k-1) + \dots + a_nay(k-na) = \\ & = b_1u(k-1) + \dots + b_nbu(k-nb) + c_1e(k-1) + \dots + c_nce(k-nc) + e(k), \end{aligned} \quad (3.20)$$

$$\begin{aligned}\hat{\boldsymbol{\theta}} &= \begin{bmatrix} a_1 & \dots & a_{na} & b_1 & \dots & b_{nb} & c_1 & \dots & c_{nc} \end{bmatrix}^T, \\ \boldsymbol{\psi}(k) &= \begin{bmatrix} -y(k-1) \dots -y(k-na) & u(k-1) \dots u(k-nb) & e(k-1) \dots e(k-nc) \end{bmatrix}^T. \end{aligned} \quad (3.21)$$

From ARMAX, other models can be derived as:

- Autoregressive (AR): $\mathcal{B} = \mathcal{C} = 1$;
- Moving Average (MA): $\mathcal{A} = \mathcal{B} = 1$;
- Autoregressive Moving Average (ARMA): $\mathcal{B} = 1$.

Observing the schematic diagram in Figure 3.2, it can be realized that the system dynamic and white-noise source have the same poles (\mathcal{A}). It makes the model suitable when the disturbance enters together with the input, which is the case of additive measurement noise, as the scenario of most of the simulations in this research ([Ljung, 2010b](#)).

The simulations comparing the ARMAX method's performance with the new iterative SSRA-DC-iCL method and other methods from SI Toolbox will be presented in Section 7.8.

3.4 Box and Jenkins

The Box and Jenkins (BJ) method for SI was developed to provide independence of the configuration related to system dynamics and noise. The rational polynomial functions ($\mathcal{B}, \mathcal{F}, \mathcal{C}, \mathcal{D}$) of the model structure are different each other, and available to be set in a separate way. BJ structure provides further resilience for noise modeling, as can be perceived from the schematic diagram of Figure 3.3:

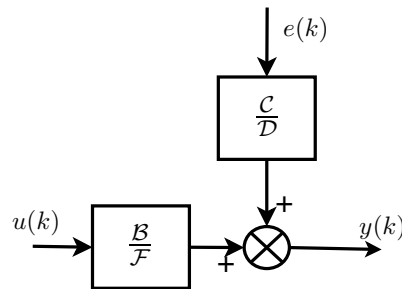


Figure 3.3 – Squematic representation of BOX and JENKINS

For the BJ method, where the poles from the input-output transfer function and the noise transfer function are distinct, the linear-regression model is not the better representation.

The use of the structure of the polynomials as defined from Equation (3.11) is more appropriate and based on Figure 3.3 it has the following expression that is employed in the SI toolbox of Matlab:

$$y(k) = \frac{\mathcal{B}(z)}{\mathcal{F}(z)}u(k) + \frac{\mathcal{C}(z)}{\mathcal{D}(z)}e(k), \quad (3.22)$$

following the same remark assigned to Equation (3.15) regarding the mathematical equation that is not in a formal agreement.

Equation (3.22) shows the polynomial ratio $\frac{\mathcal{B}(z)}{\mathcal{F}(z)}$ corresponding to the process transfer function or also called dynamical transfer function $\mathcal{G}(z)$, as already have been postulated in Equation (3.10). In a MIMO system, this transfer function is composed of 2 matrices of polynomials, one in the numerator and another in the denominator, which is equivalent to the system matrix \mathbf{A} in a state-space system realization, as defined in Equation (2.2). It is worth remarking that the number of elements of the polynomial matrices \mathcal{B} and \mathcal{F} in a MIMO system determines the order of the equivalent system matrix \mathbf{A} . In the next section, some issues related to assigning polynomials order in a MIMO system will be approached.

3.5 Polynomials sizes and orders for MIMO systems

Each polynomial is characterized in terms of dimensions and orders as previously seen, but here for MIMO systems, the correspondent configurations are presented in Table 3.2. These polynomials are specified as matrices where each matrix element is a row vector. The models composed by the polynomials are considered containing r outputs and s inputs, which states the indexes $j = 1, 2, \dots, r$ and $m = 1, 2, \dots, s$. The relation between input, output, and noise values is portrayed through the coefficients of a polynomial (Ljung, Lennart, 2014).

Table 3.2 – Polynomial sizes and orders

Polynomial matrix	Dimension	Relation described	Orders
\mathcal{A}	matrix $r \times r$ of row vectors	\mathcal{A}_{jj} containing coefficients a_1, a_2, \dots of relation between outputs y_j	na : $r \times r$ matrix; each element contains the degree of the correspondent \mathcal{A}_{jj}
\mathcal{B}	matrix $r \times s$ of row vectors	\mathcal{B}_{jm} containing coefficients b_1, b_2, \dots of relation between output y_j and input u_m	nb : $r \times s$ matrix; each element contains the degree of the correspondent \mathcal{B}_{jm}
\mathcal{F}	matrix $r \times s$ of row vectors	\mathcal{F}_{jm} containing coefficients f_1, f_2, \dots of relation between output y_j and input u_m	nf : $r \times s$ matrix; each element contains the degree of the correspondent \mathcal{F}_{jm}
\mathcal{C}	vector $r \times 1$ of row vectors	\mathcal{C}_j containing coefficients c_1, c_2, \dots of relation between output y_j and noise e	nc : $r \times 1$ vector; each element contains the degree of the correspondent \mathcal{C}_j
\mathcal{D}	vector $r \times 1$ of row vectors	\mathcal{D}_j containing coefficients d_1, d_2, \dots of relation between output y_j and noise e	nd : $r \times 1$ vector; each element contains the degree of the correspondent \mathcal{D}_j

In this work, as it will be applied at Section 7.8 for simplicity in the adjustments, without loss of generality, it was considered the assumption that the order of each polynomial (Equation (3.11)), determined by the last element of the row vector, is the same for all the polynomials inside a polynomial matrix. For instance, the polynomial matrix \mathcal{B} with r outputs and s inputs has a polynomial \mathcal{B}_{jm} in each element of the matrix \mathcal{B} . Then, the number of elements of matrix \mathcal{B} will be: $r \times s \times nb$. Each element of the matrix \mathcal{B} corresponds to a parameter from \mathcal{B}_{jm} and can be represented as follows:

$$\mathcal{B} = \begin{bmatrix} \begin{bmatrix} b_1 & \dots & b_{nb} \end{bmatrix}_{11} & \begin{bmatrix} b_1 & \dots & b_{nb} \end{bmatrix}_{12} & \dots & \begin{bmatrix} b_1 & \dots & b_{nb} \end{bmatrix}_{1s} \\ \begin{bmatrix} b_1 & \dots & b_{nb} \end{bmatrix}_{21} & \begin{bmatrix} b_1 & \dots & b_{nb} \end{bmatrix}_{22} & \dots & \begin{bmatrix} b_1 & \dots & b_{nb} \end{bmatrix}_{2s} \\ \vdots & \vdots & \ddots & \vdots \\ \begin{bmatrix} b_1 & \dots & b_{nb} \end{bmatrix}_{r1} & \begin{bmatrix} b_1 & \dots & b_{nb} \end{bmatrix}_{r2} & \dots & \begin{bmatrix} b_1 & \dots & b_{nb} \end{bmatrix}_{rs} \end{bmatrix}, \quad (3.23)$$

where $\mathcal{B}_{jm} = \begin{bmatrix} b_1 & b_2 & \dots & b_{nb} \end{bmatrix}_{jm}$.

The polynomial matrix \mathcal{F} follows the same concept of \mathcal{B} shown in Equation (3.23), but having a first additional parameter with value 1 (monic) in the polynomial \mathcal{F}_{jm} . However, the number of elements of \mathcal{F} to compute the system matrix order is: $r \times s \times nf$. The state-space system matrix $\mathbf{A} \in \mathbb{R}^{n \times n}$ loads the system dynamic, which, in equivalence with the composition of the transfer function $\mathcal{G}(z) = \frac{\mathcal{B}(z)}{\mathcal{F}(z)}$, will have its matrix order n determined as follows:

- if $nf \geq nb \implies n = r \times s \times nf$;
- if $nf < nb \implies n = r \times s \times (nb - 1)$.

For the ARX and ARMAX models, when the polynomial $\mathcal{A} \left(\mathcal{G}(z) = \frac{\mathcal{B}(z)}{\mathcal{A}(z)} \right)$ is used rather than the polynomial \mathcal{F} , the order n of the matrix \mathbf{A} from the equivalent state-space system is determined as follows:

- if $na \geq nb \implies n = r \times na$;
- if $na < nb \implies n = r \times (nb - 1)$.

A note is worthy here of calling attention to the subtle notation difference between the polynomial \mathcal{A} from the structure of linear-regression models and the matrix \mathbf{A} from a state-space system.

3.6 N4SID

The Numerical Subspace State-Space System Identification is the main Subspace Identification Method (SIM) that has fundamental support on the theory of state-space realization algorithm from Ho and Kalman ([Ho; Kalman, 1966](#); [Viberg, 1994](#)). N4SID also takes part in the SI Toolbox of Matlab. The method is not subject to the main drawback of the polynomials models previously introduced in this chapter. This problem is related to the numerical ill-conditioning from polynomial computing, especially for MIMO systems.

The establishment of parameter values in the methods calls for additional care in the identification algorithm performance. This condition happens with SSRA methods demanding a previous parametrization of the system order and the observability matrix order. These adjustments are in charge by the parameters n and p , as seen in Section 4.2. In the N4SID, the method only requires the system order as an input parameter, which can be determined by inspecting singular values after SVD decomposition, as can be verified in the SSRA methods ([Van Overschee; De Moor, 1994](#)).

The presentation of fundamental differences of algorithm steps between Subspace and Classical methods is appropriate to occur in this initial approach (Figure 3.4). The methods based on the SSRA and the linear-regression methods prior presented, which are supported by the Least-Squares method, can be considered Classical methods. Every possible step in both methods types, depending on the features wished to apply, is displayed in Figure 3.4. For instance, the classical SSRA method ends in the reduced state-space model as the last step, and the transfer matrix in the SSRA concerns the Markov parameters matrix. However, more complex and extensive matrix algebra calculations are required from the input-output data at the initial stage to the state estimates of the Subspace Methods. Next, a state-space model is obtained by computing a least-squares problem. In the last step of Subspace Methods, the transfer matrix can be easily calculated once the previously obtained state-space model.

The initial stage of subspace methods provides algorithm functions that use a geometric framework with orthogonal and oblique projections and linear algebra features like QR and SVD decomposition to obtain Kalman filter states vectors. This first step of the subspace method has the fundamental task of getting the system states, which is a significant difference from the classical techniques that do not require the finding of system states to achieve the state-space model. Once the states are known in the Subspace Identification Method (SIM), the attainment of the unknown state-space model depends only on solving a linear least-squares

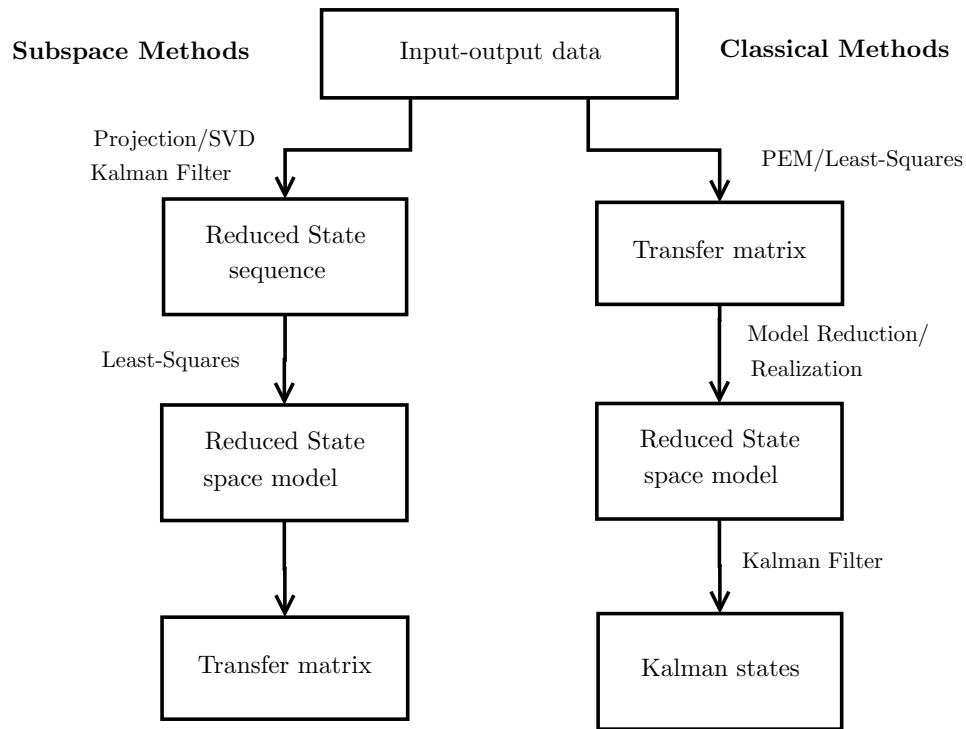


Figure 3.4 – Subspace and Classical Methods of SI

problem ([Katayama, 2005](#)).

The SIM has peculiar characteristics which were synthesized by Overschee et al. ([Van Overschee; De Moor, 1996](#)) as following: "subspace identification algorithms conditionally linearize the problem, which, when written in the classical form of prediction error methods, is a highly nonlinear optimization problem. Yet another point of view is that subspace identification algorithms do not identify input-output models, but they identify input-state-output models".

The N4SID theory is supported by the concepts of deterministic and stochastic process, that can be briefly described next:

- **Deterministic:** The variables and parameters are not random. A deterministic process will always yield the same output from a given input.
- **Stochastic:** The output of a stochastic process is random variables, characterized by uncertainties sources in any real situation. Stochastic process is a collection of random variables as the disturbances in a process. In practice, for a stochastic process, in counterpart to the deterministic approach, the output at instant t cannot be precisely determined from data related to the past ([Aguirre, 2015](#)).

The classical SSRA method, for instance, is typically a deterministic model once it does not concerns with disturbances in the state-space representation. Despite being a method stated by the same conceptual base of the ERA, the novel iterative method SSRA-DC-iCL can be considered a technique that incorporates stochastic features as it provides ways to control and minimize the disturbance from measurement noise. The N4SID method can give the solution to the combined deterministic-stochastic identification problem. The state-space representation can be defined as follows to attend both deterministic and stochastic demands ([Van Overschee; De Moor, 1996](#)):

$$\begin{aligned} \mathbf{x}(k+1) &= \mathbf{A}\mathbf{x}(k) + \mathbf{B}\mathbf{u}(k) + \mathbf{w}(k), \\ \mathbf{y}(k) &= \mathbf{C}\mathbf{x}(k) + \mathbf{D}\mathbf{u}(k) + \mathbf{v}(k), \end{aligned} \quad (3.24)$$

for a n order system, with $\mathbf{A} \in \mathbb{R}^{n \times n}$, $\mathbf{B} \in \mathbb{R}^{n \times s}$, $\mathbf{C} \in \mathbb{R}^{r \times n}$, $\mathbf{D} \in \mathbb{R}^{r \times s}$, r outputs and s inputs, where $\mathbf{w}(k) \in \mathbb{R}^{n \times 1}$ and $\mathbf{v}(k) \in \mathbb{R}^{r \times 1}$ are usually unmeasurable signals vectors, which can be considered, generally, as noise sequences. The covariance matrices involving the process noise \mathbf{w} and the measurement noise \mathbf{v} are given by:

$$E \left(\begin{bmatrix} \mathbf{w}(k) \\ \mathbf{v}(k) \end{bmatrix} \begin{bmatrix} \mathbf{w}^T(k) & \mathbf{v}^T(k) \end{bmatrix} \right) = \begin{bmatrix} \mathbf{Q} & \mathbf{S} \\ \mathbf{S}^T & \mathbf{R} \end{bmatrix}, \quad (3.25)$$

with $\mathbf{Q} \in \mathbb{R}^{n \times n}$ is the auto-covariance of \mathbf{w} , $\mathbf{S} \in \mathbb{R}^{n \times r}$ is the cross-covariance between \mathbf{w} and \mathbf{v} , and $\mathbf{R} \in \mathbb{R}^{r \times r}$ is the auto-covariance of \mathbf{v} . In subspace identification, it is typically assumed that the process noise \mathbf{w} and the measurement noise \mathbf{v} are: zero mean, stationary white noise vector sequences and uncorrelated with the inputs \mathbf{u} , and that the data are ergodic, i.e., the expected value E is replaced by the average.

Supposing the availability of a sequence of state vectors from the state-space system shown in Equation (3.24), the following form can be introduced:

$$\begin{bmatrix} \hat{\mathbf{x}}(k+1) \\ \mathbf{y}(k) \end{bmatrix} = \begin{bmatrix} \mathbf{A} & \mathbf{B} \\ \mathbf{C} & \mathbf{D} \end{bmatrix} \begin{bmatrix} \hat{\mathbf{x}}(k) \\ \mathbf{u}(k) \end{bmatrix} + \begin{bmatrix} \mathbf{w}(k) \\ \mathbf{v}(k) \end{bmatrix}, \quad (3.26)$$

where $\hat{\mathbf{x}}$ is the estimate of the state vector \mathbf{x} . If the variables in Equation (3.26) are known, this equation is a regression model with the parameter matrix given by:

$$\boldsymbol{\theta} = \begin{bmatrix} \mathbf{A} & \mathbf{B} \\ \mathbf{C} & \mathbf{D} \end{bmatrix}, \text{ where } \boldsymbol{\theta} \in \mathbb{R}^{(n+r) \times (n+s)}. \quad (3.27)$$

Employing the least-squares to figure out θ value in Equation (3.26), it gives:

$$\theta = \left(\sum_{k=1}^q \begin{bmatrix} \hat{\mathbf{x}}(k+1) \\ \mathbf{y}(k) \end{bmatrix} \begin{bmatrix} \hat{\mathbf{x}}^T(k) & \mathbf{u}^T(k) \end{bmatrix} \right) \left(\sum_{k=1}^q \begin{bmatrix} \hat{\mathbf{x}}(k) \\ \mathbf{u}(k) \end{bmatrix} \begin{bmatrix} \hat{\mathbf{x}}^T(k) & \mathbf{u}^T(k) \end{bmatrix} \right)^{-1}. \quad (3.28)$$

Based on computing the state-space's matrices and counting on with the estimated state vector, this procedure is called the Direct 4SID method (Katayama, 2005; Viberg, 1995).

As the basis of the N4SID theory, the state-space system defined in Equation (3.24) is split up into deterministic and stochastic subsystems. Many other concepts come from this algorithm definition. The related equations are presented as follows (Van Overschee; De Moor, 1994):

$$\begin{aligned} \mathbf{x}(k) &= \mathbf{x}^d(k) + \mathbf{x}^s(k), \\ \mathbf{y}(k) &= \mathbf{y}^d(k) + \mathbf{y}^s(k), \end{aligned} \quad (3.29)$$

where \mathbf{x}^d and \mathbf{y}^d are the state and output from deterministic subsystem, and \mathbf{x}^s and \mathbf{y}^s are the state and output from stochastic subsystem, according to

- Deterministic influence:

$$\begin{aligned} \mathbf{x}^d(k+1) &= \mathbf{A}\mathbf{x}^d(k) + \mathbf{B}\mathbf{u}(k), \\ \mathbf{y}^d(k) &= \mathbf{C}\mathbf{x}^d(k) + \mathbf{D}\mathbf{u}(k). \end{aligned} \quad (3.30)$$

- Stochastic influence:

$$\begin{aligned} \mathbf{x}^s(k+1) &= \mathbf{A}\mathbf{x}^s(k) + \mathbf{w}(k), \\ \mathbf{y}^s(k) &= \mathbf{C}\mathbf{x}^s(k) + \mathbf{v}(k). \end{aligned} \quad (3.31)$$

Since the complete mathematical development of N4SID is extensive, and its detailing does not take part as an objective of this research, the following sequence of equations is only motivated to provide a general view of the method restricted to the deterministic approach. Based on the state-space equations, accordingly to Equation (3.30), fundamental in subspace identification to compute the state $\mathbf{x}(k)$, is introduced here as follows, taking out the superscript d and represented in matrix form to simplify the notation (Katayama, 2005; Qin *et al.*, 2005):

$$\begin{aligned} \mathbf{Y}_p &= \mathbf{O}_k \mathbf{X}_0 + \mathbf{TU}_p, \\ \mathbf{Y}_f &= \mathbf{O}_k \mathbf{X}_k + \mathbf{TU}_f, \end{aligned} \quad (3.32)$$

where the subscript p and f denote past and future, respectively, \mathbf{O}_k is the extended observability matrix, \mathbf{T} is the Toeplitz matrix, and \mathbf{Y} and \mathbf{U} are output and input block Hankel matrices, also called the past or future outputs and inputs, respectively. The matrices \mathbf{Y}_p and \mathbf{Y}_f are following presented:

$$\mathbf{Y}_p = \mathbf{Y}_{0|k-1} = \begin{bmatrix} \mathbf{y}(0) & \mathbf{y}(1) & \dots & \mathbf{y}(q-1) \\ \mathbf{y}(1) & \mathbf{y}(2) & \dots & \mathbf{y}(q) \\ \dots & \dots & \ddots & \dots \\ \mathbf{y}(k-1) & \mathbf{y}(k) & \dots & \mathbf{y}(k+q-2) \end{bmatrix}, \quad (3.33)$$

$$\mathbf{Y}_f = \mathbf{Y}_{k|2k-1} = \begin{bmatrix} \mathbf{y}(k) & \mathbf{y}(k+1) & \dots & \mathbf{y}(k+q-1) \\ \mathbf{y}(k+1) & \mathbf{y}(k+2) & \dots & \mathbf{y}(k+q) \\ \dots & \dots & \ddots & \dots \\ \mathbf{y}(2k-1) & \mathbf{y}(2k) & \dots & \mathbf{y}(2k+q-2) \end{bmatrix}, \quad (3.34)$$

with $\mathbf{Y}_p, \mathbf{Y}_f \in \mathbb{R}^{kr \times q}$, and a similar form is valid for the matrices $\mathbf{U}_p, \mathbf{U}_f \in \mathbb{R}^{ks \times q}$. The notation $\mathbf{Y}_{0|k-1}$ relates to the upper-left (0) and lower-left ($k-1$) elements of \mathbf{Y} . The state-space system keeps its characteristics with r outputs and s inputs, where n is the system (state) order, and q is a sufficiently large number of samples.

The states \mathbf{X}_0 and \mathbf{X}_k are defined as:

$$\mathbf{X}_0 = \begin{bmatrix} \mathbf{x}(0) & \mathbf{x}(1) & \mathbf{x}(2) & \dots & \mathbf{x}(q-1) \end{bmatrix}, \quad (3.35)$$

$$\mathbf{X}_k = \begin{bmatrix} \mathbf{x}(k) & \mathbf{x}(k+1) & \mathbf{x}(k+2) & \dots & \mathbf{x}(k+q-1) \end{bmatrix}, \quad (3.36)$$

with $\mathbf{X}_0, \mathbf{X}_k \in \mathbb{R}^{n \times q}$. The extended observability \mathbf{O}_k and the Toeplitz matrix \mathbf{T} are expressed as:

$$\mathbf{O}_k = \begin{bmatrix} \mathbf{C} \\ \mathbf{CA} \\ \mathbf{CA}^2 \\ \vdots \\ \mathbf{CA}^{k-1} \end{bmatrix}, \quad \mathbf{T} = \begin{bmatrix} \mathbf{D} & \mathbf{0} & \mathbf{0} & \dots & \mathbf{0} \\ \mathbf{CB} & \mathbf{D} & \mathbf{0} & \dots & \mathbf{0} \\ \mathbf{CAB} & \mathbf{CB} & \mathbf{D} & \dots & \mathbf{0} \\ \vdots & \vdots & \vdots & \ddots & \vdots \\ \mathbf{CA}^{k-2}\mathbf{B} & \mathbf{CA}^{k-3}\mathbf{B} & \mathbf{CA}^{k-4}\mathbf{B} & \dots & \mathbf{D} \end{bmatrix}, \quad (3.37)$$

with $\mathbf{O}_k \in \mathbb{R}^{kr \times n}$ and $\mathbf{T} \in \mathbb{R}^{kr \times ks}$. The Toeplitz matrix \mathbf{T} and the extended observability matrix \mathbf{O}_k are equivalent to Equation (4.6) and Equation (4.22), respectively, which are part of the concepts that compose the SSRA theory.

The N4SID theories regarding projections, SVD decomposition, Kalman filter, etc., are supported by the basic Subspace Identification concepts previously described, which contain

fundamental issues in common with the SSRA method related to the system realization aspects will be seen in the next chapter.

3.7 Some considerations

This chapter introduced some of the most well-known System Identification methods, which follow two distinct mathematical representations for linear systems. The polynomial autoregressive algorithms (ARX, ARMAX, FIR, OE, BJ) integrate the first group of this representation that is based on the polynomial forms of the process transfer function $\mathcal{G}(z)$ and noise transfer function $\mathcal{H}(z)$. These polynomials have autoregressive representation since they can depict the conditions between each other variable (output, input, state, noise) all over the discrete-time in the past. Estimated parameters compose these representations as the variables to be attained in the system identification process. The other group uses the state-space as the mathematical representation of a linear dynamical system. The Subspace methods, as the N4SID algorithm, employ the basic concepts of the state-space realization algorithms, which will be detailed in the next chapter, but in this case, with the focus on the Classical Methods as was shown in Figure 3.4. Despite the differences in mathematical representation between the autoregressive and state-space models, it should be emphasized that the transfer function emerges to express the dynamical of the system to be identified in both method types. Hence, the transfer functions work as a core to the solution for the system identification method developed in both referred algorithm types.

4 THE NOVEL SSRA-DC-ICL METHOD AND ITS BACKGROUND

4.1 Introduction²

The State-Space Realization Algorithm (SSRA) can be considered one of the most robust and accurate systems identification methods since it has been successfully applied to several structural engineering problems under operational conditions. Since the first and classical version of Juang's algorithm in 1985 (Juang; Pappa, 1985), the algorithm incorporated some functionalities triggering other arrangements. These algorithm versions are based on the same concept from an input-output data set forming the Markov parameters matrix and composing the Hankel matrix that will be decomposed by the Singular Value Decomposition (SVD) technique.

One difficulty of the SSRA is related to the order of the identified model that has to be estimated. Most of the time, this order is overestimated to find all vibration modes in the case of mechanical structures (Zhang *et al.*, 2014). This algorithm weakness gets higher due to the presence of noise in the system. Some tools, such as the Modal Amplitude Coherence (MAC) and the Mode Singular Value (MSV), address this matter of searching for the proper order of the identified system. Most of the methods stem from the SSRA, like the SSRA-DC, were proposed to tackle the noise as a considerable drawback to the system identification process.

The traditional ERA was proposed to identify linear dynamical systems excited strictly by the impulsive signal. However, the SSRA here was implemented with an arbitrary input signal instead of using the impulsive signal. Despite the algorithm's mathematical formulation considering arbitrary input signal employment, when the change to an impulsive signal is desired, this demands to have the Markov parameters matrix determined by the outputs matrix ($\mathbf{H} = \mathbf{Y}$), which would simplify some computational steps of the SSRA.

The State-Space Realization Algorithm with Data Correlations (SSRA-DC) is complementary to the SSRA from the perspective of being more appropriate than the classical SSRA when the noise is present in the system. About the principal contribution of the research, the algorithm will also be applied in conjunction with the iterative concept to verify its behavior when an additive measurement noise exists in the system. The iterative purpose applied to the SSRA-DC is what will be seen in detail in Section 4.4 and the overall aspects of simulation

² Some parts presented in this chapter were published in the papers (Soares Jr; Serpa, 2021; Soares Jr; Serpa, 2022).

results will be shown comparatively in Chapter 7.

The following section describes the State-Space Realization Algorithm, detailing the mathematical development of the method and the subjects from the input-output data set until achieving the state-space of the identified system. Next, based on the classical SSRA concepts, the basic formulation of the SSRA-DC is presented to the attainment of the state-space equations of the identified system. Both sections mentioned are the background content to the presentation and understanding of the novel method SSRA-DC-iCL, as the main objective of this research, introduced in the last section of this chapter.

4.2 SSRA concepts and formulation

Consider the state-space representation of a discrete-time system given by

$$\begin{aligned} \mathbf{x}(k+1) &= \mathbf{A}\mathbf{x}(k) + \mathbf{B}\mathbf{u}(k), \\ \mathbf{y}(k) &= \mathbf{C}\mathbf{x}(k) + \mathbf{D}\mathbf{u}(k), \end{aligned} \tag{4.1}$$

where $k = 0, 1, 2, \dots, (q-1)$, $t = kd_t$, d_t is the sampling time, and q is the number of samples. The system matrices are: $\mathbf{A} \in \mathbb{R}^{n \times n}$, $\mathbf{B} \in \mathbb{R}^{n \times s}$, $\mathbf{C} \in \mathbb{R}^{r \times n}$, $\mathbf{D} \in \mathbb{R}^{r \times s}$, for a linear dynamical MIMO system of order n , with r outputs and s inputs, $\mathbf{y}(k) \in \mathbb{R}^{r \times q}$, and $\mathbf{u}(k) \in \mathbb{R}^{s \times q}$.

The formulation of the Eigensystem Realization Algorithm, initially developed by Juang and Pappa in 1985 (Juang; Pappa, 1985), considered system excitation as an impulsive input signal. Many of the aspects treated in their paper are briefly described here together with some concepts approached in 2008 by Callafon and Moaveni (De Callafon *et al.*, 2008), mainly those regarding the system input excitation as an arbitrary signal. This issue changes the way the Hankel matrix is reached in the algorithm. Anyway, a technical memorandum previously written by Phan and Juang in 1991 (Phan *et al.*, 1991) provided some considerations about general input-output data set and the Markov parameters construction.

4.2.1 SSRA for Single-Input-Single-Output (SISO) systems

Firstly, the SSRA basic theory for systems with one output ($r = 1$) and one input ($s = 1$) is introduced. For this setup, the auxiliary variables $\mathbf{y}_s(k) = \mathbf{y}^T(k)$ and $\mathbf{u}_s(k) = \mathbf{u}^T(k)$ are used, where $\mathbf{y}_s(k) \in \mathbb{R}^{q \times 1}$ and $\mathbf{u}_s(k) \in \mathbb{R}^{q \times 1}$, both in vector forms.

Considering the system described by Equation (4.1), and assuming the initial condition $\mathbf{x}(0) = \mathbf{0}$, the following sequence can be obtained:

$$\begin{aligned}
\mathbf{y}(0) &= \mathbf{D}\mathbf{u}(0), \\
\mathbf{y}(1) &= \mathbf{C}\mathbf{B}\mathbf{u}(0) + \mathbf{D}\mathbf{u}(1), \\
\mathbf{y}(2) &= \mathbf{C}\mathbf{A}\mathbf{B}\mathbf{u}(0) + \mathbf{C}\mathbf{B}\mathbf{u}(1) + \mathbf{D}\mathbf{u}(2), \\
\mathbf{y}(3) &= \mathbf{C}\mathbf{A}^2\mathbf{B}\mathbf{u}(0) + \mathbf{C}\mathbf{A}\mathbf{B}\mathbf{u}(1) + \mathbf{C}\mathbf{B}\mathbf{u}(2) + \mathbf{D}\mathbf{u}(3), \\
&\vdots \\
\mathbf{y}(k) &= \mathbf{C}\mathbf{A}^{k-1}\mathbf{B}\mathbf{u}(0) + \mathbf{C}\mathbf{A}^{k-2}\mathbf{B}\mathbf{u}(1) + \dots + \mathbf{C}\mathbf{A}\mathbf{B}\mathbf{u}(k-2) + \mathbf{C}\mathbf{B}\mathbf{u}(k-1) + \mathbf{D}\mathbf{u}(k).
\end{aligned} \tag{4.2}$$

According to the last equation of Equation (4.2), the output $\mathbf{y}(k)$ due to the arbitrary input signal $\mathbf{u}(k)$ can be written explicitly as

$$\begin{aligned}
\mathbf{y}(k) &= \mathbf{D}\mathbf{u}(k) + \sum_{i=1}^k h(i)\mathbf{u}(k-i), \\
h(i) &= \mathbf{C}\mathbf{A}^{i-1}\mathbf{B}, \quad i \geq 1,
\end{aligned} \tag{4.3}$$

where $h(i)$ denotes the Markov parameters, with $h(0) = \mathbf{D}$. Based on the discrete output $\mathbf{y}(k)$ and the input $\mathbf{u}(k)$, the objective is to determine the appropriate size n (model order) of the state vector $\mathbf{x}(k)$ in Equation (4.1), and to estimate a discrete-time state-space realization $(\hat{\mathbf{A}}, \hat{\mathbf{B}}, \hat{\mathbf{C}}, \hat{\mathbf{D}})$ of the dynamical system considered (De Callafon *et al.*, 2008). Thus, it can be seen that $\hat{\mathbf{D}}$ is equal to the Markov parameters matrix in the initial condition ($h(0)$). Depending on the system configuration, it can be introduced in advance what will be approached ahead in the end of Section 4.2.2 and in Chapter 5 (Figure 5.8), that $\hat{\mathbf{D}}$ is not null if accelerations take part as system's output; otherwise $\hat{\mathbf{D}} = \mathbf{0}$, which will happen in most of the simulations of this research.

Another representation of Equation (4.3) can be done through

$$\mathbf{y}_s(k) = \mathbf{T}\mathbf{u}_s(k), \tag{4.4}$$

where

$$\mathbf{y}_s(k) = \begin{bmatrix} y(0) \\ y(1) \\ y(2) \\ \vdots \\ y(q-1) \end{bmatrix}, \quad \mathbf{u}_s(k) = \begin{bmatrix} u(0) \\ u(1) \\ u(2) \\ \vdots \\ u(q-1) \end{bmatrix}, \quad \text{and} \tag{4.5}$$

$$\mathbf{T} = \begin{bmatrix} \mathbf{D} & \mathbf{0} & \mathbf{0} & \dots & \mathbf{0} \\ \mathbf{CB} & \mathbf{D} & \mathbf{0} & \dots & \mathbf{0} \\ \mathbf{CAB} & \mathbf{CB} & \mathbf{D} & \dots & \mathbf{0} \\ \vdots & \vdots & \vdots & \ddots & \vdots \\ \mathbf{CA}^{q-2}\mathbf{B} & \mathbf{CA}^{q-3}\mathbf{B} & \mathbf{CA}^{q-4}\mathbf{B} & \dots & \mathbf{D} \end{bmatrix}. \quad (4.6)$$

The matrix \mathbf{T} , known as a lower block triangular Toeplitz matrix, is often associated with the Markov parameters, and can be depicted as follows (Phan *et al.*, 1991):

$$\mathbf{T} = \begin{bmatrix} h(0) & 0 & 0 & \dots & 0 \\ h(1) & h(0) & 0 & \dots & 0 \\ h(2) & h(1) & h(0) & \dots & 0 \\ \vdots & \vdots & \vdots & \ddots & \vdots \\ h(q-1) & h(q-2) & h(q-3) & \dots & h(0) \end{bmatrix}. \quad (4.7)$$

The first column of \mathbf{T} in Equation (4.7) contains the complete Markov parameters assigned in Equation (4.3). This transposed column is denoted as the Markov matrix \mathbf{H} in the following form:

$$\mathbf{H} = \begin{bmatrix} \mathbf{D} & \mathbf{CB} & \mathbf{CAB} & \mathbf{CA}^2\mathbf{B} & \dots & \mathbf{CA}^{q-2}\mathbf{B} \end{bmatrix}. \quad (4.8)$$

Transposing Equation (4.4), and with the suppression of the sample indicator k for notation simplicity, one has

$$\mathbf{y}_s^T = \mathbf{u}_s^T \mathbf{T}^T, \quad (4.9)$$

and from Equation (4.9), the following relations can be realized

$$\begin{aligned} \mathbf{y}_s^T &= \mathbf{Y}_s, \\ \mathbf{Y}_s &= \mathbf{H} \mathbf{U}_s, \end{aligned} \quad (4.10)$$

where \mathbf{H} is the Markov matrix (Equation (4.8)), \mathbf{Y}_s and \mathbf{U}_s represent matrices with one output and one input, respectively, in the form

$$\mathbf{Y}_s = \begin{bmatrix} y(0) & y(1) & y(2) & y(3) & \dots & y(q-1) \end{bmatrix}, \quad (4.11)$$

$$\mathbf{U}_s = \begin{bmatrix} u(0) & u(1) & u(2) & u(3) & \dots & u(q-1) \\ 0 & u(0) & u(1) & u(2) & \dots & u(q-2) \\ 0 & 0 & u(0) & u(1) & \dots & u(q-3) \\ 0 & 0 & 0 & u(0) & \dots & u(q-4) \\ \vdots & \vdots & \vdots & \vdots & \ddots & \vdots \\ 0 & 0 & 0 & 0 & \dots & u(0) \end{bmatrix}. \quad (4.12)$$

Therefore, the Markov matrix \mathbf{H} takes an initial role in the steps to provide the system realization as can be seen from Equation (4.10), despite in the classical ERA from (Juang; Pappa, 1985), the Hankel matrix \mathbf{H}_h is reached directly from the measurements of the outputs with the system being excited by an impulsive signal, i.e., $\mathbf{U}_s = \mathbf{I}$ (identity matrix) and $\mathbf{H} = \mathbf{Y}_s$. In the present work, the Hankel matrix is originated from the Markov matrix that should be calculated according to

$$\begin{aligned}\mathbf{H} &= \mathbf{Y}_s \mathbf{U}_s^\dagger, \\ \mathbf{U}_s^\dagger &= \mathbf{U}_s^T (\mathbf{U}_s \mathbf{U}_s^T)^{-1},\end{aligned}\tag{4.13}$$

where \mathbf{U}_s^\dagger is called Moore-Penrose pseudoinverse (Ben-Israel, Adi and Greville, 2003; Taylor *et al.*, 1988) of \mathbf{U}_s .

The Hankel matrix \mathbf{H}_h in SISO systems is built by the Markov parameters (Equation (4.3)) according to

$$\mathbf{H}_h = \begin{bmatrix} h(1) & h(2) & h(3) & \dots & h(\frac{p}{2}) \\ h(2) & h(3) & h(4) & \dots & h(\frac{p}{2} + 1) \\ h(3) & h(4) & h(5) & \dots & h(\frac{p}{2} + 2) \\ \vdots & \vdots & \vdots & \ddots & \vdots \\ h(\frac{p}{2}) & h(\frac{p}{2} + 1) & h(\frac{p}{2} + 2) & \dots & h(p - 1) \end{bmatrix}, \tag{4.14}$$

where p is a parameter of the algorithm that determines the length of the Hankel matrix and hence the order of the observability and controllability matrices, as will be seen ahead.

4.2.2 SSRA for Multiple-Input-Multiple-Output (MIMO) systems

This section intends to present how the formulation adapts to the MIMO system. Then, rather than using the matrices \mathbf{Y}_s (Equation (4.11)) and \mathbf{U}_s (Equation (4.12)), for MIMO system it will be used \mathbf{Y} and \mathbf{U} matrices to store the output and input data set with r outputs and s inputs, respectively. Equation (4.13) for the MIMO system becomes

$$\begin{aligned}\mathbf{H} &= \mathbf{Y} \mathbf{U}^\dagger, \\ \mathbf{U}^\dagger &= \mathbf{U}^T (\mathbf{U} \mathbf{U}^T)^{-1}.\end{aligned}\tag{4.15}$$

The matrix \mathbf{U} and the matrix \mathbf{Y} have the dimensions $sp \times q$ and $r \times q$, respectively. These matrices assume the following form

$$\mathbf{U} = \begin{bmatrix} u_1(0) & u_1(1) & u_1(2) & u_1(3) & \dots & u_1(q-1) \\ u_2(0) & u_2(1) & u_2(2) & u_2(3) & \dots & u_2(q-1) \\ u_3(0) & u_3(1) & u_3(2) & u_3(3) & \dots & u_3(q-1) \\ \vdots & \vdots & \vdots & \vdots & \ddots & \vdots \\ u_s(0) & u_s(1) & u_s(2) & u_s(3) & \dots & u_s(q-1) \\ \\ 0 & u_1(0) & u_1(1) & u_1(2) & \dots & u_1(q-2) \\ 0 & u_2(0) & u_2(1) & u_2(2) & \dots & u_2(q-2) \\ 0 & u_3(0) & u_3(1) & u_3(2) & \dots & u_3(q-2) \\ \vdots & \vdots & \vdots & \vdots & \ddots & \vdots \\ 0 & u_s(0) & u_s(1) & u_s(2) & \dots & u_s(q-2) \\ \\ \vdots & \vdots & \vdots & \vdots & \vdots & \vdots \\ \\ 0 & 0 & 0 & 0 & \dots & u_1(q-p) \\ 0 & 0 & 0 & 0 & \dots & u_2(q-p) \\ 0 & 0 & 0 & 0 & \dots & u_3(q-p) \\ \vdots & \vdots & \vdots & \vdots & \ddots & \vdots \\ 0 & 0 & 0 & 0 & \dots & u_s(q-p) \end{bmatrix}, \quad (4.16)$$

$$\mathbf{Y} = \begin{bmatrix} y_1(0) & y_1(1) & y_1(2) & y_1(3) & \dots & y_1(q-1) \\ y_2(0) & y_2(1) & y_2(2) & y_2(3) & \dots & y_2(q-1) \\ y_3(0) & y_3(1) & y_3(2) & y_3(3) & \dots & y_3(q-1) \\ y_4(0) & y_4(1) & y_4(2) & y_4(3) & \dots & y_4(q-1) \\ \vdots & \vdots & \vdots & \vdots & \ddots & \vdots \\ y_r(0) & y_r(1) & y_r(2) & y_r(3) & \dots & y_r(q-1) \end{bmatrix}, \quad (4.17)$$

where u_m is the value from m th input and y_j is the value from j th output of the system, with $m = 1, \dots, s$; $j = 1, \dots, r$. The parameter p of the algorithm is an even number and limited to $p \leq q$, as can be realized directly by matrix \mathbf{U} in Equation (4.16).

The basis for the algorithm is the Hankel matrix \mathbf{H}_h and the shifted Hankel matrix \mathbf{H}_{sh} . The next equations show how they are constructed in MIMO systems. For generalized

inputs in a MIMO system, the Markov matrix \mathbf{H} , the Hankel matrix \mathbf{H}_h and the shifted Hankel matrix \mathbf{H}_{sh} are set up as follows:

$$\mathbf{H} = \begin{bmatrix} \mathbf{H}_v(0) & \mathbf{H}_v(1) & \mathbf{H}_v(2) & \mathbf{H}_v(3) & \dots & \mathbf{H}_v(i) & \dots & \mathbf{H}_v(p-1) \end{bmatrix}, \quad (4.18)$$

$$\mathbf{H}_h = \begin{bmatrix} \mathbf{H}_v(1) & \mathbf{H}_v(2) & \dots & \mathbf{H}_v(\frac{p}{2}-1) \\ \mathbf{H}_v(2) & \mathbf{H}_v(3) & \dots & \mathbf{H}_v(\frac{p}{2}) \\ \vdots & \vdots & \ddots & \vdots \\ \mathbf{H}_v(\frac{p}{2}-1) & \mathbf{H}_v(\frac{p}{2}) & \dots & \mathbf{H}_v(p-3) \end{bmatrix}, \quad (4.19)$$

$$\mathbf{H}_{sh} = \begin{bmatrix} \mathbf{H}_v(2) & \mathbf{H}_v(3) & \dots & \mathbf{H}_v(\frac{p}{2}) \\ \mathbf{H}_v(3) & \mathbf{H}_v(4) & \dots & \mathbf{H}_v(\frac{p}{2}+1) \\ \vdots & \vdots & \ddots & \vdots \\ \mathbf{H}_v(\frac{p}{2}) & \mathbf{H}_v(\frac{p}{2}+1) & \dots & \mathbf{H}_v(p-2) \end{bmatrix}, \quad (4.20)$$

where $\mathbf{H}_v(i)$ are block matrices with the dimension $(r \times s)$. Thereby, the Hankel matrices \mathbf{H}_h and \mathbf{H}_{sh} have the dimension $(r(\frac{p}{2}-1)) \times (s(\frac{p}{2}-1))$.

From now on, this section presents the steps of the traditional ERA, detailed accordingly (Juang; Pappa, 1985), and taking some concepts up to now, mainly from Hankel matrix \mathbf{H}_h that can be expressed as

$$\mathbf{H}_h = \mathbf{O}\mathbf{W}, \quad (4.21)$$

where \mathbf{O} and \mathbf{W} are the observability and controllability matrices of the system, respectively, given by:

$$\mathbf{O} = \begin{bmatrix} \mathbf{C} \\ \mathbf{C}\mathbf{A} \\ \mathbf{C}\mathbf{A}^2 \\ \vdots \\ \mathbf{C}\mathbf{A}^{\frac{p}{2}-2} \end{bmatrix}_{(r(\frac{p}{2}-1)) \times n}, \quad (4.22)$$

$$\mathbf{W} = \begin{bmatrix} \mathbf{B} & \mathbf{A}\mathbf{B} & \mathbf{A}^2\mathbf{B} & \dots & \mathbf{A}^{\frac{p}{2}-2}\mathbf{B} \end{bmatrix}_{n \times (s(\frac{p}{2}-1))}.$$

From the definitions of Equation (4.22), the shifted Hankel matrix \mathbf{H}_{sh} can be written as:

$$\mathbf{H}_{sh} = \mathbf{O}\mathbf{A}\mathbf{W}. \quad (4.23)$$

For a discrete-time state-space model of order n , showed in Equation (4.1), the Cayley-Hamilton theorem hold the concept that \mathbf{O} has full column rank n and \mathbf{W} has full row rank n . Consequently, the Hankel matrix \mathbf{H}_h has rank n (De Callafon *et al.*, 2008).

Based on \mathbf{O} and \mathbf{W} matrices' characteristics, there is a left pseudoinverse \mathbf{O}^\dagger such that $\mathbf{O}^\dagger \mathbf{O} = \mathbf{I}_{n \times n}$ and a right pseudoinverse \mathbf{W}^\dagger such that $\mathbf{W} \mathbf{W}^\dagger = \mathbf{I}_{n \times n}$. Hence, from Equation (4.23), it is clear that

$$\mathbf{A} = \mathbf{O}^\dagger \mathbf{H}_{sh} \mathbf{W}^\dagger, \quad (4.24)$$

where the previous left and right pseudoinverse are established as

$$\begin{aligned} \mathbf{O}^\dagger &= [\mathbf{O}^T \mathbf{O}]^{-1} \mathbf{O}^T, \\ \mathbf{W}^\dagger &= \mathbf{W}^T [\mathbf{W} \mathbf{W}^T]^{-1}. \end{aligned} \quad (4.25)$$

The Hankel (Equation (4.19)) and shifted Hankel (Equation (4.20)) matrices are completely known through the respective equations. In Equation (4.21), the decomposition of the Hankel matrix \mathbf{H}_h into the matrices \mathbf{O} and \mathbf{W} can be performed through a singular value decomposition (SVD), or even other decomposition, for example, Cholesky, LU, or QR decompositions. Using SVD, the decomposition carry out

$$\mathbf{H}_h = \mathbf{U} \mathbf{\Sigma}_i \mathbf{V}^T, \quad (4.26)$$

where both \mathbf{U} and \mathbf{V} are orthonormal matrices and $\mathbf{\Sigma}_i$ is a diagonal matrix with the singular values ordered in decreasing magnitude and non-negative:

$$\mathbf{\Sigma}_i = \text{diag} \left[\sigma_1, \sigma_2, \dots, \sigma_n, \sigma_{n+1}, \dots, \sigma_{\frac{p}{2}-1} \right] \quad (4.27)$$

with

$$\sigma_1 \geq \sigma_2 \geq \dots \geq \sigma_n \geq \sigma_{n+1} \geq \dots \geq \sigma_{\frac{p}{2}-1}. \quad (4.28)$$

Considering the singular values σ_i ($i = n + 1, \dots, \frac{p}{2} - 1$) are zero, the matrix \mathbf{H}_h certainly has rank equal or less than n . In case the singular values σ_i ($i = n + 1, \dots, \frac{p}{2} - 1$) are not exactly zero but are too small, there is no doubt that the matrix \mathbf{H}_h has rank not outlying from n . For instance, in a system with noise in the measurements, it would be expected real difficulties to realize a gap between the computed last non-zero singular value and what actually should be considered zero. In this case, possibly the rank n would be greater than expected. Computer round-off, and measured signal can be considered possible sources of noise in this case.

With the choice of n , the Hankel matrix \mathbf{H}_h (Equation (4.26)) can be computed to a reduced rank n matrix \mathbf{H}_{hn} following the same dimension of

$$\mathbf{H}_{hn} = \mathbf{U}_n \mathbf{\Sigma}_n \mathbf{V}_n^T. \quad (4.29)$$

Comparing the terms of Equation (4.21) and Equation (4.29), the matrices \mathbf{O} and \mathbf{W} can be computed as

$$\begin{aligned}\mathbf{O} &= \mathbf{U}_n \Sigma_n^{1/2}, \\ \mathbf{W} &= \Sigma_n^{1/2} \mathbf{V}_n^T.\end{aligned}\tag{4.30}$$

Substituting Equation (4.30) in Equation (4.25), it is obtained

$$\begin{aligned}\mathbf{O}^\dagger &= \Sigma_n^{-1/2} \mathbf{U}_n^T, \\ \mathbf{W}^\dagger &= \mathbf{V}_n \Sigma_n^{-1/2}.\end{aligned}\tag{4.31}$$

From the results of Equation (4.24) and Equation (4.31), the estimated state-space system matrix $\hat{\mathbf{A}}$ can be determined as

$$\hat{\mathbf{A}} = \Sigma_n^{-1/2} \mathbf{U}_n^T \mathbf{H}_{sh} \mathbf{V}_n \Sigma_n^{-1/2}.\tag{4.32}$$

The estimated state-space input matrix $\hat{\mathbf{B}}$ and the estimated state-space output matrix $\hat{\mathbf{C}}$ can be obtained with the first s columns of the matrix \mathbf{W} and with the first r rows of the matrix \mathbf{O} , respectively, as follows:

$$\begin{aligned}\hat{\mathbf{B}} &= \mathbf{W} \mathbf{E}_s = \Sigma_n^{1/2} \mathbf{V}_n^T \mathbf{E}_s, \\ \hat{\mathbf{C}} &= \mathbf{E}_r^T \mathbf{O} = \mathbf{E}_r^T \mathbf{U}_n \Sigma_n^{1/2},\end{aligned}\tag{4.33}$$

where

$$\begin{aligned}\mathbf{E}_s &= [\mathbf{I}_s \quad \mathbf{0} \quad \dots \quad \mathbf{0}]^T, \\ \mathbf{E}_r &= [\mathbf{I}_r \quad \mathbf{0} \quad \dots \quad \mathbf{0}]^T,\end{aligned}\tag{4.34}$$

and \mathbf{I}_s and \mathbf{I}_r are the identity matrices of orders s and r , respectively.

The system can be considered initially at rest when $k = 0$. For the case of a system that does not involve accelerations as outputs, it is appropriate to mention that $\mathbf{D} = \mathbf{H}_v(0) = \mathbf{0}$. Consequently, without loss of generality, the realization of the MIMO system to be identified is composed of the triplet $(\mathbf{A}, \mathbf{B}, \mathbf{C})$. If the system to be identified has accelerations as outputs, the matrix \mathbf{D} would be considered as the Markov parameters in the first sampling instant ($k = 0$ in the algorithm).

The main steps of the classical State-Space Realization Algorithm for MIMO systems are summarized in the following Figure 4.1.

The simulation procedures and the results of the simulations introduced ahead in this work encompass the adjustment parameters. The variables d_t , q , p and n previously mentioned in this section are considered the adjustable parameters in the simulations of the SSRA.

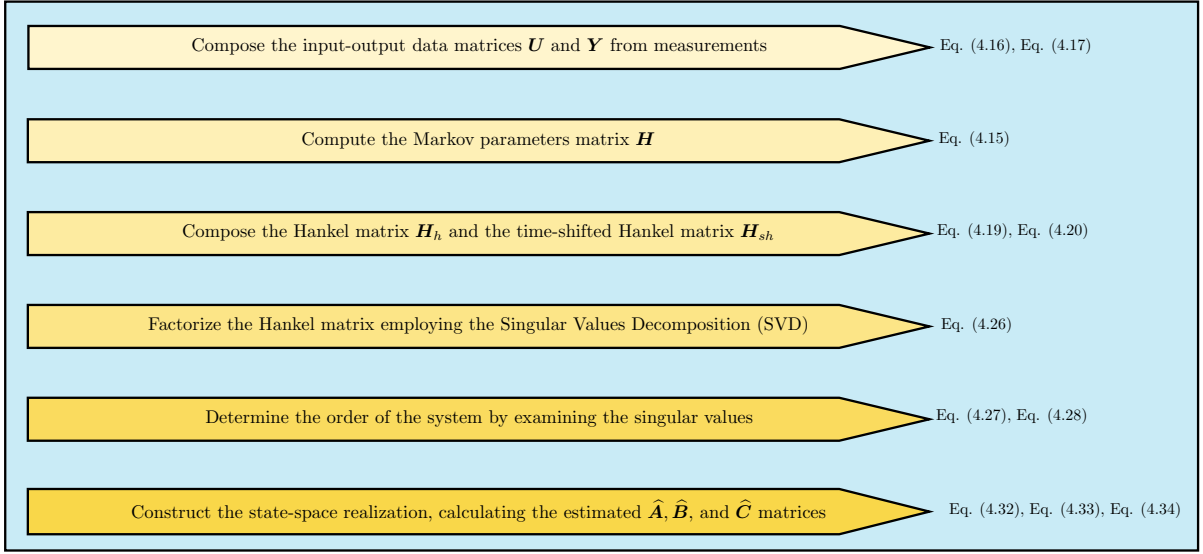


Figure 4.1 – Main steps of the classical State-space Realization Algorithm.

Even in a real-time dynamical system, the parameters p and n require to be adjusted. The other two parameters should be defined indirectly when the measurement devices are set up to establish the sampling frequency and the total time of measurement or the number of samples.

4.2.3 The Least-Squares in Markov matrix computing

This topic has no direct influence on the SSRA method formulations presented up to this point. The following subject attests to how the Markov parameters matrix inherently contains the Least-Squares concepts in its computing.

For a MIMO system, the basic relation holds

$$Y = HU, \quad (4.35)$$

where the Markov matrix H can be considered a numerical transfer function of the system, with the outputs matrix Y excited by the inputs matrix U . A prediction error with noise characteristics should arise when the transfer function H is computed. The traditional Least-Squares (LS) optimization method takes place to minimize this error when the calculation of the Markov matrix is accomplished. This LS problem can be stated by rewriting Equation (4.35) in the concept of an FIR model, as seen in Chapter 3, which includes the addition of a prediction error vector ν as

$$y(k) = \psi^T(k)\theta + \nu(k), \quad (4.36)$$

where

$$\psi(k) = [u(k-1) \quad u(k-2) \quad \dots \quad u(k-n)].$$

Representing Equation (4.36) in the matrix form, it results

$$\mathbf{Y}_n = \mathbf{\Psi}_n^T \boldsymbol{\theta} + \boldsymbol{\Lambda}_n, \quad (4.37)$$

where

$$\begin{aligned} \mathbf{Y}_n &= [\mathbf{y}(1) \quad \mathbf{y}(2) \quad \dots \quad \mathbf{y}(n)]^T, \\ \mathbf{\Psi}_n &= [\boldsymbol{\psi}(1) \quad \boldsymbol{\psi}(2) \quad \dots \quad \boldsymbol{\psi}(n)]^T, \\ \boldsymbol{\theta} &= [\mathbf{H}_v^T(1) \quad \mathbf{H}_v^T(2) \quad \dots \quad \mathbf{H}_v^T(n)]^T, \\ \boldsymbol{\Lambda}_n &= [\boldsymbol{\nu}(1) \quad \boldsymbol{\nu}(2) \quad \dots \quad \boldsymbol{\nu}(n)]^T, \end{aligned}$$

with $\mathbf{Y}_n \in \mathbb{R}^{n \times r}$, $\boldsymbol{\Lambda}_n \in \mathbb{R}^{n \times r}$, $\mathbf{\Psi}_n \in \mathbb{R}^{sn \times n}$, $\boldsymbol{\theta} \in \mathbb{R}^{sn \times r}$, for r outputs and s inputs ($\mathbf{H}_v \in \mathbb{R}^{r \times s}$ is the block Hankel matrix), where $\mathbf{y}(i)$ is a row vector with r output elements and $\mathbf{u}(i)$ is a column vector with s input elements.

The Least-Squares solution of the system portrayed by Equation (4.37) is well known ([Chen *et al.*, 2012a](#)):

$$\begin{aligned} \hat{\boldsymbol{\theta}}_n^{LS} &= \arg \min_{\boldsymbol{\theta}} \boldsymbol{\nu}_n(\boldsymbol{\theta}), \\ \boldsymbol{\nu}_n(\boldsymbol{\theta}) &= \|\mathbf{Y}_n - \mathbf{\Psi}_n^T \boldsymbol{\theta}\|^2 = \sum_{k=1}^n (\mathbf{y}(k) - \boldsymbol{\psi}^T(k) \boldsymbol{\theta})^2, \\ \hat{\boldsymbol{\theta}}_n^{LS} &= [\mathbf{\Psi}_n \mathbf{\Psi}_n^T]^{-1} \mathbf{\Psi}_n \mathbf{Y}_n. \end{aligned} \quad (4.38)$$

Comparing Equation (4.15) with the last equation in Equation (4.38), it can be realized the equivalence between the Markov matrix \mathbf{H} and the estimator $\boldsymbol{\theta}$. It is possible to see that in the Markov matrix's computing, the error minimization related to the attainment of the system transfer function, rendered by the Markov matrix itself, occurs.

4.3 SSRA-DC concepts and formulation

4.3.1 Fundamentals concepts

An LTI State-Space discrete-time system, shown in Equation (3.24) and the following reintroduced in Equation (4.39), commonly models a System Identification method of a characteristically stochastic process.

$$\begin{aligned} \hat{\mathbf{x}}(k+1) &= \mathbf{A} \hat{\mathbf{x}}(k) + \mathbf{B} \mathbf{u}(k) + \mathbf{w}(k), \\ \hat{\mathbf{y}}(k) &= \mathbf{C} \hat{\mathbf{x}}(k) + \mathbf{D} \mathbf{u}(k) + \mathbf{v}(k). \end{aligned} \quad (4.39)$$

with its variables defined as the correspondent ones from the deterministic state-space representation (Equation (4.1)), where $\mathbf{w}(k) \in \mathbb{R}^{n \times 1}$ and $\mathbf{v}(k) \in \mathbb{R}^{r \times 1}$ are the stochastic disturbances

related to input noise and measurement noise, respectively. $\mathbf{u}(k)$ is the input excitation, $\hat{\mathbf{x}}(k)$ is the estimated state of the system, and $\hat{\mathbf{y}}(k)$ is the estimated output.

For the purposes and characteristics of the SSRA-DC method, as the basis of the method focus of this work, the measurement noise $\mathbf{v}(k)$ will be considered by handling the output data by adding a typical random white noise signal, and due to the present scope of this research, no input noise is considered ($\mathbf{w}(k) = \mathbf{0}$). The lack of these disturbances in the state-space modeling would probably lead to bias terms affecting the conventional State-Space Realization Algorithm, presented in Section 4.2. According to the data correlation features of the method, the mathematical modeling presented in Section 4.3.2 is based on the deterministic State-Space system given by Equation (4.1) (Hou; Hsu, 1991).

The system defined by Equation (4.1) typically operates in an open-loop condition, which is inherent to the conventional SSRA-DC method, the basis of this research. Hence, a possible bias is avoided due to the non-correlation between the input and the measurement noise. The input excitation is assumed as a signal of rich spectral excitation and zero-mean with unit-variance. So, and considering that the measurement noise and the input excitation are uncorrelated in this work, the data correlation treatment of the input-output data set allows for reducing the influence of the measurement noise $\mathbf{v}(k)$ in the system identification process. For simplicity, a Single-Input-Single-Output system is applied to support this concept, employing the input $u(k)$ and the output $y(k)$ in the following formulation. Some concepts applied to data series and stochastic systems are introduced as the basis for this issue.

The cross-correlation function r_{uy} of $\mathbf{u}(k)$ and $\mathbf{y}(k)$, and autocorrelation function r_u of $\mathbf{u}(k)$ can be defined and estimated as (Soderstrom; Stoica, 1989; Aguirre, 2015):

$$r_{uy}(k, i) = E[u(k)y(k+i)], \quad \hat{r}_{uy}(k) = \frac{1}{q} \sum_{i=0}^{q-k} u(i)y(i+k), \quad (4.40)$$

$$r_u(k, i) = E[u(k)u(k+i)], \quad \hat{r}_u(k) = \frac{1}{q} \sum_{i=0}^{q-k} u(i)u(i+k), \quad (4.41)$$

where i is an integer and the operator $E(\cdot)$ is the statistical expected value.

The equation of Wiener-Hopf depicts the relation between $r_{uy}(k)$ and $r_u(k)$ as follows (Soderstrom; Stoica, 1989; Aguirre, 2015):

$$r_{uy}(k) = \sum_{i=0}^{\infty} h(i)r_u(k-i), \quad (4.42)$$

which in a matrix form can be expressed as

$$\begin{bmatrix} r_{uy}(0) \\ r_{uy}(1) \\ r_{uy}(2) \\ \vdots \end{bmatrix} = \begin{bmatrix} r_u(0) & r_u(-1) & r_u(-2) & \dots \\ r_u(1) & r_u(0) & r_u(-1) & \dots \\ r_u(2) & r_u(1) & r_u(0) & \dots \\ \vdots & \vdots & \vdots & \vdots \end{bmatrix} \begin{bmatrix} h(0) \\ h(1) \\ h(2) \\ \vdots \end{bmatrix}, \quad (4.43)$$

$$\mathbf{r}_{uy} = \mathbf{R}_u \mathbf{h}, \quad (4.44)$$

considering here that the autocorrelation matrix \mathbf{R}_u is truncated in a finite number of samples, where $h(i)$ is the impulse response of the system at instant i .

From Equation (4.44), it can be stated:

$$\mathbf{h} = \mathbf{R}_u^{-1} \mathbf{r}_{uy}, \quad (4.45)$$

with \mathbf{R}_u a non-singular matrix.

Considering a general solution for the proposed problem that comes from Equation (4.45), and with the objective to simplify the current analysis, the input $u(k)$ is chosen to perform a null autocorrelation ($r_u(k) = 0$) when $k \neq 0$, which is ensured in this work as the input excitations are Gaussian White Noise signals. Then, \mathbf{R}_u becomes a diagonal matrix with all elements equals to $r_u(0)$, and Equation (4.44) can be stated as (Soderstrom; Stoica, 1989; Aguirre, 2015):

$$\mathbf{r}_{uy} = r_u(0) \mathbf{I} \mathbf{h} \Rightarrow \mathbf{h} = \frac{1}{\sigma_u^2} \mathbf{r}_{uy}, \quad (4.46)$$

where \mathbf{I} is the identity matrix and $\sigma_u^2 = r_u(0)$ is the variance of $u(k)$.

Since the measured output $y(k)$ is corrupted by the noise $v(k)$, then $y(k) = y^c(k) + v(k)$, where $y^c(k)$ represents the output part ideally without noise. Composing Equation (4.40) with the measured output that contains noise, it is possible to write (Soderstrom; Stoica, 1989; Aguirre, 2015):

$$\begin{aligned} r_{uy}(k) &= \frac{1}{q} \sum_{i=0}^{q-k} u(i) [y^c(i+k) + v(i+k)], \\ r_{uy}(k) &= \frac{1}{q} \sum_{i=0}^{q-k} u(i) y^c(i+k) + \frac{1}{q} \sum_{i=0}^{q-k} u(i) v(i+k), \\ r_{uy}(k) &= r_{uy}^c(k) + r_{uv}(k). \end{aligned} \quad (4.47)$$

Substituting the last equation from Equation (4.47) into Equation (4.46) yields (Soderstrom; Stoica, 1989; Aguirre, 2015):

$$\mathbf{r}_{uy}^c + \mathbf{r}_{uv} = r_u(0) \mathbf{I} \mathbf{h} \Rightarrow \mathbf{h} = \frac{1}{\sigma_u^2} (\mathbf{r}_{uy}^c + \mathbf{r}_{uv}). \quad (4.48)$$

Firstly, as can be seen by the cross-correlation in Equation (4.40), \mathbf{r}_{uy}^c is relatively robust against noises due to the averaging effect present, which depends on the k value, clearly better if $q \rightarrow \infty$. Equation (4.48) shows that a way to eliminate the parcel coming from the noise effect is making $r_{uv}(k) = 0$, being this attribute feasible in the present work according to the characteristics of both excitation signal $u(k)$ and measurement noise $v(k)$ applied. Thus, the data correlation treatment imposed on the input data set of the algorithm can ensure a reduction of the influence of measurement noise $v(k)$, providing an even more unbiased identification result.

The Wiener-Hopf equation (Equation (4.42)) can be applied to MIMO systems (Song; Ritcey, 1997; Benesty *et al.*, 2008). In the case of this work, the SISO formulation was presented to simplify the formulation since it allows an extension to MIMO systems. The basic proposition keeps valid, relying on the similarity with the data correlation method, for instance, between Equation (4.45) and Equation (4.15), once the Markov parameters matrix \mathbf{H} is submitted to the data correlation properties.

4.3.2 SSRA-DC basic formulation

The SSRA-DC (Juang *et al.*, 1988) is supported by transforming the Markov parameters block matrices with different sizes and shifts into block correlation matrices. From Equation (4.18) and Equation (4.19), the generalized Hankel matrix is composed as following:

$$\mathbf{H}_k = \begin{bmatrix} \mathbf{H}_v(k+1) & \mathbf{H}_v(k+2) & \dots & \mathbf{H}_v(k+\beta) \\ \mathbf{H}_v(k+2) & \mathbf{H}_v(k+3) & \dots & \mathbf{H}_v(k+\beta+1) \\ \vdots & \vdots & \ddots & \vdots \\ \mathbf{H}_v(k+\alpha) & \mathbf{H}_v(k+\alpha+1) & \dots & \mathbf{H}_v(k+\alpha+\beta-1) \end{bmatrix}, \quad (4.49)$$

where $\mathbf{H}_v(k+i)$ is a block matrix of r rows (number of outputs) and s columns (number of inputs), and $(k+i)$ represents the lag time values with $i = 1, 2, \dots, (\alpha + \beta - 1)$. α and β are integers that determine the number of block rows and columns from the matrix \mathbf{H}_k .

SSRA-DC has the data correlation matrix $\mathcal{R}\mathbf{h}$ as basis of the method, following defined:

$$\mathcal{R}\mathbf{h}_k = \mathbf{H}_k \mathbf{H}_0^T, \quad (4.50)$$

with $\mathcal{R}h_0 = H_0 H_0^T$ and

$$H_0 = \begin{bmatrix} H_v(1) & H_v(2) & \dots & H_v(\beta) \\ H_v(2) & H_v(3) & \dots & H_v(\beta+1) \\ \vdots & \vdots & \ddots & \vdots \\ H_v(\alpha) & H_v(\alpha+1) & \dots & H_v(\alpha+\beta-1) \end{bmatrix}. \quad (4.51)$$

Similar to the SSRA method, a block correlation Hankel matrix \mathcal{H}_k can be formed as the primary data to be used in the state-space matrices expressions. The matrix \mathcal{H}_k works to compose the SSRA-DC method, aiming for the attainment of the state-space equations of the identified system. This matrix is defined as follows:

$$\mathcal{H}_k = \begin{bmatrix} \mathcal{R}h(k) & \mathcal{R}h(k+\tau) & \dots & \mathcal{R}h(k+\gamma\tau) \\ \mathcal{R}h(k+\tau) & \mathcal{R}h(k+2\tau) & \dots & \mathcal{R}h(k+(\gamma+1)\tau) \\ \vdots & \vdots & \ddots & \vdots \\ \mathcal{R}h(k+\xi\tau) & \mathcal{R}h(k+(\xi+1)\tau) & \dots & \mathcal{R}h(k+(\xi+\gamma)\tau) \end{bmatrix}, \quad (4.52)$$

where $\mathcal{R}h(k) = \mathcal{R}h_k$; this matrix notation is used with the intent of working as a block matrix element of the matrix \mathcal{H}_k . The variables τ , ξ , and γ are integers that determine the size of the blocks $\mathcal{R}h$ and the matrix \mathcal{H}_k .

For the purposes of this work and its correspondent simulations, the variables α , β , τ , ξ and γ , from Equation (4.49) and Equation (4.52), will be treated with the following assumptions without loss of generality:

- a) $\alpha = \beta$, then β can be disregarded in the algorithm;
- b) $\tau = \alpha$, considering the condition of $\tau \geq \alpha$ to avoid overlap of adjacent correlation terms in the block correlation matrix (Juang, 1994);
- c) Based on the assumptions a) and b), and considering that $\mathcal{R}h((\xi+\gamma)\alpha+1)$ is the last element of the matrix \mathcal{H}_1 (Equation (4.52)) for $k=1$, this element is calculated as defined in Equation (4.50). Substituting $((\xi+\gamma)\alpha+1)$ as the variable k in Equation (4.49), its last element corresponds to the last element of the matrix of parameters of Markov (Equation (4.18)). With that, the parameter p can be taken to determine the value of the parameter α , as follows:

$$\begin{aligned} p-1 &= k + \alpha + \beta - 1 = (\xi+\gamma)\alpha + 1 + \alpha + \alpha - 1, \\ p-1 &= \xi\alpha + \gamma\alpha + 2\alpha = (\xi+\gamma+2)\alpha, \\ \alpha &= \frac{p-1}{\xi+\gamma+2}, \end{aligned} \quad (4.53)$$

where $\alpha \in \mathbb{N}_1$ is rounded for lower.

- d) ξ and γ are configurable parameters of the algorithm and will be adjusted together to the other required settings of the classical SSRA.

The SSRA algorithm (Section 4.2.2) was assembled to have an even number assigned to the parameter p , whereas here in the SSRA-DC, this condition is not required, but both algorithms demand $p \leq q$.

In the sequel, it is presented the formulas based on $\mathcal{H}(0) = \mathcal{H}_0$ and $\mathcal{H}(1) = \mathcal{H}_1$ computed from Equation (4.52), where $\mathcal{H}(1)$ is the time-shifted block correlation Hankel matrix. Firstly the factorization of the block correlation Hankel matrix is undertaken with the application of singular value decomposition:

$$\mathcal{H}(0) = \mathcal{U} \Sigma_i \mathcal{V}^T, \quad (4.54)$$

where $\Sigma_i = \text{diag} \left[\sigma_1, \sigma_2, \dots, \sigma_n, \sigma_{n+1}, \dots, \sigma_{\frac{p}{2}} \right]$.

Similar to the traditional SSRA, a reduced rank n matrix taken from Equation (4.54) can be given as follows:

$$\mathcal{H}_n(0) = \mathcal{U}_n \Sigma_n \mathcal{V}_n^T, \quad (4.55)$$

where it is considered the first n singular values σ_i that are non-negative and decreasingly ordered, then,

$$\Sigma_n = \text{diag}[\sigma_1, \sigma_2, \dots, \sigma_i, \sigma_{i+1}, \dots, \sigma_n]. \quad (4.56)$$

Defining the following matrices:

$$\begin{aligned} E_r^T &= [\mathbf{I}_r \quad \mathbf{0}_r \quad \dots \quad \mathbf{0}_r], \\ E_s^T &= [\mathbf{I}_s \quad \mathbf{0}_s \quad \dots \quad \mathbf{0}_s], \\ E_\alpha^T &= [\mathbf{I}_\alpha \quad \mathbf{0}_\alpha \quad \dots \quad \mathbf{0}_\alpha], \end{aligned} \quad (4.57)$$

where \mathbf{I}_i and $\mathbf{0}_i$ are identity matrix and null matrix of order i , respectively.

Thus, the estimated state-space realization system $[\hat{A}, \hat{B}, \hat{C}, \hat{D}]$ can be attained with the following expressions:

$$\begin{aligned} \hat{A} &= \Sigma_n^{-\frac{1}{2}} \mathcal{U}_n^T \mathcal{H}(1) \mathcal{V}_n \Sigma_n^{-\frac{1}{2}}, \\ \hat{B} &= [E_\alpha^T \mathcal{U}_n \Sigma_n^{\frac{1}{2}}]^\dagger H_0 E_s, \\ \hat{C} &= E_r^T \mathcal{U}_n \Sigma_n^{\frac{1}{2}}, \\ \hat{D} &= H_v(0), \end{aligned} \quad (4.58)$$

being proper the same considerations assigned for SSRA (Section 4.2.2) related to the conditions when $\hat{D} = H_v(0) = 0$.

The main steps of the mathematical formulation detailing the development to obtain Equations (4.58) are described in Appendix A.

Estimation bias inherent in working of Singular Value Decomposition of a Hankel data matrix with added noise can be significantly reduced by incorporating data correlation in the identification algorithm. For the SSRA-DC, the bias terms can be omitted by adequately choosing the integer k , considering that the measurement noise V added to the output matrix Y is typically a random-normally distributed signal, as will be presented at Section 5.3. As the basis of the method and as established in Section 4.3.1, the correlation function employed in the Hankel matrices allows having an unbiased algorithm for system identification (Hou; Hsu, 1991; Juang, 1994).

4.4 The novel method SSRA-DC-iCL

This section introduces the proposed method coming from the SSRA-DC presented in Section 4.3.2. Besides the main characteristics that determine the combined technique's steps, a concept to update the Markov parameters matrix as the core to the method's effectiveness will be established. The method's proposition is to be a complementary technique to the classical methods based on state-space realization, improving the SI process in the presence of measurement noise under a reduced number of samples acquired from the process in a linear system.

The main contribution of the present research is the concept of feedbacking the Markov parameters in the identification algorithm, which is distinct from the works (Juang, 1994; Phan *et al.*, 1994) where the closed-loop is in the system plant, thus known as a closed-loop identification. In this work, the state-space realization algorithm for identifying dynamical systems was modified to include the Markov parameters' feedback in an iterative model. This feedback was performed using the Markov matrix residue structured for each output to obtain a dynamic gain computed at each iteration and reconfigured accordingly to the residue's covariance. Thus, the noise effect is reduced at each algorithm iteration with the proposed algorithm feedback technique that continuously updates the Markov parameters.

Before presenting the proposed iterative method, the following section provides the essential condition that led the iterative algorithm application to be justified as better than the

classical state-space realization methods. After, a block diagram of the integrated algorithm is introduced, highlighting the algorithm modules that compose the whole iterative method. To better understand the block diagram, a detailed description of each step of the general method is presented. The closed-loop control strategy adopted for the feedback of the Markov parameters is approached at this point. The last section of this chapter shows the complete algorithm of the novel iterative method.

4.4.1 Condition of small samples set available

The iterative algorithm developed in this research aims to tackle the limitation of not having a sufficiently large number of samples acquired from the process, avoiding degradation of the identification accuracy. This restriction sounds even more eminent for performance in high-order systems and with many input-output variables.

Considering that system dynamics are depicted in the data, the increase of the model's effectiveness has a straightforward relationship with the size of the data set. In the system identification process characterized by a relatively small data size, uncertainties that lead to significant drawbacks in the identification accuracy motivated some works, as in Gu and Wei (Gu; Wei, 2018). This concern is suitably synthesized by Gu and Wei (Gu; Wei, 2018): “For small data modeling problems, the difficulty of finding reliable models is often exacerbated due to the small sample size of data. Reliable model identification from small sample data is a challenging problem frequently encountered in practical system identification.”

The SSRA-DC-iCL method should be applied to have its algorithm settings complying with a number of samples sufficiently small to achieve identification effectiveness better than for the conventional SSRA-DC algorithm. For this work's objective with linear systems, the parameter q for the SSRA-DC-iCL was adjusted with half of the value that the SSRA-DC algorithm would need to achieve almost full effectiveness under noiseless conditions. This assumed condition will be reported and analytically endured at Section 7.3.

4.4.2 The proposed method

The block diagram of the developed method (Figure 4.2) represents a combination of the technique related to updating the Markov parameters iteratively in a closed-loop with the state-space identification method based on data correlation. The figure highlights three areas integrated into the algorithm's purposes. The lower area corresponds to the new concept of pro-

viding Markov parameters feedback iteratively. The outputs $\hat{Y}_{(i)}$ have resulted from an updated state-space identified system attained at each iteration i . The other two bounded areas represent the data set generation and the validation of the system identified, assigning an evaluation index related to the model accuracy.

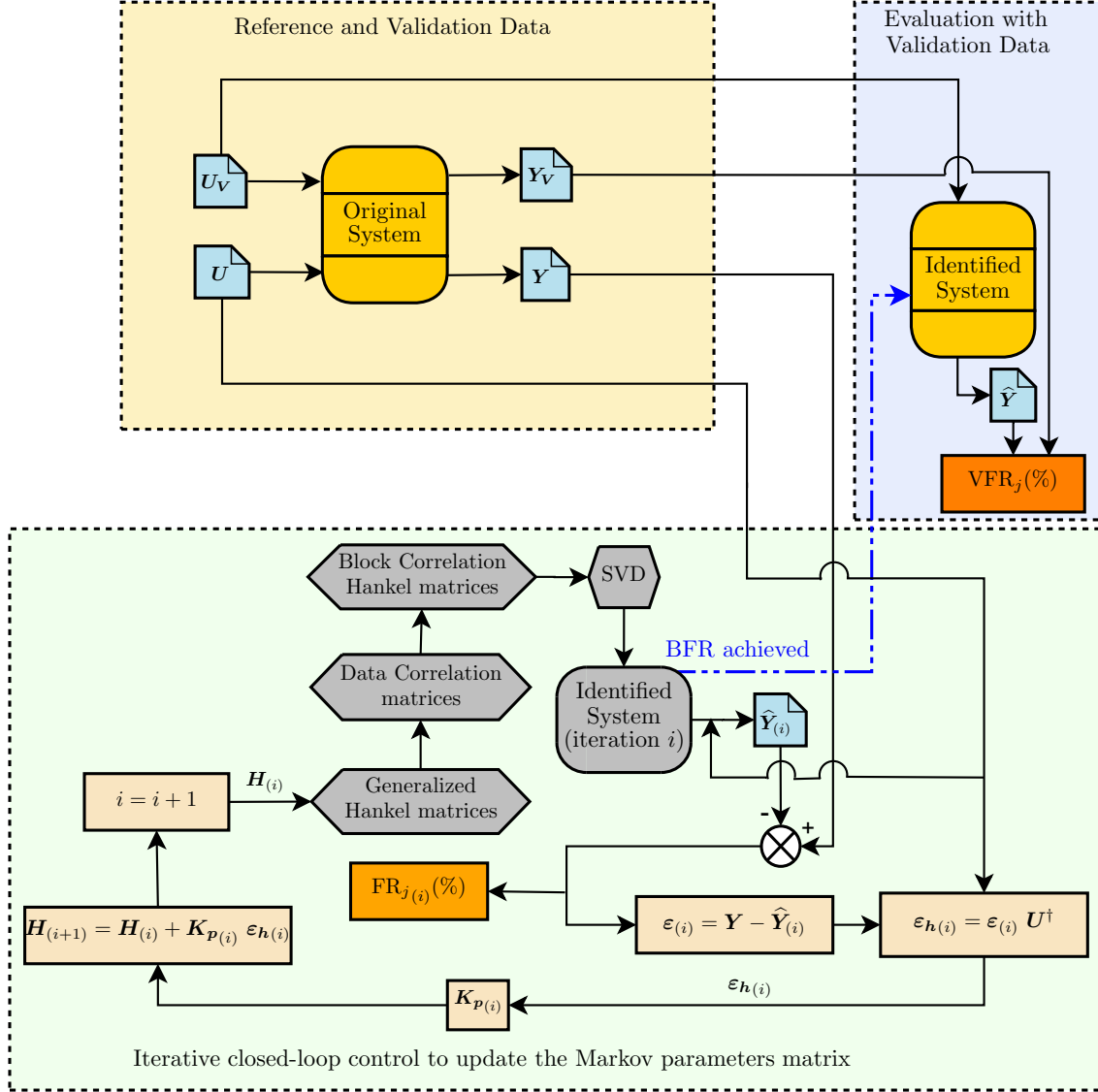


Figure 4.2 – Block diagram of SSRA-DC-iCL

The state-space representation of a mass-spring-damper model or the differential equations of a cart-pendulum model, like those approached in Section 5.4 and Section 5.5, is used to generate the output data from simulations considering the input excitation. Each of these dynamical systems is called the original system (OS) to distinguish it from the identified system (IS). The computational steps of SSRA-DC-iCL are based on the input data set obtained from simulations, in which the steps are presented in Figure 5.11. In a real process, this data set would come from experimental measurements. Two sets of data are considered in the algorithm,

one for the attainment of the state-space realization (inputs \mathbf{U} and outputs \mathbf{Y}), which work as reference data to the closed-loop iterative algorithm, and the other is the validation data for the evaluation of the identified system (inputs \mathbf{U}_V and outputs \mathbf{Y}_V).

The Fit Rate (FR_j and VFR_j) shown in Figure 4.2 represents a quantitative evaluation index to measure the adherence of the IS compared to the OS . The index is calculated individually for each output j . For each identification cycle, an average $\overline{\text{FR}}$ from all outputs is used to represent the SI process's effectiveness. The FR_j for each output, and $\overline{\text{FR}}$ are calculated as following

$$\text{FR}_j = \left(1 - \sqrt{\left(\frac{\sum_{k=0}^{(q-1)} (y_j(k) - \hat{y}(k))^2}{\sum_{k=0}^{(q-1)} (y_j(k) - \bar{y})^2} \right)} \right) \times 100\%, \quad (4.59)$$

$$\overline{\text{FR}} = \frac{1}{r} \sum_{j=1}^r \text{FR}_j, \quad (4.60)$$

with

$$\bar{y} = \frac{1}{q} \sum_{k=0}^{(q-1)} y_j(k),$$

where $\hat{\mathbf{y}}$ (vector element $\hat{y}(k)$) is the estimated value of one output from the identified system, \mathbf{y}_j (vector element $y_j(k)$) represents the output vector from the original (true) system, which comes from matrix \mathbf{Y} for FR_j computing (Roll *et al.*, 2005; Piga *et al.*, 2015). The index FR_j is called Validated Fit Rate (VFR_j) when it is computed at the validation stage using the output \mathbf{Y}_V to compose $y_j(k)$ elements. Similarly, the average of VFR_j is called $\overline{\text{VFR}}$.

The percentage value calculated at each iteration composes a series of values that increase when better identification is obtained, reaching $\overline{\text{FR}} = 100\%$ when the identified response is precisely the same as the original system. Since the objective of the SSRA-DC-iCL is to attain the state-space realization of the identified system with BFR (Best Fit Rate), the algorithm SSRA-DC-iCL is set to stop when the $\overline{\text{FR}}$ of one iteration reaches the BFR set-point (SFR in the Algorithm 1) or when the desired number of iterations is achieved. In the present research, the algorithm was set to stop only by the number of iterations, allowing to study of the $\overline{\text{FR}}$ behavior throughout the iterations. The BFR is a Fit Rate value obtained at the iteration stage of the algorithm, whereas the $\overline{\text{VFR}}$ comes from the validation stage, both computed for the same identified system at any simulation. The IS is stored when the highest BFR value is achieved in the iteration stage, where that IS also yields a $\overline{\text{VFR}}$ value for the correspondent simulation.

The basic computational steps of the iterative closed-loop SSRA-DC-iCL algorithm are:

- I $i = 0$; where (i) represents the i th algorithm iteration.
- II Compute the Markov parameters matrix's initial condition $\mathbf{H}_{(0)}$ (Equation (4.15)) from \mathbf{U} and \mathbf{Y} .
- III Compose the Generalized Hankel matrices \mathbf{H}_k (Equation (4.49)).
- IV Compose the Data Correlation matrices $\mathcal{R}h_k$ (Equation (4.50)).
- V Compose the Block Correlation Hankel matrices \mathcal{H}_k (Equation (4.52)).
- VI Obtain the matrices of the state-space identified system (IS) from Singular Value Decomposition of the Block Correlation Hankel matrix \mathcal{H}_0 (using equations from (4.54) to (4.58)).
- VII By simulating the iterative IS with inputs \mathbf{U} (*lsim* function in the algorithm), generate the estimated data output $\hat{\mathbf{Y}}_{(i)}$.
- VIII Calculate the Fit Rate indicator FR_j (%) for each output j using \mathbf{Y} and $\hat{\mathbf{Y}}_{(i)}$, and calculate the \overline{FR} .
- IX Compute the residual output matrix: $\boldsymbol{\varepsilon}_{(i)} = \mathbf{Y} - \hat{\mathbf{Y}}_{(i)}$.
- X Compute the Markov parameters residual matrix:

$$\boldsymbol{\varepsilon}_{h(i)} = \boldsymbol{\varepsilon}_{(i)} \mathbf{U}^\dagger, \quad (4.61)$$

where \mathbf{U}^\dagger is the pseudoinverse of \mathbf{U} .

- XI Obtain the updated Markov parameters matrix to be used in the computation process:

$$\mathbf{H}_{(i+1)} = \mathbf{H}_{(i)} + \mathbf{K}_{p(i)} \boldsymbol{\varepsilon}_{h(i)}, \quad (4.62)$$

being \mathbf{K}_p a gain matrix or simply a scalar K_p , that will be discussed ahead in the next section.

- XII $i = i + 1$, return to step III and repeat the loop for the next iteration.

The iterative loop process performed from step III to step XII is determined by the set-point of the number of iterations or by the set-point of the Fit Rate \overline{FR} . In the simulations accomplished in this research, the purpose was to work with the setting of a number of iterations

at each configuration tested to perceive the algorithm behavior in terms of expected results. The adjustment of several iterations numbers for different settings of the algorithm parameters was needed in this investigative aspect of the method. Besides these conditions to end the algorithm iterations, a stop condition was defined from the iterative loop when the Fit Rate $\overline{\text{FR}}$ of any iteration takes a negative value. This situation characterizes a great drop of the Fit Rate values, called all over this work as a convergence loss, which will be better discussed in Chapter 7.

4.4.3 Markov matrix updating

The Markov parameters matrix, updated at each iteration, considering the residue computed in the previous iteration, allows a newly identified system to be recalculated.

Accordingly to Equations (4.15), (4.16) and (4.17), the Markov matrix \mathbf{H} has each row originated from an output located in each correspondent row of the matrix \mathbf{Y} . The matrix \mathbf{K}_p is defined as a diagonal matrix, with each diagonal element being a gain related to the correspondent row of the Markov matrix. Then, \mathbf{K}_p is represented as follows

$$\mathbf{K}_p = \text{diag}[K_{p_1}, K_{p_2}, \dots, K_{p_j}, \dots, K_{p_r}], \quad (4.63)$$

with $\mathbf{K}_p \in \mathbb{R}^{r \times r}$ and $K_{p_j} > 0$, $j = 1, 2, \dots, r$.

It is proposed here an approach for \mathbf{K}_p to be dynamically updated at each algorithm iteration. Taking into account that the Markov matrix \mathbf{H} reflects the system input-output data, which interferes in the residue ε_h , the covariance Φ_j of the matrix row ε_{h_j} is applied to establish the value of the gain K_{p_j} . This gain value behaves as a counterpart to minimize the variability of the residues values. Concisely, K_{p_j} is established to be inversely proportional to the respective covariance Φ_j of the row vector ε_{h_j} from the residue matrix ε_h , which can be better clarified next.

The Markov parameters residual matrix is composed as follows:

$$\varepsilon_h = \begin{bmatrix} \varepsilon_{h_1} \\ \varepsilon_{h_2} \\ \vdots \\ \varepsilon_{h_j} \\ \vdots \\ \varepsilon_{h_r} \end{bmatrix} = \begin{bmatrix} \varepsilon_{h_1}(0) & \varepsilon_{h_1}(1) & \dots & \varepsilon_{h_1}(k) & \dots & \varepsilon_{h_1}(sp-1) \\ \varepsilon_{h_2}(0) & \varepsilon_{h_2}(1) & \dots & \varepsilon_{h_2}(k) & \dots & \varepsilon_{h_2}(sp-1) \\ \vdots & \vdots & \ddots & \vdots & \ddots & \vdots \\ \varepsilon_{h_j}(0) & \varepsilon_{h_j}(1) & \dots & \varepsilon_{h_j}(k) & \dots & \varepsilon_{h_j}(sp-1) \\ \vdots & \vdots & \ddots & \vdots & \ddots & \vdots \\ \varepsilon_{h_r}(0) & \varepsilon_{h_r}(1) & \dots & \varepsilon_{h_r}(k) & \dots & \varepsilon_{h_r}(sp-1) \end{bmatrix}, \quad (4.64)$$

where

$$\varepsilon_{h_j} = (\mathbf{y}_j - \hat{\mathbf{y}}) \mathbf{U}^\dagger, \quad (4.65)$$

with $\hat{\mathbf{y}}$ containing the estimated values of the output j from the identified system and \mathbf{y}_j represents the same correspondent j output vector from \mathbf{Y} (original system).

The row vector ε_{h_j} represents the Markov parameters residues related to one of the r outputs. The elements of this vector ($\varepsilon_{h_j}(k)$) can have magnitudes of relevant differences, which lead to distinct variability between the vectors ε_{h_j} . The solution adopted to iteratively update \mathbf{H} was in the way of assigning a specific gain value to each row vector ε_{h_j} . As this updating gain works in the feedback of the closed-loop concept, it was established for actuating inversely proportional to the variability of the $\varepsilon_{h_j}(k)$ elements in a row vector ε_{h_j} . Thus, when the variability of the ε_{h_j} elements gets higher, the gain should act to decrease the values of the correspondent row of the Markov parameters residues matrix ε_h that is added to the Markov parameters \mathbf{H} last computed. The calculation of the ε_{h_j} covariance was dynamically applied at each iteration to represent the amount of the $\varepsilon_{h_j}(k)$ elements variability. In this case, the covariance calculation of a vector with itself has been obtained in the same way as its variance computing.

The covariance Φ_j of the Markov parameters residues ε_{h_j} related to an output j is:

$$\begin{aligned}\Phi_j &= E((\varepsilon_{h_j} - E(\varepsilon_{h_j}))(\varepsilon_{h_j} - E(\varepsilon_{h_j}))^T) = E((\varepsilon_{h_j} - \bar{\varepsilon}_{h_j})(\varepsilon_{h_j} - \bar{\varepsilon}_{h_j})^T), \\ \Phi_j &= \frac{1}{sp-1} \sum_{k=0}^{sp-1} (\varepsilon_{h_j}(k) - \bar{\varepsilon}_{h_j})(\varepsilon_{h_j}(k) - \bar{\varepsilon}_{h_j})^T, \quad \bar{\varepsilon}_{h_j} = \frac{1}{sp} \sum_{k=0}^{sp-1} \varepsilon_{h_j}(k),\end{aligned}\tag{4.66}$$

$$\Phi = [\Phi_1 \quad \Phi_2 \quad \dots \quad \Phi_j \quad \dots \quad \Phi_r]^T, \tag{4.67}$$

where the operator $E(\cdot)$ is the statistical expected value.

The gain K_{p_j} , as an element of Equation (4.63), is computed as follows:

$$K_{p_j} = \ell \left(\frac{\max(\Phi) - \min(\Phi)}{\Phi_j} \right), \tag{4.68}$$

where $\max(\Phi)$ and $\min(\Phi)$ are the maximum and minimum values from the vector Φ , respectively. The variable ℓ is an adjustable parameter of the algorithm, working as a weighting factor in K_{p_j} computing. The difference between the maximum and minimum covariances of any residue ε_{h_j} at the ratio's numerator of Equation (4.68) refers to a normalization of values in the range of the Φ_j variability to result in a K_{p_j} value coherent with the expected correction to be performed for the Markov parameters matrix at each iteration. The ratio $\frac{\max(\Phi) - \min(\Phi)}{\Phi_j}$ provides a value lower than unity if the variability of the residues from any output j is higher than the range of variability from all outputs' residues and vice-versa. In Section 7.4, graphs

showing K_{p_j} values over the iterations are paired with the FR_j values to portray the behavior of the dynamical gain in some undertaken simulations.

As a remarking, for systems that have only one output, Multiple-Input-Single-Output (MISO) or Single-Input-Single-Output (SISO), the normalization that appears in Equation (4.68) becomes undue given that the numerator of the ratio gets null. To overcome this aspect, the numerator can be alternatively selected as a unit value, and the factor ℓ should be appropriately adjusted with a weight in the same magnitude order of Φ_j . With that, it provides an initial K_{p_j} with a reference value around the unity, allowing the corrections at each iteration according to Φ_j dynamics.

It should be highlighted that ℓ acts as a multiplicative factor to the dynamical update part in the computing of the Markov parameters matrix \mathbf{H} . As ℓ is the only adjustable variable in the iterative computing of \mathbf{H} , it was designed as a parameter of the algorithm to enable higher or less increment of the updating part, which is in charge by the Markov parameters residues ε_{h_j} .

In addition to the \mathbf{K}_p definition previously presented regarding the concept of having a variable gain value at each iteration, this function can also be performed by a fixed gain value throughout the iterations. So that, instead of using a \mathbf{K}_p matrix, a scalar K_p with a fixed value for all the iterations is employed. In this case, the K_p value is the only multiplicative gain acting on all rows ε_{h_j} of the Markov parameters residual. As can be taken from Equation (4.68), when considering the ratio $\frac{\max(\Phi) - \min(\Phi)}{\Phi_j} = 1$, the natural reference to the fixed K_p value is to assume the ℓ value, what was considered in some of the simulations approached in Chapter 7, when applicable.

Concluding, updating the Markov parameters matrix is accomplished at each iteration (i) in a way typical of iterative algorithms to solve a minimization problem. They are characterized by a current value attained in the prior iteration being updated with a corrective part related to some error or residual computed. In Equation (4.62), the \mathbf{K}_p gain works similarly to the step size in the steepest descent minimization algorithm. Anyway, the gain depicts a factor with a centesimal magnitude value to gradually add the residual amount needed to update \mathbf{H} . At first glance, the iterative concept would theoretically refer to the complete application of the residual amount. Although, the enhancement of this iterative control showed the necessity to assign the gain factor \mathbf{K}_p to dose the possible correction in charge by the $\varepsilon_{h(i)}$ without losing the algorithm convergence, which still occurred a few times, as seen in Chapter 7.

4.4.4 The algorithm of SSRA-DC-iCL

The Algorithm 1 contains the SSRA-DC-iCL method.

Algorithm 1 SSRA-DC-iCL

Input: Excitations: U, U_V
 Outputs: Y, Y_V
 Settings: $d_t, q, p, n, \xi, \gamma, \ell$ or K_p
 Fit Rate set-point: SFR
 Number of iterations set-point: ite

Output: Best Fit Rate: BFR
 Validated Fit Rate: VFR_j, \overline{VFR}
 State-space realization $\hat{A}, \hat{B}, \hat{C}, \hat{D}$ of the Identified system (IS) with BFR: BIS

- 1: **Compose** $t = [0, d_t, 2d_t, 3d_t, \dots, (q-1)d_t]$
- 2: **Compute** Markov parameters matrix $H_{(0)}$ at the initial condition ▷ as in (4.15)
- 3: $i \leftarrow 0$ ▷ To count the number of iterations
- 4: $\overline{FR}(i) \leftarrow 0$
- 5: $BFR \leftarrow 0$
- 6: **while** ($\overline{FR}(i) < SFR$) **and** ($i < ite$) **do**
- 7: **Assemble** Generalized Hankel matrix H_k ▷ as in (4.49)
- 8: **Assemble** Data Correlation matrices $\mathcal{R}h_k$ ▷ as in (4.50)
- 9: **Assemble** Block Correlation Hankel matrix $\mathcal{H}(0)$ and Block correlation time-shifted Hankel matrix $\mathcal{H}(1)$ ▷ as in (4.52)
- 10: **Compute** SVD: $\mathcal{H}(0) = \mathcal{U}\Sigma\mathcal{V}^T$ ▷ as in (4.54) and (4.55)
- 11: **Compute** estimated state-space realization $IS: (\hat{A}, \hat{B}, \hat{C}, \hat{D})$ ▷ as in (4.57) and (4.58)
- 12: **Compute** $\hat{Y}_{(i)} = lsim(IS, U, t)$ ▷ $lsim$: simulate the response of the identified system to U excitation in the iterative stage
- 13: **Compute** $\varepsilon_{(i)} = Y - \hat{Y}_{(i)}$
- 14: **Compute** $\varepsilon_{h(i)} = \varepsilon_{(i)} U^\dagger$ ▷ as in (4.61)
- 15: **Compute** Covariance $\Phi_{(i)}$ of Markov matrix residue (only when the K_p matrix is applied) ▷ from (4.64) to (4.67)
- 16: **Compute** $K_{p(i)}$ (or employ K_p for a fix gain value) ▷ as in (4.63) and (4.68)
- 17: **Compute** FR_j ▷ as in (4.59) using Y and $\hat{Y}_{(i)}$ for each output j in the iteration stage
- 18: **Compute** FR ▷ as in (4.60)
- 19: $\overline{FR}(i) \leftarrow \overline{FR}$
- 20: **if** $\overline{FR}(i) < 0$ **then** ▷ triggered condition to escape from "while" function and stop with the iterations
- 21: $\overline{FR}(i) \leftarrow 0$
- 22: $i \leftarrow ite$
- 23: **else**
- 24: **Compute** Markov parameters matrix updated: $H_{(i+1)} = H_{(i)} + K_{p(i)} \varepsilon_{h(i)}$ ▷ as in (4.62)
- 25: **end if**
- 26: **if** $\overline{FR}(i) \geq BFR$ **then**
- 27: $BFR \leftarrow \overline{FR}(i)$
- 28: $BIS \leftarrow IS$
- 29: **end if**
- 30: $i \leftarrow i + 1$
- 31: **end while**
- 32: **Compute** $\hat{Y} = lsim(BIS, U_V, t)$ ▷ $lsim$: simulate the response of the best IS to U_V excitation in the validation stage
- 33: **Compute** VFR_j ▷ like FR_j in (4.59) but using Y_V and $\hat{Y}_{(i)}$ for each output j in the validation stage
- 34: **Compute** \overline{VFR} ▷ as in (4.60) using VFR_j rather than FR_j
- 35: **Plot** Fit Rate evolution: $plot(\overline{FR})$ ▷ \overline{FR} is a vector with i \overline{FR} elements

5 SYSTEMS AND MODELS CONFIGURATION

5.1 Introduction³

The present chapter describes the characteristics and features required to constitute the systems and simulations for testing the algorithms involved in the present research. Firstly, PRBS, CHIRP, and GWN signals applied as excitation along the work are introduced. In the sequel, the concepts of measurement noise added in most simulation cases are presented. After that, the systems simulated, their respective configurations, and the procedure used in simulations are detailed. Lastly, the discretization task that allows the systems simulation, and establishes the constraints and assumptions for the system's configuration, are specified.

This research, which focused mainly on MIMO systems with models of 5, 50, and 100 degrees of freedom, was developed in two parts that determine the topics presented in this chapter. In the first part, a linear model of 5 degrees of freedom is simulated with the classical SSRA to introduce some concepts about algorithm settings and their influence on the results. In the second part, linear models with 50 and 100 degrees of freedom and additive measurement noise are simulated to assess the new proposed iterative SSRA-DC-iCL method, including additional evaluations and comparisons with some reference methods. The same approach of simulations is performed for a nonlinear model with 2 degrees of freedom. This chapter describes and discusses the information supporting these elements related to the definitions of systems, models, and simulations.

5.2 Excitation signals

The input signals play an important role in SI since only with them it is possible to realize the behavior of the process, generate and collect the desired output data. The input signal should provide enough knowledge about the system and affect equally all the operating frequencies ([Rehman; Verma, 2014](#)).

A typical persistently exciting signal has an important feature to a trustworthy identification of a system if its inputs hold this characteristic. In a frequency domain, a signal can be interpreted as persistently exciting of order m when the frequency spectrum is not zero at

³ Some parts presented in this chapter were published in the papers ([Soares Jr; Serpa, 2021](#); [Soares Jr; Serpa, 2022](#)).

least in m frequencies at the $[-\pi, \pi]$ interval. A simple signal \mathbf{u} (vector element $u(k)$) of order m is considered persistently exciting if the following limits exist and if the matrix \mathbf{R}_u^m is not singular, i.e., it is a full rank matrix:

$$\begin{aligned}\bar{u} &= \lim_{N \rightarrow \infty} \frac{1}{N} \sum_{k=1}^N u(k), \\ r_u(k) &= \lim_{N \rightarrow \infty} \frac{1}{N} \sum_{i=1}^N (u(i) - \bar{u})(u(i+k) - \bar{u}), \\ \mathbf{R}_u^m &= [r_u(i-j)]_{ij}; i = 1, \dots, m; j = 1, \dots, m.\end{aligned}\tag{5.1}$$

Considering $\mathbf{u}(k)$ ergodic, i.e., the expected value E is substituted by the average, the matrix \mathbf{R}_u^m represents the autocorrelation function of $\mathbf{u}(k)$ signal ([Åström; Torsten, 1965](#); [Aguirre, 2015](#)). Roughly speaking, a persistently exciting signal carries sufficiently many different frequencies, which means having enough large number of harmonics in its spectrum. ([Ljung, 1971](#)).

The choice related to the type of excitation signal comes to be a fundamental concern that determines the SI effectiveness. All the three signals employed in the present research (PRBS, CHIRP, and GWN) comply with being persistently exciting.

5.2.1 Pseudo Random Binary Sequence (PRBS)

Pseudo Random Binary Sequence (PRBS) signals were applied as excitation forces mainly to the system's inputs with 5 degrees of freedom. The PRBS provides characteristics for an excitation signal as persistently exciting, which is a desired condition for consistently estimating a linear system ([Soderstrom; Stoica, 1989](#)). These signals, commonly used in electrical and electronic application fields, have a sequence of pulses randomly generated that can be repeated in a periodic shape, or the signal period can be unique, which would mean the complete signal is uncorrelated with itself. Another attractive attribute of the PRBS signal is the cross-correlation with noise signals that can be considered low. The same happens for the signal autocorrelation that is very low for all delays except zero ([Lee et al., 2007](#); [Nguyen et al., 2018](#)).

As pointed out by Ljung ([Ljung, 1999](#)): “A Pseudo Random Binary Sequence (PRBS) is a periodic, deterministic signal with white-noisy-like properties.” The most common PRBS signal type uses a shift register of order m that works executing an OR-EXCLUSIVE logical operation between some displacement registry bits, as can be seen in Figure 5.1. When

the clock pulse is applied, each bit's value is transferred to each XOR logical command, shifting the value to the next bit. Then, one PRBS bit is generated, and the process continues cyclically at each clock pulse.

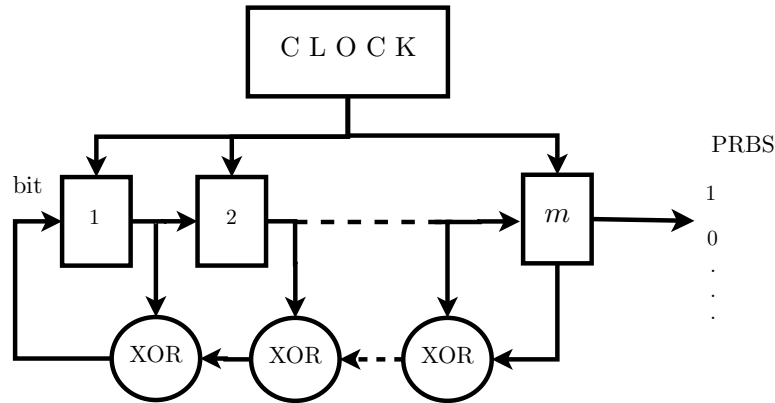


Figure 5.1 – Circuit of m bits shift register to generate the PRBS

Ljung (Ljung, 1999) introduced an implementation method to generate a PRBS signal based in the three following steps:

- Generate a white zero mean Gaussian noise signal;
- Apply to the signal a 5th order Butterworth filter with the pass band $1 \leq \omega \leq 2$ (rad/s) for instance;
- Take the sign of the filtered signal where the positive values become 1 and the negative values become 0 or -1 .

The generated PRBS excitation signal for most of the simulations of this work assumes the values 0 or 1, following as the procedure previously described. The basic three steps, prior introduced, are represented by Figure (5.2) to develop a 500 samples signal. Possible changes in the pass band value of ω permit varying the switching rate of the PRBS, i.e., the clock frequency ($\mathcal{C}_{\mathcal{F}}$) which the PRBS is generated. Regarding the adherence between the simulation and a real process, the $\mathcal{C}_{\mathcal{F}}$ should be appropriately chosen to have compatibility with the input signal features from the process.

In Section 6.2, the influence of the PRBS switching rate in the SI performance will be analyzed. Two PRBS signals of 500 samples being one with approximately ten times the clock frequency ($\mathcal{C}_{\mathcal{F}}$) of the other are exhibited in Figure 5.3.

The feature of exciting equally all frequencies supports PRBS signal application, widely used for linear SI, following the White-Noise as a reference in the deterministic signal

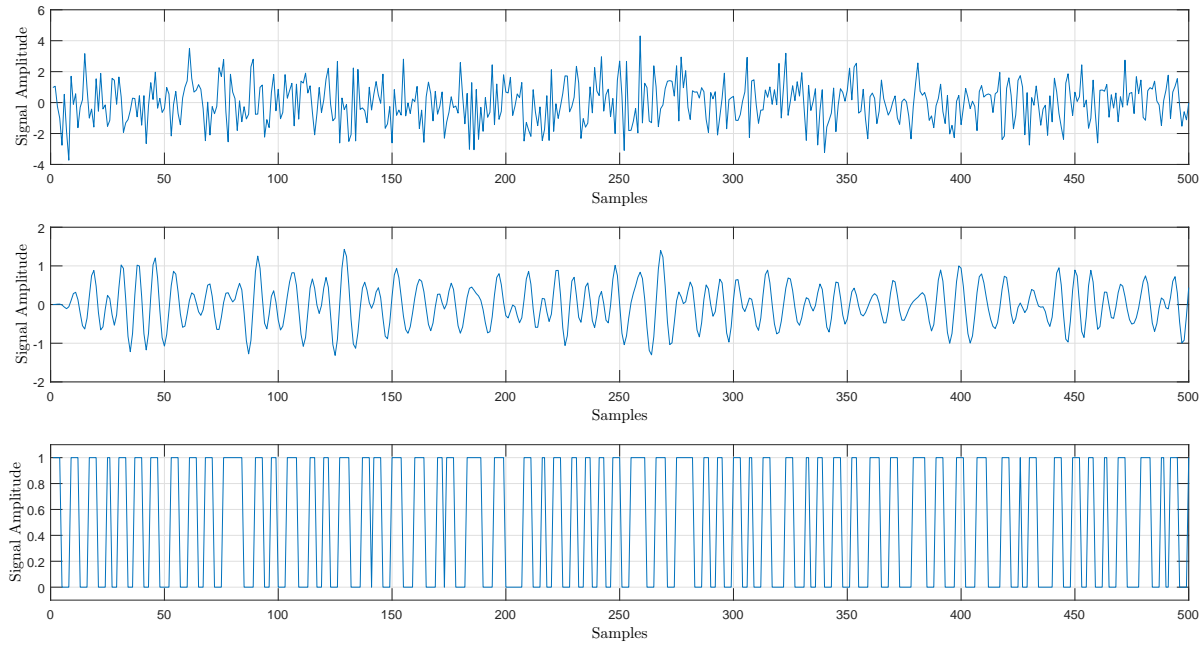


Figure 5.2 – PRBS generation steps yielding 500 samples; from top to bottom, the steps of the signal: white zero mean Gaussian noise, 5th order Butterworth filter in the pass band $1 \leq \omega \leq 2$ (rad/s), PRBS generated signal.

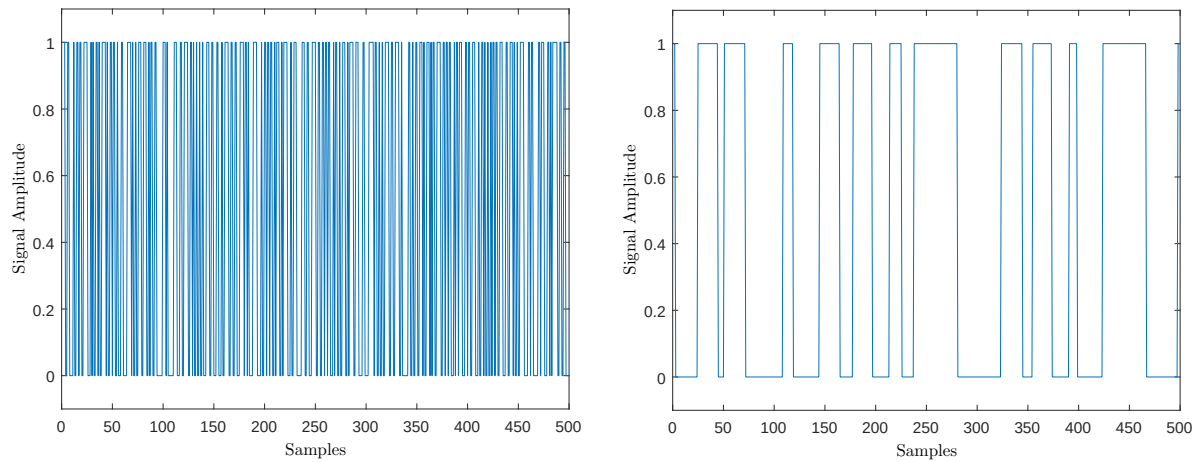


Figure 5.3 – PRBS signal for 500 samples in the range $[0,1]$ with 0.1 s sampling time, and with $C_F = 14.88$ rad/s (left) and $C_F = 1.52$ rad/s (right).

(Nelles, 2001). Analysis of systems in the frequency domain demands a convenient excitation signal. The excitation signals decision is often driven by the type of system to be identified and the desired signal processing method when the goal is to be close to white-noise. However, the white-noise signal's practical use for system identification does not have the same features as the PRBS. The White-Noise possesses a high crest factor, unlike the PRBS that shows the lowest crest factor among input excitation signals (Tangirala, Arun K, 2017). As described by Ljung (Ljung, 1999): “A good signal waveform is consequently one that has a small crest factor

C_r , which for a zero mean signal is defined as

$$C_r = \sqrt{\frac{\max_k (u(k))^2}{\lim_{N \rightarrow \infty} \frac{1}{N} \sum_{k=1}^N (u(k))^2}} \quad (5.2)$$

where $u(k)$ is the input signal in a discrete-time system. Binary and symmetric signals, that achieves the lower bound of $C_r = 1$, can be considered to have this advantage.

The Pseudo Random Binary Sequence (PRBS) can be applied to identify linear systems, where the state-space realization systems are resultant from the algorithms focus of the present work. However, the PRBS should present some limitations for nonlinear systems because the signal typically provides only two amplitude levels, which can not be a sufficient information to identify nonlinear behavior, since more input levels in the signal amplitude can be suitable to deal with nonlinearities. Therefore, the Gaussian White-Noise signal can be an alternative in such situations (Shariff *et al.*, 2013; Sarvat Mushtaq Ahmad, 2001).

In the reference (Fairweather *et al.*, 2011), the relevance of the PRBS signal was highlighted when the authors mentioned: “the PRBS finds applications over many disciplines for parameter identification since the frequency spectrum of the PRBS is known to approximate to band-limited white-noise, and thus they form a useful stimulus for frequency response analysis.” The stimulus signal can be injected in a separate way, as it was applied in this work, or in addition to another kind of input/control signal.

5.2.2 Sine Sweep (CHIRP)

The CHIRP is also a persistently exciting signal composed of a sinusoidal signal that continuously changes its frequency over a range from a minimum value to a maximum one. As the signal vary the frequency sweeping up or sweeping down in one period, the CHIRP is also called the swept signal. The CHIRP signal, as adopted in this work, is mathematically defined as follows:

$$u(t) = A_m \sin \left(2\pi f_{min} t + \frac{\pi(f_{max} - f_{min})t^2}{T} \right), \quad (5.3)$$

where A_m is the signal amplitude, T is the period ($0 \leq t \leq T$), f_{min} and f_{max} are the minimum and maximum frequencies, respectively. The sweep rate, that is, the rate that the frequency changes in the CHIRP signal, is $\frac{f_{max}-f_{min}}{T}$. The Crest factor of CHIRP, that depicts the ratio of peak values to the effective value (root mean square) is considered low, being the same as a sinusoidal signal, i.e., $C_r = \sqrt{2}$ (Ljung, 1999).

The frequency range of the CHIRP, formed by the frequencies f_{min} and f_{max} , has to be chosen to encompass the range of interest frequencies from the process. In contrast, even if the frequencies would be appropriated selected to the process, other frequencies will also excite the system and not only relevant ones. However, this signal behavior does not impact linear systems, which represent the research's overall cases. Thus, some care should be taken to avoid disturbing the systems with nonlinearities conditions for other spectral lines of excited frequencies than those of interest (Vuojolainen *et al.*, 2017; Pintelon; Schoukens, 2012).

Two CHIRP signals are displayed in Figure 5.4 with amplitude $A_m = 1$, $T = 10$ s, and $f_{min} = 0.2$ Hz, being the left graph with $f_{max} = 7$ Hz, and the right graph with $f_{max} = 14$ Hz. It is easy to realize that, as the minimum and maximum frequencies get close, the signal becomes a sinusoidal curve, which effectively happens when $f_{min} = f_{max}$ in Equation (5.3).

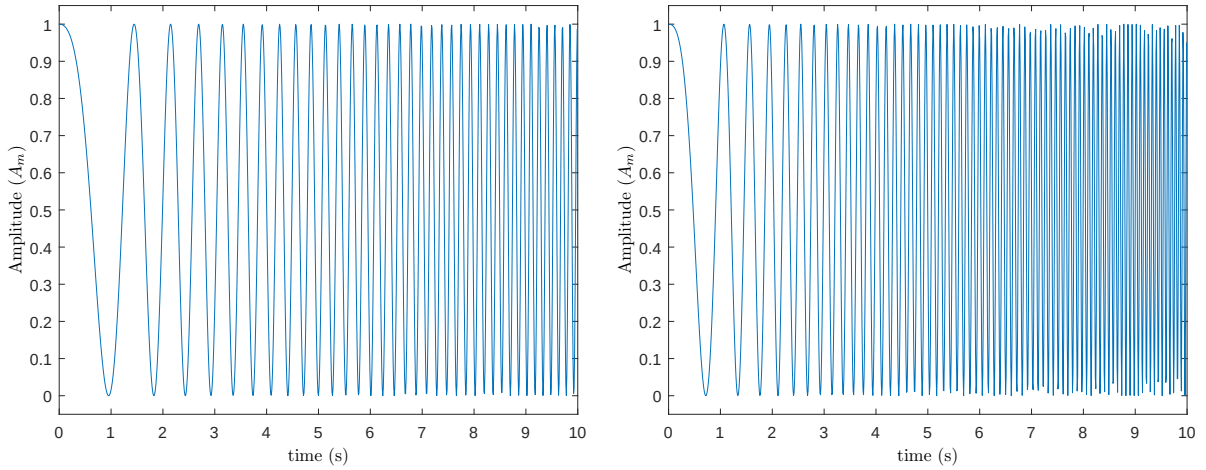


Figure 5.4 – CHIRP signals with $f_{min} = 0.2$ Hz, and $f_{max} = 7$ Hz (on the left graph) and $f_{max} = 14$ Hz (on the right graph).

As pointed out by Uyanlk et al. (Uyanlk *et al.*, 2015): “The correct choice of input signals plays a crucial role in the system identification process. Input signals must be designed to expose as much dynamical behavior in the system as possible. The accuracy of the identification critically depends on particular aspects of these CHIRP inputs, such as their duration, frequency range, and sweep rate”. Simulations excited by CHIRP signal were configured to have the frequency f_{max} randomly generated at some specific range, objectifying to have different inputs signals and different input data sets from each other, as a practice implemented for the CHIRP excitations throughout this work. Table 6.5 presents different f_{max} frequencies generated and used in the simulations analysis with CHIRP excitations at Section 6.5. In the

simulations excited by CHIRP at this work, the signal was adjusted to have only one cycle over the period T .

The CHIRP signal application has many examples in engineering research as an excitation input for system identification and process simulations. In the work of Chen et al. (Chen *et al.*, 2020), a CHIRP signal is exploited as a sweeping force to excite a bridge in a typical structural system identification problem. On another example, the CHIRP and the PRBS are the excitation signals in SI of an Active Magnetic Bearing. Here, they are analyzed and compared for their impact on the identification results (Vuojolainen *et al.*, 2017).

An interesting approach comparing CHIRP and PRBS signals was provided by Montonen et al. (Montonen *et al.*, 2018), where an identification experimental research of a mechanical driveline of a hybrid bus is presented. This mentioned work presents a concern regarding the differential gear backlash when the excitation signals are a pure PRBS, causing nonlinearities in the mechanical driveline. For that nuisance, PRBS being superimposed by an offset signal mitigated the trouble. Even though CHIRP and PRBS signals are rich enough in frequency content, the CHIRP signal showed practical limitations in some experiment steps. Then, taking care of gear backlash through some rearrangement in the PRBS construction, this excitation signal performed better than the CHIRP signal for this identification experience.

5.2.3 Gaussian White-Noise (GWN)

Gaussian White-Noise (GWN) is an excitation signal vastly applied all over the control area, signals processing, and correlated fields of application. White-Noise is a sequence of independent and identically distributed random variables with a certain variance, having equal intensity at different frequencies, giving it a constant power spectral density (Soderstrom; Stoica, 1989; Carter; Mancini, 2003). When each sample has a normal distribution with zero mean, the signal is said to be Gaussian White-Noise. Then, this signal is typically an arbitrary zero-mean White-Noise, and was set with unit-variance in this work, similarly to what was applied in the paper of Chen et al. (Chen *et al.*, 2012a). For systems identification, the GWN is broadly employed in structural applications. A fundamental property of the GWN signal relates to containing all frequencies uniformly. A White-Noise signal was precisely and briefly characterized by Nelles (Nelles, 2001): "... measuring a white-noise source at one instant reveals no information about the next. White-Noise contains no systematical part; it is totally unpredictable." A GWN signal configured as the ones used in this work is shown in Figure 5.5.

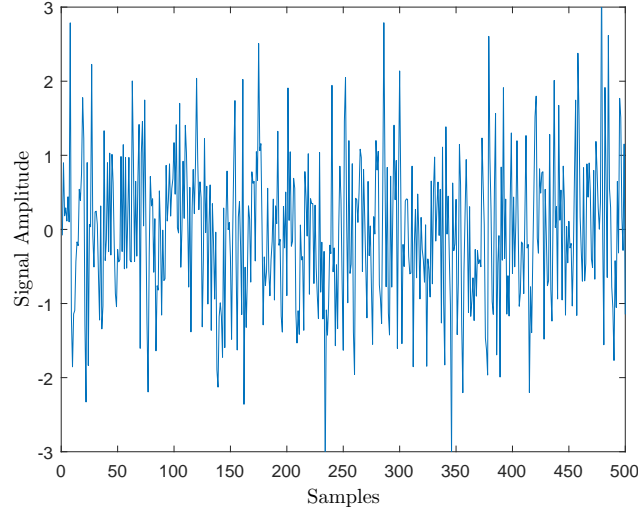


Figure 5.5 – GWN signal with unit-variance

5.3 Measurement noise

The additive noise in the output measurement variables of the systems is one premiss of this work handled on the procedure that generates the data set to the simulations. For numerical simulations, the measurement noise \mathbf{V} comes from a characteristic random signal formed by the actual amplitude of the corresponding output signal where the noise is added (Juang; Pappa, 1986). The input set-point value of the noise, represented by the variable $S_N(\%)$ on the algorithm, determines the percentage value applied to the amplitude of the output signal. Firstly, it should be defined the structure of the output and the noise that will be added:

$$\mathbf{Y} = \begin{bmatrix} \mathbf{Y}_1 \\ \mathbf{Y}_2 \\ \vdots \\ \mathbf{Y}_j \end{bmatrix}, \mathbf{V}_x = \begin{bmatrix} \mathbf{V}_{x_1} \\ \mathbf{V}_{x_2} \\ \vdots \\ \mathbf{V}_{x_j} \end{bmatrix}, \overline{\mathbf{V}}_x = \begin{bmatrix} \overline{V}_{x_1} \\ \overline{V}_{x_2} \\ \vdots \\ \overline{V}_{x_j} \end{bmatrix}, \quad (5.4)$$

with $\mathbf{Y}_j \in \mathbb{R}^{1 \times q}$, $\mathbf{V}_{x_j} \in \mathbb{R}^{1 \times q}$, $\mathbf{V}_x \in \mathbb{R}^{j \times q}$, and $\overline{\mathbf{V}}_x \in \mathbb{R}^{j \times 1}$.

Considering S_N as the desired percentage value of the measurement noise added to the outputs \mathbf{Y} , it is possible to write:

$$\mathbf{V}_{x_j} = S_N(Y_{j_{\max}} - Y_{j_{\min}})\mathcal{R}, \quad (5.5)$$

where $\mathcal{R} \in \mathbb{R}^{1 \times q}$ is a row vector of independent values randomly generated in the range [0,1], and $Y_{j_{\max}}$ and $Y_{j_{\min}}$ are the maximum and minimum values from \mathbf{Y}_j , respectively, and

$$\bar{V}_{x_j} = \frac{1}{q} \sum_{k=1}^q V_{x_j}(k). \quad (5.6)$$

Defining the matrix $\bar{\mathbf{V}} \in \mathbb{R}^{j \times q}$ with $j = \{1, 2, \dots, r\}$:

$$\bar{\mathbf{V}} = \bar{\mathbf{V}}_x \mathbb{1}, \quad \text{where} \quad \mathbb{1} = [1 \quad 1 \quad \dots \quad 1]_{1 \times q}. \quad (5.7)$$

Finally, the measurement noise $\mathbf{V} \in \mathbb{R}^{j \times q}$ can be defined for the simulations as:

$$\mathbf{V} = \mathbf{V}_x - \bar{\mathbf{V}}. \quad (5.8)$$

5.4 Mass-Spring-Damper models

The mass-spring-damper models applied all over this research work are linear dynamical systems of finite-dimensional composed by the following equations, beginning with the second order differential equation (Gawronski, 2005; Juang, 1994):

$$\mathcal{M}\ddot{\mathbf{y}} + \mathcal{D}\dot{\mathbf{y}} + \mathcal{K}\mathbf{y} = \mathbf{B}_0\mathbf{u}, \quad (5.9)$$

with \mathcal{M} , \mathcal{D} , and \mathcal{K} representing the mass matrix, damper matrix and stiffness matrix, respectively. \mathbf{B}_0 is an input influence matrix, characterizing the locations and type of inputs.

Equation (5.9) can be rewritten as follows:

$$\ddot{\mathbf{y}} + \mathcal{M}^{-1}\mathcal{D}\dot{\mathbf{y}} + \mathcal{M}^{-1}\mathcal{K}\mathbf{y} = \mathcal{M}^{-1}\mathbf{B}_0\mathbf{u}. \quad (5.10)$$

The state vector \mathbf{x} is a combination of the structural displacements \mathbf{y} , and velocities $\dot{\mathbf{y}}$, i.e.,

$$\mathbf{x} = \begin{bmatrix} \mathbf{x}_1 \\ \mathbf{x}_2 \end{bmatrix} = \begin{bmatrix} \mathbf{y} \\ \dot{\mathbf{y}} \end{bmatrix}. \quad (5.11)$$

Substituting the states of Equation (5.11) into Equation (5.10), it is obtained:

$$\dot{\mathbf{x}}_2 + \mathcal{M}^{-1}\mathcal{D}\mathbf{x}_2 + \mathcal{M}^{-1}\mathcal{K}\mathbf{x}_1 = \mathcal{M}^{-1}\mathbf{B}_0\mathbf{u}, \quad (5.12)$$

From Equation (5.11) and Equation (5.12), the first-order differential equations of the states can be expressed as:

$$\dot{\mathbf{x}}_1 = \mathbf{x}_2, \quad \dot{\mathbf{x}}_2 = -\mathcal{M}^{-1}\mathcal{K}\mathbf{x}_1 - \mathcal{M}^{-1}\mathcal{D}\mathbf{x}_2 + \mathcal{M}^{-1}\mathbf{B}_0\mathbf{u}, \quad (5.13)$$

which yields

$$\dot{\mathbf{x}} = \begin{bmatrix} \dot{x}_1 \\ \dot{x}_2 \end{bmatrix} = \underbrace{\begin{bmatrix} 0 & \mathbf{I} \\ -\mathcal{M}^{-1}\mathcal{K} & -\mathcal{M}^{-1}\mathcal{D} \end{bmatrix}}_{\mathbf{A}} \begin{bmatrix} x_1 \\ x_2 \end{bmatrix} + \underbrace{\begin{bmatrix} 0 \\ \mathcal{M}^{-1}B_0 \end{bmatrix}}_{\mathbf{B}} u \quad (5.14)$$

From Equation (5.11), the outputs regarding specific displacements and velocities can be established as follows:

$$\mathbf{y} = \begin{bmatrix} C_d & 0 \end{bmatrix} \begin{bmatrix} x_1 \\ x_2 \end{bmatrix} + \begin{bmatrix} 0 \end{bmatrix} u, \quad (5.15)$$

$$\dot{\mathbf{y}} = \begin{bmatrix} 0 & C_v \end{bmatrix} \begin{bmatrix} x_1 \\ x_2 \end{bmatrix} + \begin{bmatrix} 0 \end{bmatrix} u, \quad (5.16)$$

where C_d and C_v are in charge to make the outputs selection for displacement and velocity, respectively.

For the outputs $\ddot{\mathbf{y}}$ referred to accelerations, substituting the states from Equation (5.11) into Equation (5.10) yields:

$$\ddot{\mathbf{y}} = -\mathcal{M}^{-1}\mathcal{K}x_1 - \mathcal{M}^{-1}\mathcal{D}x_2 + \mathcal{M}^{-1}B_0u, \quad (5.17)$$

which should have each term multiplied by the matrix C_a to make the outputs selection in the state-space form, as following:

$$\ddot{\mathbf{y}} = C_a \begin{bmatrix} -\mathcal{M}^{-1}\mathcal{K} & -\mathcal{M}^{-1}\mathcal{D} \end{bmatrix} \begin{bmatrix} x_1 \\ x_2 \end{bmatrix} + \begin{bmatrix} C_a\mathcal{M}^{-1}B_0 \end{bmatrix} u. \quad (5.18)$$

A mass-spring-damper system to model the three types of outputs (displacement, velocity, acceleration) simultaneously should consider Equation (5.15), Equation (5.16), and Equation (5.18) together to compose the matrices \mathbf{C} and \mathbf{D} according to the following state-space equation:

$$\begin{bmatrix} \mathbf{y} \\ \dot{\mathbf{y}} \\ \ddot{\mathbf{y}} \end{bmatrix} = \underbrace{\begin{bmatrix} C_d & 0 \\ 0 & C_v \\ -C_a\mathcal{M}^{-1}\mathcal{K} & -C_a\mathcal{M}^{-1}\mathcal{D} \end{bmatrix}}_{\mathbf{C}} \begin{bmatrix} x_1 \\ x_2 \end{bmatrix} + \underbrace{\begin{bmatrix} 0 \\ 0 \\ C_a\mathcal{M}^{-1}B_0 \end{bmatrix}}_{\mathbf{D}} u \quad (5.19)$$

The mass-spring-damper system, used in simulations with the classical SSRA for the first phase of this work is a typical MIMO system with 5 degrees of freedom called here

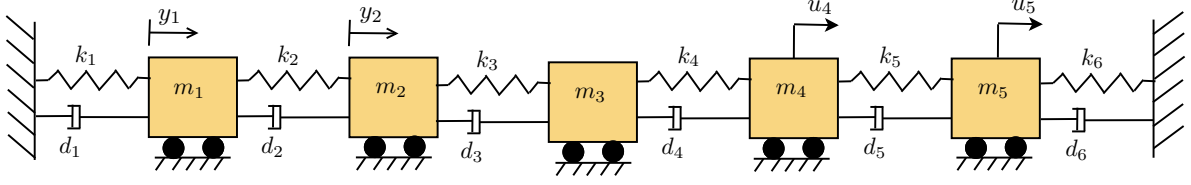


Figure 5.6 – Schematic 5 degree of freedom model (M5DOF), where m_i :masses, k_i :stiffnesses and d_i :dampings. Friction not considered.

M5DOF model. Excitation forces were applied in the fourth and fifth masses (u_4 and u_5), and the displacements were measured in the first and second masses (y_1 and y_2), as can be seen in Figure 5.6 related to the schematic representation of this model.

The values to generate the mass matrix \mathcal{M} , the stiffness matrix \mathcal{K} , and the damping matrix \mathcal{D} of the M5DOF model are presented next and were chosen similar to the reference (Yu *et al.*, 2014):

$$\mathcal{M} = \begin{bmatrix} 1 & 0 & 0 & 0 & 0 \\ 0 & 2 & 0 & 0 & 0 \\ 0 & 0 & 2 & 0 & 0 \\ 0 & 0 & 0 & 2 & 0 \\ 0 & 0 & 0 & 0 & 3 \end{bmatrix}, \quad \mathcal{K} = \begin{bmatrix} 800 & -800 & 0 & 0 & 0 \\ -800 & 2400 & -1600 & 0 & 0 \\ 0 & -1600 & 4000 & -2400 & 0 \\ 0 & 0 & -2400 & 6400 & -4000 \\ 0 & 0 & 0 & -4000 & 7200 \end{bmatrix},$$

$$\mathcal{D} = 0.5\mathcal{M} + 0.0004\mathcal{K}. \quad (5.20)$$

For most of the simulations, the mass-spring-damper models are typical MIMO systems with 50 degrees of freedom (M50DOF) and 100 degrees of freedom (M100DOF) models. The elements where the displacements were measured and where the excitation forces were applied are presented in Table 5.1. The respective positions of the inputs forces and the outputs sensors were chosen considering a more homogeneous distribution along with the elements, in a way not to have forces or sensors more concentrated in a part of the model with the rest more empty. The schematic representation for the M100DOF model, being the M50DOF model analogous to that, is displayed in Figure 5.7. The elements values of the mass matrix $\mathcal{M} = \text{diag}[m_1, m_2, \dots, m_i]$, the stiffness matrix \mathcal{K} and the damping matrix \mathcal{D} from the models were selected based on the reference (Yu *et al.*, 2014) and adapting the respective values to the attainment of higher natural frequencies of the systems in relation to the respective frequency values employed in the mentioned reference. The damping matrix \mathcal{D} and the stiffness matrices \mathcal{K} are composed as in Equation (5.20) and Equation (5.21), respectively, and the cor-

respondent mass and stiffness values of the elements are shown in Table 5.2.

$$\mathcal{K} = \begin{bmatrix} k_1 + k_2 & -k_2 & 0 & \dots & 0 \\ -k_2 & k_2 + k_3 & -k_3 & \dots & 0 \\ 0 & -k_3 & k_3 + k_4 & \dots & 0 \\ \vdots & \vdots & \vdots & \ddots & \vdots \\ 0 & 0 & 0 & \dots & k_i + k_{i+1} \end{bmatrix}, \quad (5.21)$$

with $i = 50$ for the M50DOF and $i = 100$ for the M100DOF.

Table 5.1 – Displacements measured and excitation forces in the M50DOF and M100DOF models

Model	Displacements measured (outputs)	Excitation forces (inputs)
M50DOF	$y_5, y_{17}, y_{26}, y_{33}, y_{48}$	u_{18}, u_{36}
M100DOF	$y_{10}, y_{34}, y_{52}, y_{66}, y_{96}$	$u_{18}, u_{36}, u_{49}, u_{67}, u_{89}$

Table 5.2 – Mass and stiffness values from the elements of the M50DOF and M100DOF models

Masses m_n					Stiffness $k_i (\times 1000)^{(1)}$				
$m_1 = 1$	$m_2 = 2$	$m_3 = 2$	$m_4 = 2$	$m_5 = 3$	$k_1 = 0.4$	$k_2 = 0.8$	$k_3 = 1.6$	$k_4 = 2.4$	$k_5 = 4$
$m_6 = 2$	$m_7 = 1$	$m_8 = 1$	$m_9 = 2$	$m_{10} = 2$	$k_6 = 3.2$	$k_7 = 1$	$k_8 = 4.1$	$k_9 = 1.4$	$k_{10} = 2.2$
$m_{11} = 1$	$m_{12} = 3$	$m_{13} = 1$	$m_{14} = 1$	$m_{15} = 3$	$k_{11} = 1.1$	$k_{12} = 1.3$	$k_{13} = 2.7$	$k_{14} = 2.3$	$k_{15} = 3.3$
$m_{16} = 2$	$m_{17} = 1$	$m_{18} = 2$	$m_{19} = 3$	$m_{20} = 2$	$k_{16} = 1.5$	$k_{17} = 1.1$	$k_{18} = 2.4$	$k_{19} = 2$	$k_{20} = 1.8$
$m_{21} = 3$	$m_{22} = 3$	$m_{23} = 3$	$m_{24} = 2$	$m_{25} = 2$	$k_{21} = 3.4$	$k_{22} = 0.8$	$k_{23} = 1.4$	$k_{24} = 4.2$	$k_{25} = 1.1$
$m_{26} = 1$	$m_{27} = 1$	$m_{28} = 3$	$m_{29} = 2$	$m_{30} = 3$	$k_{26} = 2.3$	$k_{27} = 1.5$	$k_{28} = 3$	$k_{29} = 1.5$	$k_{30} = 1.7$
$m_{31} = 1$	$m_{32} = 2$	$m_{33} = 2$	$m_{34} = 3$	$m_{35} = 2$	$k_{31} = 0.9$	$k_{32} = 2.4$	$k_{33} = 1.1$	$k_{34} = 4.3$	$k_{35} = 0.7$
$m_{36} = 1$	$m_{37} = 2$	$m_{38} = 1$	$m_{39} = 3$	$m_{40} = 2$	$k_{36} = 3.4$	$k_{37} = 0.6$	$k_{38} = 2.2$	$k_{39} = 3.4$	$k_{40} = 1.8$
$m_{41} = 1$	$m_{42} = 1$	$m_{43} = 2$	$m_{44} = 2$	$m_{45} = 1$	$k_{41} = 2.5$	$k_{42} = 1.1$	$k_{43} = 2.6$	$k_{44} = 2.2$	$k_{45} = 2.8$
$m_{46} = 3$	$m_{47} = 2$	$m_{48} = 1$	$m_{49} = 1$	$m_{50} = 3$	$k_{46} = 2.4$	$k_{47} = 1.3$	$k_{48} = 0.8$	$k_{49} = 1.7$	$k_{50} = 0.5$
$m_{51} = 2$	$m_{52} = 1$	$m_{53} = 2$	$m_{54} = 3$	$m_{55} = 1$	$k_{51} = 1.3$	$k_{52} = 0.8$	$k_{53} = 2.1$	$k_{54} = 1.3$	$k_{55} = 2$
$m_{56} = 3$	$m_{57} = 3$	$m_{58} = 1$	$m_{59} = 1$	$m_{60} = 3$	$k_{56} = 4.2$	$k_{57} = 1.5$	$k_{58} = 1.1$	$k_{59} = 3.2$	$k_{60} = 2.3$
$m_{61} = 3$	$m_{62} = 1$	$m_{63} = 2$	$m_{64} = 1$	$m_{65} = 2$	$k_{61} = 3.9$	$k_{62} = 1$	$k_{63} = 1.8$	$k_{64} = 4.2$	$k_{65} = 1.7$
$m_{66} = 3$	$m_{67} = 2$	$m_{68} = 1$	$m_{69} = 1$	$m_{70} = 3$	$k_{66} = 1.5$	$k_{67} = 3.3$	$k_{68} = 4.3$	$k_{69} = 2.1$	$k_{70} = 1.8$
$m_{71} = 2$	$m_{72} = 1$	$m_{73} = 2$	$m_{74} = 1$	$m_{75} = 1$	$k_{71} = 2.2$	$k_{72} = 2.3$	$k_{73} = 3.5$	$k_{74} = 3.7$	$k_{75} = 1.1$
$m_{76} = 3$	$m_{77} = 3$	$m_{78} = 2$	$m_{79} = 1$	$m_{80} = 2$	$k_{76} = 3.3$	$k_{77} = 3.1$	$k_{78} = 2$	$k_{79} = 1.5$	$k_{80} = 1.2$
$m_{81} = 3$	$m_{82} = 1$	$m_{83} = 1$	$m_{84} = 1$	$m_{85} = 3$	$k_{81} = 0.9$	$k_{82} = 2.8$	$k_{83} = 0.7$	$k_{84} = 3.4$	$k_{85} = 1.1$
$m_{86} = 2$	$m_{87} = 3$	$m_{88} = 2$	$m_{89} = 1$	$m_{90} = 3$	$k_{86} = 4.3$	$k_{87} = 1.2$	$k_{88} = 3.3$	$k_{89} = 1.3$	$k_{90} = 1.8$
$m_{91} = 2$	$m_{92} = 2$	$m_{93} = 3$	$m_{94} = 3$	$m_{95} = 2$	$k_{91} = 1.6$	$k_{92} = 1.1$	$k_{93} = 3.9$	$k_{94} = 2.2$	$k_{95} = 1.7$
$m_{96} = 1$	$m_{97} = 3$	$m_{98} = 2$	$m_{99} = 2$	$m_{100} = 3$	$k_{96} = 2.4$	$k_{97} = 1$	$k_{98} = 0.8$	$k_{99} = 3.1$	$k_{100} = 0.5$
					$k_{101} = 2.2$				

¹ Stiffness values presented in the table should be multiplied by 1000

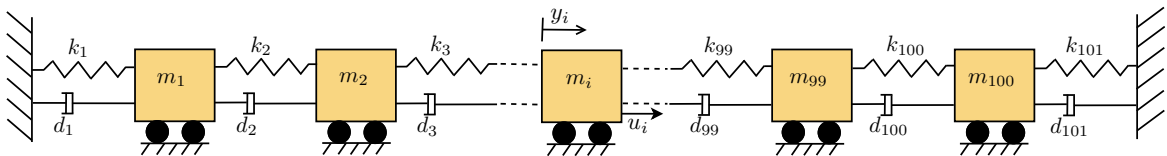


Figure 5.7 – Schematic 100 degree of freedom model (M100DOF), where m_i :masses, k_i :stiffnesses and d_i :dampings. Friction not considered.

An M50DOF system was reconfigured, as presented in Figure 5.8, to have a system with the matrix \mathbf{D} of the state-space representation (Equation (4.1)) not null. The displacements measurements were changed to accelerometers (y_i) located at the same masses of the M50DOF (Table 5.1), except y_{17} and y_{33} that were changed to y_{18} and y_{36} where the excitation forces (u_i) are applied, i.e.: $m_5, m_{18}, m_{26}, m_{36}, m_{48}$. The excitation forces were applied accordingly to Table 5.1. The location of accelerometers (output) together with excitation forces (input) in the same body took into consideration Equation (5.19) to obtain the feed-through matrix \mathbf{D} .

Since the matrix \mathbf{M} is diagonal, the matrices \mathbf{C}_a and \mathbf{B}_0 cannot be orthogonal to avoid a null matrix \mathbf{D} . It was established the accelerometers positioned in the same masses of the excitation forces, therefore providing a non-null feed-through matrix \mathbf{D} (Gawronski, 2005), that depicts the system dynamic from accelerometers. To differentiate how the system is called, this one configuration using accelerometers rather than displacement measurements will be nominated M50DOF-a and has the same matrices compositions of the M50DOF system prior described.

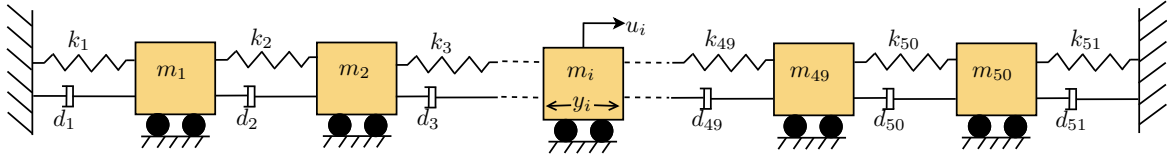


Figure 5.8 – Schematic 50 degree of freedom model with accelerometers in y_i (M50DOF-a), where m_i :masses, k_i :stiffnesses and d_i :dampings. Friction not considered.

It shall be highlighted that all the models (M5DOF, M50DOF, M50DOF-a, and M100DOF) previously presented were chosen as stable systems (damped). Then, for an impulse response excitation, it is considered the same assumption as in the work of Kung (Kung, 1978), where the matrix block of Markov parameters, defined in Equation (4.18), obeys the following premiss:

$$\mathbf{H}_v(p-1) \rightarrow 0 \quad \text{as} \quad p \rightarrow \infty, \quad (5.22)$$

thus, Equation (5.22) assumes that the Markov parameters decay with time, when submitted to an impulsive excitation (Kramer; Gorodetsky, 2018).

5.5 Cart-Pendulum model

The Cart-Pendulum is a classic mechanical model commonly applied to control area studies. Since this dynamical model can provide nonlinear characteristics of a system, the

model was simulated in the present research to verify and analyze its identification result when submitted to the SSRA-DC-iCL method. A schematic representation of the Cart-Pendulum model (C-PEN) is displayed in Figure 5.9, where CG and I are the Center of Gravity and the Moment of Inertia, respectively, from the pendulum rod.

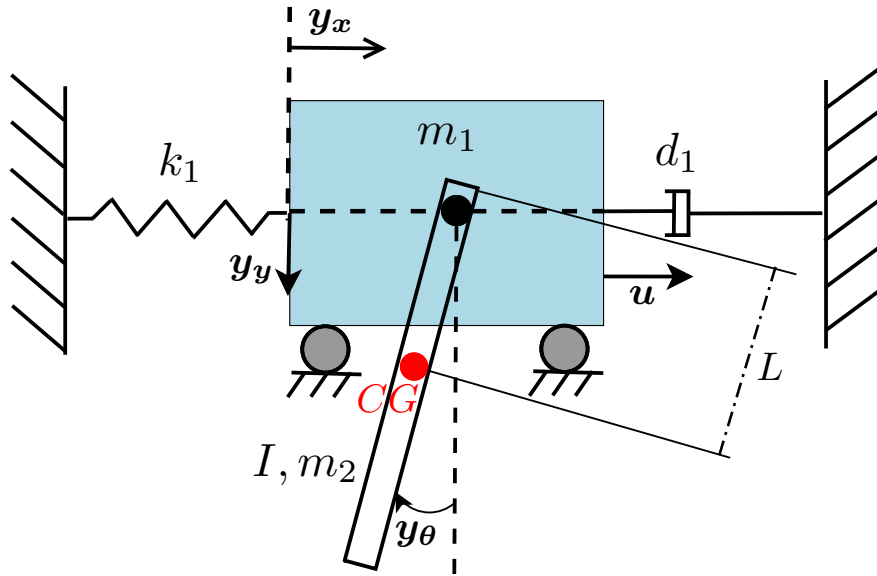


Figure 5.9 – Schematic representation of the C-PEN. Friction not considered on the rolls.

From Figure 5.10, the dynamical equations of the system are developed, representing the free body diagrams of Cart and Pendulum rod.

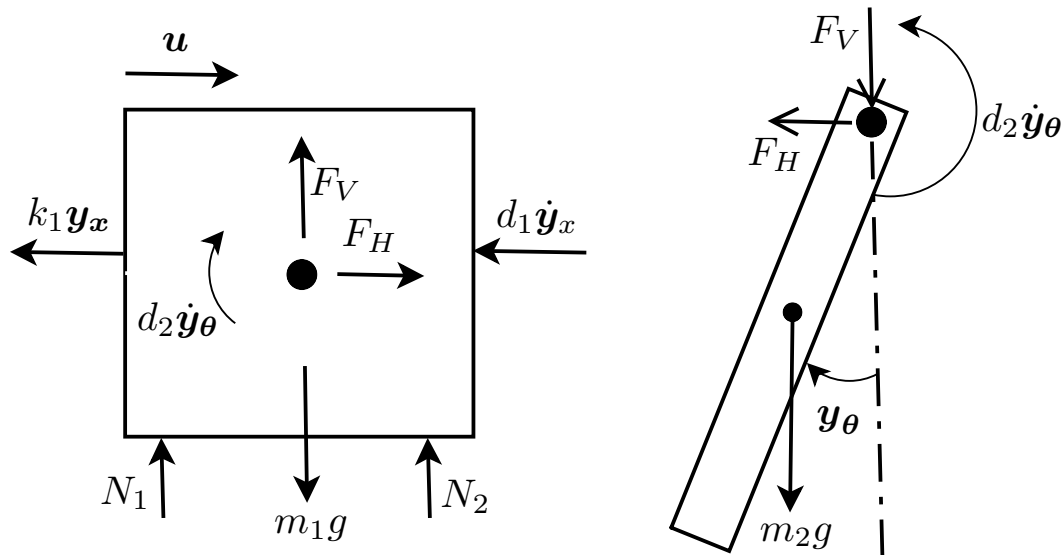


Figure 5.10 – Free body diagrams of cart (left) and pendulum rod (right).

The following sequence of equations was built up to the attainment of the second-order differential equations of the cart displacement y_x and the pendulum rod angle y_θ that

are considered outputs from the system, which is excited by the input force \mathbf{u} . The referred differential equations were integrated by the Runge Kutta 4th order numerical method (RK4), using the 'ode45' function from Matlab, to calculate the outputs values \mathbf{y}_x and \mathbf{y}_θ accordingly to the input values \mathbf{u} . The input force is composed of a series of values based on a GWN signal with unit-variance as defined in Section 5.2.3.

From Figure 5.9 and 5.10, the following equations are taken and should be considered for mathematical development of the dynamical model:

$$m_1 \ddot{\mathbf{y}}_x = -k_1 \mathbf{y}_x - d_1 \dot{\mathbf{y}}_x + F_H + \mathbf{u}, \quad (5.23)$$

$$m_2 \frac{d^2}{dt^2} (\mathbf{y}_x - L \sin \mathbf{y}_\theta) = -F_H, \quad (5.24)$$

$$m_2 \frac{d^2}{dt^2} (L \cos \mathbf{y}_\theta) = m_2 g + F_V, \quad (5.25)$$

$$I \ddot{\mathbf{y}}_\theta = F_V L \sin \mathbf{y}_\theta - F_H L \cos \mathbf{y}_\theta - d_2 \dot{\mathbf{y}}_\theta. \quad (5.26)$$

Substituting F_H from Equation (5.24) into Equation (5.23), it holds:

$$m_1 \ddot{\mathbf{y}}_x = -k_1 \mathbf{y}_x - d_1 \dot{\mathbf{y}}_x - m_2 \frac{d^2}{dt^2} (\mathbf{y}_x - L \sin \mathbf{y}_\theta) + \mathbf{u}, \quad (5.27)$$

$$m_1 \ddot{\mathbf{y}}_x = -k_1 \mathbf{y}_x - d_1 \dot{\mathbf{y}}_x - m_2 \ddot{\mathbf{y}}_x + m_2 L (\ddot{\mathbf{y}}_\theta \cos \mathbf{y}_\theta - \dot{\mathbf{y}}_\theta^2 \sin \mathbf{y}_\theta) + \mathbf{u}, \quad (5.28)$$

$$(m_1 + m_2) \ddot{\mathbf{y}}_x + d_1 \dot{\mathbf{y}}_x + k_1 \mathbf{y}_x - \mathbf{u} - m_2 L \ddot{\mathbf{y}}_\theta \cos \mathbf{y}_\theta + m_2 L \dot{\mathbf{y}}_\theta^2 \sin \mathbf{y}_\theta = 0. \quad (5.29)$$

Substituting F_H and F_V from Equation (5.24) and Equation (5.25), respectively, into Equation (5.26), it holds:

$$I \ddot{\mathbf{y}}_\theta = \left(m_2 \frac{d^2}{dt^2} (L \cos \mathbf{y}_\theta) - m_2 g \right) L \sin \mathbf{y}_\theta + \left(m_2 \frac{d^2}{dt^2} (\mathbf{y}_x - L \sin \mathbf{y}_\theta) \right) L \cos \mathbf{y}_\theta - d_2 \dot{\mathbf{y}}_\theta, \quad (5.30)$$

$$I \ddot{\mathbf{y}}_\theta + d_2 \dot{\mathbf{y}}_\theta = \left(L \frac{d}{dt} (-\dot{\mathbf{y}}_\theta \sin \mathbf{y}_\theta) - g \right) m_2 L \sin \mathbf{y}_\theta + \left(\ddot{\mathbf{y}}_x - L \frac{d}{dt} (\dot{\mathbf{y}}_\theta \cos \mathbf{y}_\theta) \right) m_2 L \cos \mathbf{y}_\theta, \quad (5.31)$$

$$\begin{aligned}
I\ddot{\mathbf{y}}_{\theta} + d_2\dot{\mathbf{y}}_{\theta} = & \left(-L\ddot{\mathbf{y}}_{\theta} \sin \mathbf{y}_{\theta} - L\dot{\mathbf{y}}_{\theta}^2 \cos \mathbf{y}_{\theta} - g\right) m_2 L \sin \mathbf{y}_{\theta} + \\
& + \left(\ddot{\mathbf{y}}_x - L\ddot{\mathbf{y}}_{\theta} \cos \mathbf{y}_{\theta} + L\dot{\mathbf{y}}_{\theta}^2 \sin \mathbf{y}_{\theta}\right) m_2 L \cos \mathbf{y}_{\theta},
\end{aligned} \tag{5.32}$$

$$\ddot{\mathbf{y}}_{\theta} (I + m_2 L^2) + d_2\dot{\mathbf{y}}_{\theta} + m_2 L g \sin \mathbf{y}_{\theta} - m_2 L \ddot{\mathbf{y}}_x \cos \mathbf{y}_{\theta} = 0, \tag{5.33}$$

From Equation (5.29) and Equation (5.33), the second order derivative terms $\ddot{\mathbf{y}}_x$ and $\ddot{\mathbf{y}}_{\theta}$ can be taken isolated as follows:

$$\begin{aligned}
\ddot{\mathbf{y}}_x = & \frac{\mathbf{u} (m_2 L^2 + I) - d_2 m_2 L \dot{\mathbf{y}}_{\theta} \cos \mathbf{y}_{\theta} - m_2 L (m_2 L^2 + I) \dot{\mathbf{y}}_{\theta}^2 \sin \mathbf{y}_{\theta} - d_1 \mathbf{y}_x (m_2 L^2 + I)}{I (m_1 + m_2) + m_2^2 L^2 + L^2 m_1 m_2 - m_2^2 L^2 (\cos \mathbf{y}_{\theta})^2} + \\
& + \frac{-k_1 \mathbf{y}_x (m_2 L^2 + I) - m_2^2 L^2 g \cos \mathbf{y}_{\theta} \sin \mathbf{y}_{\theta}}{I (m_1 + m_2) + m_2^2 L^2 + L^2 m_1 m_2 - m_2^2 L^2 (\cos \mathbf{y}_{\theta})^2},
\end{aligned} \tag{5.34}$$

$$\begin{aligned}
\ddot{\mathbf{y}}_{\theta} = & \frac{m_2 L \mathbf{u} \cos \mathbf{y}_{\theta} - d_2 (m_1 + m_2) \dot{\mathbf{y}}_{\theta} - m_2^2 L^2 \dot{\mathbf{y}}_{\theta}^2 \cos \mathbf{y}_{\theta} \sin \mathbf{y}_{\theta} - g (m_1 + m_2) m_2 L \sin \mathbf{y}_{\theta}}{I (m_1 + m_2) + m_2^2 L^2 + L^2 m_1 m_2 - m_2^2 L^2 (\cos \mathbf{y}_{\theta})^2} + \\
& + \frac{(-d_1 \dot{\mathbf{y}}_x - k_1 \mathbf{y}_x) m_2 L \cos \mathbf{y}_{\theta}}{I (m_1 + m_2) + m_2^2 L^2 + L^2 m_1 m_2 - m_2^2 L^2 (\cos \mathbf{y}_{\theta})^2}.
\end{aligned} \tag{5.35}$$

The integration of Equation (5.34) and Equation (5.35) employing the RK4 method calculates the respective outputs \mathbf{y}_x and \mathbf{y}_{θ} , which are determined by the input \mathbf{u} . This task represents how to compose the data set from the dynamical model of the nonlinear Cart-Pendulum system required to simulate the identification methods presented in Chapters 3 and 4.

A linearization of the C-PEN can be performed considering the following conditions:

$$\cos \mathbf{y}_{\theta} \simeq 1; \quad \sin \mathbf{y}_{\theta} \simeq \mathbf{y}_{\theta}; \quad \mathbf{y}_{\theta} \dot{\mathbf{y}}_{\theta}^2 \simeq 0. \tag{5.36}$$

Applying the linearization, Equation (5.29) and Equation (5.33) assumes the following representation:

$$(m_1 + m_2)\ddot{\mathbf{y}}_x - m_2 L \ddot{\mathbf{y}}_{\theta} + d_1 \dot{\mathbf{y}}_x + k_1 \mathbf{y}_x = \mathbf{u}, \tag{5.37}$$

$$\ddot{\mathbf{y}}_{\theta} (I + m_2 L^2) - m_2 L \ddot{\mathbf{y}}_x + d_2 \dot{\mathbf{y}}_{\theta} + m_2 g L \mathbf{y}_{\theta} = 0. \tag{5.38}$$

Considering $x_1 = y_x$, $x_2 = y_\theta$, $x_3 = \dot{y}_x$, $x_4 = \dot{y}_\theta$, the state-space equations of the linearized C-PEN can be developed from Equation (5.37) and Equation (5.38) as follows:

$$\underbrace{\begin{bmatrix} 1 & 0 & 0 & 0 \\ 0 & 1 & 0 & 0 \\ 0 & 0 & (m_1 + m_2) & -m_2 L \\ 0 & 0 & -m_2 L & I + m_2 L^2 \end{bmatrix}}_{\mathbf{E}} \underbrace{\begin{bmatrix} \dot{x}_1 \\ \dot{x}_2 \\ \dot{x}_3 \\ \dot{x}_4 \end{bmatrix}}_{\mathbf{F}} + \underbrace{\begin{bmatrix} 0 & 0 & -1 & 0 \\ 0 & 0 & 0 & -1 \\ k_1 & 0 & d_1 & 0 \\ 0 & m_2 g L & 0 & d_2 \end{bmatrix}}_{\mathbf{F}} \underbrace{\begin{bmatrix} x_1 \\ x_2 \\ x_3 \\ x_4 \end{bmatrix}}_{\mathbf{H}} = \underbrace{\begin{bmatrix} 0 \\ 0 \\ 1 \\ 0 \end{bmatrix}}_{\mathbf{H}} \mathbf{u} \quad (5.39)$$

Hence, the state-space equations are attained:

$$\dot{\mathbf{x}} = \underbrace{-\mathbf{E}^{-1}\mathbf{F}}_{\mathbf{A}} \mathbf{x} + \underbrace{\mathbf{E}^{-1}\mathbf{H}}_{\mathbf{B}} \mathbf{u}, \quad (5.40)$$

$$\underbrace{\begin{bmatrix} y_x \\ y_\theta \end{bmatrix}}_{\mathbf{y}} = \underbrace{\begin{bmatrix} 1 & 0 & 0 & 0 \\ 0 & 1 & 0 & 0 \end{bmatrix}}_{\mathbf{C}} \underbrace{\begin{bmatrix} x_1 \\ x_2 \\ x_3 \\ x_4 \end{bmatrix}}_{\mathbf{x}}, \quad (5.41)$$

and $\mathbf{D} = \mathbf{0}$.

The constant values used in the present research related to the variables from the C-PEN, as shown in Figure 5.9 and Figure 5.10, were obtained from a set of user manuals of the components of the C-PEN (Inc., 2012). The respective values assumed from this reference are:

- $m_1 = 0.75 \text{ kg}$;
- $m_2 = 0.364 \text{ kg}$;
- $k_1 = 142 \text{ N/m}$;
- $d_1 = 4.3 \text{ N-m-s/rad}$;
- $d_2 = 0.0024 \text{ N-m-s/rad}$;
- $L = 0.26825 \text{ m}$;
- $I = 0.00788 \text{ kg-m}^2$;
- $g = 9.81 \text{ m/s}^2$.

5.6 Procedure of data supply to the algorithms

Different data sets of input excitation signals yield hereafter the basis for the algorithms' processing. A data set of input excitation signals aims to create data for the execution of the algorithm to obtain the identified system. Other data sets of signals excite the applied system for generating the output variables to be used as validation data to evaluate the identified system. The data set comes from inputs and outputs measurement devices in experimental tasks undertaken in an actual process. Similarly to that, the computational steps to generate the input data set of algorithms required in a simulation environment are summarized in Figure 5.11. For the linear mass-spring-damper system, the Original System OS is represented by a state-space model, whereas for the nonlinear C-PEN, the data set of the OS is obtained from the dynamical model described by differential equations and submitted to the RK4 numerical method.

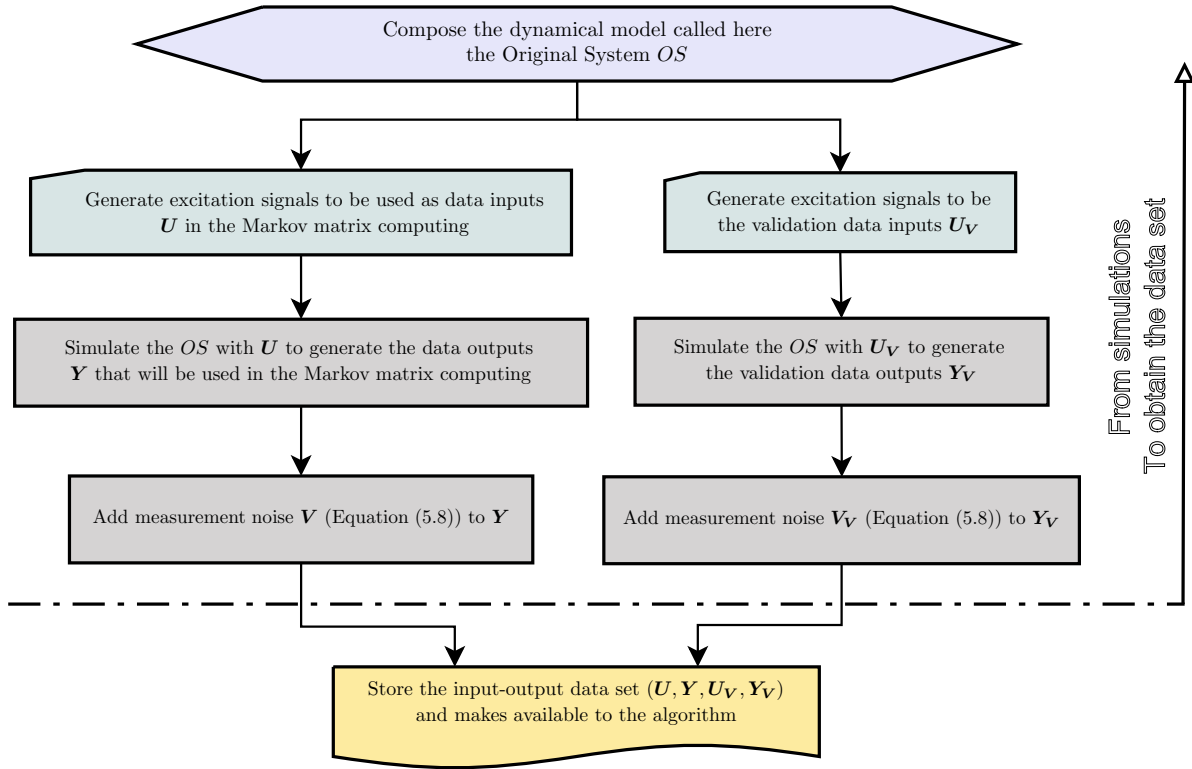


Figure 5.11 – Computational steps of systems simulations to make available the algorithm data set.

5.7 Systems discretization

This work is based on simulations that demand a hypothetical continuous-time system, directly coming from a dynamical model, to be represented as a discrete-time system. The

discretization method applied was defined accordingly to one of the application's processes simulated in this research, as will be introduced at the current topic.

5.7.1 For the Mass-Spring-Damper system

The continuous-time system, defined here by the matrices \mathcal{M} , \mathcal{K} and \mathcal{D} , were discretized using the zero-order hold (ZOH) method for the time response analysis. The bilinear method (Tustin) was chosen to discretization in the frequency response analysis for SSRA simulations of the M5DOF model. This discretization method was selected considering the better results of VFR_j attained in the case of frequency response analysis, which will be reported ahead in Section 6.3, and was also supported to keep the system's expected natural frequencies.

The determination of the system sampling time d_t shall regard the appropriate selection of the sampling frequency ω_s to attend the Nyquist Sampling Theorem, as follows

$$\omega_s \geq 2 \omega_{max}, \text{ and } \omega_s = \frac{2\pi}{d_t}, \quad (5.42)$$

where ω_{max} is the maximum frequency of the discretized system (Han, 2010), with the frequencies defined in rad/s.

Besides the previous basic concerns for the determination of the minimum sampling frequency suitable to the current SSRA applications, the work of Moaveni et al. (Moaveni; Masoumi, 2019) also considers the maximum sampling frequency. In the ERA method, a high sampling frequency related to structural systems with low bandwidth can lead to very small values the difference between two consecutive input-output measurements. This condition forms Hankel matrices (Equation (4.19) and Equation (4.20)) close to being singular, taking the ERA computing to fail in the identification results. Then, accordingly to this reference work (Moaveni; Masoumi, 2019), the definition of sampling frequencies limits is based on the following expressions:

$$2 \omega_{dmax} < \omega_s < 4\pi \omega_{dmax}, \text{ and } \omega_{dmax} = \max \left\{ \omega_{d_i} = \omega_{n_i} \sqrt{1 - \zeta_i^2} \right\} \text{ with } i = 1, 2, \dots, n/2, \quad (5.43)$$

where ω_{n_i} and ζ_i are the i th natural frequency in rad/s and the corresponding damping ratio, respectively. As mentioned in the work of Moaveni et al., for data sets coming from experiments, the maximum damping frequency ω_{dmax} can be determined using the power spectral of the output measurable variables.

The sampling time computed and established for each specific mass-spring-damper system involved in the algorithms simulations is presented in Section 6.3 and Section 7.2.

5.7.2 For the Cart-Pendulum system

The dynamical model of the C-PEN portrayed by Equation (5.34) and Equation (5.35), when submitted to the RK4 method, requires establishing a sampling time to perform the technique. This sampling time determines the frequency of the outputs data set generation. The outputs y_x and y_θ of the C-PEN were generated with a sampling frequency of the RK4 method equal to the sampling frequency applied in the identification algorithm. This setting assured that the frequencies of the identified system coincide with the frequencies of the linearized system, which were represented in state-space and were obtained from Equations (5.39), (5.40), and (5.41).

The determination of the sampling time d_t for the system identification process, employing the methods studied in the present research, should consider the Nyquist Sampling Theorem as defined in Equation (5.42). For that, the maximum frequency ω_{max} taken from the linearized system was made as a reference in the application of the Nyquist sampling Theorem. The sampling frequency value employed for the RK4 method and the identification methods is presented in Section 7.9.1, which introduces the conditions of the simulations performed.

6 ANALYSIS OF THE SETTINGS INFLUENCE ON SSRA

This chapter presents numerical results and graphs related to the classical SSRA simulating the M5DOF system to provide an introductory concept of the algorithm settings and its influence on the results. In Section 6.5, the M100DOF system is also simulated in the SSRA method to grant comparative results between the three excitation signals introduced at Section 5.2.⁴

6.1 Specific settings and system configurations for the SSRA simulations

The input data set to the SSRA are available from the simulation steps described in Figure 5.11 of Section 5.6. In the sequel, going along with what is presented in Figure 4.1, the following computational steps are performed to the attainment of the SSRA identified system and its effectiveness evaluation:

- a) Compose the input-output data set matrices U_V , Y_V , U , Y .
- b) Compute the Markov parameters matrix H .
- c) Compose the Hankel matrix H_h and the time-shifted Hankel matrix H_{sh} .
- d) Factorize the Hankel matrix H_h employing the Singular Values Decomposition (SVD).
- e) Determine the order of the system by examining the singular values ($\Sigma_i = \text{diag}[\sigma_1, \sigma_2, \dots, \sigma_n, \sigma_{n+1}, \dots, \sigma_{\frac{p}{2}-1}]$) (Equation 4.27).
- f) Construct the state-space realization of the identified system IS , calculating the estimated \hat{A} , \hat{B} , \hat{C} , and \hat{D} matrices.
- g) Proceed with the validation step, simulating the IS with inputs U_V to generate estimated data outputs \hat{Y} .
- h) Evaluate the identified system IS , comparing \hat{Y} and Y_V through the calculation of the Fit Rate indicator $VFR_j(\%)$ (Equation 4.59), where $y_j(k)$ comes from the output Y_V , and $\hat{y}(k)$ comes from the estimated output \hat{Y} .

⁴ Except for Section 6.5 of the present thesis, the content of this chapter is part of the paper published on the reference (Soares Jr; Serpa, 2021).

Referring to the classical State-Space Realization Algorithm, its configuration requires to be appropriately adjusted for the achievement of a better result of VFR_j in the SI process. Aiming to show and discriminate the settings done in each result that will be reported ahead, the respective algorithm parameters are described, where the matrices or mathematical expressions related to them were presented in Chapter 4:

- d_t : sampling time of the system in the simulation;
- q : number of samples;
- p : determines the Hankel matrix size;
- n : state-space order of the realization (identified system order).

Generally, after q is defined, per simulations' experience, the parameter p can start with at about 10% to 20% of q as an early reference. It can be increased gradually after the initial adjustment of parameter n has been done. In a real system, the starting value of the parameter n should be estimated, considering the knowledge about the system characteristics. This approach to the determination of parameter n for real systems was used in the classical SSRA (Juang; Pappa, 1985), and even in the General Realization Algorithm (GRA) (De Callafon *et al.*, 2008). The initial attainment of the coherent rank of the Hankel matrix takes into account what should be the singular value close to zero.

In a simulation environment, the order of the original system works as a reference for the identified system order definition, hence it determines the effective rank of the Hankel matrix H_h . In the M5DOF model, the state-space system of order 10 (order of the matrix A) can be, as a reference, the system's initial order to be identified. After all other parameters adjusted, it is suitable to come back to the system order in the attempt of providing a low order than the previous one setting, if this can be done without loss of the \overline{VFR} value. Although simulations analysis is the focus of this work, one of the possible noise sources is related to computer round-off. However, rather than defining $n = 10$ at this time, this work will exercise here the setting of this parameter, considering that the system was not previously established.

The use of \overline{VFR} value represents a good driver for the parameters adjustment to better system identification results. Thereby, to get the first information of the algorithm response to system characteristics, as pointed from Equation (4.27), it is worthwhile to plot the singular values to get some reference of the system order (n), with attention to the interference

of computational rounding. The singular values for 0% of noise presented in Figure 6.1 show that the parameter n can start with the value 13 since all of them are closer to zero from the 14th singular value. This choice of the order (n) considered only visual inspection of the singular values on the graph of Figure 6.1. As will be shown ahead, this aspect of the order choice works as a reference without an accuracy commitment once the Fit Rate indicator drives the parameter selection.

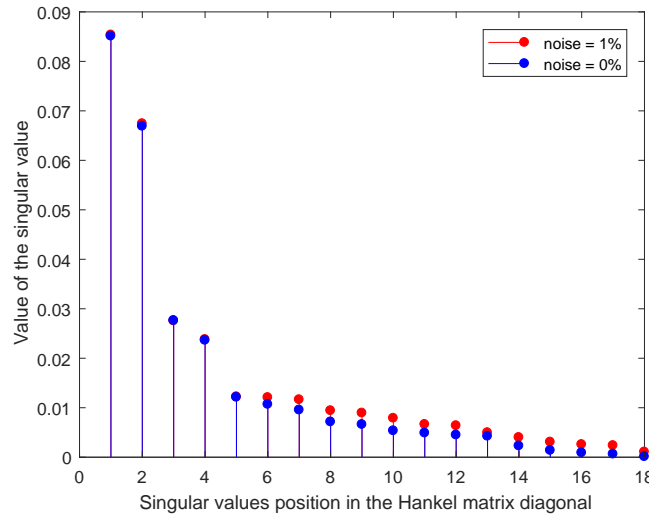


Figure 6.1 – Singular values from Hankel matrix for: M5DOF, $d_t = 0.5$ s, $q = 100$, $p = 20$, noises of 0% and 1%.

The singular values graph for 1% of measurement noise added to the system is also shown in Figure 6.1 in comparison to the condition without noise. Both graphs were plotted with the same algorithm settings. Comparing the graphs, since it is not easy to determine from which order the singular value is closer to zero, the system with noise confirms the difficulty of using the singular values information as an initial reference to determine the system order. In addition to that, the searching for a more appropriate system order, in this context, has the purpose of being a complementary tool. For instance, the well-known methods Modal Amplitude Coherence and Mode Singular Value introduced by (Juang; Pappa, 1985; Juang; Pappa, 1986) from the traditional ERA are the main tools to take the system order parameter. However, according to the results for the noisy system presented in Section 6.4, the searching for the true system order can consider the Fit Rate index as a guide and recalibration tool to attain the system order closer to the true one.

For the M5DOF model, the system discretization analysis and the corresponding more appropriate sampling time values for each simulation will be shown in Section 6.3 after

presenting the results of the time response analysis.

6.2 Time response analysis to the M5DOF system

Applying the VFR_j indicator (Equation (4.59)), the results of the system identification, using the SSRA excited by PRBS signals in the M5DOF system, are portrayed in the figures and tables that are shown in this section. PRBS signals, switching between 0 and 1 (Figure 5.3), yield the excitation forces with amplitudes multiplied in u_4 and u_5 by proposed factors 2.5 and 3.33, respectively. These employed factors were chosen to provide more suitable amplitudes levels for the results assessment. The figures show the curve of one of the outputs y generated by the original system (red color) compared to the curve of the correspondent estimated output \hat{y} generated by the identified system (blue color). The time response analysis was performed for three sampling times (d_t): 0.5, 0.1, and 0.02 seconds. The graphs show the time at the horizontal axis in seconds (s) and the displacement at the vertical axis in meters (m).

A data set summarizing the time response results is reported in Table 6.1. From Figure 6.2 to Figure 6.9, it is shown the worst and the best results for all sampling times simulated in terms of the value of VFR_j . The figures regarding other adjustments will not be shown here, although they were simulated, and its \overline{VFR} (Equation (4.60)) values are presented in Table 6.1.

From the same sampling time, the sequence of results presentation shows an increase in the number of samplings (q), which interferes in the size of system inputs and outputs matrices, determining the Markov matrix composition (H). The sequence of parameter values was set to realize the influence of each one in the Fit Rate result. Firstly, q is doubled up and p is fixed; next, q is fixed and p is doubled up. This sequence is applied for the three sampling times. It can be seen from the variable C_F in Table 6.1 that the PRBS excitation is maintained fixed for the same q value with the purpose to perceive the effect simply from the changes of the other parameters (p and n). And when the best result of \overline{VFR} value is achieved, the system order (n) is reduced from the initial value ($n = 13$) to analyze its effect in the system identification result.

The improvement in the results according to the sequence of parameters configuration applied is portrayed in Table 6.1. The increment in p always results in \overline{VFR} increment, and the increase of q results in the \overline{VFR} increment either. Generally, this means that the \overline{VFR} value goes up following the parameters q and p that had increased either. For the maximum value of p , when $p = q$ (Equation (4.16)), it can be seen a significant decay of \overline{VFR} value, mainly for $dt = 0.02$ s, denoting the importance of searching for the best SSRA settings for fewer compu-

tational efforts, which do not follow an automatic guideline. Additionally, it is possible to see in Table 6.1 that the maximum $\overline{\text{VFR}}$ value is kept up to the adjustment of $p = q/2$. For $p > q/2$, the $\overline{\text{VFR}}$ value starts to decrease, and from this baseline, the deterioration on the system identification increase as p gets up.

Table 6.1 – Time response results

d_t	q	p	n	$\mathcal{C}_{\mathcal{F}}^{(1)}$	$\overline{\text{VFR}}^{(2)}$	Figures
0.5	100	20	13	2.97	76.10	6.2
0.5	200	20	13	3.10	87.83	–
0.5	200	40	13	3.10	99.37	–
0.5	400	40	13	2.99	99.52	–
0.5	400	80	13	2.99	99.73	–
0.5	400	80	10	2.99	100.00	6.3
0.5	400	80	8	2.99	99.98	–
0.5	400	200	10	2.99	100.00	–
0.5	400	202	10	2.99	99.85	–
0.5	400	400	10	2.99	86.62	–
0.1	500	100	13	15.36	97.17	6.4
0.1	1000	100	13	15.64	97.82	–
0.1	1000	200	13	15.64	99.69	–
0.1	2000	200	13	15.05	99.77	–
0.1	2000	400	13	15.05	100.00	–
0.1	2000	400	10	15.05	100.00	6.5
0.1	2000	400	8	15.05	99.88	6.6
0.1	2000	400	10	1.43 ⁽³⁾	100.00	–
0.1	2000	400	8	1.43 ⁽³⁾	99.65	6.7
0.1	2000	1000	10	15.05	100.00	–
0.1	2000	1002	10	15.05	99.88	–
0.1	2000	2000	10	15.05	87.44	–
0.02	2500	500	13	74.99	92.31	6.8
0.02	5000	500	13	75.04	97.05	–
0.02	5000	1000	13	75.04	99.11	–
0.02	10000	1000	13	75.08	99.89	–
0.02	10000	2000	13	75.08	100.00	–
0.02	10000	2000	10	75.08	100.00	6.9
0.02	10000	2000	8	75.08	97.80	–
0.02	10000	5000	10	75.08	100.00	–
0.02	10000	5002	10	75.08	97.74	–
0.02	10000	10000	10	75.08	79.02	–

¹ PRBS Clock frequency (rad/s) - average from inputs values² Average from outputs values (y_1 and y_2) - values in %³ Simulation with $\mathcal{C}_{\mathcal{F}}$ reduction in the PRBS signal

For $dt = 0.1$ s, with half than the maximum values of q and p , $\overline{\text{VFR}}$ achieves values

of 99.69% for $n = 13$ (higher order than the known order in this case), leading one to think if the increase in computational processing is worthwhile for the improvement of the results.

The analysis of the PRBS clock frequency (\mathcal{C}_F) reduction in terms of its impact on the performance of the system identification was accomplished for the best adjustments of the algorithm in the 0.1 s sampling time. As previously mentioned in Section 5.2.1, sometimes the real process is not compatible with an excitation input in the same frequency the sensors measure the response, which determines the system's time response. A reduction of 10-fold in \mathcal{C}_F of PRBS was performed to handle this analysis condition through a PRBS clock frequency reduction (Figure 6.7 in comparison with Figure 6.6), both situations for system order of $n = 8$. Despite there were no decreases in the VFR_j value for $n = 10$ with PRBS reduction, as shown in Table 6.1, when the system order was reduced to 8, the reduction of 10-fold in the PRBS clock frequency led to a slightly worse system identification result. The qualitative analysis comparing the correspondent figures early mentioned, clearly shows the difference of curves, where the curves with PRBS \mathcal{C}_F reduction are visually different with more slits.

Regarding the influence of changes in the system order (parameter n), the results point out that the $\overline{\text{VFR}}$ value can be a useful drive to the determination of the actual system order. A minimum realization with a model reduction takes part as one of the objectives of the traditional Eigensystem Realization Algorithm described by Juang and Pappa in 1985 (Juang; Pappa, 1985). Then, after achieving the possible best result of the presumed system order from the singular values graph (Figure 6.1), it is feasible to check for the reduction of that order. As demonstrated in the results, the system order reduction from 13 to 10 kept the VFR_j value or even increased this value, suggesting that this could be a valid system order. However, a next trial to reduce the parameter n from 10 to 8 provided a worse result, mainly when $dt = 0.02$ s, indicating that the actual system order is not 8.

Nevertheless, the decision to increase or decrease the system order should be well evaluated, depending on whether the gains or losses in the system identification results match any of the objectives. The system identification process should be carefully analyzed concerning reducing the identified system order beyond the original system order. This concern happens due to the decrease in the number of system poles, representing a loss of physical system effects.

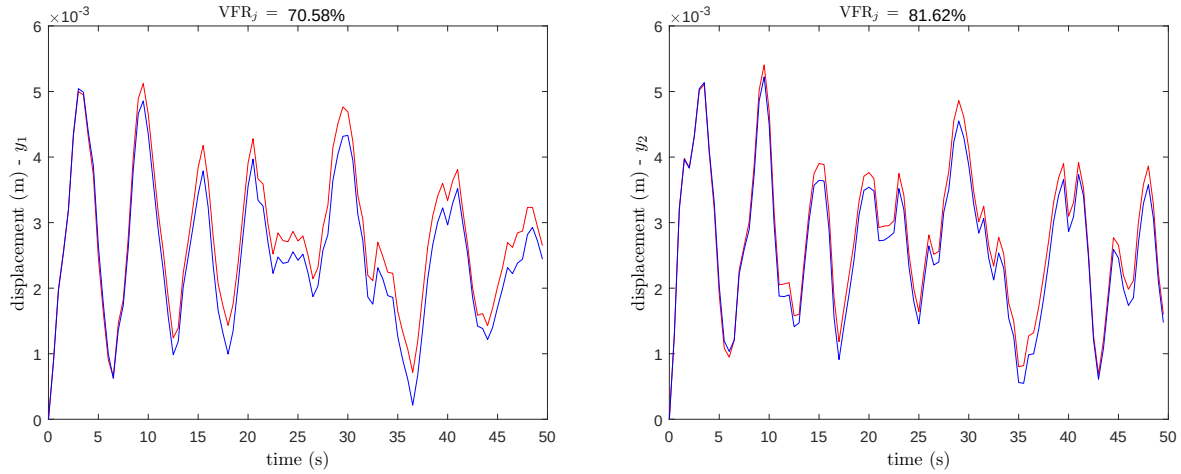


Figure 6.2 – Original (red) and identified (blue) systems: outputs y_1 (left) and y_2 (right) for $d_t = 0.5$ s, $q = 100$, $p = 20$, $n = 13$.

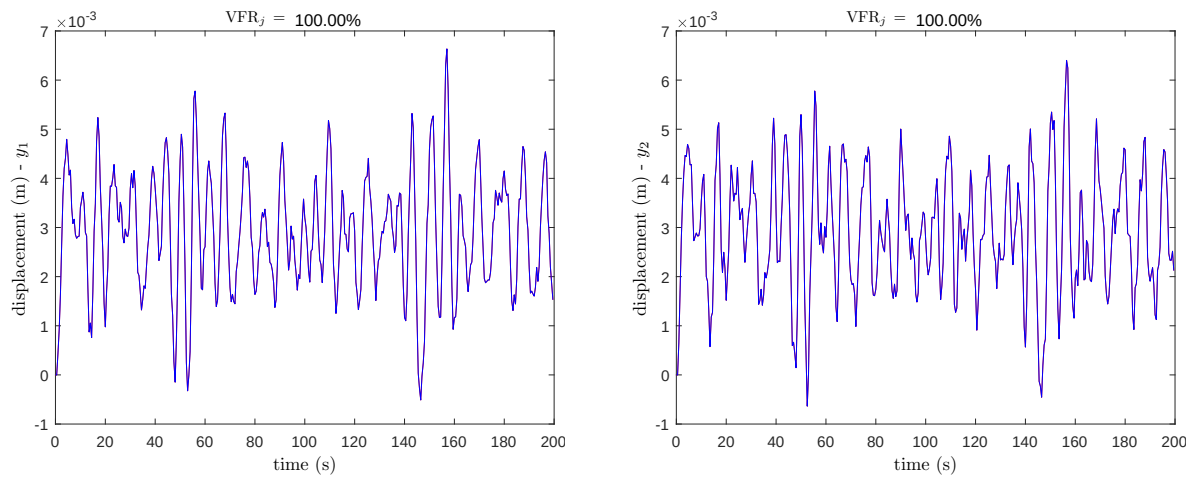


Figure 6.3 – Original (red) and identified (blue) systems: outputs y_1 (left) and y_2 (right) for $d_t = 0.5$ s, $q = 400$, $p = 80$, $n = 10$.

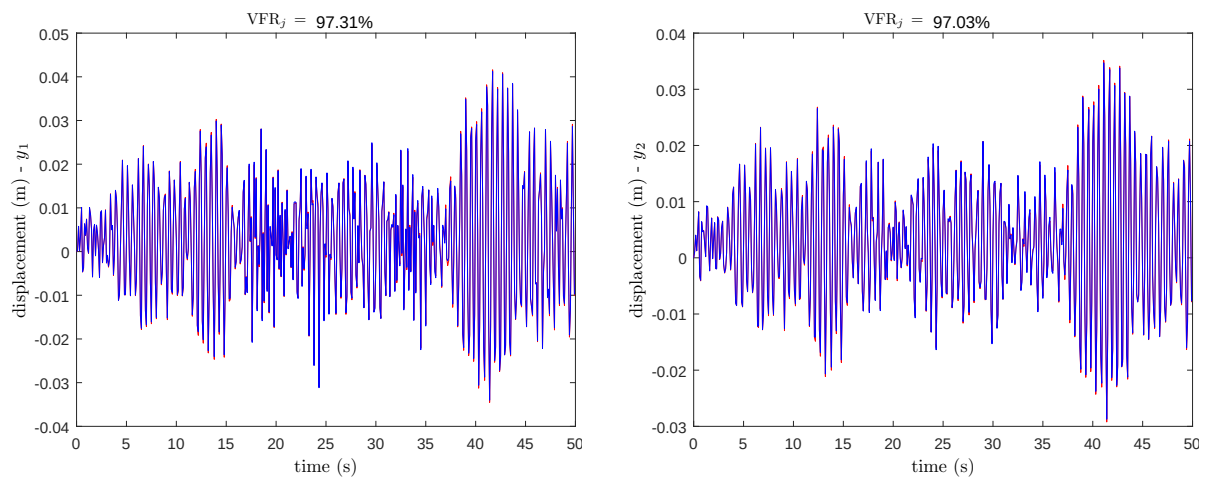


Figure 6.4 – Original (red) and identified (blue) systems: outputs y_1 (left) and y_2 (right) for $d_t = 0.1$ s, $q = 500$, $p = 100$, $n = 13$.

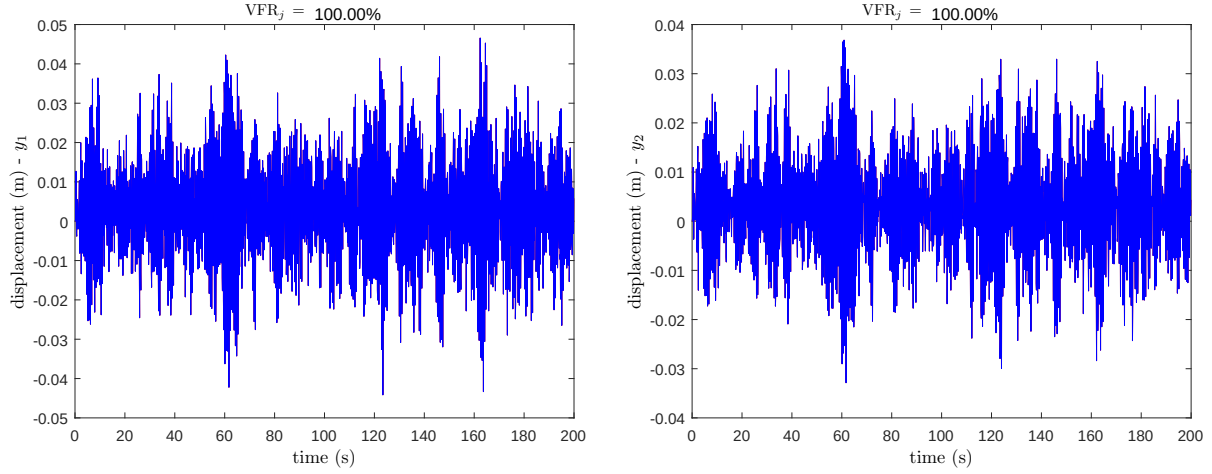


Figure 6.5 – Original (red) and identified (blue) systems: outputs y_1 (left) and y_2 (right) for $d_t = 0.1$ s, $q = 2000$, $p = 400$, $n = 10$.

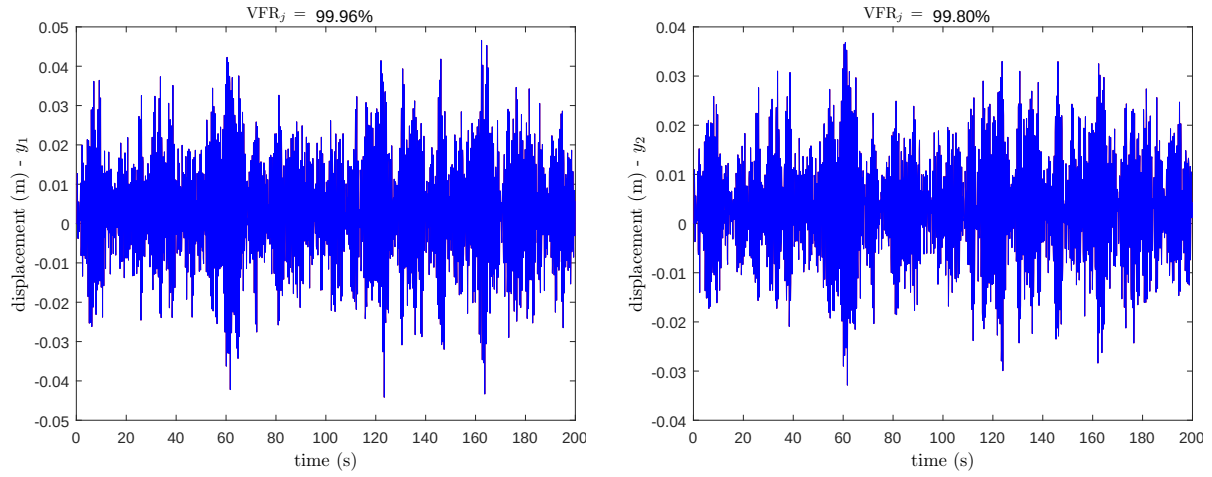


Figure 6.6 – Original (red) and identified (blue) systems: outputs y_1 (left) and y_2 (right) for $d_t = 0.1$ s, $q = 2000$, $p = 400$, $n = 8$.

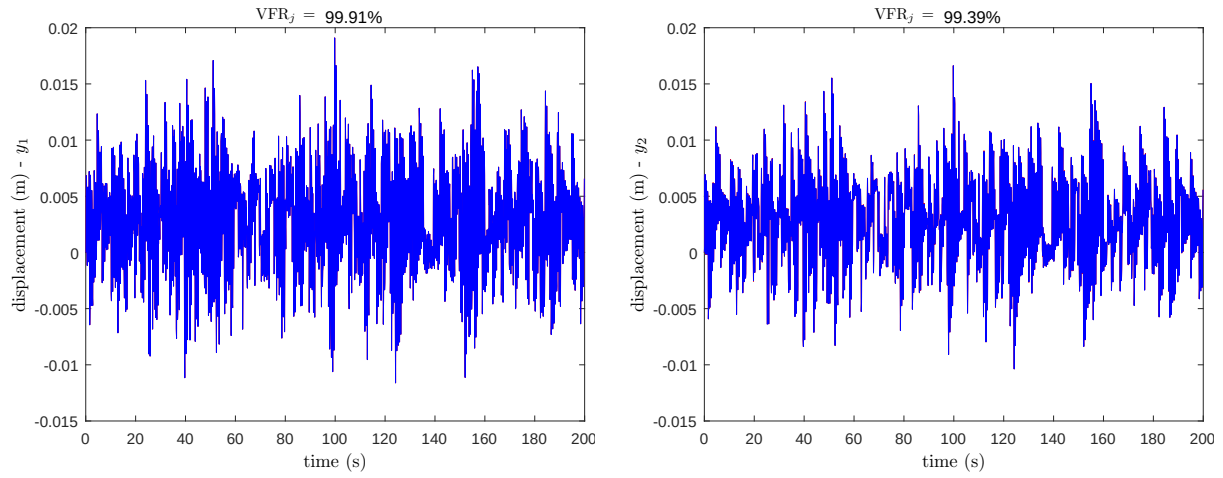


Figure 6.7 – Original (red) and identified (blue) systems: outputs y_1 (left) and y_2 (right) for $d_t = 0.1$ s, $q = 2000$, $p = 400$, $n = 8$, $\mathcal{C}_{\mathcal{F}} = 1.47$ rad/s.

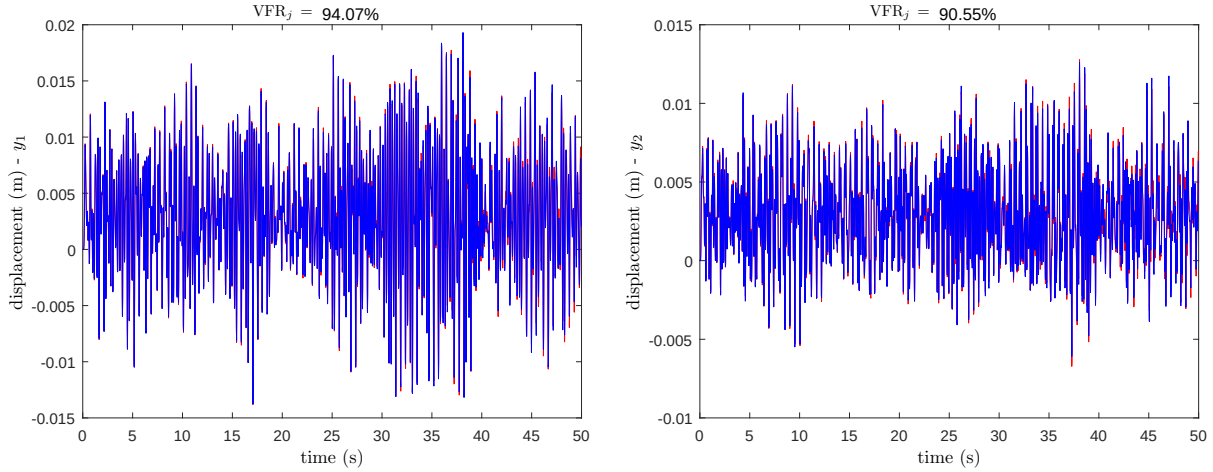


Figure 6.8 – Original (red) and identified (blue) systems: outputs y_1 (left) and y_2 (right) for $d_t = 0.02$ s, $q = 2500$, $p = 500$, $n = 13$.

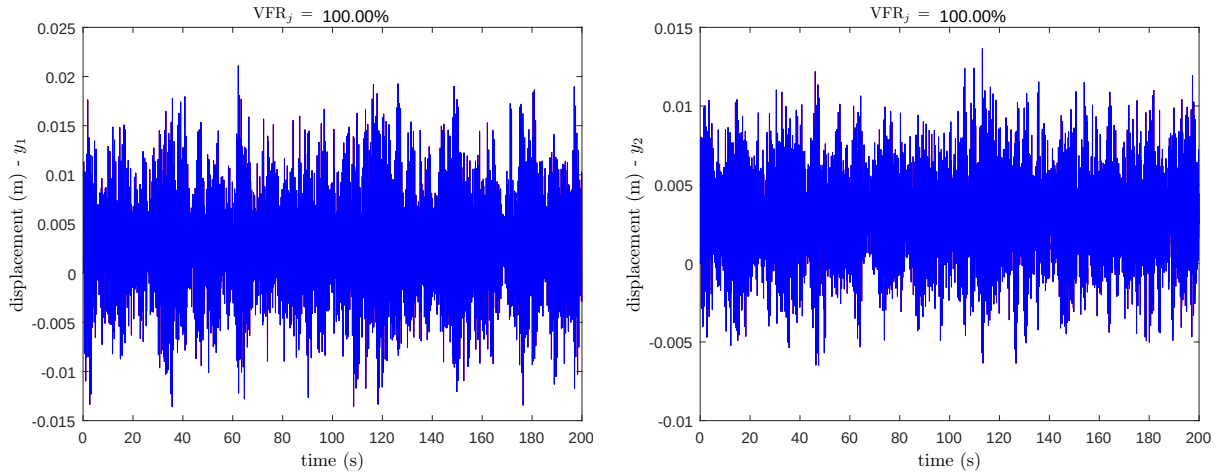


Figure 6.9 – Original (red) and identified (blue) systems: outputs y_1 (left) and y_2 (right) for $d_t = 0.02$ s, $q = 10000$, $p = 2000$, $n = 10$.

6.3 Frequency response analysis to the M5DOF system

For frequency response analysis, to measure the adherence of the identified system related to the original one, the VFR_j value was computed analogously as in Equation (4.59). The frequencies presented at Figure 6.10, Figure 6.11, and Figure 6.12 depict the discretization frequency employed in the simulations for the respective sampling times. The discretization frequencies are obtained by the ratio $\frac{(\omega_{max} - \omega_{min})}{q}$, where $(\omega_{max} - \omega_{min})$ is the frequency range in rad/s displayed at each figure, and q is the number of samples employed. These discretization frequencies assume the following values:

- $d_t = 0.5$ s $\Rightarrow \frac{(6.2-4.8)}{400} = 0.0035$ rad/s,
- $d_t = 0.1$ s $\Rightarrow \frac{(30-9)}{2000} = 0.0105$ rad/s,

- $d_t = 0.02 \text{ s} \Rightarrow \frac{(70-10)}{10000} = 0.006 \text{ rad/s}$.

The definition of discretization frequency value took into account the premise to maintain the same number of samples (parameter q) used in each sampling time of the time response analysis. Still, the analysis should be done in a frequency range, comprehending and encompassing the system's natural frequencies. The natural frequencies ω_{n_i} of the continuous-time are shown in Table 6.2. The frequencies of the discretized system obtained by the Tustin discretization method are also presented there. It can be seen the significant shifting in natural frequencies for $d_t = 0.5 \text{ s}$ regarding the continuous-time system. For $d_t = 0.02 \text{ s}$, the shifting is much lower.

Table 6.2 – Natural frequencies [rad/s] of the continuous-time and discretized system

ω_{n_i}	continuous-time ⁽¹⁾	$d_t = 0.5 \text{ s}$	$d_t = 0.1 \text{ s}$	$d_t = 0.02 \text{ s}$
ω_{n_1}	11.6708	4.9628	10.5654	11.6183
ω_{n_2}	26.4333	5.6825	18.4623	25.8425
ω_{n_3}	37.6496	5.8598	21.6506	36.0087
ω_{n_4}	50.1105	5.9646	23.8218	46.4543
ω_{n_5}	69.5450	6.0534	25.8162	60.7696

¹ Natural frequencies of the hypothetical continuous-time system

Instead of a Bode diagram that uses only one output/input pair at a time to measure the adherence of the identified system, it was used the singular values of the MIMO system transfer matrix. The objective of this approach is to have an analysis of the MIMO system behavior as a whole. The singular value response of a SISO system, composed by an output/input pair, is the same of its Bode magnitude response. A singular value plot of a transfer matrix portrays the function of maximum and minimum singular values of a plant for frequency response. These singular values work as a robust tool for characterizing the MIMO system when the maximum singular value comes to represent the greatest gains of the plant (Albertos *et al.*, 2005; Brecher *et al.*, 2018).

The Maximum Singular Values (MSV) diagrams for $dt = 0.5 \text{ s}$ (Figure 6.10), $dt = 0.1 \text{ s}$ (Figure 6.11), and $dt = 0.02 \text{ s}$ (Figure 6.12), were generated for the adjustments that meet the best results of the Fit Rate attained in the time response analysis in the prior section. Besides the same adjustments accomplished in the time response analysis, the respective PRBS excitation signals were also kept the same for comparison purposes. The $\overline{\text{VFR}}$ value for MSV is calculated at the same frequency values for the original and identified system curves. The $\overline{\text{VFR}}$ value calculated uses the respective magnitude values expressed in decimals, whereas the plotted values of magnitude are expressed in decibels (dB). This difference explains, why

visually, the singular values magnitude graph (in dB) seems to be with a $\overline{\text{VFR}}$ value lower than the respective value placed in the figures.

For the sampling time of 0.5 s, the low $\overline{\text{VFR}}$ value achieved portrays the inefficiency of the system identification from the perspective of frequency response analysis for this sampling frequency. For 0.1 s of sampling time, it can be realized only some discrepancy between the identified and original system, which are expressed by the lower values of $\overline{\text{VFR}}$ in comparison with the values achieved (100%) from time response analysis. For the higher sampling frequency with $d_t = 0.02$ s, the results improved considerably, where the $\overline{\text{VFR}}$ values shows the complete adherence of the identified system. As expected, in comparison with 0.5 s sampling time, this best outcome shows an absolute overlapping of the curves. Thus, the increase in the Fit Rate for the frequency response analysis is evident as the sampling frequency increases, which was not too clear for time response analysis.

The expected five peaks in the identified system curves are well portrayed for 0.1 s and 0.02 s sampling time, which does not happen with $dt = 0.5$ s, where two peaks are not present. This situation supports what is mentioned by Juang (Juang, 1994): “if one wishes to interpret the natural frequencies of the physical system, either the sample time interval Δt must be sufficiently short or a filter must be added to prevent the frequencies beyond the Nyquist frequency from being folded into a lower frequency in the realization”.

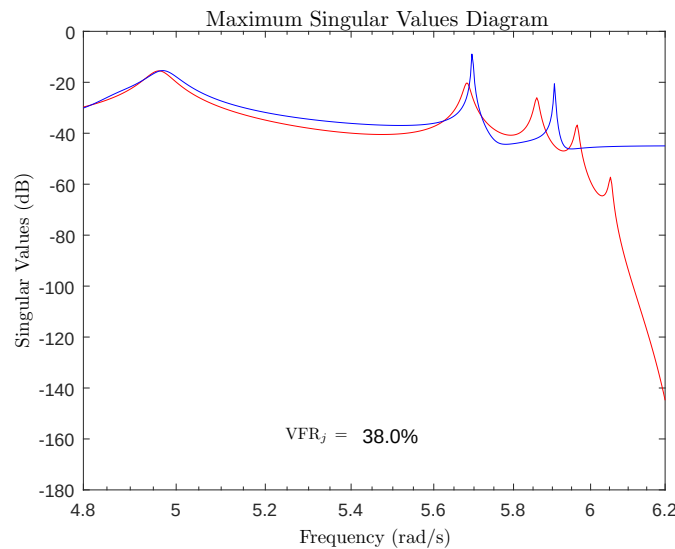


Figure 6.10 – Original (red) and identified (blue) systems: MSV diagram for $d_t = 0.5$ s, $q = 400$, $p = 80$, $n = 10$.

Despite the number of peaks compatibility in most of the MSV curves, but accordingly with what is presented in Table 6.2, there are significant shifting of the natural frequencies

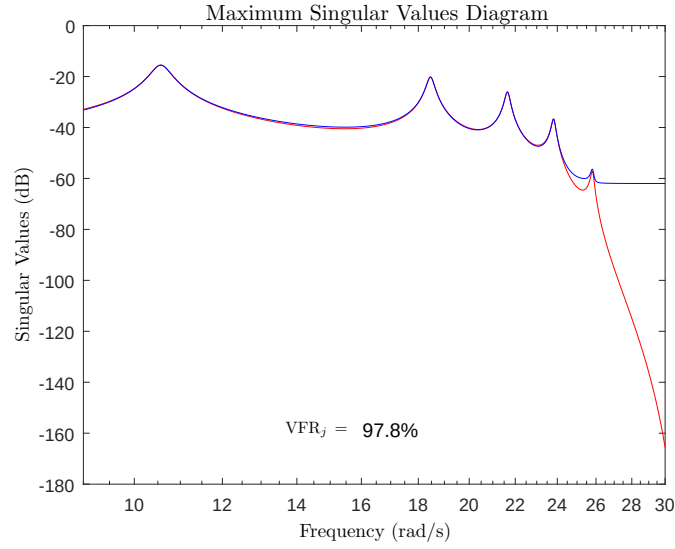


Figure 6.11 – Original (red) and identified (blue) systems: MSV diagram for $d_t = 0.1$ s, $q = 2000$, $p = 400$, $n = 10$.

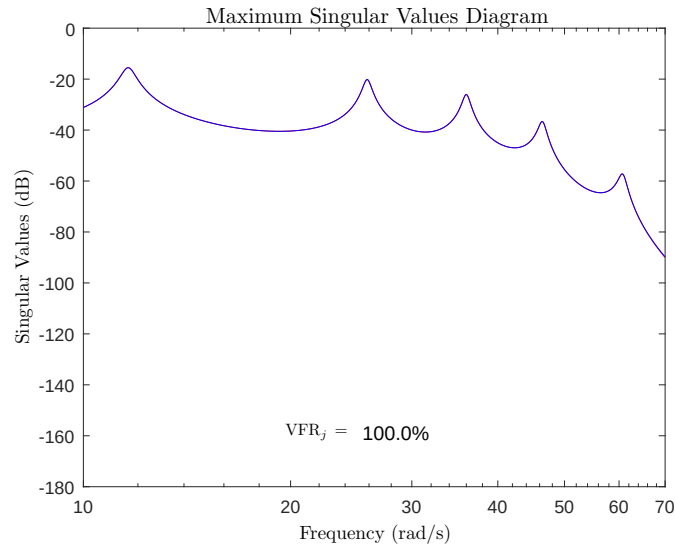


Figure 6.12 – Original (red) and identified (blue) systems: MSV diagram for $d_t = 0.02$ s, $q = 10000$, $p = 2000$, $n = 10$.

of discretized systems concerning the continuous-time system frequencies, where the shifting increases as the sampling frequency decreases. This remark leads to weighing up if the sampling frequencies applied are appropriated to the discretized systems.

The definition of sampling frequency application limits to the SSRA should be assessed based on the Nyquist Sampling Theorem, and from Equation (5.43) established in the work of Moaveni and Masoumi (Moaveni; Masoumi, 2019). The sampling frequency f_s states the minimum and maximum frequency limits to attend the system characteristics. Using ω_{n_i} from the continuous-time system indicated in Table 6.2, where $\omega_{dmax} = 69.5344$ rad/s ($\zeta_i = 0.0175$), the sampling frequency limits takes the following values, straightly attained from

Equation (5.43): $\omega_{s_{min}} = 139.069$ rad/s and $\omega_{s_{max}} = 873.795$ rad/s, determining the sampling time range of $d_t = [0.0072 \ 0.0452]$ s. Hence, only the simulated sampling time of 0.02 s should be used in system identification with SSRA for the M5DOF system proposed in this work, corroborating with what is realized from Figure 6.10 to Figure 6.12.

6.4 Analysis for white-noise excitation and measurement noise in the M5DOF

For comparative purposes, the simulations were extended to incorporate two different scenarios under the conditions of the system excited by Gaussian White-Noise (GWN) signal and with the introduction of measurement noise to the outputs. The results from these scenarios were tested with the same algorithm settings employed in the simulations accomplished in Section 6.2, where the system was excited by PRBS. The GWN signals employed as excitation in the simulations were set with unit-variance. Also, the zero-mean typical characteristic was shifted to have only positive values, i.e., to be a biased signal the same way as the PRBS excitation, for comparison purposes.

The time response results for some simulations using the GWN signal are presented in Table 6.3 with the same settings employed in Table 6.1. Considering the frequency response results, for these simulations, only the discrete-time $d_t = 0.02$ s was performed. The difference between the $\overline{\text{VFR}}$ values achieved when the system was excited by GWN compared to the values presented in Table 6.1, when the PRBS excitation was applied, can be considered small. A remark should be carried out for $n = 8$ when the GWN excitation lead to 1% more accurate Fit Rate index. It can be realized that for both PRBS and GWN excitations the results of identification effectiveness were practically the same.

Table 6.3 – Comparison of Fit Rate index for PRBS and GWN excitations

$q^{(1)}$	p	n	$\overline{\text{VFR}}$ for PRBS	$\overline{\text{VFR}}$ for GWN	Gap ⁽²⁾
2500	500	13	92.31%	93.23%	0.92%
5000	500	13	97.05%	96.17%	-0.88%
5000	1000	13	99.11%	99.36%	0.25%
10000	1000	13	99.89%	99.84%	-0.05%
10000	2000	13	100.00%	100.00%	0.00%
10000	2000	10	100.00%	100.00%	0.00%
10000	2000	8	97.80%	98.80%	1.00%

¹ Sampling time: $d_t = 0.02$ s

² Difference between $\overline{\text{VFR}}$ achieved with GWN and PRBS excitations

Simulations with 1% of additive measurement noise were also performed to ver-

ify the choice of the algorithm settings under the situation of measurement noise. For this approach, both PRBS and GWN were used to provide a comparative analysis. The measurement noise is composed of a typical signal as defined in Section 5.3 with $S_N = 1\%$. For this condition of measurement noise introduced in the simulated system, the GWN signal was kept with unit-variance. The same data sets of the excitation signals U and U_V , used at simulations without noise (Table 6.3), were applied to allow an analysis of the specific influence of additive measurement noise in the results.

The $\overline{\text{VFR}}$ values attained for each excitation following the same sequence of parameters configurations of Table 6.1 and Table 6.3 are presented in Table 6.4. Firstly, for both excitations, the results confirm that the algorithm settings, accomplished step by step, follow the learning sequence that provides better $\overline{\text{VFR}}$ to the identified system. For the PRBS excitation, the best $\overline{\text{VFR}}$ of 98.09% is achieved with $q = 5000$ and $p = 1000$, and for the GWN excitation when $q = 10000$ and $p = 1000$ a smaller $\overline{\text{VFR}}$ of 97.93% is obtained. Increasing p to 2000 for this GWN case, the $\overline{\text{VFR}}$ takes a slightly lower value of 97.88%, and the system order n of 10 or 13 leads to the same $\overline{\text{VFR}}$ results. When $n = 8$ is tried, it should be highlighted the relevant decrease of FR, which ratifies the benefit of this procedure as a complementary tool to indicate the system order, even in a situation with measurement noise.

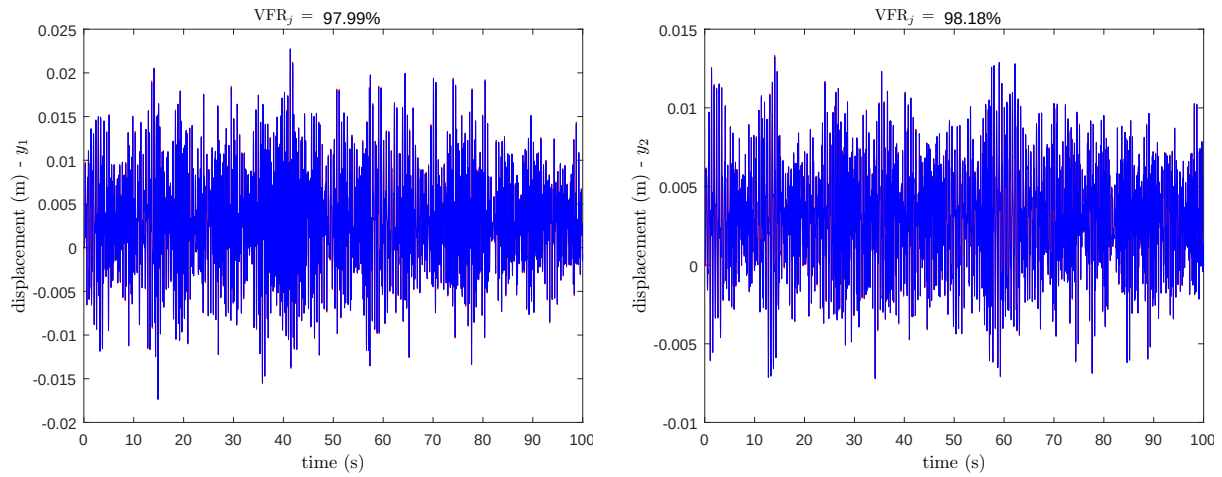
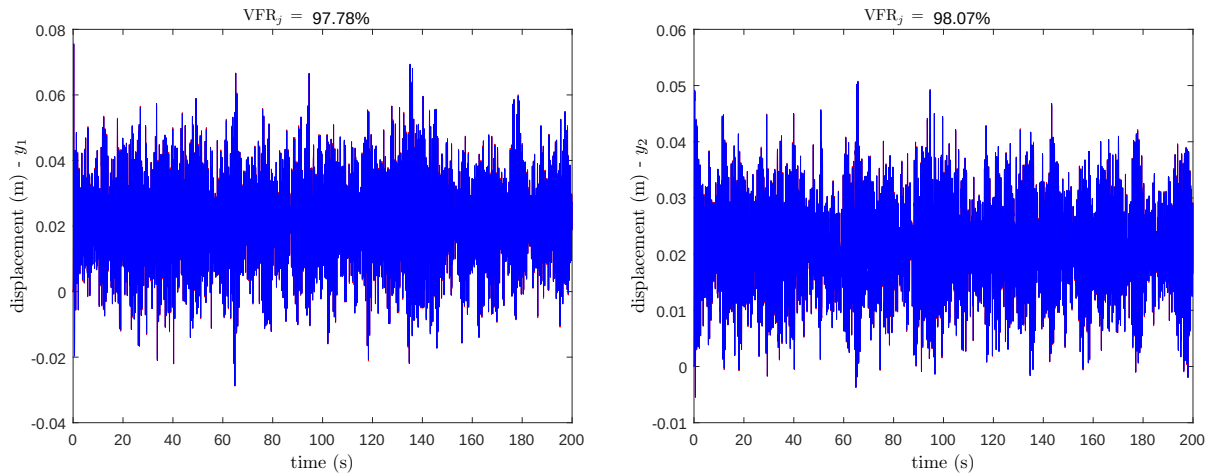
Comparing the influence of the excitation in the results from Table 6.4, for the best $\overline{\text{VFR}}$ achieved to each excitation, the difference of 0.16% can be considered small. For $n = 8$, a more significant $\overline{\text{VFR}}$ decrease for PRBS excitation evidence that this system order assigned is not the best choice. The PRBS excitation led to the best identified system with 5000 samples, and the GWN required a higher number of samples. Hence, the smaller data size along the algorithm processing can be considered another advantage for the PRBS excitation in this case.

The graphs related to the outputs from the best results for the PRBS excitation (Figure 6.13) and GWN excitation (Figure 6.14) have their mean shifted positively due to the amplitudes of both excitations being positive either. Moreover, in the case of the data set coming from measurement devices of an actual plant that inherently carries nonlinear characteristics, attention should be considered related to biased excitations.

The assessments supported by the Fit Rate index to evaluate the algorithm settings choice allow generating a comprehensive guide in the task of SSRA parameters configuration, contributing to making more accessible the searching of the appropriate settings.

Table 6.4 – Time response results with 1% of measurement noise added into the system

$q^{(1)}$	p	n	$\overline{\text{VFR}}$ for PRBS	$\overline{\text{VFR}}$ for GWN	Gap ⁽²⁾
2500	500	13	91.48%	90.79%	-0.69%
5000	500	13	95.78%	94.71%	-1.07%
5000	1000	13	98.09%	97.79%	-0.30%
5000	1000	10	98.09%	97.79%	-0.30%
5000	1000	8	97.08%	97.40%	0.32%
10000	1000	13	98.01%	97.93%	-0.08%
10000	1000	10	98.01%	97.93%	-0.08%
10000	1000	8	96.78%	97.37%	0.59%
10000	2000	13	98.01%	97.88%	-0.13%
10000	2000	10	98.00%	97.88%	-0.12%
10000	2000	8	96.78%	97.37%	0.59%

¹ Sampling time: $d_t = 0.02$ s² Difference between $\overline{\text{VFR}}$ achieved with GWN and PRBS excitationsFigure 6.13 – Original (red) and identified (blue) systems: $d_t = 0.02$ s, $q = 5000$, $p = 1000$, $n = 10$, PRBS excitation, and 1% of additive measurement noise.Figure 6.14 – Original (red) and identified (blue) systems: $d_t = 0.02$ s, $q = 10000$, $p = 1000$, $n = 10$, GWN excitation, and 1% of additive measurement noise.

6.5 SSRA performance comparison for the 3 excitation signals in the M100DOF

The current topic was developed using the State-Space Realization Algorithm introduced in Section 4.2.2 for each type of excitation described in Section 5.2, considering some systems and simulation conditions defined in Chapter 5. Two hundred simulations were performed for each set of excitation signal types and two measurement noise levels. Each of the three excitation signals was configured to yield a range of values with zero-mean, i.e., typically unbiased excitations, contrary to the simulations performed in the previous section when the M5DOF system was excited by biased signals. Then, six sets of simulations were performed to construct boxplot graphs that grant statistical analysis of the results.

The simulation results shown in this section were accomplished by setting $q = 9000$ as the number of samplings for the system with one hundred degrees of freedom (M100DOF), with the sampling time $d_t = 0.03$ s. The reason for establishing this sampling time will be reported in Section 7.2 when some simulation characteristics of the M100DOF system are presented. The variable in charge of setting the Hankel matrix size was adjusted with $p = 900$. The simulations were fulfilled adding two levels of measurement noise discriminated in the results: 1% and 3%. Each result presented at the set of 200 simulations for the same type of excitation signal and measurement noise level had different input data set and also distinct additive noise signals, but in both cases keeping the same statistical characteristics between the signals.

From Figure 6.15 to Figure 6.17, the boxplot graphs for simulations with 1% of measurement noise are shown. From Figure 6.18 to Figure 6.20, the graphs refer to 3% of measurement noise. A graph displaying the full positive range of VFR_j and its outliers is presented, on the left, for each simulation set. The picture on the right side employs zoom to allow a detailed view of the boxes, whiskers, and the values dispersion. The maximum and median values of VFR_j bear the numerical statistical analysis for each simulation set with the three excitations (Table 6.6).

A more significant number of outliers in the PRBS excitation signal is evident than the other two excitation signals. Although, the CHIRP signals confer higher variability than the PRBS, which is even more dispersed than GWN excitation. The CHIRP signal presents several outliers but more concentrated close to the boxes. The number of outliers for the GWN excitation is lower, mainly for 1% of measurement noise condition, where a small dispersion of the values is portrayed in the graph. This perspective led to the correspondent GWN graph with the zoom at boxes (Figure 6.17 on the right) practically having the same graph view that shows

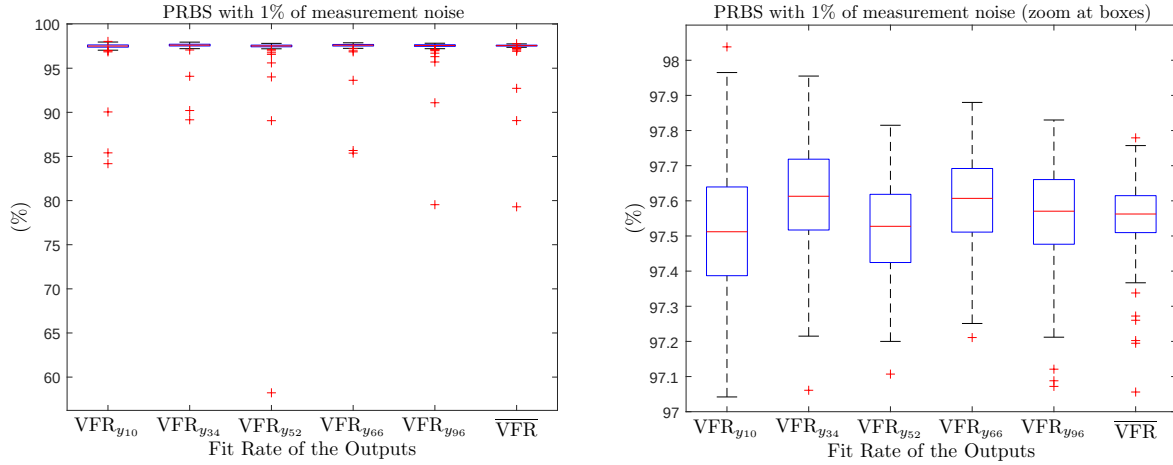


Figure 6.15 – Boxplot of 200 simulations of M100DOF system, PRBS excitation:
 $d_t = 0.03$ s, $q = 9000$, $S_N = 1\%$.

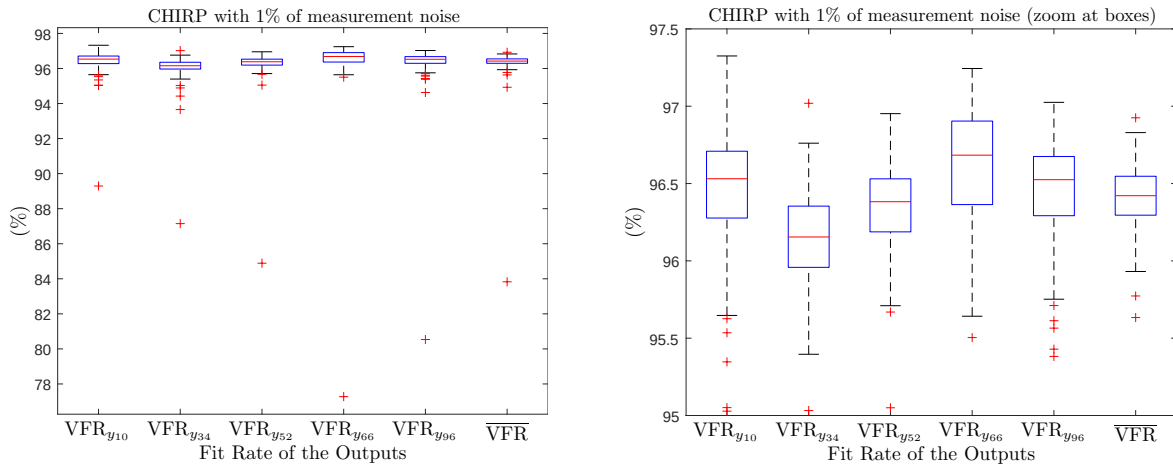


Figure 6.16 – Boxplot of 200 simulations of M100DOF system, CHIRP excitation:
 $d_t = 0.03$ s, $q = 9000$, $S_N = 1\%$.

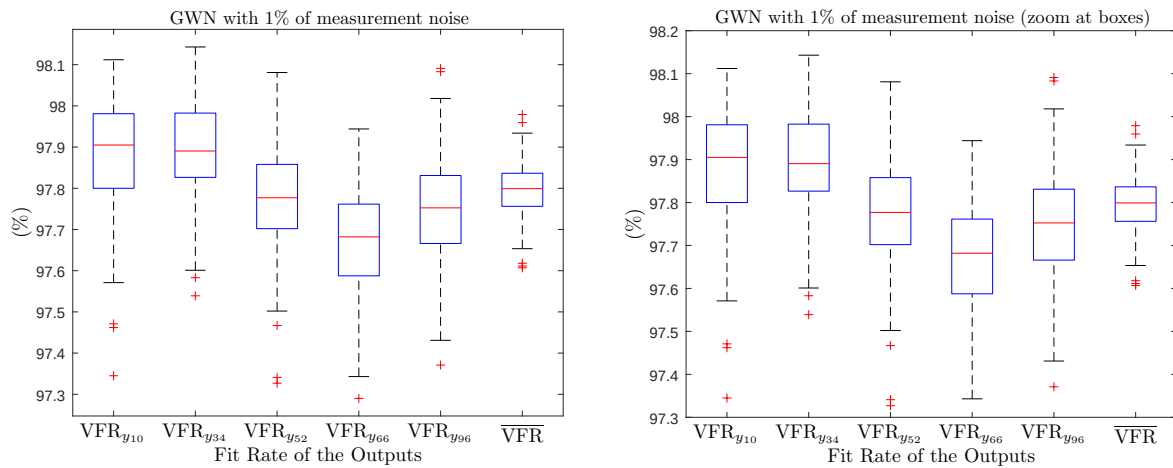


Figure 6.17 – Boxplot of 200 simulations of M100DOF system, GWN excitation:
 $d_t = 0.03$ s, $q = 9000$, $S_N = 1\%$.

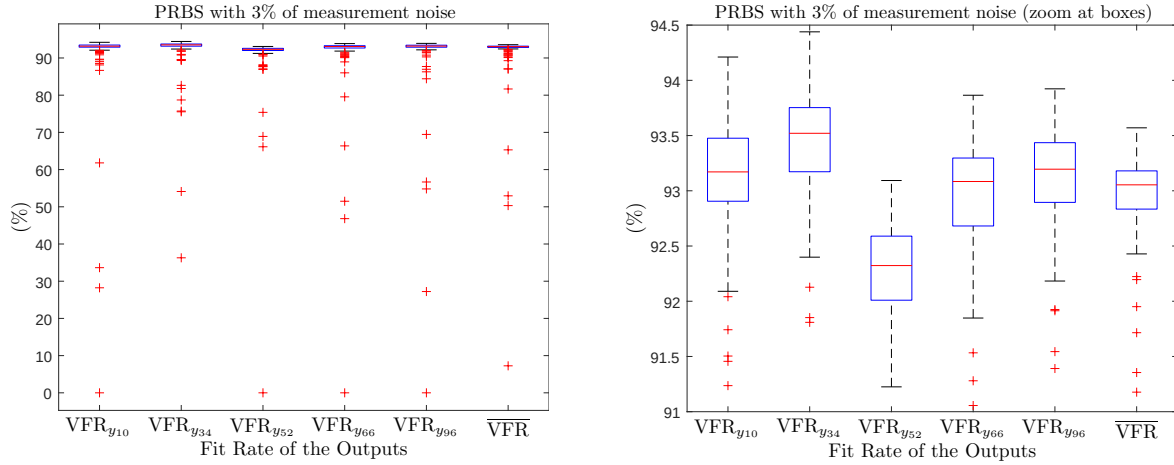


Figure 6.18 – Boxplot of 200 simulations of M100DOF system, PRBS excitation:
 $d_t = 0.03$ s, $q = 9000$, $S_N = 3\%$.

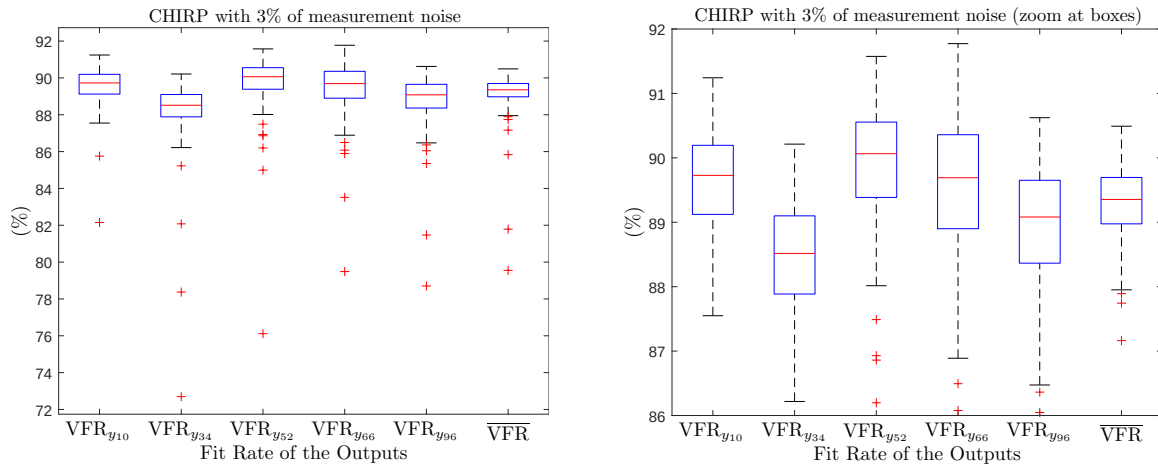


Figure 6.19 – Boxplot of 200 simulations of M100DOF system, CHIRP excitation:
 $d_t = 0.03$ s, $q = 9000$, $S_N = 3\%$.

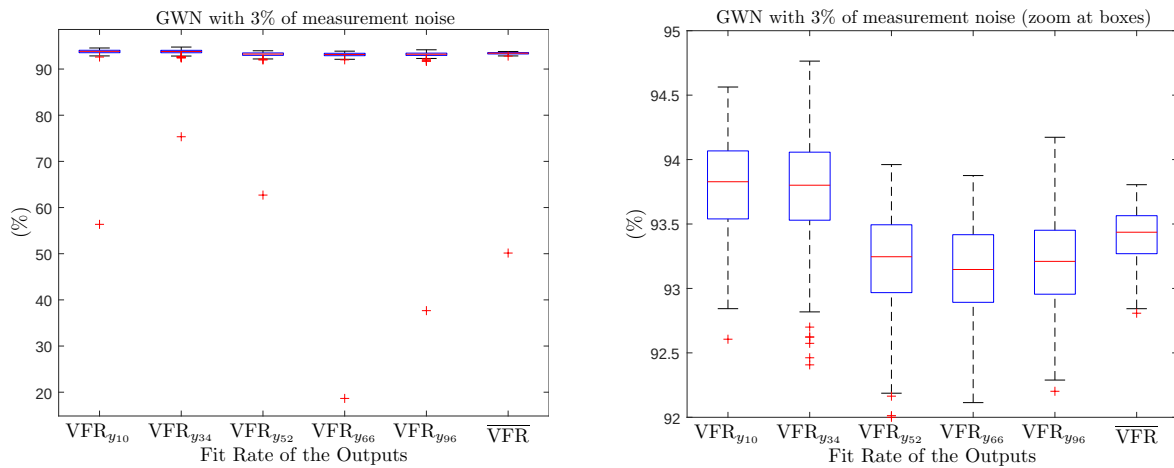


Figure 6.20 – Boxplot of 200 simulations of M100DOF system, GWN excitation:
 $d_t = 0.03$ s, $q = 9000$, $S_N = 3\%$.

all outliers (Figure 6.17 on the left).

It should be mentioned that the results presented for the CHIRP signal occurred with a f_{max} adjusted from 3 to 10 times the sampling frequency $f_s = 1/d_t$. When the CHIRP signal was adjusted with a f_{max} up to 5 times the f_s value, the number of unstable identified systems (loss of convergence, which will be better discussed in Section 7.5) achieved levels of 10% of the simulations performed. The frequency band increment of the CHIRP excitation signal was beneficially applied in this case and at many works as in the paper of Nevaranta et al. (Nevaranta et al., 2016). The maximum frequencies f_{max} employed for the inputs excited by CHIRP are presented in Table 6.5 for the simulations in which the maximum value of $\overline{\text{VFR}}$ was achieved. The minimum frequency was set with a constant value of $f_{min} = 1.26$ rad/s for all input excitations.

Table 6.5 – Maximum Frequency (f_{max}) of the simulated CHIRP signals.

S_N	Inputs set ($u_{18}, u_{36}, u_{49}, u_{67}, u_{89}$)	CHIRP f_{max} (in rad/s)
1%	U	2079, 2085, 1862, 1573, 1266
	U_V	2003, 1783, 1877, 1370, 1367
3%	U	733, 2083, 1682, 631, 1558
	U_V	1474, 1145, 1765, 1451, 1999

The VFR_j medians state a better response of the GWN, which is considerably close to the PRBS values. Both GWN and PRBS results are considerably better than CHIRP results. The results for maximum VFR_j values follow the behavior of median VFR_j results.

The increase of measurement noise from 1% to 3%, besides causing an expected more significant effect with a higher decrease of VFR_j , also led to amplifying the data dispersion and the discrepancies between the performance of excitation signals in the system identification effectiveness.

This section analysed three types of excitation signals commonly employed in different system identification approaches with the focus on state-space identification algorithm based on the traditional ERA. Considering the suitability of using this algorithm for structural identification, the Gaussian White-Noise (GWN) can be considered the most appropriate signal in this scenario of engineering application. However, the VFR_j values for the PRBS signal are considerably close to the GWN values, making the PRBS signal a feasible excitation alternative in this case.

Table 6.6 – Comparative results of the excitation signals for the M100DOF system with: $d_t = 0.03$ s, $q = 9000$, and $p = 900$.

S_N	Output	Statistical group	PRBS	CHIRP	GWN
1%	y_{10}	Maximum VFR _j	98.04%	97.33%	98.11%
		Median VFR _j	97.51%	96.54%	97.91%
	y_{34}	Maximum VFR _j	97.96%	97.02%	98.14%
		Median VFR _j	97.61%	96.16%	97.89%
	y_{52}	Maximum VFR _j	97.82%	96.95%	98.08%
		Median VFR _j	97.53%	96.38%	97.78%
	y_{66}	Maximum VFR _j	97.88%	97.24%	97.94%
		Median VFR _j	97.61%	96.69%	97.68%
	y_{96}	Maximum VFR _j	97.83%	97.03%	98.09%
		Median VFR _j	97.57%	96.53%	97.75%
	$\overline{\text{VFR}}$	Maximum VFR _j	97.78%	96.93%	97.98%
		Median VFR _j	97.56%	96.42%	97.80%
3%	y_{10}	Maximum VFR _j	94.21%	91.24%	94.56%
		Median VFR _j	93.17%	89.73%	93.83%
	y_{34}	Maximum VFR _j	94.44%	90.21%	94.76%
		Median VFR _j	93.52%	88.52%	93.80%
	y_{52}	Maximum VFR _j	93.09%	91.58%	93.96%
		Median VFR _j	92.32%	90.06%	93.25%
	y_{66}	Maximum VFR _j	93.87%	91.77%	93.88%
		Median VFR _j	93.08%	89.69%	93.15%
	y_{96}	Maximum VFR _j	93.92%	90.62%	94.17%
		Median VFR _j	93.20%	89.08%	93.21%
	$\overline{\text{VFR}}$	Maximum VFR _j	93.57%	90.49%	93.81%
		Median VFR _j	93.05%	89.35%	93.44%

The CHIRP signals are widely applied to excite structures using devices as an eccentric mass vibrator or linear actuator, whereas a transient force is typically produced by snap-back test or hammer test, this one better for exciting high-frequency modes (Ghee Koh *et al.*, 1995). The PRBS signal can be found applied by piezoelectric actuators in beams at several references (Choi; Kim, 1996; Butcher *et al.*, 2016). However, the present work opens a further analysis regarding the applicability of the PRBS signal as excitation to large MIMO systems once the signal showed up competitive for systems identification in the results of the simulated cases.

7 RESULTS AND DISCUSSION OF THE SSRA-DC-ICL METHOD

7.1 Introduction⁵

This chapter presents the results and the assessment of the developed algorithm SSRA-DC-iCL, excited by GWN signals as characterized and described in Section 5.2. The method was first applied to the mass-spring-damper models of 50 and 100 degrees of freedom introduced in Section 5.4. In the last section of this chapter, the algorithm was submitted to simulations of the nonlinear Cart-Pendulum system presented in Section 5.5. For the mass-spring-damper systems covered throughout the chapter, firstly, it is described the systems and algorithm characteristics related to the undertaken simulations. Next, establishing the reduced number of samples as a requirement and at the same time as a reason for the method utilization, this issue is approached through simulations of some SSRA-DC settings. Simulation results of the SSRA-DC-iCL algorithm are presented to highlight the method performance. A comparative statistical analysis between the SSRA-DC and SSRA-DC-iCL is provided based on 100 simulations for each algorithm settings and conditions tested. Following, the algorithm simulation results are shown for the M50DOF-a (Figure 5.8 at Section 5.4), reconfigured to have accelerometers located at the same masses where the excitation forces were applied. Also, a brief section is created through statistical analysis to show the relation of noise influence on the results. The following two sections of this chapter underscore the validation and frequency response analysis results by comparing the identified systems attained in the previous simulations performed.

7.2 Specific settings and system configurations for the SSRA-DC-iCL simulations

The parameters configuration of the classical SSRA-DC should be appropriately adjusted to achieve better results of the Fit Rate (Equation (4.59)) in the SI process. The respective algorithm parameters selection are following described, where the related matrices and mathematical expressions were presented in Chapter 4:

- d_t : sampling time of the system in the simulation;
- q : number of samples;

⁵ Some parts presented in this chapter were published in the paper ([Soares Jr; Serpa, 2022](#)).

- p : determines the matrices sizes stem from generalized Hankel matrix;
- ξ : determines the number of block rows of the block correlation matrices;
- γ : determines the number of block columns of the block correlation matrices;
- n : state-space order of the realization (identified system order).

For the purposes of this work regarding simulations with M50DOF and M100DOF models, from now on, the parameter n will be fixed in 100 or 200, considering the orders of the M50DOF and M100DOF systems to be identified are already known. The task of achieving the most appropriated order of the identified system (McMillan degree) is supported by many methods as in the traditional ERA, when Juang and Pappa (Juang; Pappa, 1985; Juang; Pappa, 1986) proposed the Modal Amplitude Coherence and the Mode Singular Value. These methods distinguish the system from noise and use the number of retained singular values to determine the system realization order. Additional techniques were developed for system order determination, using the power spectral density of the variables as in the work of Moaveni et al. (Moaveni; Masoumi, 2019).

The choice of the system sampling time d_t shall regard the appropriate selection of the sampling frequency ω_s to attend the Nyquist Sampling Theorem, following Equation (5.42). It was considered the sampling time of $d_t = 0.02$ s ($\omega_s = 314.16$ rad/s for M50DOF) and $d_t = 0.03$ s ($\omega_s = 209.44$ rad/s for M100DOF), due to the natural frequencies being in the range of $[1.57 \ 97.52]$ rad/s for M50DOF and $[1.46 \ 97.52]$ rad/s for M100DOF, assuring that the sampling frequency ω_s exceeds the maximum frequency $\omega_{max} = 97.52$ rad/s in at least two times.

Since the present work is based on a simulated system, where ω_{n_i} and ζ_i are known, the sampling frequencies limits ($\omega_{s_{min}}, \omega_{s_{max}}$) and the sampling time limits ($d_{t_{min}}, d_{t_{max}}$) are computed accordingly by Equation (5.43), and the results are indicated in Table 7.1. It follows that sampling times of $d_t = 0.02$ s and $d_t = 0.03$ s, which are inside of limits presented in this table, can be considered satisfactory to be used in both M50DOF and M100DOF systems.

Table 7.1 – Limits of sampling frequency (ω_s) and sampling time (d_t) for the discretized systems

System	$\omega_{dmax}^{(1)}$	$\omega_{s_{min}}$	$\omega_{s_{max}}$	$d_{t_{min}}$	$d_{t_{max}}$
M50DOF	97.52 rad/s	195.04 rad/s	1225.47 rad/s	0.0051 s	0.0322 s
M100DOF	97.52 rad/s	195.04 rad/s	1225.47 rad/s	0.0051 s	0.0322 s

¹ ω_{dmax} : maximum damping frequency of the continuous-time system, considering that ζ_i has a negligible value.

The Maximum Singular Values diagrams shown in Figure 7.1 confirm the choices of $d_t = 0.02$ s and $d_t = 0.03$ s, depicting that the systems after discretization and the continuous-time system coincide as the peaks of natural frequencies that nearly overlap each other. A possible choice for lower sampling time values to the limit of 5 milliseconds, even though attending the limits shown in Table 7.1, would provide better compatibility than the condition represented by Figure 7.1. However, it would grow the Markov and Hankel matrix sizes, thus increasing the computational processing time (CPT).

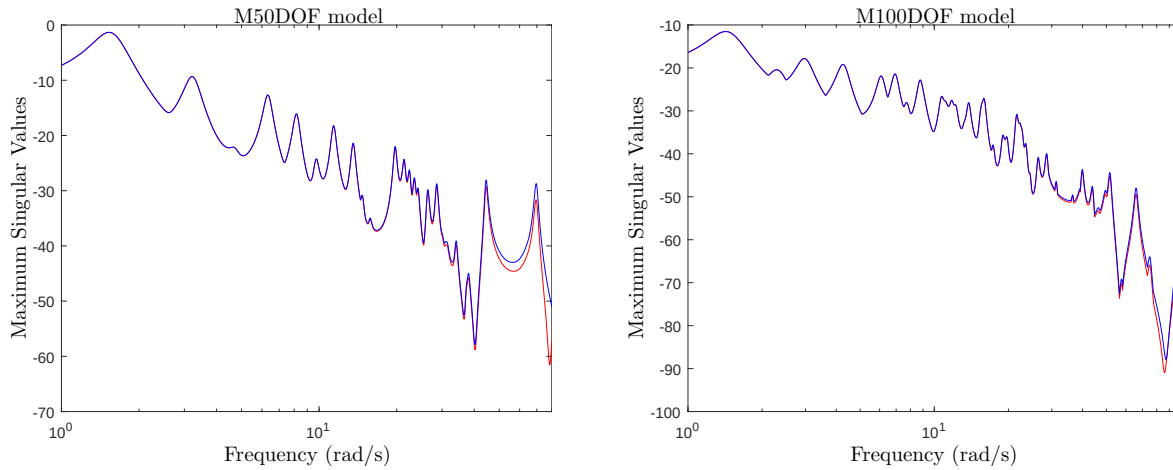


Figure 7.1 – Maximum Singular Values of continuous-time system (red) and discrete-time system (blue) for M50DOF (left) and M100DOF (right).

7.3 Analysis of the number of samples reduction in the SSRA-DC simulations

The objective of this section is to contextualize the issues and definitions presented in Section 4.4.1 that supported the choice of half the number of samples, where the total amount of samples would be sufficient to obtain full SI effectiveness in the SSRA-DC simulations.

For the M50DOF system, the State-Space Realization Algorithm with Data Correlation was submitted to simulations where the number of samples was decreased starting from $q = 3000$ for settings of the algorithm parameters that outcome an identified system with the Validated Fit Rate $\overline{\text{VFR}} = 99.89\%$ in a noiseless condition. This parameters configuration applied at 100 simulations statistically synthesized and portrayed in Figure 7.2 had measurement noise $S_N = 0.3\%$ and the parameter p starting from $p = 1200$ when $q = 3000$. The parameter p was adjusted for decreasing at the same ratio of q . The algorithm parameters related to data correlation were set with: $\xi = 2$ and $\gamma = 2$. The maximum $\overline{\text{VFR}}$ and median $\overline{\text{VFR}}$ were the statistical parameters applied over the 100 simulations performed for each algorithm settings.

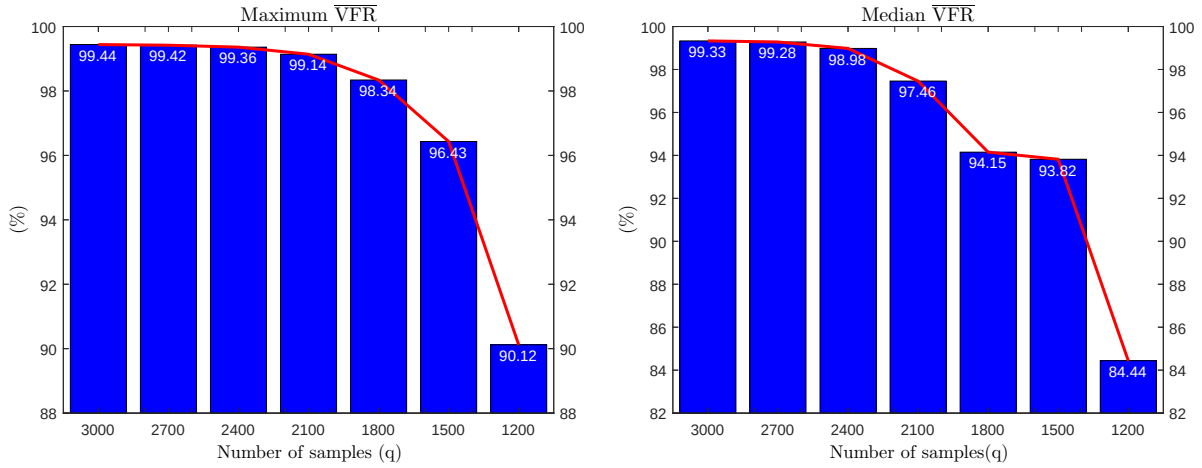


Figure 7.2 – Maximum and Median $\overline{\text{VFR}}$ throughout the reductions of q in the SSRA-DC simulations for M50DOF.

A small $\overline{\text{VFR}}$ drop for the firsts q reductions is shown in Figure 7.2. When $q = 1500$, achieving half of its initial value, the relevant decrement in the $\overline{\text{VFR}}$ result seems to be an appropriate choice, which is confirmed due to the significant drop that happened at the next reduction point with $q = 1200$. The median $\overline{\text{VFR}}$ bar graph follows the behaviour of the maximum $\overline{\text{VFR}}$ bar graph, in this case with even more significant drops, except from $q = 1800$ to $q = 1500$. This could lead one to choose $q = 1800$, but in this case, not following the premise of searching for lower data size and, hence, often contributing to a smaller computational processing time (CPT).

Related to the equivalent bar graphs for the M100DOF system (Figure 7.3), the number of samples starts with $q = 6000$ and $p = 1000$, attaining a Validated Fit Rate $\overline{\text{VFR}} = 99.95\%$ in a noiseless condition for this case. Other algorithm parameters were adjusted with the following values: $S_N = 0.3\%$, $\xi = 2$, and $\gamma = 1$. The maximum $\overline{\text{VFR}}$ graph shows an equivalent result as the graph from the M50DOF system. For the median $\overline{\text{VFR}}$ graph, however, the point $q = 2400$ was not displayed, because it got null value, ratifying that this number of samples would be too low and not suitable to the algorithm performance. Thus, from Figure 7.3, half number of samples is also appropriated to the M100DOF system complying with the condition defined in Section 4.4.1.

Concluding this topic, the number of samples $q = 1500$ and $q = 3000$ for the M50DOF and M100DOF systems, respectively, were accounted as proper to simulations objectives of making the comparison between the SSRA-DC and the SSRA-DC-iCL to present the SI improvement from the novel method, what will be approached in the following sections.

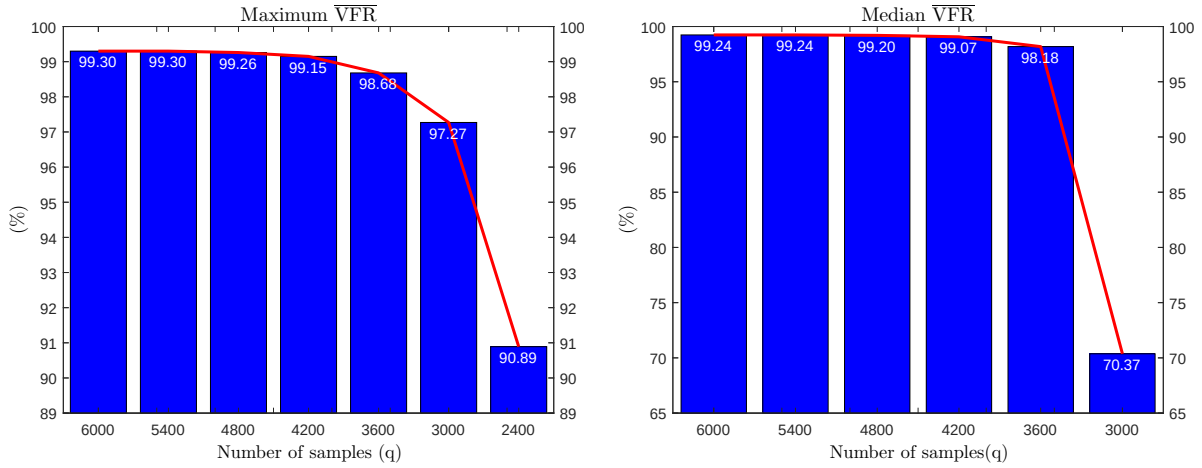


Figure 7.3 – Maximum and Median $\overline{\text{VFR}}$ throughout the reductions of q in the SSRA-DC simulations for M100DOF.

7.4 SSRA-DC-iCL algorithm performance

This section aims to report results for some settings of the method SSRA-DC-iCL that were introduced in Section 4.4. For this, the Algorithm 1 (section 4.4.4) was executed with a certain number of iterations. In a scenario of a statistical analysis (Section 7.5) based on several simulations performed, after undertaking the last simulation, the stored IS , for the simulation with the highest $\overline{\text{VFR}}$, has its evolution curve of $\overline{\text{FR}}$ plotted to show the algorithm performance for this attained identified system. Then, the $\overline{\text{FR}}$ evolution curve represents the identification results over the iterations, yielding the identified system with the highest Fit Rate $\overline{\text{FR}}$. Thus, the State-Space Realization of the identified system is stored for the highest point in the $\overline{\text{FR}}$ evolution curve, which represents the BFR value. Both BFR and $\overline{\text{VFR}}$ are displayed at the top of the referred graph.

The parameters for the algorithm settings established for the results in this section were presented in Section 7.2. Besides those parameters, the variable ℓ , related to the weighting factor of the gain K_{p_j} (Equation (4.68)), should be treated as a setting parameter for the SSRA-DC-iCL algorithm simulating M50DOF and M100DOF systems, considering that this type of gain was applied in that systems. Since ℓ was kept fixed with a 0.01 value throughout the M50DOF and M100DOF systems simulations, both K_{p_j} and ℓ will not be mentioned in the results referred. Despite the employment of a variable K_p gain defined through Equation (4.63) and Equation (4.68), the application of a fixed K_p gain was verified as viable, providing the same level of results performed by the variable K_p gain. This condition of a fixed K_p gain employed is fully shown in the simulations presented in the paper (Soares Jr; Serpa, 2022). In

this case, K_p becomes the gain parameter to be used, usually taking the same values that would be suitable for the parameter ℓ .

The results of two conditions employed in the simulations of the iterative algorithm for the M50DOF systems are illustrated by the graphs in Figure 7.4. The curves present the Fit Rate evolution ($\overline{\text{FR}}$) for the following parameters: $d_t = 0.02$ s, $q = 1500$, $p = 600$, $S_N = 0.3\%$ for the graph on the left at Figure 7.4, and $S_N = 1\%$ for the graph on the right. The Validated Fit Rate ($\overline{\text{VFR}}$) value, also displayed at the top of the graph, comes from the $\overline{\text{FR}}$ of the validation stage of identification. The curves regarding the evolution of $\overline{\text{FR}}$ reflect the improvement after some iterations, where the curves tend to go upward as iterations increase. The benefit of the algorithm feedback, updating the Markov parameters at each iteration, is witnessed by the $\overline{\text{FR}}$ increasing values.

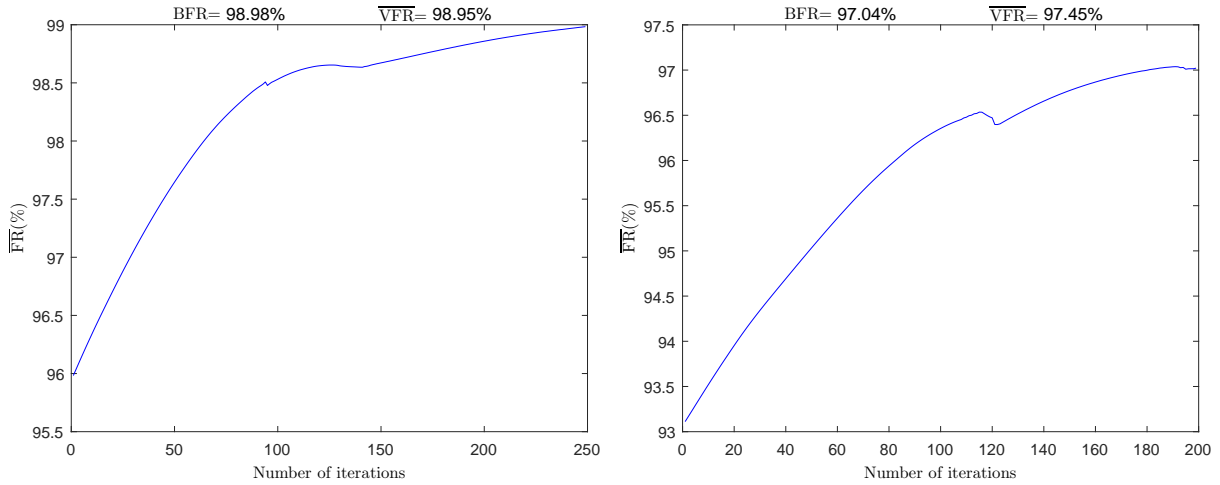


Figure 7.4 – $\overline{\text{FR}}(\%)$ evolution of SSRA-DC-iCL for M50DOF with $d_t = 0.02$ s, $q = 1500$, $p = 600$, and $S_N = 0.3\%$ (left), $S_N = 1\%$ (right).

The K_{p_j} gains applied to each output and the correspondent FR_j related to the same simulation that is depicted in Figure 7.4 (on the left) are presented in Figure 7.5. The graphs' objective is to show how the gain (Figure 7.5, on the left) behaves over the iterations in simulations with the results effectiveness as in Figure 7.5, on the right. In this condition, the gain rate increment leads to the increase of the FR_j . It can be observed that the opposite action also occurs, as expected by the iterative concept adopted in the algorithm SSRA-DC-iCL. It is remarked that the outputs y_{17} and y_{26} that take lower gains values provide a more smooth FR_j curve without any drops or oscillation points. Nevertheless, an unfavorable identification simulation for the same algorithm settings is presented in Figure 7.6, wherein, in this case, the BFR achieved was considerably worse. In this simulation, the K_{p_j} gains starting from about

100 iterations take a significant variability that triggers FR_j evolution curves that do not obey what would be a predicted result. Accordingly to the K_{p_j} definition (Equation (4.68)), considering that $\ell = 0.01$ in these algorithm settings, the mentioned K_{p_j} variabilities are due to the large discrepancy of the covariance of the Markov parameters residues (Φ_j) computed from each output.

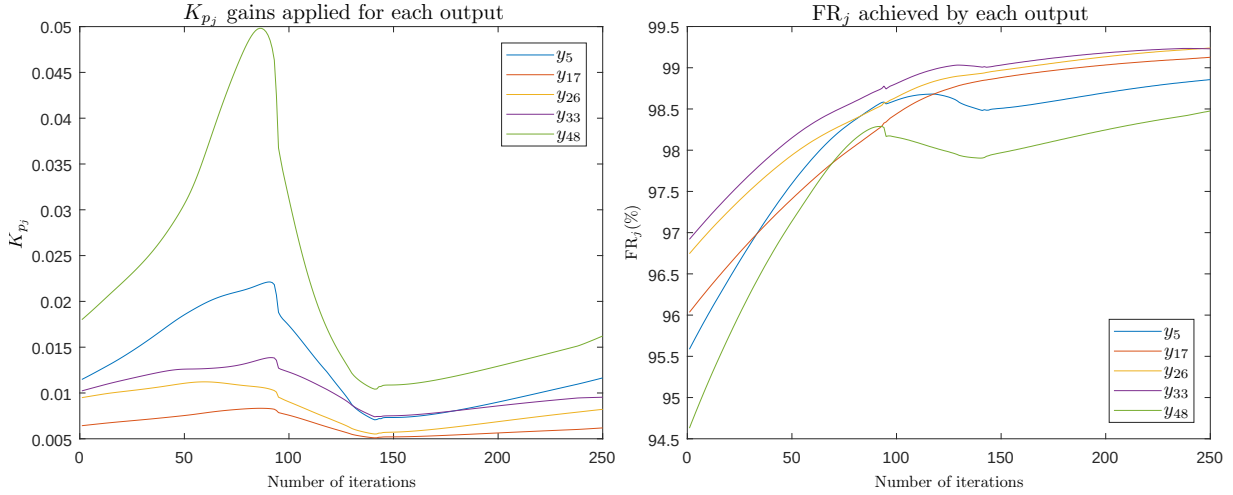


Figure 7.5 – K_{p_j} gain (left) and the FR_j (right) from SSRA-DC-iCL for M50DOF with $d_t = 0.02$ s, $q = 1500$, $p = 600$, and $S_N = 0.3\%$, in the simulation of BFR=98.98%.

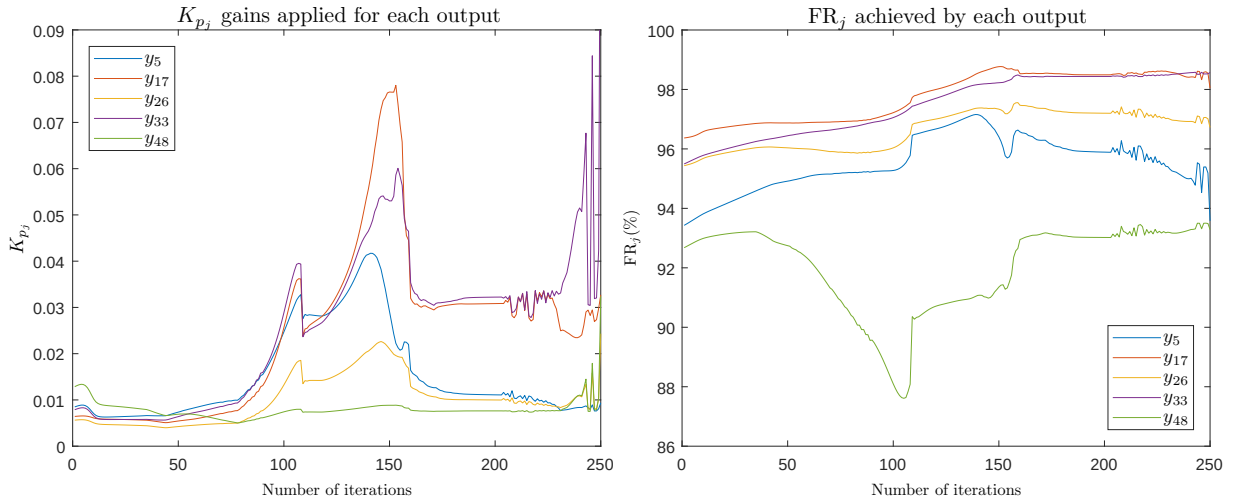


Figure 7.6 – K_{p_j} gain (left) and the FR_j (right) from SSRA-DC-iCL for M50DOF with $d_t = 0.02$ s, $q = 1500$, $p = 600$, and $S_N = 0.3\%$, in the simulation of BFR=96.81%.

The SSRA-DC-iCL algorithm results applied for the M100DOF system (Figure 7.7) counted on with the following main parameters in its configuration: $d_t = 0.03$ s, $q = 3000$, $p = 500$. The graph on the left shows the results for $S_N = 0.3\%$ and on the right for $S_N = 1\%$. Both curves confirm the Fit Rate improvement with only a few minor drops of \overline{FR} over the

iterations. For this simulation with $S_N = 1\%$, 100 iterations would be sufficient to attain the same results, according to the graph on the right at Figure 7.7.

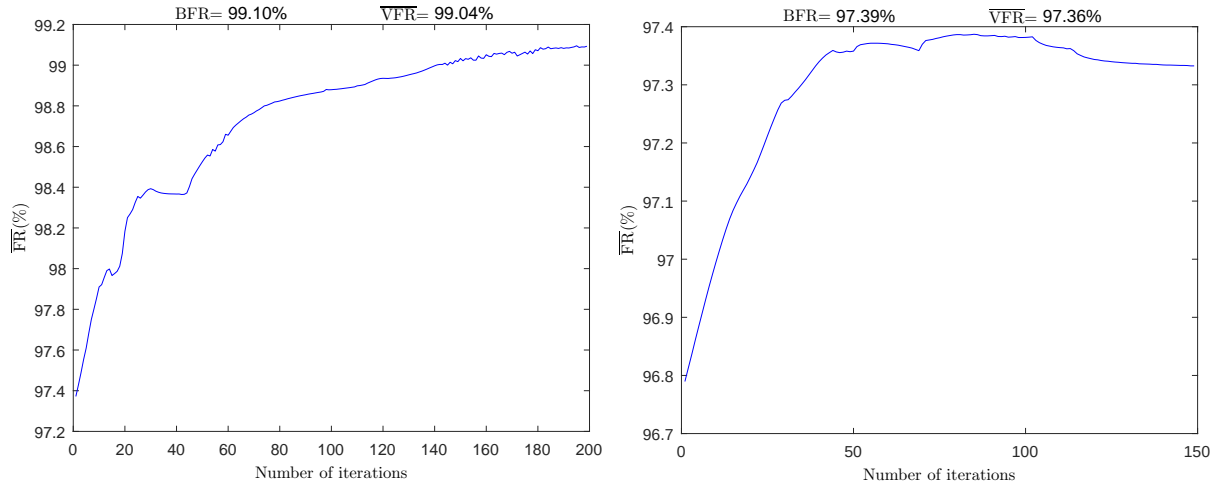


Figure 7.7 – $\overline{FR}(\%)$ evolution of SSRA-DC-iCL for M100DOF with $d_t = 0.03$ s, $q = 3000$, $p = 500$, and $S_N = 0.3\%$ (left), $S_N = 1\%$ (right).

7.5 Statistical analysis of the SSRA-DC and SSRA-DC-iCL methods

This section simulates the M50DOF and M100DOF systems with the same algorithm settings settled in the previous section for both SSRA-DC and SSRA-DC-iCL methods comparatively. One hundred simulations with distinct inputs data sets were applied to provide a statistical analysis of the results. The objective is to realize the variability of the overall results and verify the maximum VFR_j and \overline{VFR} values that really matter to the attainment of the identified system with better effectiveness all over the 100 simulations.

As introduced in sections 4.4.1 and 7.3, the experiments were set with half of the number of samples related to the condition when the conventional SSRA-DC achieves Fit Rate results close to 100%. Accordingly to what was presented in Section 7.3, when the number of samples is reduced in the identification algorithm, the identification performance worsens considerably. This degradation is verified not only with the decrease of the maximum FR_j . It is also confirmed by more variability of the overall results, mainly in some simulations when FR_j values drop unbounded, meaning loss of convergence. In this scenario, the proposed iterative SSRA-DC-iCL method is compared with the conventional SSRA-DC. A fundamental statistical assessment was carried out based on 100 simulation experiments executed for each algorithm configuration.

Besides the parameters settings, additive measurement noises of 0.3% and 1% were employed to analyze the simulation response of the SSRA-DC-iCL algorithm. For comparison, the SSRA-DC-iCL algorithm response for each level of noise was submitted to the same set of parameters that led the SSRA-DC algorithm to achieve the highest $\overline{\text{VFR}}$.

The numerical results are summarized in Table 7.2 and Table 7.3, where some fundamental statistical parameters are shown numerically to portray the boxplot graphs of the simulations. These statistical graphs reveal the $\overline{\text{VFR}}$ and VFR_j behavior throughout the simulated experiments, representing the following statistical groups presented in the tables: maximum value, median value, interquartile range, and the unstable *IS* (Identified System). Unstable *IS* at boxplot graphs means simulations where the values dropped unbounded, achieving negative values, but are represented as nulls in the graphs.

7.5.1 Simulations analysis of the M50DOF system

Boxplot graphs with and without outliers are presented in Figure 7.8 and Figure 7.9, respectively, for 100 simulations of the M50DOF system with $d_t = 0.02$ s, $q = 1500$, $p = 600$, $\xi = 2$, $\gamma = 2$, and $S_N = 1\%$. Comparing the left and right graphs in Figure 7.8, the view of the outliers and the variability stayed close, as can be seen with practically the same values of interquartile range, which are confirmed with numeric values presented in Table 7.2. On the other hand, the graphs without outliers in Figure 7.9 have the boxes and whiskers at a higher level for the graph of the iterative algorithm SSRA-DC-iCL, standing out the difference in median values attained.

The outliers with null values in Figure 7.8 mean that there were some simulations where the input data set led the identified system to be unstable, and hence the FR_j values had dropped unbounded. The statistical values maximum and median of VFR_j and $\overline{\text{VFR}}$ introduced in Table 7.2 confirm the improvement of the identified system with the application of the SSRA-DC-iCL.

The algorithm performance for each configuration of parameters determined a different number of iterations employed. Sometimes, a fixed number of iterations can use more computational processing time (CPT) because the BFR could already have been achieved with fewer iterations. Thus, in this case, an SFR adjusted with the same value of the BFR attained would lead the algorithm to require less CPT. On the other hand, when the iterations end and the $\overline{\text{FR}}$ curve continues to show a growth trend, probably, the simulation could attain a higher

Table 7.2 – SSRA-DC-iCL and SSRA-DC comparative results for M50DOF system:
 $d_t = 0.02$ s, $q = 1500$, $p = 600$, $\xi = 2$, $\gamma = 2$.

$i^{(1)}$	noise (S_N)	Statistical group	Algorithm	VFR _{y₅}	VFR _{y₁₇}	VFR _{y₂₆}	VFR _{y₃₃}	VFR _{y₄₈}	$\overline{\text{VFR}}$	$\Delta\overline{\text{VFR}}^{(2)}$
250	0.3%	Maximum	SSRA-DC	96.40%	97.24%	98.44%	97.01%	95.56%	96.43%	–
			SSRA-DC-iCL	98.94%	99.14%	99.25%	99.20%	98.46%	98.95%	2.52%
		Median	SSRA-DC	93.21%	95.29%	94.94%	94.50%	92.05%	93.82%	–
			SSRA-DC-iCL	95.45%	98.15%	97.53%	97.50%	94.94%	96.67%	2.85%
		Interquartile range	SSRA-DC	5.34%	3.79%	4.90%	4.39%	7.21%	4.80%	–
			SSRA-DC-iCL	6.11%	3.40%	4.39%	4.63%	5.64%	4.78%	0.02%
		Unstable $IS^{(3)}$	SSRA-DC	6%	6%	7%	7%	7%	6%	–
			SSRA-DC-iCL	6%	6%	6%	6%	6%	6%	0%
		Maximum	SSRA-DC	95.27%	97.06%	96.87%	96.63%	94.61%	95.87%	–
			SSRA-DC-iCL	97.36%	97.76%	97.82%	97.67%	96.88%	97.45%	1.58%
200	1%	Median	SSRA-DC	91.03%	93.63%	93.31%	92.84%	89.77%	91.79%	–
			SSRA-DC-iCL	94.02%	96.29%	95.85%	96.29%	92.73%	95.05%	3.26%
		Interquartile range	SSRA-DC	5.93%	3.56%	3.97%	4.26%	5.95%	4.44%	–
			SSRA-DC-iCL	5.82%	2.89%	3.80%	3.97%	6.18%	4.67%	-0.23%
		Unstable $IS^{(3)}$	SSRA-DC	3%	3%	3%	3%	3%	3%	–
			SSRA-DC-iCL	6%	6%	6%	6%	6%	6%	-3%

¹ i : number of iterations set-point for each one of 100 simulations;

² Improvement gain of SSRA-DC-iCL algorithm over SSRA-DC algorithm for the $\overline{\text{VFR}}$;

³ Percentual of unstable IS (Identified System) over the 100 simulations when $\text{VFR}_j = 0$ or $\overline{\text{VFR}} = 0$.

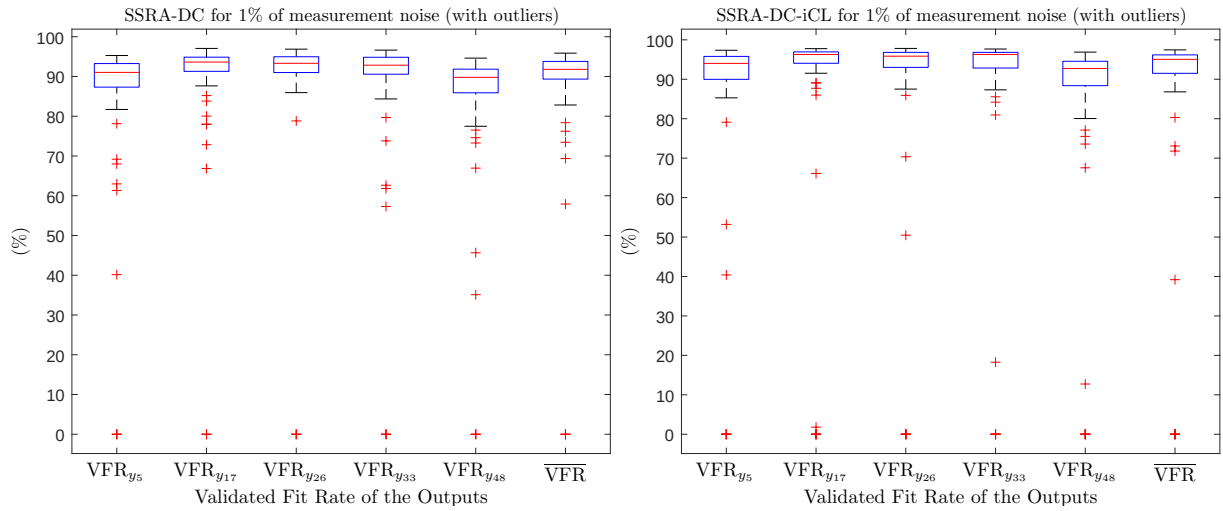


Figure 7.8 – Boxplot with outliers of 100 simulations at the M50DOF system applying SSRA-DC (left) and SSRA-DC-iCL (right) algorithms.

Parameters: $d_t = 0.02$ s, $q = 1500$, $p = 600$, $\xi = 2$, $\gamma = 2$, and $S_N = 1\%$.

BFR with the iterations, which occurred in the simulation depicted in the graph on the left in Figure 7.4.

Besides the number of simulations and iterations applied, the K_p gain adjustment could be analyzed regarding its influence on algorithm performance. When previously adjusted, this gain can be a practical choice to achieve a higher Best Fit Rate (BFR) with fewer iterations. For instance, in a simulation test, when the weighting factor ℓ of the K_p gain (Equation (4.68)) was increased from 0.01 to 0.02 and the number of iterations reduced from 200 to 100 in the same configuration of Table 7.2 for $S_N = 1\%$, then the maximum Validated Fit Rate $\overline{\text{VFR}}$

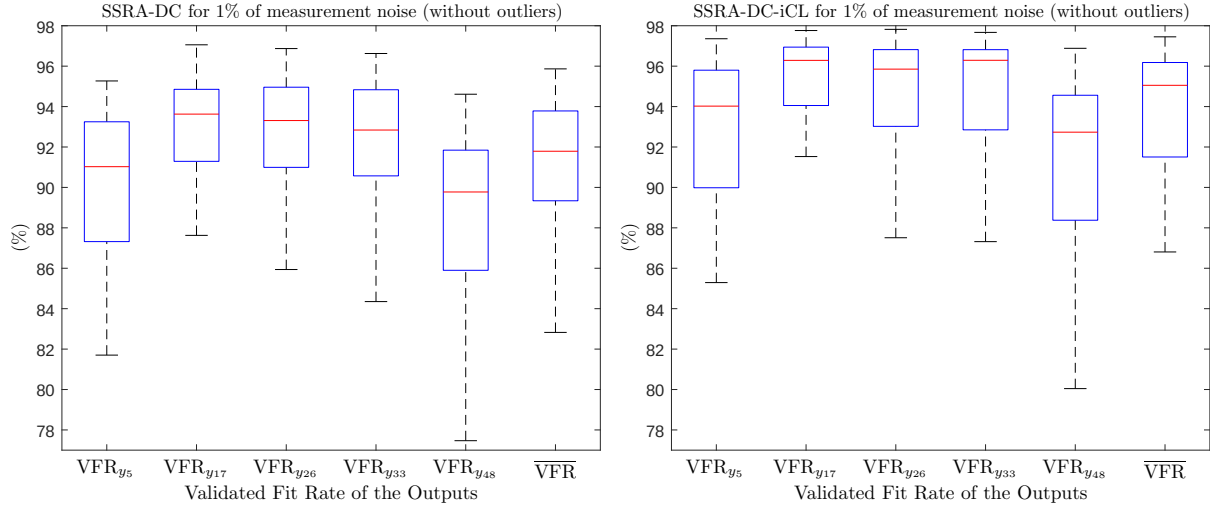


Figure 7.9 – Boxplot without outliers of 100 simulations at the M50DOF system applying SSRA-DC (left) and SSRA-DC-iCL (right) algorithms.

Parameters: $d_t = 0.02$ s, $q = 1500$, $p = 600$, $\xi = 2$, $\gamma = 2$, and $S_N = 1\%$.

increased from 97.45% to 98.02%.

7.5.2 Simulations analysis of the M100DOF system

Boxplot graphs with and without outliers are presented in Figure 7.10 and Figure 7.11, respectively, for 100 simulations of the M100DOF system with $d_t = 0.03$ s, $q = 3000$, $p = 500$, $\xi = 2$, $\gamma = 0$, and $S_N = 1\%$. It can be verified a significant reduction of results variability with the employment of SSRA-DC-iCL algorithm through the graphs on Figure 7.10. In contrast, the graphs on Figure 7.11 aims to highlight the improvement of the maximum and median VFR_j and \overline{VFR} values.

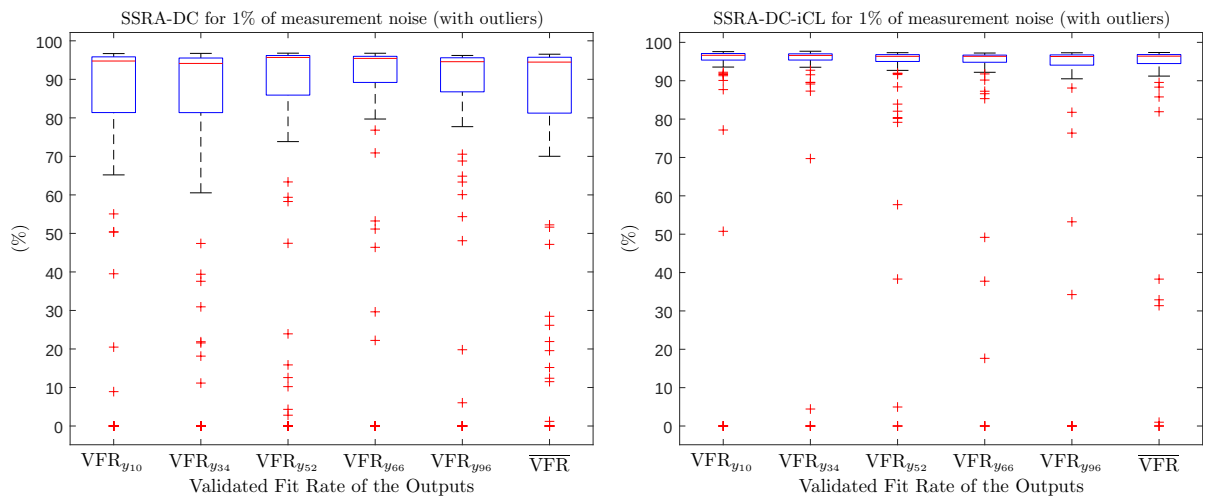


Figure 7.10 – Boxplot with outliers of 100 simulations at the M100DOF system applying SSRA-DC (left) and SSRA-DC-iCL (right) algorithms.

Parameters: $d_t = 0.03$ s, $q = 3000$, $p = 500$, $\xi = 2$, $\gamma = 0$, and $S_N = 1\%$.

Table 7.3 – SSRA-DC-iCL and SSRA-DC comparative results for M100DOF system:
 $d_t = 0.03$ s, $q = 3000$, $p = 500$, $\xi = 2$.

γ	$i^{(1)}$	noise (S_N)	Statistical group	Algorithm	VFR _{y₁₀}	VFR _{y₃₄}	VFR _{y₅₂}	VFR _{y₆₆}	VFR _{y₉₆}	$\overline{\text{VFR}}$	$\Delta\overline{\text{VFR}}^{(2)}$
1	200	0.3%	Maximum	SSRA-DC	97.65%	97.34%	97.86%	97.88%	97.09%	97.27%	1.77%
				SSRA-DC-iCL	99.19%	99.12%	99.03%	99.01%	98.96%	99.04%	
			Median	SSRA-DC	70.25%	64.66%	75.95%	72.76%	69.22%	70.37%	23.41%
				SSRA-DC-iCL	94.13%	92.80%	95.90%	95.47%	94.30%	93.78%	
			Interquartile range	SSRA-DC	95.62%	95.28%	96.64%	96.08%	95.21%	95.81%	-2.30%
				SSRA-DC-iCL	97.96%	97.82%	98.50%	98.49%	98.33%	98.11%	
			Unstable $IS^{(3)}$	SSRA-DC	43%	44%	42%	43%	46%	39%	3%
				SSRA-DC-iCL	39%	40%	39%	37%	37%	36%	
			Maximum	SSRA-DC	96.69%	96.74%	96.80%	96.78%	96.20%	96.52%	0.84%
				SSRA-DC-iCL	97.59%	97.69%	97.32%	97.22%	97.29%	97.36%	
0	150	1%	Maximum	SSRA-DC	94.76%	94.13%	95.68%	95.44%	94.58%	94.48%	1.93%
				SSRA-DC-iCL	96.63%	96.59%	96.36%	96.36%	96.32%	96.41%	
			Median	SSRA-DC	14.46%	14.17%	10.28%	6.78%	8.84%	14.51%	12.17%
				SSRA-DC-iCL	1.71%	1.62%	1.78%	1.86%	2.67%	2.34%	
			Interquartile range	SSRA-DC	14%	13%	10%	11%	12%	8%	5%
				SSRA-DC-iCL	6%	5%	3%	4%	5%	3%	
			Unstable $IS^{(3)}$	SSRA-DC	14%	13%	10%	11%	12%	8%	5%
				SSRA-DC-iCL	6%	5%	3%	4%	5%	3%	

¹ i : number of iterations set-point for each one of 100 simulations;

² Improvement gain of SSRA-DC-iCL algorithm over SSRA-DC algorithm for the $\overline{\text{VFR}}$;

³ Percentual of unstable IS (Identified System) over the 100 simulations when $\text{VFR}_j = 0$ or $\overline{\text{VFR}} = 0$.

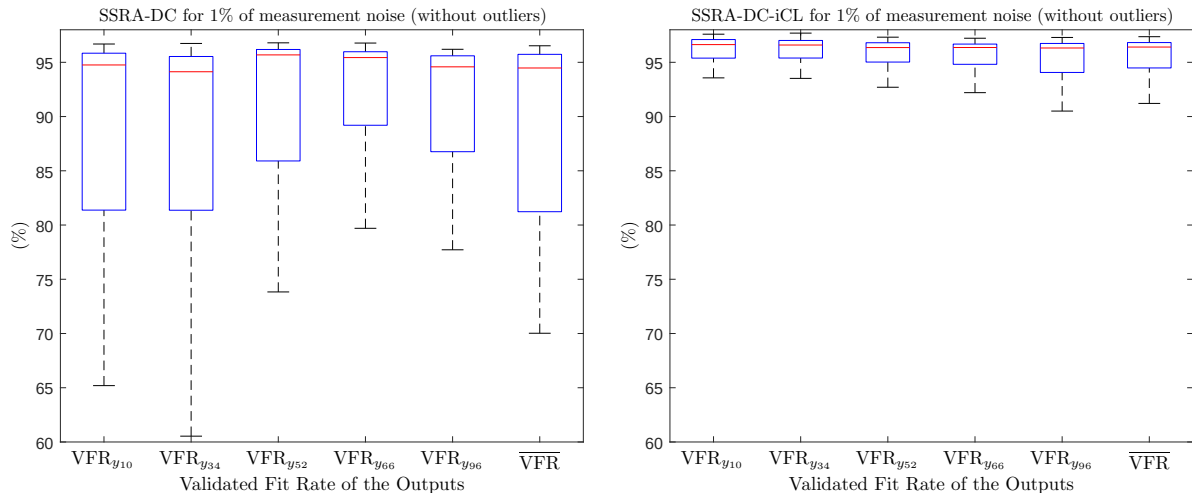


Figure 7.11 – Boxplot without outliers of 100 simulations at the M100DOF system applying SSRA-DC (left) and SSRA-DC-iCL (right) algorithms.

Parameters: $d_t = 0.03$ s, $q = 3000$, $p = 500$, $\xi = 2$, $\gamma = 0$, and $S_N = 1\%$.

In addition to the simulation results of the configuration presented in the boxplot graphs of Figure 7.10 and Figure 7.11, numerical results for 0.3% of measurement noise are shown in Table 7.3. This result attests to the improvement carried out by the SSRA-DC-iCL algorithm despite the meaningful increase of the interquartile range compared to the other simulations of the SSRA-DC-iCL. The high values of the interquartile range for $S_N = 0.3\%$ in Table 7.3 mean the large variability was distributed all over the VFR_j and $\overline{\text{VFR}}$ range (0 to 100%), which is reflected in the considerable amount of 39% and 36% of unstable IS achieved for SSRA-DC and SSRA-DC-iCL, respectively.

A considerable number of cases with convergence loss in both algorithms come from the conditions of systems with a reduced number of samples in conjunction with the system working at some level of measurement noise. The same configuration shown in Table 7.3, but for 1% of measurement noise, had 8% and 3% of the simulations attaining value zero in the $\overline{\text{VFR}}$ of SSRA-DC and SSRA-DC-iCL, respectively. For the intrinsic algorithm condition of working with a reduced number of samples, when the measurement noise level reduced from 1% to 0.3%, it substantially increased unstable identified systems. On the other hand, SSRA-DC simulations have shown that by maintaining 0.3% of noise but increasing samples from 3000 to 4200, the null values in $\overline{\text{VFR}}$ were reduced from 39% to only 2%. In fact, when the system presented a convergence loss, as previously mentioned, the attained identified system was unstable for that input data set.

The gain reduction of the maximum statistical parameter when the measurement noise goes from 0.3% to 1% is evident in Table 7.3, indicating that the SSRA-DC-iCL effectiveness worsens as the noise level increase. A substantial median value improvement verified in Table 7.3, mainly for $S_N = 0.3\%$, ratifies the results enhancement for this configuration. The significant increment of the median for all the simulated cases can be considered a relevant benefit assigned to the iterative SSRA-DC-iCL method.

7.5.3 Simulations analysis of the M50DOF-a system (with accelerometers)

As mentioned in Section 5.4, the objective of utilizing acceleration measurement is to verify the SSRA-DC-iCL performance when the matrix \mathbf{D} of the state-space system realization is not null. The simulation results presented for the M50DOF-a system considered some of the same configurations used before for the M50DOF system shown in Table 7.2. Despite some of the main algorithm settings used are the same ($d_t = 0.02$ s, $q = 1500$, $p = 600$), the input excitation signals and noise signals generated for simulations are distinct.

The M50DOF and M50DOF-a systems have a distinct type of output measurement, which leads the iterative identification process not to have the same way of acting throughout the simulations. Besides that, the output measurement devices were positioned at different bodies in the mechanical system. Then, the parameters $\xi = 1$ and $\gamma = 1$, related to the data correlation configuration, and the weighting factor ℓ from the K_{p_j} statement (Equation (4.68)) had different adjustment values for working with the M50DOF-a system. The significant difference required and employed to ensure the SSRA-DC-iCL effectiveness was the large reduction

of the value ℓ to tackle the different dynamical responses from accelerometers in contrast to displacement sensors. The parameter ℓ , that was kept with 0.01 for systems with displacement sensors, had to be reduced 20 times to $\ell = 0.0005$ in the systems with accelerometers. Even though several simulation tests with many different settings have been performed, unlike simulations previously presented for M50DOF and M100DOF systems, the employment of a fixed K_p value in M50DOF-a did not work as expected in benefiting the method SSRA-DC-iCL upon the conventional SSRA-DC.

The numerical values regarding comparative results between the SSRA-DC and SSRA-DC-iCL (Table 7.4) objectify attesting the effectiveness of the SSRA-DC-iCL method when the accelerometers are the measurement sensors applied. For the M50DOF-a system simulated, it should be pointed out that a lower improvement gain was achieved for 0.3% of measurement noise compared to the M50DOF system (Table 7.2), but attaining a higher $\overline{\text{VFR}}$ value. On the other hand, for 1% of measurement noise, a more significant improvement gap took place, although with a lower $\overline{\text{VFR}}$ value achieved.

Table 7.4 – SSRA-DC-iCL and SSRA-DC comparative results for M50DOF-a system:

$$d_t = 0.02 \text{ s}, q = 1500, p = 600, \xi = 1, \gamma = 1, \ell = 0.0005.$$

$i^{(1)}$	noise (S_N)	Statistical group	Algorithm	VFR_{y_5}	$\text{VFR}_{y_{18}}$	$\text{VFR}_{y_{26}}$	$\text{VFR}_{y_{36}}$	$\text{VFR}_{y_{48}}$	$\overline{\text{VFR}}$	$\Delta\overline{\text{VFR}}^{(2)}$
300	0.3%	Maximum	SSRA-DC	97.31%	99.33%	98.50%	99.37%	96.23%	98.00%	–
			SSRA-DC-iCL	99.17%	99.37%	99.06%	99.37%	99.06%	99.12%	1.12%
		Median	SSRA-DC	95.88%	99.16%	97.73%	99.21%	94.87%	97.36%	–
			SSRA-DC-iCL	97.98%	99.22%	98.71%	99.21%	98.25%	98.66%	1.30%
		Interquartile range	SSRA-DC	0.74%	0.14%	0.46%	0.15%	1.07%	0.38%	–
			SSRA-DC-iCL	1.10%	0.21%	0.50%	0.24%	1.83%	0.65%	-0.27%
		Unstable $IS^{(3)}$	SSRA-DC	0%	0%	0%	0%	0%	0%	–
			SSRA-DC-iCL	0%	0%	0%	0%	0%	0%	0%
		Maximum	SSRA-DC	93.48%	97.81%	96.32%	97.89%	90.48%	94.64%	–
			SSRA-DC-iCL	96.32%	98.00%	97.32%	97.94%	96.73%	96.94%	2.30%
250	1%	Median	SSRA-DC	89.56%	97.19%	94.65%	96.98%	81.77%	91.90%	–
			SSRA-DC-iCL	93.64%	97.39%	96.17%	97.41%	93.07%	95.45%	3.55%
		Interquartile range	SSRA-DC	3.79%	1.17%	1.53%	1.88%	5.01%	2.33%	–
			SSRA-DC-iCL	2.79%	0.54%	1.29%	0.75%	3.64%	1.93%	0.40%
		Unstable $IS^{(3)}$	SSRA-DC	1%	0%	0%	0%	0%	0%	–
			SSRA-DC-iCL	1%	0%	0%	0%	3%	0%	0%

¹ i : number of iterations set-point for each one of 100 simulations;

² Improvement gain of SSRA-DC-iCL algorithm over SSRA-DC algorithm for the $\overline{\text{VFR}}$;

³ Percentual of unstable IS (Identified System) over the 100 simulations when $\text{VFR}_j = 0$ or $\overline{\text{VFR}} = 0$.

The Fit Rate evolution ($\overline{\text{FR}}$) is pictured in Figure 7.12 for the following parameters: $d_t = 0.02 \text{ s}$, $q = 1500$, $p = 600$, $S_N = 0.3\%$ for the graph on the left and $S_N = 1\%$ for the graph on the right. These graphs portray the evolution of iterations of the identified system that attained BFR, which $\overline{\text{VFR}}$ results are displayed in Table 7.4. Comparing the profile of the curves from both graphs with the correspondent one in Figure 7.4, which represents the M50DOF system with displacement sensors, the curves from the system containing accelerometers reflect

less smoothness and more variability in several segments, mainly for the graph with $S_N = 1\%$.

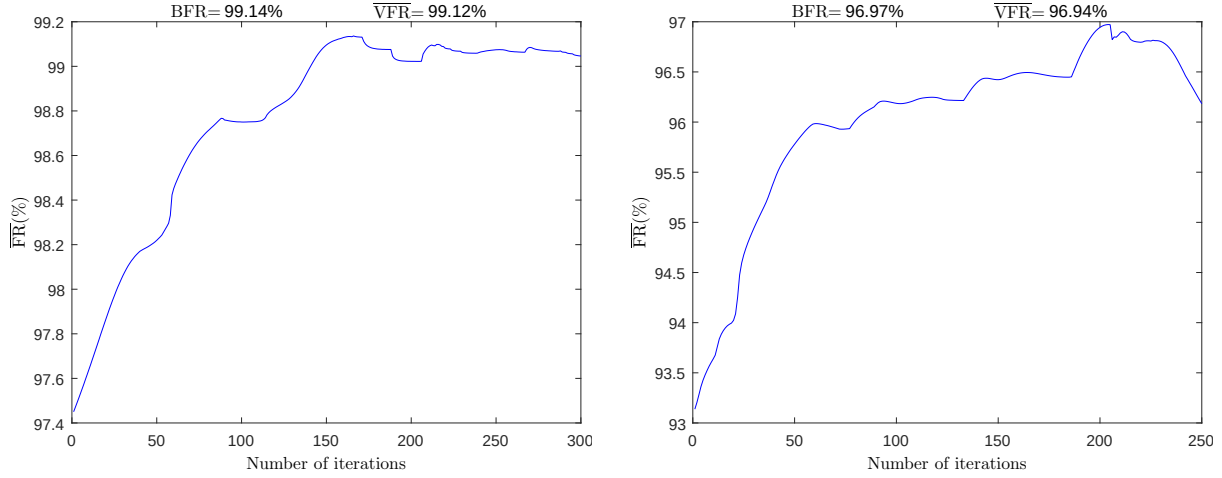


Figure 7.12 – $\overline{\text{FR}}(\%)$ evolution of SSRA-DC-iCL for M50DOF-a with $d_t = 0.02$ s, $q = 1500$, $p = 600$, and $S_N = 0.3\%$ (left), $S_N = 1\%$ (right).

Boxplot graphs for the simulations with 1% of measurement noise are shown in Figure 7.13 and Figure 7.14, graphically portraying the numerical results displayed at Table 7.4. Figure 7.13 is related to the graphs of SSRA-DC (left) and SSRA-DC-iCL (right), showing its outliers. And the graphs without outliers are depicted in Figure 7.14, which provide a better view of the respective gaps of improvement.

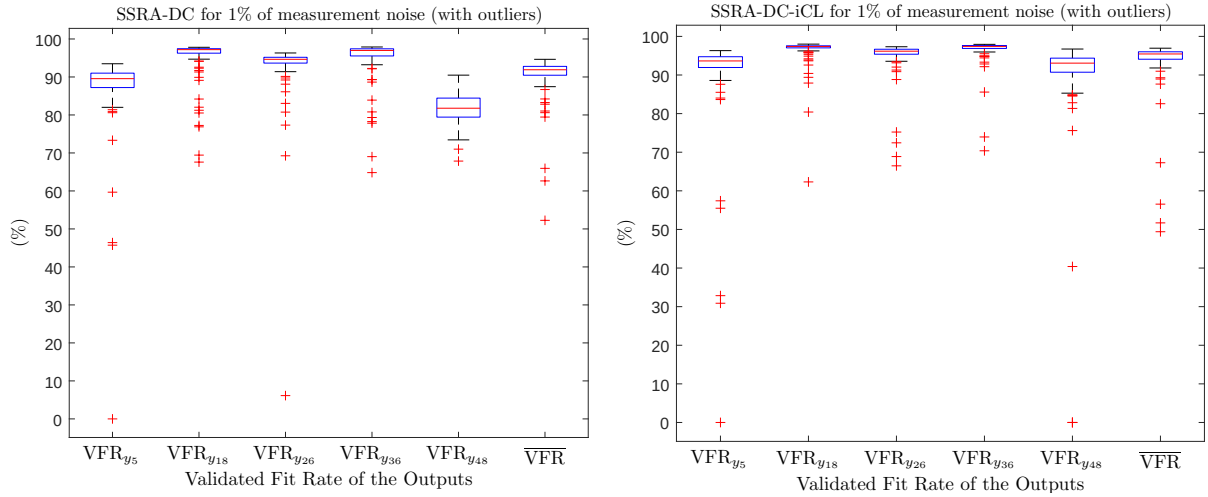


Figure 7.13 – Boxplot with outliers of 100 simulations at the M50DOF-a system applying SSRA-DC (left) and SSRA-DC-iCL (right) algorithms. Parameters: $d_t = 0.02$ s, $q = 1500$, $p = 600$, $\xi = 1$, $\gamma = 1$, $\ell = 0.0005$, and $S_N = 1\%$.

7.5.4 Influence of the noise levels on the results

Statistical analysis related to the influence of the noise level S_N in the result portrayed through the maximum $\overline{\text{VFR}}$ indicator is presented in Figure 7.15, supported by 100

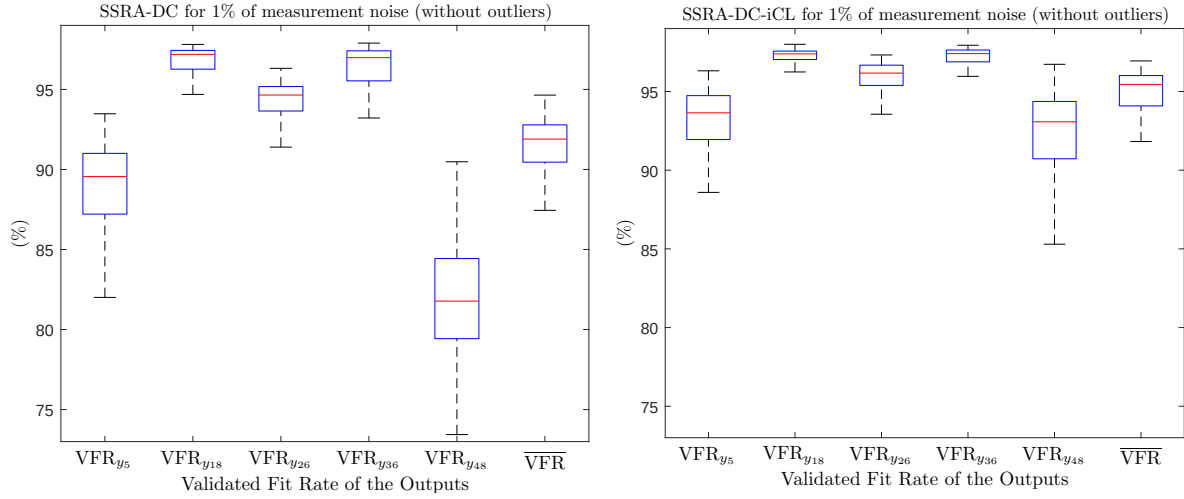


Figure 7.14 – Boxplot without outliers of 100 simulations at the M50DOF-a system applying SSRA-DC (left) and SSRA-DC-iCL (right) algorithms. Parameters: $d_t = 0.02$ s, $q = 1500$, $p = 600$, $\xi = 1$, $\gamma = 1$, $\ell = 0.0005$, and $S_N = 1\%$.

simulations for each one with a specific input data set. In this case, objectifying to have at least five points to depict the trend curves of the graphs, besides 0.3% and 1% of noise (S_N), three more values of noise S_N were included for simulations: 0.6%, 1.5%, and 2% for M50DOF and M100DOF systems. The graphs show straight line relations for both systems, depicting an overlapping between the tendency trace of the actual points and the theoretical linear curve. Each correspondent polynomial equation is displayed jointly to the respective theoretical curve. The variable e_r in the graphs means the absolute value of the difference between actual and theoretical values of $\overline{\text{VFR}}$. $\text{AVG}(e_r)$ and $\text{VAR}(e_r)$ represent the average and variance computing from e_r , respectively.

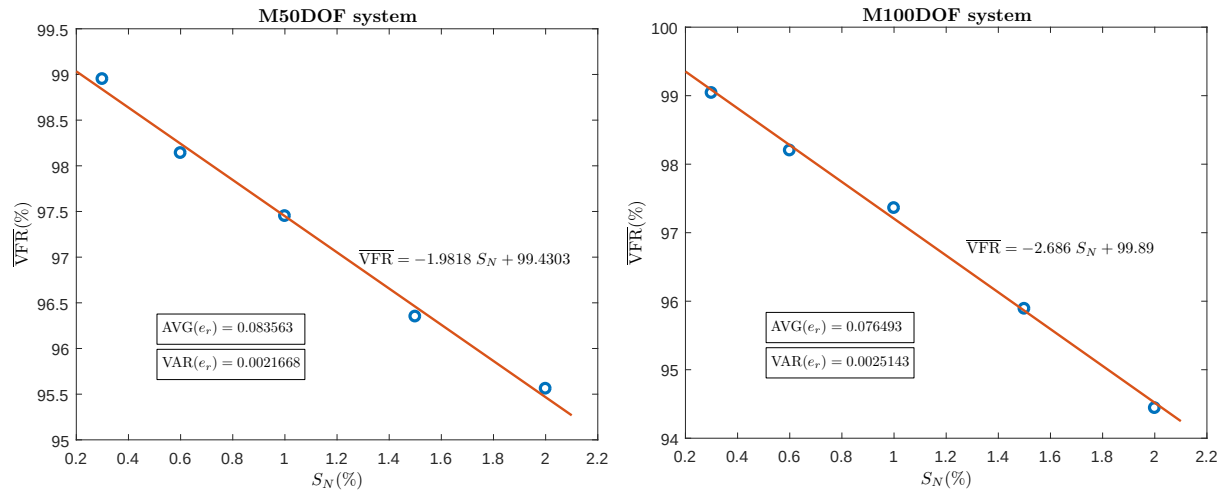


Figure 7.15 – Theoretical linear curves of the relation between added noise S_N and attained $\overline{\text{VFR}}$ for M50DOF and M100DOF

7.6 Validation aspects to ratify the results

This section analyzes how the fit rate results of the identification process, coming from several methods, are a reliable representation of the identified system's effectiveness for comparative purposes. For that, considering some of the identified systems obtained at the results previously presented, it will be applied a repetition of one thousand simulations of the validation stage, employing the same characteristics as the ones when the system was identified by the SSRA-DC or SSRA-DC-iCL algorithm. These characteristics include the number of samples q , the sampling time d_t , and the measurement noise level S_N . The procedure reported in Figure 5.11 generates an input-output data set. The data will be available to run the validation task repetitively, at the same number of times that the amount of data set was generated.

A statistical analysis of the simulations and also considering boxplot graphs was accomplished to synthesize the individual results. The boxplot graphs from the results presented in Table 7.5, regarding the comparison of two identified systems achieved in the simulations stated in Section 7.5.2, are presented in Figure 7.16. These identified systems were chosen based on different levels of $\overline{\text{VFR}}$ achieved, aiming to analyze the variability of 1000 validation tasks performed under these conditions.

Table 7.5 – Validation of 1000 simulations for identified systems from the original M100DOF at $d_t = 0.03$ s and $q = 3000$.

$\overline{\text{VFR}}_{IS}^{(1)}$	Statistical group	$\text{VFR}_{y_{10}}$	$\text{VFR}_{y_{34}}$	$\text{VFR}_{y_{52}}$	$\text{VFR}_{y_{66}}$	$\text{VFR}_{y_{96}}$	$\overline{\text{VFR}}$
99.04%	Maximum	99.14%	99.07%	98.94%	98.99%	98.98%	98.99%
	Median	99.01%	98.91%	98.79%	98.84%	98.82%	98.87%
	Interquartile range	0.07%	0.08%	0.08%	0.07%	0.07%	0.04%
	Outliers ⁽²⁾	10%	6%	6%	10%	13%	5%
96.52%	Maximum	96.82%	96.85%	96.50%	96.44%	95.99%	96.22%
	Median	96.24%	96.24%	95.81%	95.97%	95.32%	95.91%
	Interquartile range	0.30%	0.29%	0.25%	0.23%	0.29%	0.16%
	Outliers ⁽²⁾	8%	9%	12%	12%	9%	6%

¹ $\overline{\text{VFR}}$ of the IS (Identified system) used to the validations tasks;

² Percentage of outliers over the 1000 simulations.

The difference between the two graphs is depicted in Figure 7.16. The boxplot graph on the right (lower fit rate values) had four times more dispersed values than the boxplot graph on the left (higher fit rate values), which is evident when comparing the interquartile range values 0.04% and 0.16% in Table 7.5. This situation is underscored by the gap between the maximum and minimum $\overline{\text{VFR}}$ that increased from 0.22% to 0.75% when the $\overline{\text{VFR}}$ of the identified system dropped from 99.04% to 96.52%. Thus, this analysis reveals that as the iden-

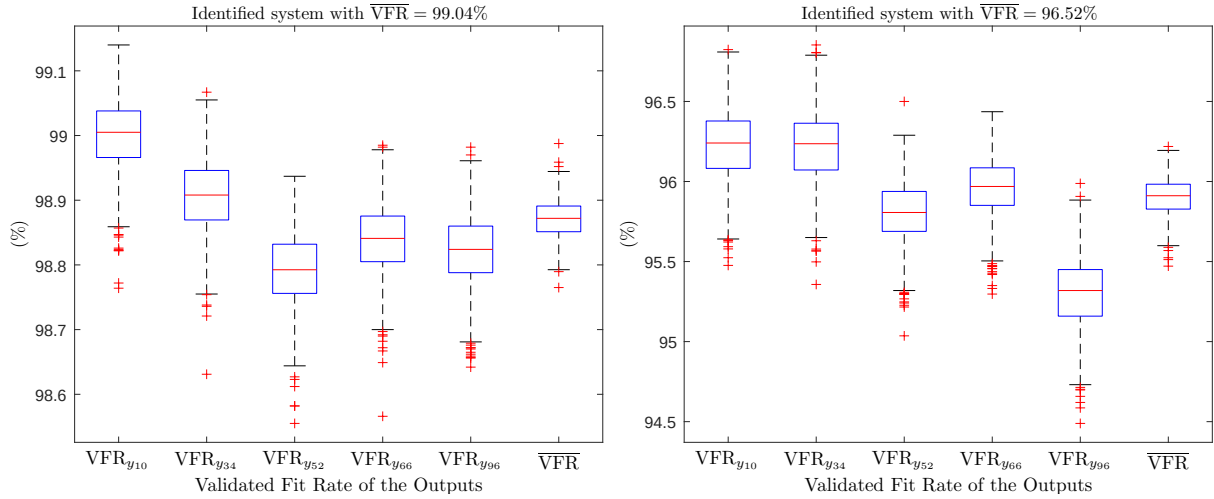


Figure 7.16 – Boxplot of 1000 simulations of validation at identified systems from the original M100DOF system. Parameters: $d_t = 0.03$ s, $q = 3000$, $S_N = 0.3\%$ (left), $S_N = 1\%$ (right).

tified system achieves higher $\overline{\text{VFR}}$ levels, the system becomes less susceptible to performance variability due to different input data sets. On the other hand, for lower values of $\overline{\text{VFR}}$ achieved, the correspondent identified system presents a broader range of fit rate values when submitted to several different input data sets.

7.7 Frequency response analysis to attest the previous results

The comparison of Maximum Singular Values (MSV) from the two identified systems used in the last section portrays in Figure 7.17 the effectiveness difference between these systems qualitatively.

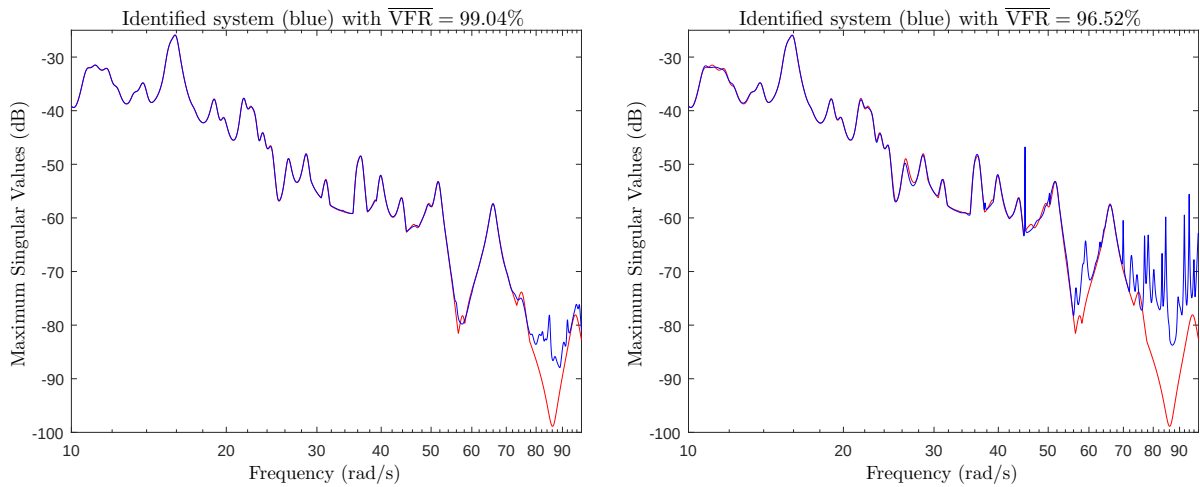


Figure 7.17 – MSV of original system (red) and identified system (blue) from M100DOF model with $\overline{\text{VFR}} = 99.04\%$ (left) and $\overline{\text{VFR}} = 96.52\%$ (right).

The objective of confronting the discrepancy between each identified system and the original M100DOF system is fulfilled visually through Figure 7.17. The graph on the left shows only a slight difference between the curves (original system and the identified system with $\overline{\text{VFR}} = 99.04\%$) starting at about 55 rad/s and increasing significantly for higher frequencies, greater than 75 rad/s, where the identified system curve (blue) can not keep up anymore the original system (red).

The graph on the right, related to the identified system with $\overline{\text{VFR}} = 96.52\%$, displays some slight discrepancy even at lower frequencies, starting at about 26 rad/s, with the difference increasing gradually and showing an excessive oscillation of the identified system curve for higher frequencies. The MSV graphs presented allow one to realize what represents the difference between the identified systems for the $\overline{\text{VFR}}$ levels here proposed.

7.8 Comparative statistical analysis with reference identification methods

This section aims to compare the traditional SSRA-DC and the novel method SSRA-DC-iCL with the SI methods presented in Chapter 3. Following the characteristics of the simulations undertaken in Section 7.2, the comparative analysis of this section was accomplished for both M50DOF and M100DOF systems applying 100 simulations for most of each algorithm settings, in the way to allow a fundamental statistical analysis supported by the maximum and median values attained from simulations. Besides the Validated Fit Rate index, the analysis counted on the computational processing time of the algorithm as another comparative parameter.

The fulfilled simulations employed Gaussian White-Noise (GWN) as the excitation signal and added 0.3% or 1% of measurement noise. For the N4SID method, due to the algorithm expending considerable more time on the simulations, in this case, ten simulations were executed for the M50DOF system and only one simulation for the M100DOF system, which will be presented ahead at numerical results in the respective tables.

The results considered the computational processing time in seconds of each set of the algorithms' simulations and the Validated Fit Rate ($\overline{\text{VFR}}$) index obtained. The simulations were accomplished in the same computational system and software, with the employment of Matlab's SI Toolbox methods, as described in Chapter 3. Despite using the Matlab SI Toolbox methods, the toolbox software environment was not used for comparison purposes. The methods presented in Chapter 3 were applied through the command of its respective Matlab's

function in the same basic script code of SSRA-DC and SSRA-DC-iCL, which encompass the calculation of $\overline{\text{VFR}}$ and the parts to measure the processing time. It should be pointed out that the function "COMPARE" from Matlab returned the exact value of $\overline{\text{VFR}}$ performed in the script code used.

The characteristics of the computational system where the algorithms were simulated are:

- Processor: Intel(R) Core(TM) i7-10510U CPU @ 1.80GHz (8 CPUs), ~ 2.3GHz;
- Memory: 16384MB RAM.
- Matlab version: R2018b

From the methods presented in Chapter 3, it should be mentioned that the FIR method is a particular arrangement from the OE method. Since the FIR presented results significantly worse than the OE, its simulations will not be shown in this comparative approach. OE, ARMAX, and BJ are methods that work estimating the identified system iteratively using the Prediction Error Minimization (PEM) method or just called the Prediction-error method. An equal number of iterations i used in the SSRA-DC-iCL method was set to those iterative autoregressive algorithms as a reference for providing a more fair comparison of $\overline{\text{VFR}}$ and CPT indicators.

The ARX is a non-iterative model that uses the least-squares method to estimate linear systems. ARX can be a choice to the starting polynomial model since it has a straightforward estimate structure. The N4SID is also a non-iterative algorithm composed through a subspace state-space concept described in Section 3.6, which leads to an even more complex algorithm and hence slower in the SI process. The N4SID, as a non-iterative method, allows the choice of one of the following weighting scheme used for singular value decomposition: MOESP, CVA, and SSARX. These options can be configured, or one can lead the N4SID estimating function in Matlab to automatically choose the better method like was set in this work.

The four polynomials ($\mathcal{B}(z)$, $\mathcal{F}(z)$, $\mathcal{C}(z)$, $\mathcal{D}(z)$) orders and the equivalent state-space system order of the Box and Jenkins (BJ) algorithm were configured to provide the same order applied at the SSRA-DC and SSRA-DC-iCL. That is, a system matrix \mathbf{A} of size (100×100) for M50DOF system or with size (200×200) for M100DOF system. As there are several combinations of order values to the polynomials $\mathcal{B}(z)$ and $\mathcal{F}(z)$ to provide the same order of the matrix \mathbf{A} , the configuration applied was the one that yielded the best numerical result presented for

each setting. When appropriate, the polynomials $\mathcal{C}(z)$ and $\mathcal{D}(z)$ were set with the order value equal to 1 to afford lower computational processing time without compromising results.

The weighting factor ℓ from the K_{p_j} gain (Equation (4.68)) was set all over this section with values 0.01, 0.02 and 0.04, instead of the configurations made in sections 7.4 and 7.5, where the ℓ was kept fixed in 0.01. This proposition intends to yield a higher maximum $\overline{\text{VFR}}$ even if it increases its variability, considering that the attainment of an identified system with a higher $\overline{\text{VFR}}$ value results in the best method due to providing better identification performance.

7.8.1 Comparison for the M50DOF system

Comparative results for the M50DOF system, $d_t = 0.02$ s, 1500 samples (q), and submitted to 0.3% and 1% of measurement noise, are presented in Table 7.6 and Table 7.7, respectively. Besides the comparative methods in the first column and the maximum and median VFR_j and $\overline{\text{VFR}}$ values computed from the simulations provided, the computational processing time is introduced at the last column. The tables also show the values assigned to each parameter configuration, which are the same between some methods but are specific for most of the algorithms simulated.

The parameter ℓ configuration, released to increase the dynamic gain K_p , provided the achievement of higher $\overline{\text{VFR}}$ values for the SSRA-DC-iCL. However, this increment led to fit rate variability growth, as can be seen, comparing the difference between the maximum and median values of the SSRA-DC-iCL from Table 7.6 and Table 7.7 with the values displayed in Table 7.2.

For both $S_N = 0.3\%$ and $S_N = 1\%$, ARMAX is by far the autoregressive algorithm that achieves the best result, but simultaneously with a higher computational processing time. The traditional method SSRA-DC is much better than ARMAX, with fit rate values significantly higher and a processing time more than ten times faster. Confirming what had already been shown in Section 7.5.1, the novel method SSRA-DC-iCL yields a gain of at least 1% related to the SSRA-DC. From this scenario clearly depicted by the tables, the algorithm SSRA-DC-iCL presents fit rate values closer to the subspace state-space method N4SID, with a maximum $\overline{\text{VFR}}$ difference of only 0.2% on average.

Regarding the computational processing time, the SSRA-DC-iCL takes approximately 30% less time than the ARMAX for the same 100 simulations accomplished. Compared with N4SID that provided only 10 simulations, the iterative SSRA-DC-iCL was on average 13

Table 7.6 – Comparative results for: M50DOF, $dt = 0.02$ s, $q = 1500$, $S_N = 0.3\%$

Method	Configuration ⁽¹⁾⁽²⁾	Stat ⁽³⁾	VFR _{y₅}	VFR _{y₁₇}	VFR _{y₂₆}	VFR _{y₃₃}	VFR _{y₄₈}	$\overline{\text{VFR}}$	CPT (s) ⁽⁴⁾
SSRA-DC	$p = 600, \xi = 2, \gamma = 1,$ $n = 100, i = 100, \ell = 0.04^{(5)}$	Max	97.23%	97.81%	98.28%	97.75%	96.44%	97.45%	304
		Mdn	91.31%	92.99%	92.49%	91.60%	88.69%	91.74%	
SSRA-DC-iCL		Max	99.31%	99.38%	99.48%	99.36%	99.11%	99.30%	3099
		Mdn	94.34%	95.79%	94.96%	95.42%	93.07%	94.62%	
ARX	$na = nb = 20$	Max	79.24%	84.84%	88.72%	83.33%	70.00%	80.86%	260
		Mdn	68.67%	75.21%	78.70%	73.80%	59.80%	71.15%	
ARMAX	$na = nb = nc = 20, i = 100$	Max	96.61%	96.95%	97.51%	96.72%	91.63%	94.79%	4995
		Mdn	84.86%	88.40%	90.56%	88.62%	73.31%	85.00%	
⁽⁶⁾ OE	$nb = nf = 10,$ $nc = nd = 1, i = 100$	Max	62.38%	74.88%	88.23%	73.72%	50.82%	61.54%	1112
		Mdn	31.61%	58.14%	72.63%	49.87%	17.98%	40.77%	
⁽⁶⁾ BJ		Max	54.42%	69.77%	84.68%	69.12%	35.15%	44.53%	1193
		Mdn	16.66%	34.03%	34.19%	29.26%	8.28%	22.22%	
⁽⁷⁾ N4SID	$n = 100$	Max	99.53%	99.55%	99.60%	99.55%	99.49%	99.53%	44560
		Mdn	99.44%	99.47%	99.53%	99.48%	99.38%	99.46%	

¹ n : state-space system order;² na, nb, nc, nd, nf : related to the polynomials order accordingly to Equation (3.11);³ Statistical parameters coming from the total of simulations: Maximum (Max) and Median (Mdn);⁴ Computational processing time in seconds (s);⁵ The number of iterations i and the weighting factor ℓ are applied in the SSRA-DC-iCL;⁶ OE and BJ settings were conceived with the same parameters values;⁷ N4SID had 10 simulations performed, whereas the other methods had 100 simulations.Table 7.7 – Comparative results for: M50DOF, $dt = 0.02$ s, $q = 1500$, $S_N = 1\%$

Method	Configuration ⁽¹⁾⁽²⁾	Stat ⁽³⁾	VFR _{y₅}	VFR _{y₁₇}	VFR _{y₂₆}	VFR _{y₃₃}	VFR _{y₄₈}	$\overline{\text{VFR}}$	CPT (s) ⁽⁴⁾
SSRA-DC	$p = 600, \xi = 1, \gamma = 1,$ $n = 100, i = 100, \ell = 0.02^{(5)}$	Max	97.12%	97.13%	97.27%	97.05%	96.72%	97.06%	287
		Mdn	92.07%	92.49%	92.18%	91.66%	91.32%	91.85%	
SSRA-DC-iCL		Max	98.28%	98.25%	98.25%	98.21%	97.81%	98.15%	3412
		Mdn	95.01%	95.58%	95.53%	95.41%	94.90%	95.26%	
ARX	$na = nb = 20$	Max	78.41%	85.36%	87.30%	83.37%	69.95%	80.24%	310
		Mdn	69.17%	76.63%	79.04%	73.99%	59.72%	71.61%	
ARMAX	$na = nb = nc = 20, i = 100$	Max	92.48%	95.20%	95.92%	95.46%	89.81%	93.77%	5274
		Mdn	84.32%	87.46%	90.54%	88.89%	73.28%	84.69%	
⁽⁶⁾ OE	$nb = nf = 10,$ $nc = nd = 1, i = 100$	Max	69.49%	74.82%	88.19%	73.22%	63.09%	61.14%	1167
		Mdn	34.11%	53.10%	74.43%	52.01%	21.25%	42.31%	
⁽⁶⁾ BJ		Max	40.54%	66.31%	83.46%	62.92%	40.13%	44.52%	1248
		Mdn	16.00%	28.68%	41.62%	13.25%	10.22%	21.07%	
⁽⁷⁾ N4SID	$n = 100$	Max	98.31%	98.43%	98.57%	98.59%	98.08%	98.33%	41613
		Mdn	98.17%	98.25%	98.37%	98.27%	97.90%	98.19%	

¹ n : state-space system order;² na, nb, nc, nd, nf : related to the polynomials order accordingly to Equation (3.11);³ Statistical parameters coming from the total of simulations: Maximum (Max) and Median (Mdn);⁴ Computational processing time in seconds (s);⁵ The number of iterations i and the weighting factor ℓ are applied in the SSRA-DC-iCL;⁶ OE and BJ settings were conceived with the same parameters values;⁷ N4SID had 10 simulations performed, whereas the other methods had 100 simulations.

times faster in these cases. As the median and maximum values of the fit rate are very close at the N4SID, portraying a minimal variability, even if considering only one simulation as required for the algorithm, this method would already be slower than the SSRA-DC-iCL in the computational processing time.

Since the median value of $\overline{\text{VFR}}$ in the SSRA-DC-iCL is substantially lower than the maximum value, the amount of 100 simulations performed can be considered suitable in

this case. It happens due to the significant variability of results and taking into account that the main objective of a SI algorithm is the achievement of the highest maximum $\overline{\text{VFR}}$ value, notably considering what was presented in Section 7.6. Decreasing or increasing the number of simulations in the SSRA-DC-iCL and trying other algorithm settings can lead to a fit rate performance close to the N4SID, or even a little smaller. Still, with a significant time reduction, the SSRA-DC-iCL can be more attractive for the user of systems identification.

7.8.2 Comparison for the M100DOF system

The comparative results when simulating the M100DOF system with 3000 samples are depicted in Table 7.8 and Table 7.9, for 0.3% and 1% of additive measurement noise, respectively. These tables were built in the same format used at Table 7.6 and Table 7.7 for M50DOF system, but here the results of SSRA-DC-iCL were presented for ℓ set with 0.01 and 0.02, which reproduced the best results attained. These simulations were also performed maintaining the number of iterations $i = 100$.

Table 7.8 – Comparative results for: M100DOF, $dt = 0.03$ s, $q = 3000$, $S_N = 0.3\%$

Method	Configuration ⁽¹⁾⁽²⁾	Stat ⁽³⁾	VFR _{y_{10}}	VFR _{y_{34}}	VFR _{y_{52}}	VFR _{y_{66}}	VFR _{y_{96}}	$\overline{\text{VFR}}$	CPT (s) ⁽⁴⁾
SSRA-DC	$p = 500, \xi = 2, \gamma = 1,$ $n = 200, i = 100, \ell = 0.02^{(5)}$	Max	97.65%	97.34%	97.86%	97.88%	97.09%	97.27%	2675
		Mdn	70.25%	64.66%	75.95%	72.76%	69.22%	70.37%	
SSRA-DC-iCL		Max	99.26%	99.18%	99.03%	98.97%	99.03%	99.09%	2900
		Mdn	87.56%	87.55%	91.78%	92.00%	91.63%	87.94%	
ARX	$na = nb = 40$	Max	97.09%	96.15%	93.00%	80.27%	83.20%	89.37%	4619
		Mdn	96.21%	94.93%	91.02%	76.86%	79.33%	87.61%	
ARMAX	$na = nb = nc = 40, i = 100$	Max	99.09%	98.69%	98.30%	88.83%	91.12%	94.63%	45787
		Mdn	98.40%	98.21%	96.14%	83.63%	84.39%	92.04%	
OE ⁽⁶⁾	$nb = nf = 8,$ $nc = nd = 1, i = 100$	Max	70.83%	64.58%	55.54%	44.49%	47.87%	43.30%	3145
		Mdn	20.38%	36.78%	43.52%	23.89%	14.57%	12.23%	
BJ ⁽⁶⁾		Max	39.17%	49.08%	54.65%	41.89%	36.84%	35.31%	3330
		Mdn	13.85%	11.10%	4.49%	27.52%	13.01%	1.70%	
N4SID ⁽⁷⁾	$n = 100$	–	99.43%	99.43%	99.39%	99.35%	99.45%	99.41%	485264

¹ n : state-space system order;

² na, nb, nc, nd, nf : related to the polynomials order accordingly to Equation (3.11);

³ Statistical parameters coming from the total of simulations: Maximum (Max) and Median (Mdn);

⁴ Computational processing time in seconds (s);

⁵ The number of iterations i and the weighting factor ℓ are applied in the SSRA-DC-iCL;

⁶ OE and BJ settings were conceived with the same parameters values;

⁷ N4SID had only 1 simulation performed, whereas the other methods had 100 simulations.

The comparative results analysis between the methods for the M100DOF system was similar to the M50DOF system regarding the VFR_j and $\overline{\text{VFR}}$ attained. All the methods had a significant increment of computational processing time, except the SSRA-DC-iCL, which kept the same order of magnitude. This drawback related to the processing time spent was

Table 7.9 – Comparative results for: M100DOF, $dt = 0.03$ s, $q = 3000$, $S_N = 1\%$

Method	Configuration ⁽¹⁾⁽²⁾	Stat ⁽³⁾	VFR _{y10}	VFR _{y34}	VFR _{y52}	VFR _{y66}	VFR _{y96}	$\overline{\text{VFR}}$	CPT (s) ⁽⁴⁾
SSRA-DC	$p = 500, \xi = 1, \gamma = 1,$ $n = 200, i = 100, \ell = 0.01^{(5)}$	Max	96.97%	96.90%	96.81%	96.79%	96.51%	96.60%	1573
		Mdn	95.73%	95.37%	96.06%	95.84%	95.38%	95.70%	
SSRA-DC-iCL		Max	97.86%	97.84%	97.27%	97.31%	97.33%	97.46%	5974
		Mdn	96.88%	96.82%	96.74%	96.67%	96.78%	96.82%	
ARX	$na = nb = 40$	Max	94.17%	92.37%	90.14%	79.52%	83.34%	86.55%	4599
		Mdn	92.39%	90.06%	86.46%	75.90%	78.77%	84.71%	
ARMAX	$na = nb = nc = 40, i = 100$	Max	97.67%	97.73%	96.70%	87.82%	91.85%	93.35%	54152
		Mdn	97.20%	97.06%	93.89%	83.97%	86.71%	91.67%	
OE ⁽⁶⁾	$nb = nf = 8,$ $nc = nd = 1, i = 100$	Max	56.28%	54.84%	55.73%	46.37%	42.02%	40.11%	3471
		Mdn	15.12%	36.86%	44.02%	26.44%	13.90%	19.05%	
BJ ⁽⁶⁾		Max	58.23%	47.96%	55.45%	40.06%	34.48%	31.27%	3976
		Mdn	13.60%	12.71%	38.53%	27.43%	11.34%	13.21%	
N4SID ⁽⁷⁾	$n = 100$	–	98.02%	98.17%	98.02%	97.89%	98.07%	98.03%	474972

¹ n : state-space system order;

² na, nb, nc, nd, nf : related to the polynomials order accordingly to Equation 3.11;

³ Statistical parameters coming from the total of simulations: Maximum (Max) and Median (Mdn);

⁴ Computational processing time in seconds (s);

⁵ The number of iterations i and the weighting factor ℓ are applied in the SSRA-DC-iCL;

⁶ OE and BJ settings were conceived with the same parameters values;

⁷ N4SID had only 1 simulation performed, whereas the other methods had 100 simulations.

much smaller for the iterative SSRA-DC-iCL method. Despite being expected to increase the CPT when the system's size doubled, the time increased by about 10-fold for most algorithms.

On the other hand, it can be realized a significant difference in processing time in the SSRA-DC and SSRA-DC-iCL from $S_N = 0.3\%$ (Table 7.8) to $S_N = 1\%$ (Table 7.9), which is not expected and did not happen with other methods. The processing time of SSRA-DC-iCL was approximately half for $S_N = 0.3\%$ compared with $S_N = 1\%$, due to the occurrence of several unstable identified systems with convergence loss, as explained in Section 7.5.2. At this condition, the SSRA-DC-iCL algorithm goes away from the iterations loop before the respective set-point is achieved, complying with the requirements established in lines 20 to 22 of the Algorithm 1. In several simulations, the expected time spent with 100 iterations was reduced with fewer iterations performed. For the SSRA-DC algorithm, the convergence loss can occur, but this does not lead to a significant processing time reduction in the non-iterative algorithm. Here, the time was affected by the matrices' sizes, as $\xi = 2$ at Table 7.8 and $\xi = 1$ at Table 7.9.

It should be emphasized the computational processing time spent by the N4SID algorithm in this case. The increase in the MIMO system order and the number of input-output variables led to an expressive increment in the computational processing for the N4SID method. For only one simulation of the method N4SID, it spent more than five days running the algorithm, which means the processing time increased more than 100 times when the system

size doubled from 50 to 100 degrees of freedom.

Following the M50DOF simulations, the N4SID continued presenting better fit rate values than the SSRA-DC-iCL for the M100DOF system, here with an increment in the $\overline{\text{VFR}}$ from 0.2% to 0.45% on average. It should be considered the more significant difference is coming from the increase of the system size, which mainly happened for $S_n = 1\%$, owing to the smaller fit rate values attained by the SSRA-DC-iCL algorithm. So, the SI effectiveness improvement with the N4SID employment compared to the SSRA-DC-iCL method should be well analyzed regarding the computational processing time spent, even considering that the time required for the novel method's configuration demands some trials to get the better settings.

7.8.3 Overview of the comparative analysis

Bars graph (Figure 7.18) provided a summarization of the maximum Validated Fit Rate ($\overline{\text{VFR}}$) results over the several simulations presented from Table 7.6 to Table 7.9 for the methods that had results with $\max(\overline{\text{VFR}}) \geq 90\%$, thereby excluding the polynomial regression methods, except the ARMAX. However, it can be seen that this autoregressive method is not competitive with the state-space identification methods for systems and conditions established until now in this chapter. The graph highlights that the SSRA-DC-iCL and N4SID methods attain close $\overline{\text{VFR}}$ results, mostly for the M50DOF system simulated. The non-iterative method SSRA-DC brings forward a more remarkable performance difference than the N4SID, which could be minimized with the release of the iterative technique employing the novel SSRA-DC-iCL method.

The bar graph equivalent to the one shown in Figure 7.18 is displayed in Figure 7.19 for the CPT. In this case, as the higher bars in Figure 7.19 represent a drawback for the method performance, and considering that the magnitude in vertical axis is on a logarithmic scale, it can be perceived a significantly worse performance of N4SID than the other methods, notably in comparison to the new iterative method with the M100DOF system. The method SSRA-DC-iCL provides a CPT considerably better than the ARMAX, mainly for the M100DOF system. As expected, the novel iterative method only has worse CPT results than the non-iterative method SSRA-DC, presenting a significant improvement of the maximum Validated Fit Rate $\overline{\text{VFR}}$ as shown previously in Section 7.5. At the M100DOF system with $S_N = 0.3\%$, it should be highlighted a remarkably close CPT level between the SSRA-DC and SSRA-DC-iCL. This situation occurred due to many simulations when the SSRA-DC-iCL lost the convergence, lead-

ing the algorithm not to perform the complete number of iterations at each simulation, as explained in the last section.

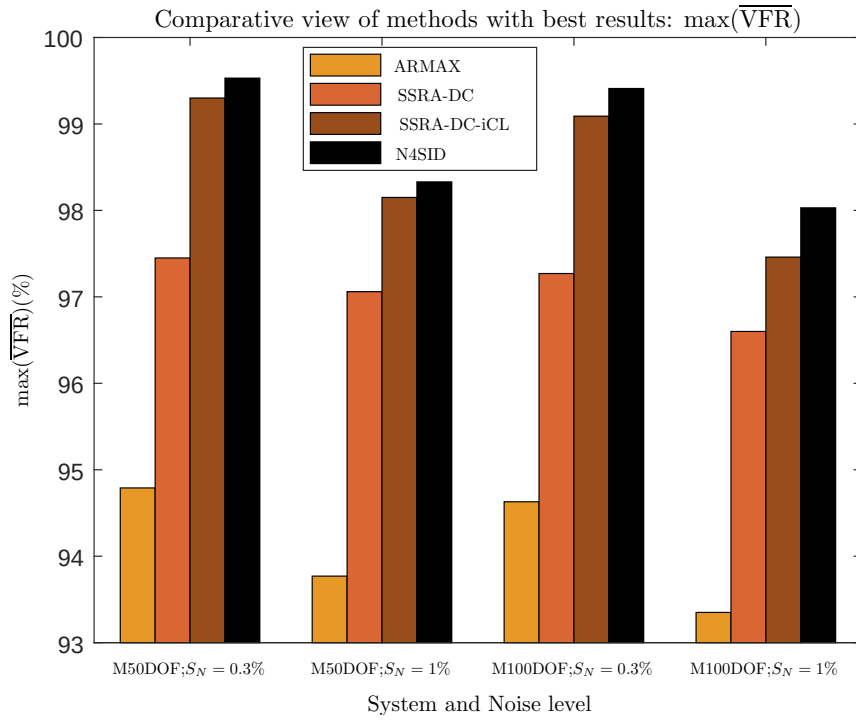


Figure 7.18 – Comparative view ($\overline{\text{VFR}}$) of methods with best results for M50DOF and M100DOF systems.

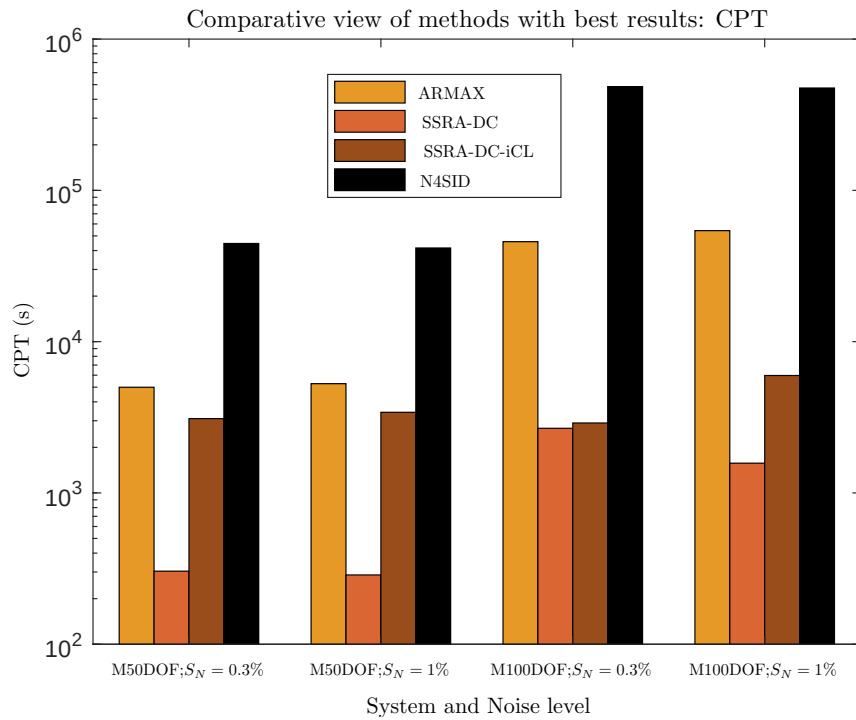


Figure 7.19 – Comparative view (CPT) of methods with best results for M50DOF and M100DOF systems.

Here, the analysis considers the comparative parameters $\overline{\text{VFR}}$ and CPT separately. Firstly, the significant difference in magnitude of values encompassing the respective parameters would require employing some weighting factor that could be unfair and inappropriate in this proposition. Also, the choice between the computational processing speed and the methods' accuracy should be an issue of loss and gains assessment in charge by the user interests.

7.9 Cart-Pendulum system simulations results

This section introduces the results and analysis from the simulations of the iterative method SSRA-DC-iCL applied for the C-PEN, as well as providing a comparison with the main other methods being discussed in the present research. The complete system characteristics that determine the model dynamics are described in Section 5.5. The data set for this SIMO (Single Input Multiple Output) system identification is composed by the input force u , and the outputs cart displacement y_x and pendulum rod angle y_θ . The procedure to obtain the data set required for the identification is depicted in Figure 5.11.

7.9.1 Specific settings for simulations with the C-PEN system

The C-PEN system has the system order directly set with a fixed value, which in this case is $n = 4$. The other parameters of the SSRA-DC-iCL algorithm follow the same aspects as described in Section 7.2.

As introduced in Section 5.7.2, the definition of the sampling time for the system identification, that is the same to generate the data set employing the RK4 method, relies on the value of the system maximum frequency to be calculated using the Nyquist Sampling Theorem. For that, the linearized system was considered as the reference in its continuous-time state-space representation. From Equation (5.39) and Equation (5.40), and the respective values of its variables introduced in Section 5.5, the state-space matrices of the linearized system are determined as follows:

$$\mathbf{A} = \begin{bmatrix} 0 & 0 & 1 & 0 \\ 0 & 0 & 0 & 1 \\ -170.23 & -3.29 & -5.15 & -0.0082 \\ -487.82 & -37.54 & -14.77 & -0.0941 \end{bmatrix}, \mathbf{B} = \begin{bmatrix} 0 \\ 0 \\ 1.1988 \\ 3.4354 \end{bmatrix}, \mathbf{C} = \begin{bmatrix} 1 & 0 & 0 & 0 \\ 0 & 1 & 0 & 0 \end{bmatrix}. \quad (7.1)$$

From the state-space matrices with the values shown in Equation (7.1), the linearized Cart-Pendulum system has the natural frequencies: 5.14 rad/s and 13.5 rad/s. The determination of the minimum sampling frequency ω_s accordingly to the Nyquist Sampling Theorem (Equation (5.42)) leads to the condition of $\omega_s \geq 2\omega_{max} = 27$ rad/s. If the sampling frequency should be higher than 27 rad/s (4.297 Hz), the sampling time applied to the C-PEN should comply with $d_t \leq 0.233$ s. Since the sampling time of the identification and the RK4 methods are the same, the values 0.01 s and 0.02 s were adopted for the two configurations used in the simulations, as presented in the next section.

7.9.2 SSRA-DC-iCL simulation results and analysis

Similar to Section 7.4 where the results for the mass-springer-damper systems are presented, the proposal here is also to analyze the algorithm SSRA-DC-iCL. But now, the focus of this section is showing how the method behaves in the iterative evolution when the system to be identified has nonlinear characteristics as in the C-PEN. The graphs report the algorithm performance for the best simulations results of each configuration that performed 100 simulations, which the statistical analysis is the subject of the next section.

The graphs on Figure 7.20 state a comparative analysis between the two configuration options of the gain in charge for updating the Markov parameters at each iteration. The left graph refers to the gain K_p variable at each iteration, and the graph on the right depicts the algorithm function when the gain K_p is fixed. The curves represent the Fit Rate evolution (\overline{FR}) for the following parameters setting: $d_t = 0.01$ s, $q = 1600$, $p = 800$, $S_N = 0.3\%$. In all the simulations with the C-PEN system, the algorithm parameters $\xi = 2$ and $\gamma = 2$ were adjusted with these values due to generally providing better results. When K_p is used, it worthy the adjustment $\ell = 0.02$, while for K_p fixed, the gain was set with the value $K_p = 0.05$.

The graphs on Figure 7.21 are equivalent to those on Figure 7.20 but for $S_N = 1\%$, also objectifying to present more significant oscillations of $\overline{FR}(\%)$, mainly in the beginning of the iterations, for the functioning when the algorithm works with the variable gain that is updated accordingly to the Markov residues covariance. In both figures, the graphs on the right, despite the employment of a fixed K_p gain with value more than double ℓ value, confirm this gain configuration of the SSRA-DC-iCL as smoother and more proper for this kind of system application. It should be noted that almost the same level of $\overline{FR}(\%)$ was attained with the double number of iterations for the lower gain condition, as expected. Anyway, these evolution curves

of $\overline{\text{FR}}(\%)$ along with the iterations, ratify the effectiveness of the iterative algorithm SSRA-DC-iCL for the C-PEN nonlinear system under the characteristics once established in Section 5.5.

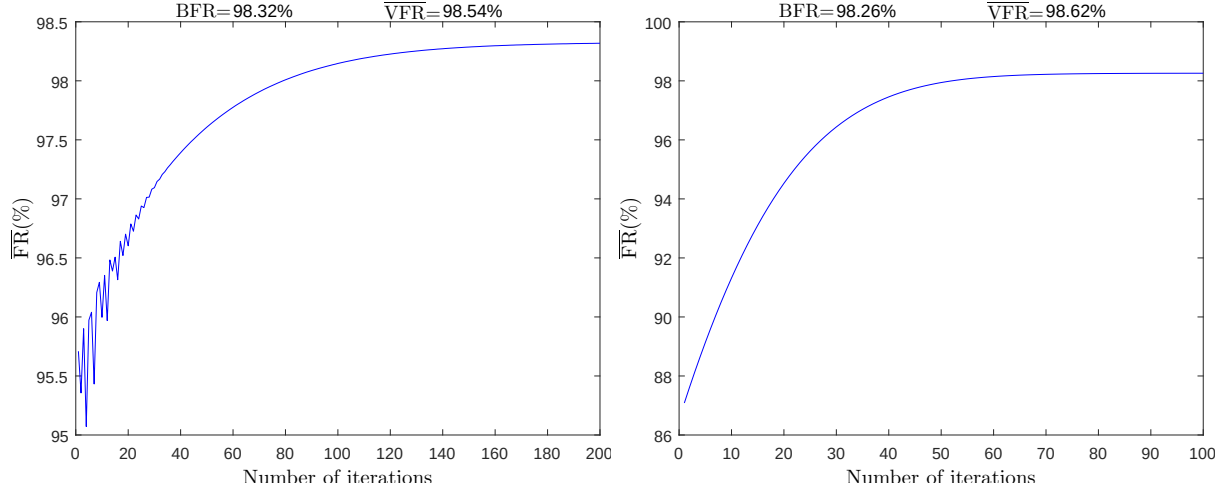


Figure 7.20 – $\overline{\text{FR}}(\%)$ evolution of SSRA-DC-iCL for C-PEN with $d_t = 0.01$ s, $q = 1600$, $p = 800$, $S_N = 0.3\%$, and $\ell = 0.02$ (left), $K_p = 0.05$ (right).

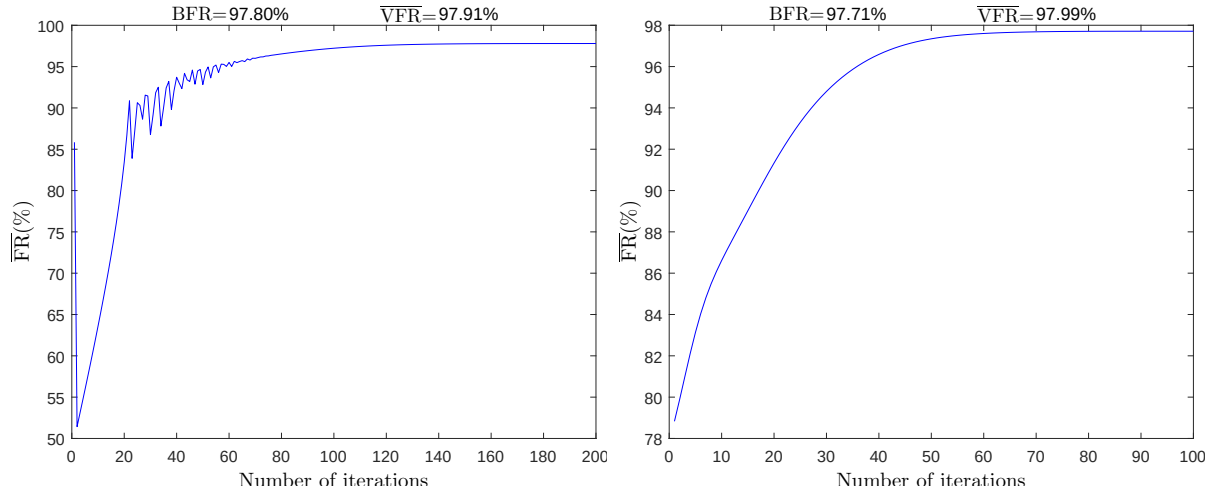


Figure 7.21 – $\overline{\text{FR}}(\%)$ evolution of SSRA-DC-iCL for C-PEN with $d_t = 0.01$ s, $q = 1600$, $p = 800$, $S_N = 1\%$, and $\ell = 0.02$ (left), $K_p = 0.05$ (right).

Another algorithm configuration was simulated with its graphs shown on Figure 7.22 regarding the following parameters settings: $d_t = 0.02$ s, $q = 2000$, $p = 500$, $K_p = 0.05$, $S_N = 0.3\%$ on the left graph, and $S_N = 1\%$ on the right graph. These simulations with $d_t = 0.02$ s were realized only at the fixed K_p condition. The curves also portray a smooth upward profile with a significant $\overline{\text{FR}}(\%)$ increment from the first to the last iteration. However, the $\overline{\text{VFR}}$ values are considerably lower compared to the simulations prior presented for $d_t = 0.01$ s. For C-PEN simulations, a degradation of the results as the sampling time increases was realized. In

this system case, unlike in the mass-spring-damper systems, the number of samples q decrement was not considered a preponderant condition to justify the Fit Rate improvement when applying the SSRA-DC-iCL rather than SSRA-DC. For instance, at $d_t = 0.02$ s and $S_N = 0.3\%$, with a q reduction from 4000 to 2000, despite the SSRA-DC simulations presenting a slight drop from 94.6% to 93.22% in the $\overline{\text{VFR}}$, the SSRA-DC-iCL simulations kept the same level shown in Fig. 7.22 on the left.

In the SSRA-DC-iCL simulations of the C-PEN system, the reduction of the sampling time showed to be a more determining way to improve the SI results. Still, as the sampling time applied for the RK4 is the same as the identification, it should be recalled that as higher the RK4 sampling frequency is closer to a continuous-time system, the integrated variable values by RK4 will be more effective in depicting the dynamical of the system.

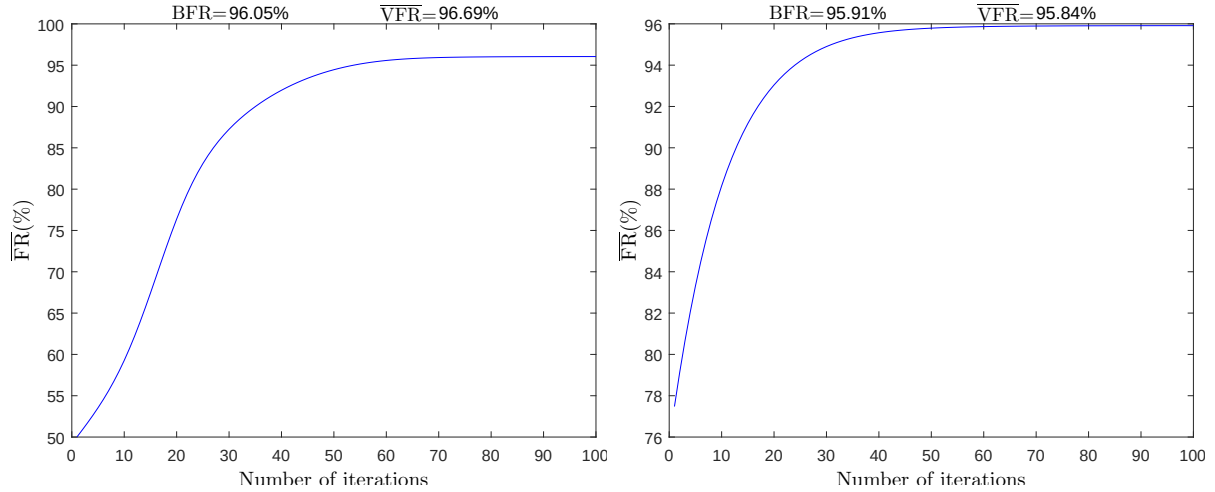


Figure 7.22 – $\overline{\text{FR}}(\%)$ evolution of SSRA-DC-iCL for C-PEN with $d_t = 0.02$ s, $q = 2000$, $p = 500$, $K_p = 0.05$, and $S_N = 0.3\%$ (left), $S_N = 1\%$ (right).

The magnitudes and characteristics of the outputs signals \mathbf{y}_x and \mathbf{y}_θ are depicted in Figure 7.23. The outputs curves comes from the response of the IS to the input excitation force u from the same simulation that achieved the BFR shown in the graph on the left of Figure 7.22. From the graphs, it can be seen that the output \mathbf{y}_x presents a considerable lower VFR value than the output \mathbf{y}_θ , which will be verified as a common aspect in the statistical assessment introduced in the next section.

7.9.3 Comparative statistical analysis with reference identification methods

The present section performs the statistical analysis in the same way as presented for the mass-spring-damper system in Section 7.5. Besides showing the improvement provided

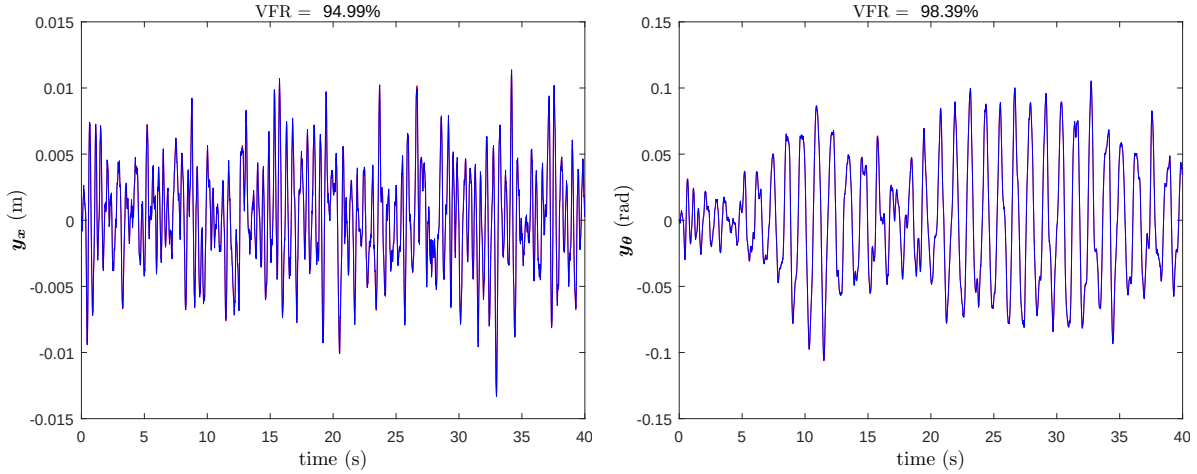


Figure 7.23 – Outputs y_x (left) and y_θ (right) from *OS* (red) and *IS* (blue) for: $d_t = 0.02$ s, $q = 2000$, $p = 500$, $K_p = 0.05$, and $S_N = 0.3\%$.

by the new iterative SSRA-DC-iCL method from the comparative values with the non-iterative SSRA-DC, this section also included the N4SID and the ARMAX in the comparison as methods that acquired the bests $\overline{\text{VFR}}$ results in the mass-spring-damper system simulations. All the 100 simulations accomplished for both 0.01 s and 0.02 s of sampling time had 100 iterations (parameter i) with a fixed gain of $K_p = 0.05$. Moreover, the data correlation algorithm parameters ξ and γ were set with fixed value 2. Hence, considering that all these parameters are constant values in the simulations, they do not need to be presented in the following tables that portray the results from this section.

Table 7.10 contains the statistical results for the following configuration: $d_t = 0.01$ s, $q = 1600$, $p = 800$. And Table 7.11 is the analogue one for the following configuration: $d_t = 0.02$ s, $q = 2000$, $p = 500$. The results data for $\overline{\text{VFR}}$ from the specific comparison between SSRA-DC and SSRA-DC-iCL, which are presented in the mentioned tables, are summed up by the boxplot graph in Figure 7.24.

In Table 7.10, it can be seen the iterative SSRA-DC-iCL with a significantly better result than the non-iterative method SSRA-DC to both noise conditions (0.3% and 1%). The improvement gain depicted by $\Delta\overline{\text{VFR}}$ shows greater values considerably higher than in the simulations of mass-spring-damper systems, which happens for both the maximum and median statistical parameters. The $\Delta\overline{\text{VFR}}$ of the interquartile range with 8.55% and 14.42% higher in the SSRA-DC for 0.3% and 1% of noise, respectively, is viewed in the boxplot graph with a larger box, which also happens for the simulations when $d_t = 0.02$ s. That means that here, in the C-PEN system simulations, the iterative method significantly reduces the variability of the result, which had not been verified in the mass-spring-damper (MDOF) systems. Despite

Table 7.10 – Comparative results for C-PEN system: $d_t = 0.01$ s, $q = 1600$, $p = 800$.

noise (S_N)	Statistical group	Algorithm ⁽¹⁾	VFR _{y_x}	VFR _{y_θ}	$\overline{\text{VFR}}$	$\Delta\overline{\text{VFR}}$ ⁽²⁾	CPT (s) ⁽³⁾
0.3%	Maximum	SSRA-DC-iCL	98.06%	99.32%	98.62%	–	1451
		SSRA-DC	97.37%	92.65%	94.79%	3.83%	258
		N4SID	97.43%	98.51%	97.89%	0.73%	396
		ARMAX	99.60%	99.72%	99.66%	-1.04%	458
	Median	SSRA-DC-iCL	97.67%	98.63%	98.15%	–	–
		SSRA-DC	91.76%	63.80%	78.72%	19.43%	–
		N4SID	97.01%	97.01%	97.05%	1.10%	–
		ARMAX	99.53%	99.58%	99.54%	-1.39%	–
	Interquartile range	SSRA-DC-iCL	3.72%	16.63%	11.73%	–	–
		SSRA-DC	7.20%	37.71%	20.28%	8.55%	–
		N4SID	0.27%	1.79%	0.93%	-10.80%	–
		ARMAX	0.05%	0.10%	0.05%	-11.68%	–
	Unstable IS ⁽⁴⁾	SSRA-DC-iCL	1%	8%	1%	–	–
		SSRA-DC	1%	12%	1%	0%	–
		N4SID	0%	0%	0%	-1%	–
		ARMAX	0%	0%	0%	-1%	–
1%	Maximum	SSRA-DC-iCL	97.68%	98.63%	97.99%	–	1568
		SSRA-DC	97.27%	91.19%	93.34%	4.65%	238
		N4SID	97.02%	97.65%	97.22%	0.77%	418
		ARMAX	98.64%	98.71%	98.58%	-0.59%	412
	Median	SSRA-DC-iCL	97.15%	97.99%	97.61%	–	–
		SSRA-DC	92.19%	62.89%	77.15%	20.46%	–
		N4SID	96.41%	93.98%	95.25%	2.36%	–
		ARMAX	98.36%	98.37%	98.36%	-0.75%	–
	Interquartile range	SSRA-DC-iCL	0.70%	8.39%	4.61%	–	–
		SSRA-DC	6.07%	31.83%	19.03%	14.42%	–
		N4SID	0.37%	4.36%	2.33%	-2.28%	–
		ARMAX	0.18%	0.25%	0.16%	-4.45%	–
	Unstable IS ⁽⁴⁾	SSRA-DC-iCL	0%	2%	0%	–	–
		SSRA-DC	0%	6%	0%	0%	–
		N4SID	0%	0%	0%	0%	–
		ARMAX	0%	0%	0%	0%	–

¹ Polynomials orders of the ARMAX: $na = nb = nc = 2$, to agree with the same order $n = 4$ of the state-space methods;

² Improvement gain ($\overline{\text{VFR}}$) of the SSRA-DC-iCL algorithm over the other algorithms;

³ Computational Processing Time in seconds (independent from the parameters of the statistical group);

⁴ Percentual of unstable IS (Identified System) over the 100 simulations when $\text{VFR}_j = 0$ or $\overline{\text{VFR}} = 0$.

the more significant improvement gain with the C-PEN system than with the MDOF systems, the maximum and median magnitude values attained with the SSRA-DC-iCL algorithm were considerably lower in the C-PEN system simulations.

Comparing the statistical results of the iterative method with the N4SID, contrary to what was seen in the results with the MDOF systems, for the C-PEN systems, the SSRA-DC-iCL achieved better results than N4SID, being the $\Delta\overline{\text{VFR}}$ even higher than when MDOF systems were simulated. Whereas here, the $\Delta\overline{\text{VFR}}$ values of the maximum statistical parameter go from 0.70% to 0.98%, for the MDOF systems, the equivalent results achieved values from 0.18% to 0.57%. On the other hand, the variability of the SSRA-DC-iCL results, represented by the interquartile range parameter, was significantly higher than in the N4SID. The unstable IS parameter followed this difference presented in the interquartile range statistical parameter.

Table 7.11 – Comparative results for C-PEN system: $d_t = 0.02$ s, $q = 2000$, $p = 500$.

noise (S_N)	Statistical group	Algorithm ⁽¹⁾	VFR _{y_x}	VFR _{y_θ}	$\overline{\text{VFR}}$	$\Delta\overline{\text{VFR}}$ ⁽²⁾	CPT (s) ⁽³⁾
0.3%	Maximum	SSRA-DC-iCL	94.99%	98.39%	96.69%	–	789
		SSRA-DC	94.17%	92.72%	93.22%	3.46%	340
		N4SID	94.19%	97.73%	95.71%	0.98%	289
		ARMAX	99.54%	99.48%	99.48%	-2.79%	449
	Median	SSRA-DC-iCL	94.05%	97.19%	95.55%	–	–
		SSRA-DC	91.57%	67.22%	79.41%	16.14%	–
		N4SID	93.55%	94.44%	94.06%	1.49%	–
		ARMAX	99.43%	99.18%	99.30%	-3.75%	–
	Interquartile range	SSRA-DC-iCL	0.49%	5.18%	2.77%	–	–
		SSRA-DC	3.48%	26.86%	15.66%	12.89%	–
		N4SID	0.37%	3.24%	1.59%	-1.18%	–
		ARMAX	0.07%	0.30%	0.16%	-2.61%	–
	Unstable IS ⁽⁴⁾	SSRA-DC-iCL	1%	6%	1%	–	–
		SSRA-DC	1%	8%	1%	0%	–
		N4SID	0%	0%	0%	-1%	–
		ARMAX	0%	0%	0%	-1%	–
1%	Maximum	SSRA-DC-iCL	94.49%	97.79%	95.84%	–	445
		SSRA-DC	94.04%	90.24%	92.05%	3.79%	382
		N4SID	94.08%	96.75%	95.14%	0.70%	303
		ARMAX	98.52%	98.56%	98.48%	-2.64%	444
	Median	SSRA-DC-iCL	93.69%	96.56%	95.16%	–	–
		SSRA-DC	90.94%	65.63%	77.97%	17.19%	–
		N4SID	93.33%	94.06%	93.68%	1.48%	–
		ARMAX	98.21%	98.17%	98.19%	-3.03%	–
	Interquartile range	SSRA-DC-iCL	0.62%	8.59%	4.59%	–	–
		SSRA-DC	4.73%	25.00%	14.38%	9.79%	–
		N4SID	0.43%	3.51%	1.89%	-2.70%	–
		ARMAX	0.20%	0.29%	0.21%	-4.38%	–
	Unstable IS ⁽⁴⁾	SSRA-DC-iCL	2%	8%	2%	–	–
		SSRA-DC	2%	10%	2%	0%	–
		N4SID	0%	0%	0%	-2%	–
		ARMAX	0%	0%	0%	-2%	–

¹ Polynomials orders of the ARMAX: $na = nb = nc = 2$, to agree with the same order $n = 4$ of the state-space methods;² Improvement gain ($\overline{\text{VFR}}$) of the SSRA-DC-iCL algorithm over the other algorithms;³ Computational Processing Time in seconds (independent from the parameters of the statistical group);⁴ Percentual of unstable IS (Identified System) over the 100 simulations when $\text{VFR}_j = 0$ or $\overline{\text{VFR}} = 0$.

Differently from what has been verified in the MDOF systems, the ARMAX presented unexpected results once the algorithm had significantly higher values of maximum and median $\Delta\overline{\text{VFR}}$ compared to the new iterative method SSRA-DC-iCL. Also, the ARMAX had lower results variability, even better than the N4SID. The other Matlab SI Toolbox techniques were not presented here because they obtained worse results, as occurred in the tests for the MDOF systems.

From Table 7.10 and Table 7.11, for most of the simulations and mainly for the SSRA-DC-iCL, it can be realized higher values of maximum and median VFR_{y_θ} than VFR_{y_x} . Also, a higher variability indicated by the interquartile range and unstable IS was seen. Comparing the tables, it is well evident the significant difference at about 2% between the $\Delta\overline{\text{VFR}}$ in the sampling time conditions $d_t = 0.01$ s and $d_t = 0.02$ s. That degradation of FR results, when

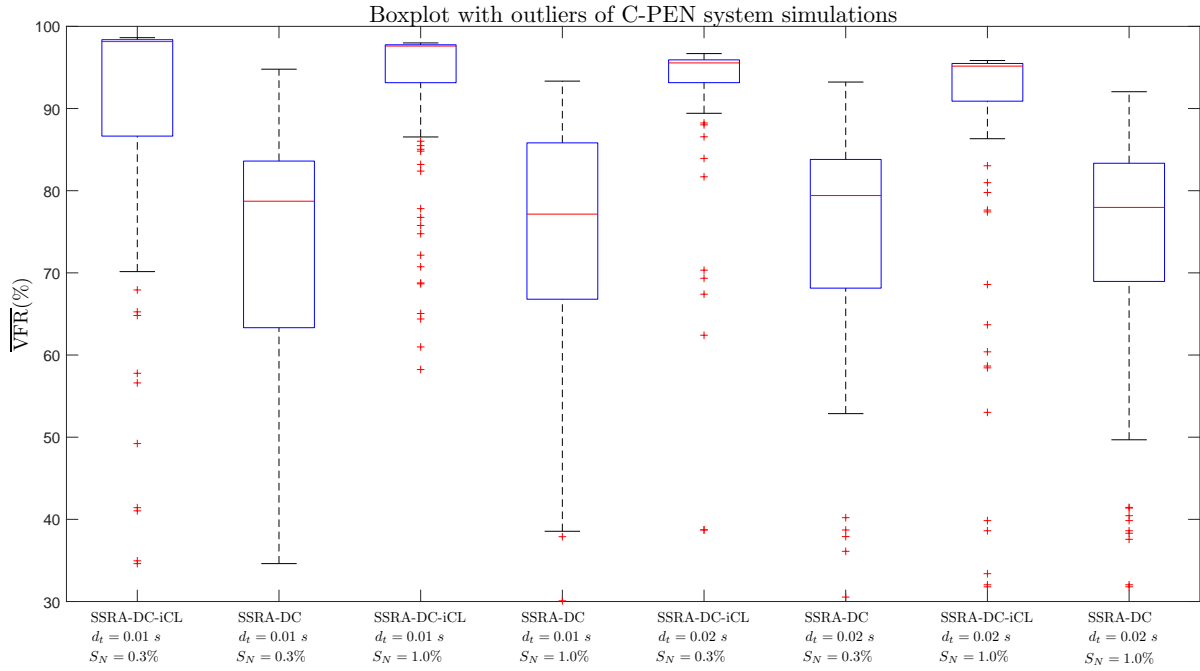


Figure 7.24 – Boxplot with outliers of C-PEN system simulations.

the sampling time increases in the C-PEN, was already approached in Section 7.9.2.

Considering all simulation results presented in the tables, the Computational Processing Time spent by the iterative method was almost three times higher, on average, than the N4SID, which did not happen in MDOF systems, where the CPT for the N4SID was more than 100 times higher than the SSRA-DC-iCL. For the C-PEN system, N4SID, ARMAX, and the conventional SSRA-DC had similar CPT values in general. The higher values of CPT for SSRA-DC-iCL when $d_t = 0.01$ s concerning simulations with $d_t = 0.02$ s can be arguable at first glance; however, this situation is justified by the difference of $8/5$ in the parameter p , which loads the computational processing significantly as from the singular value decomposition. Also, the increment of interquartile range and unstable IS in the SSRA-DC-iCL from $S_N = 0.3\%$ to $S_N = 1\%$ when $d_t = 0.02$ s justify the great decrement on CPT. These statistical parameters with higher values indicate more simulations that the algorithms may have had to stop before achieving the number of iterations set-point.

Two bar graphs summarizing the results, comparatively among the methods, are displayed in Figure 7.25 and Figure 7.26 for the maximum \overline{VFR} and CPT, respectively. Comparing Figure 7.25 from the C-PEN system with Figure 7.18 from MDOF systems simulated, it is evident that a performance change between the methods takes place for the nonlinear C-PEN system. The significant improvement of the iterative method SSRA-DC-iCL over the N4SID is covered up. It seems not to be so relevant in the face of the startling result of the ARMAX,

considering that it was the worst result for MDOF systems, but here presenting by far the best $\overline{\text{VFR}}$ values.

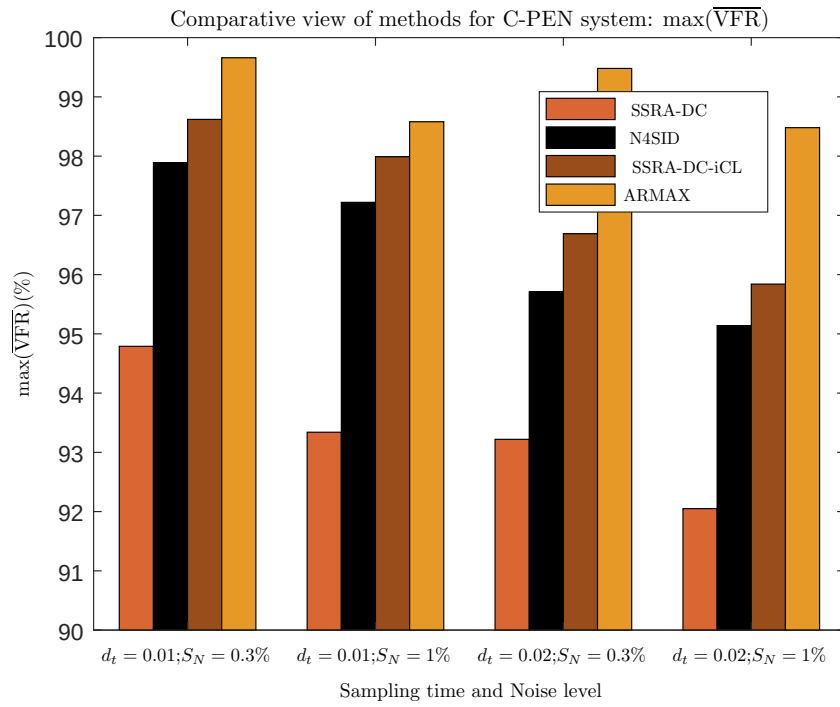


Figure 7.25 – Comparative view ($\overline{\text{VFR}}$) of methods for C-PEN system.

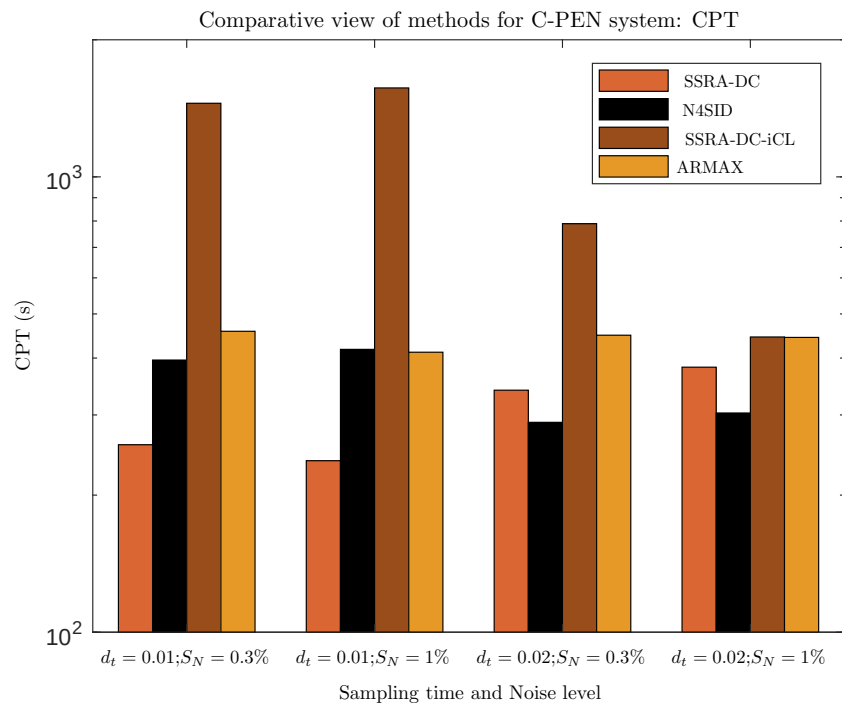


Figure 7.26 – Comparative view (CPT) of methods for C-PEN system.

Some care should be taken when comparing Figure 7.26 and Figure 7.19 since the bars size difference can lead to a close difference in CPT between the systems simulations.

However, as the scale of the y-axis is logarithmic, the time differences between the SSRA-DC-iCL and the other methods are significantly lower in the C-PEN systems simulations. Here, the steady level of CPT attained by the ARMAX throughout the simulations should be highlighted. The algorithm required, on average, a considerably lower time than the SSRA-DC-iCL and approximately the same level as the N4SID, primarily for simulations with $d_t = 0.01$ s.

7.9.4 Comparative analysis between nonlinear and linearized C-PEN systems

To conclude the simulation analysis for the C-PEN system, the verification of the identified systems from the simulations in terms of similarity with the linearized system introduced in Section 7.9.1 (state-space system defined by Equation (7.1)) is performed through the quality assessment of Maximum Singular Values (MSV) graphs and step responses graphs. For that, the analysis considered two identified systems from SSRA-DC-iCL with the best and worst maximum $\overline{\text{VFR}}$ values obtained in the simulations accomplished in this section. The Identified System (*IS*) are compared in each graph with the linearized system called here as Original System (*OS*).

Maximum Singular Values (MSV) graphs are displayed in Figure 7.27 to qualitatively compare the adherence of the *IS* related to the *OS* for the *IS* attained with the best (graph on the left) and worst (graph on the right) values of $\overline{\text{VFR}}$ among the configurations simulated in the present section. The natural frequencies of 5.14 rad/s and 13.5 rad/s from the C-PEN system are indicated on the graphs. It can be seen only a small difference between the *OS* and *IS* when $\overline{\text{VFR}} = 95.84\%$, whereas for the best *IS* when $\overline{\text{VFR}} = 98.62\%$ there is an overlap of the curves. As for the evaluation through the step response curves presented in Figure 7.28 and Figure 7.29 for the best and worst *IS*, respectively, the graphs can be better realized for comparative purposes, mainly for the output y_x . They are pointing out the situation where the *IS* with higher $\overline{\text{VFR}}$ becomes closer in equivalence to the *OS*.

From the C-PEN linearized in its state-space continuous-time representation (Equation (7.1)), the equivalent discrete-time representation can be obtained for the C-PEN discretized employing the ZOH method, as follows:

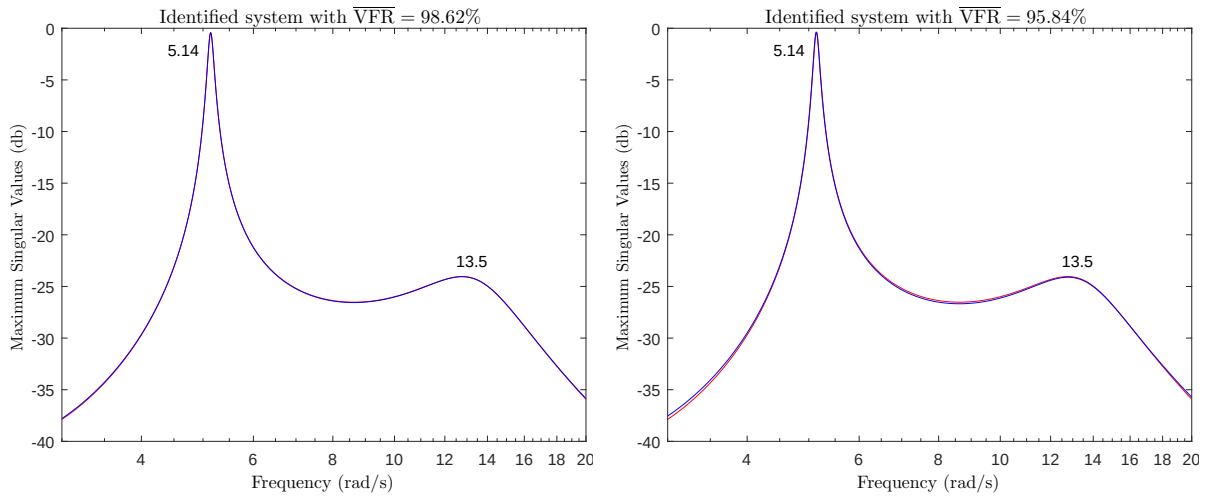


Figure 7.27 – MSV of the *OS* (red) and the *IS* (blue), comparing the best (left) and worst (right) results of $\overline{\text{VFR}}$.

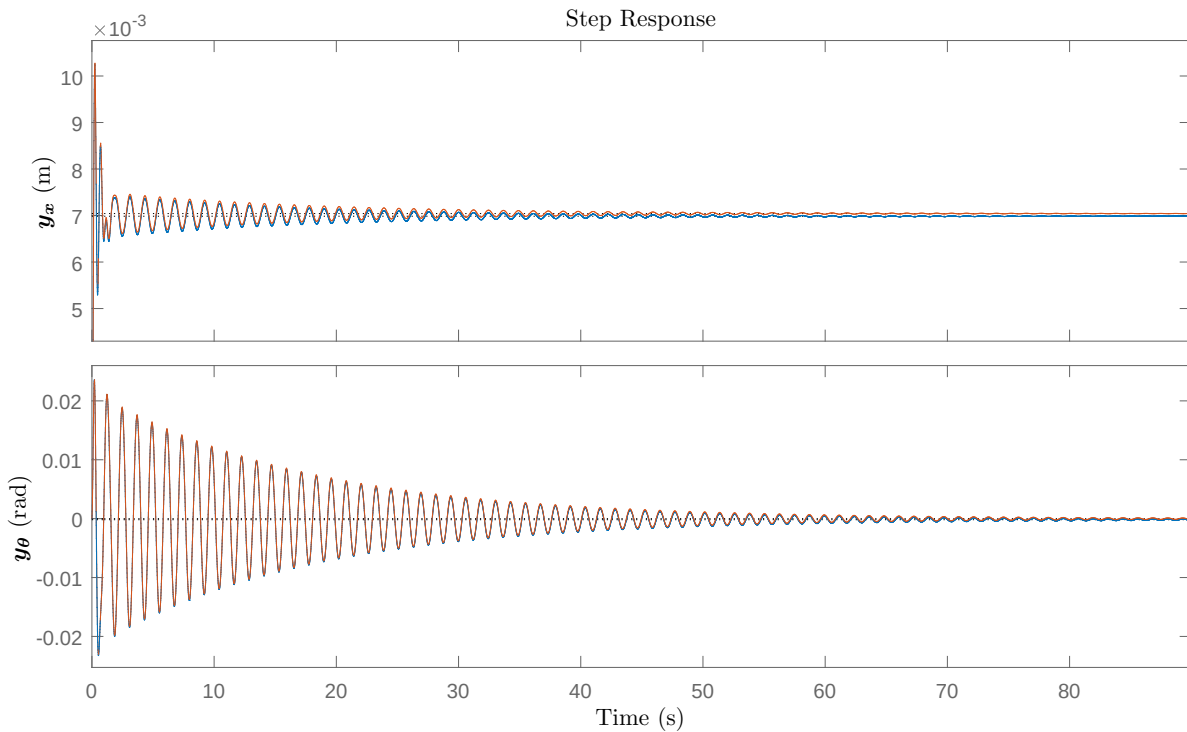


Figure 7.28 – Step Response graphs from the *OS* (red) and *IS* (blue) when $\overline{\text{VFR}} = 98.62\%$ for both outputs of the C-PEN system ($d_t = 0.01$ s).

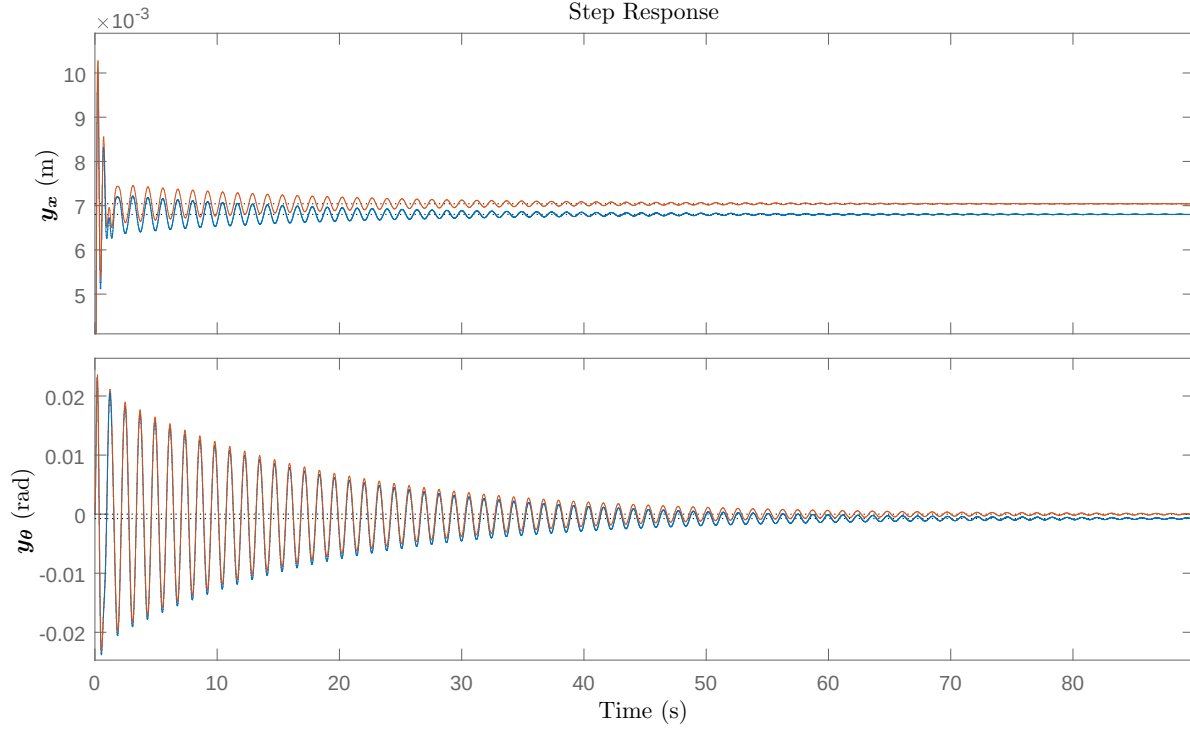


Figure 7.29 – Step Response graphs from the *OS* (red) and *IS* (blue) when $\overline{\text{VFR}} = 95.84\%$ for both outputs of the C-PEN system ($d_t = 0.02$ s).

1. $d_t = 0.01$ s

$$\mathbf{A} = \begin{bmatrix} 0.9916 & -1.61 \times 10^{-4} & 0.0097 & -9.45 \times 10^{-7} \\ -0.0239 & 0.9981 & -8.05 \times 10^{-4} & 0.01 \\ -1.6540 & -0.0319 & 0.9416 & -2.41 \times 10^{-4} \\ -4.7359 & -0.3724 & -0.1673 & 0.9972 \end{bmatrix}, \mathbf{B} = \begin{bmatrix} 5.88 \times 10^{-5} \\ 1.69 \times 10^{-4} \\ 0.0116 \\ 0.0334 \end{bmatrix}, \quad (7.2)$$

2. $d_t = 0.02$ s

$$\mathbf{A} = \begin{bmatrix} 0.9673 & -6.31 \times 10^{-4} & 0.0188 & -5.84 \times 10^{-6} \\ -0.0936 & 0.9926 & -0.0035 & 0.0199 \\ -3.1956 & -0.0616 & 0.8705 & -7.86 \times 10^{-4} \\ -9.1333 & -0.7369 & -0.3702 & 0.9907 \end{bmatrix}, \mathbf{B} = \begin{bmatrix} 2.30 \times 10^{-4} \\ 6.59 \times 10^{-4} \\ 0.0225 \\ 0.0643 \end{bmatrix}. \quad (7.3)$$

The state-space matrices from the best *IS* ($\overline{\text{VFR}} = 98.62\%$) have the following composition:

$$\mathbf{A} = \begin{bmatrix} 1.0030 & 0.0553 & 0.0081 & 3.55 \times 10^{-4} \\ -0.0583 & 0.9891 & -0.0094 & -0.0146 \\ -0.0189 & -0.0203 & 0.9749 & -0.1052 \\ 0.0041 & 0.0478 & 0.1445 & 0.9615 \end{bmatrix}, \mathbf{B} = \begin{bmatrix} -0.0393 \\ -0.1207 \\ -0.1438 \\ 0.2535 \end{bmatrix}, \quad (7.4)$$

$$C = \begin{bmatrix} -9.28 \times 10^{-4} & -0.0010 & -0.0024 & -0.0014 \\ 0.0037 & -0.0105 & -0.0061 & -0.0059 \end{bmatrix}.$$

And the state-space matrices from the worst *IS* ($\overline{\text{VFR}} = 95.84\%$) have the following composition:

$$A = \begin{bmatrix} 0.9895 & 0.1006 & 0.0122 & 0.0030 \\ -0.1153 & 0.9916 & -0.0189 & -0.0162 \\ -0.0271 & -0.0519 & 0.9161 & -0.2113 \\ 0.0108 & 0.0639 & 0.2818 & 0.9245 \end{bmatrix}, B = \begin{bmatrix} -0.0634 \\ -0.1557 \\ -0.2413 \\ 0.3359 \end{bmatrix}, \quad (7.5)$$

$$C = \begin{bmatrix} -9.63 \times 10^{-4} & -0.0012 & -0.0039 & -0.0016 \\ 0.0098 & -0.0145 & -0.0108 & -0.0071 \end{bmatrix}.$$

The transfer functions of the discrete-time systems with the state-space representation given by Equation (7.2) and Equation (7.4), for comparisons are:

- *OS* discretized with $d_t = 0.01$ s:

1. :

$$\frac{5.883 \times 10^{-5} z^3 - 5.963 \times 10^{-5} z^2 - 5.665 \times 10^{-5} z + 5.778 \times 10^{-5}}{z^4 - 3.929 z^3 + 5.806 z^2 - 3.826 z + 0.9489} \quad (7.6)$$

2. :

$$\frac{1.685 \times 10^{-4} z^3 - 1.714 \times 10^{-4} z^2 - 1.627 \times 10^{-4} z + 1.656 \times 10^{-4}}{z^4 - 3.929 z^3 + 5.806 z^2 - 3.826 z + 0.9489} \quad (7.7)$$

- *IS* with $\overline{\text{VFR}} = 98.62\%$:

1. :

$$\frac{1.715 \times 10^{-4} z^3 - 3.984 \times 10^{-4} z^2 - 2.831 \times 10^{-4} z - 5.589 \times 10^{-5}}{z^4 - 3.929 z^3 + 5.806 z^2 - 3.826 z + 0.9489} \quad (7.8)$$

2. :

$$\frac{4.898 \times 10^{-4} z^3 - 1.139 \times 10^{-3} z^2 - 8.088 \times 10^{-4} z - 1.594 \times 10^{-4}}{z^4 - 3.929 z^3 + 5.806 z^2 - 3.826 z + 0.9489} \quad (7.9)$$

The transfer functions of the *OS* and the best *IS* presented from Equation (7.6) to Equation (7.9) have precisely the same polynomial in the denominator, hence, showing that the respective systems have the same poles.

The transfer functions of the discrete-time systems with the state-space representation given by Equation (7.3) and Equation (7.5), for comparisons are:

- *OS* discretized with $d_t = 0.02$ s:

1. :

$$\frac{2.303 \times 10^{-4} z^3 - 2.352 \times 10^{-4} z^2 - 1.122 \times 10^{-4} z + 2.222 \times 10^{-4}}{z^4 - 3.821 z^3 + 5.545 z^2 - 3.623 z + 0.900} \quad (7.10)$$

2. :

$$\frac{6.591 \times 10^{-4} z^3 - 6.818 \times 10^{-4} z^2 - 6.137 \times 10^{-4} z + 6.364 \times 10^{-4}}{z^4 - 3.821 z^3 + 5.545 z^2 - 3.623 z + 0.900} \quad (7.11)$$

- *IS* with $\overline{\text{VFR}} = 95.84\%$:

1. :

$$\frac{6.481 \times 10^{-4} z^3 - 1.5 \times 10^{-3} z^2 - 1.069 \times 10^{-3} z + 2.121 \times 10^{-4}}{z^4 - 3.822 z^3 + 5.546 z^2 - 3.624 z + 0.901} \quad (7.12)$$

2. :

$$\frac{1.851 \times 10^{-3} z^3 - 4.32 \times 10^{-3} z^2 - 3.086 \times 10^{-3} z + 6.171 \times 10^{-4}}{z^4 - 3.822 z^3 + 5.546 z^2 - 3.624 z + 0.901} \quad (7.13)$$

The transfer functions of the *OS* and the worst *IS* presented from Equation (7.10) to Equation (7.13) offer a difference only at the third decimal place of each term from the polynomial in the denominator, hence, showing a small discrepancy between the system's poles.

A comparative analysis for the condition when the *OS* is implemented as the non-linear C-PEN system from the simulations previously presented in this section, and the situation with an *OS* implemented as the linearized C-PEN (state-space Equation (5.40)), is performed based on the results shown in Table 7.12. For the nonlinear *OS* was used the same simulations data prior presented in Table 7.10 and Table 7.11, and for the linearized *OS* the simulations were performed with the same data set of excitations and noises employed for the nonlinear *OS*. In the comparison of the results, it is evident, as expected, a great increase of $\Delta \overline{\text{VFR}}$ for the maximum and median statistical parameters when the *OS* is turned to be linearized. This difference is considerably higher when the sampling time increase from 0.01 s to 0.02 s. It should be pointed out that the gap between the nonlinear *OS* and the *IS* with the output \mathbf{y}_x in the step response for $d_t = 0.02$ s (Figure 7.29) does not happen to the linearized *OS*. In this

case, the curve from IS follows the OS curve without any deviation as the curves become more stable.

Table 7.12 – Comparative results of C-PEN system under nonlinear OS and linearized OS .

Configuration ⁽¹⁾	Statistical group	SSRA-DC-iCL	VFR _{y_x}	VFR _{y_θ}	$\overline{\text{VFR}}$	$\Delta\overline{\text{VFR}}$ ⁽²⁾
$d_t = 0.01,$ $q = 1600,$ $p = 800,$ $S_N = 0.3\%.$	Maximum	nonlinear OS	98.06%	99.32%	98.62%	–
		linearized OS	99.60%	99.75%	99.68%	1.06%
	Median	nonlinear OS	97.67%	98.63%	98.15%	–
		linearized OS	99.47%	99.35%	99.42%	1.27%
	Interquartile range	nonlinear OS	3.72%	16.63%	11.73%	–
		linearized OS	5.27%	20.31%	14.07%	-2.34%
	Unstable $IS^{(3)}$	nonlinear OS	1%	8%	1%	–
		linearized OS	1%	8%	1%	0%
$d_t = 0.01,$ $q = 1600,$ $p = 800,$ $S_N = 1\%.$	Maximum	nonlinear OS	97.68%	98.63%	97.99%	–
		linearized OS	98.57%	98.78%	98.63%	0.64%
	Median	nonlinear OS	97.15%	97.99%	97.61%	–
		linearized OS	98.22%	98.31%	98.30%	0.69%
	Interquartile range	nonlinear OS	0.70%	8.39%	4.61%	–
		linearized OS	1.13%	5.17%	3.29%	1.32%
	Unstable $IS^{(3)}$	nonlinear OS	0%	2%	0%	–
		linearized OS	0%	2%	0%	0%
$d_t = 0.02,$ $q = 2000,$ $p = 500,$ $S_N = 0.3\%.$	Maximum	nonlinear OS	94.99%	98.39%	96.69%	–
		linearized OS	99.53%	99.56%	99.53%	2.84%
	Median	nonlinear OS	94.05%	97.19%	95.55%	–
		linearized OS	99.37%	99.00%	99.21%	3.66%
	Interquartile range	nonlinear OS	0.49%	5.18%	2.77%	–
		linearized OS	0.82%	6.96%	3.83%	-1.06%
	Unstable $IS^{(3)}$	nonlinear OS	1%	6%	1%	–
		linearized OS	1%	6%	1%	0%
$d_t = 0.02,$ $q = 2000,$ $p = 500,$ $S_N = 1\%.$	Maximum	nonlinear OS	94.49%	97.79%	95.84%	–
		linearized OS	98.48%	98.63%	98.54%	2.70%
	Median	nonlinear OS	93.69%	96.56%	95.16%	–
		linearized OS	98.11%	97.89%	98.01%	2.85%
	Interquartile range	nonlinear OS	0.62%	8.59%	4.59%	–
		linearized OS	0.84%	7.47%	4.09%	0.50%
	Unstable $IS^{(3)}$	nonlinear OS	2%	8%	2%	–
		linearized OS	2%	7%	2%	0%

¹ Parameters adjusted with the same values for all simulations: $\xi = 2, \gamma = 2, i = 100, K_p = 0.05$.

² Improvement gain of linearized OS algorithm over nonlinear OS for the $\overline{\text{VFR}}$;

³ Percentual of unstable IS (Identified System) over the 100 simulations when $\text{VFR}_j = 0$ or $\overline{\text{VFR}} = 0$.

8 HIGHLIGHTS AND CONCLUDING REMARKS

8.1 Overview of the thesis⁶

In this work, we reviewed the Eigensystem Realization Algorithm's characteristics and features applied for MIMO systems (Chapter 4) when excited by a Pseudo Random Binary Sequence (PRBS) signal (Chapter 5) as a novelty in terms of input excitation to the ERA. Related to this first phase of the research, the simulations for a model with 5 degrees of freedom (M5DOF) aimed to show the influences of each parameter from the algorithm settings in the SI process's effectiveness. The Fit Rate index was employed as a quantitative tool to evaluate the SI performance to the overall research, substantially introduced in this phase, to work as a drive to achieve the best algorithm settings. Besides the PRBS signal in this phase, the Gaussian White-Noise signal (GWN) and the CHIRP signal were also employed as input excitation to compare the influence of each one in the identification process. The comparative analysis was introduced through two hundred simulations of the M100DOF system provided for each algorithm settings. Some parts presented throughout this chapter was published in the paper ([Soares Jr; Serpa, 2021](#)).

In the second phase of this work, regarding the more significant contribution, a new method stem from the State-Space Realization Algorithm with Data Correlation (SSRA-DC) was developed. The novel method aimed to improve an identification process of a system submitted to additive measurement noise with a reduced number of samples available for identification in the case of linear systems. For the nonlinear system C-PEN, this supposed condition of having a reduced number of samples was not evidenced as a requirement in the simulations, which was discussed in Section 7.9.2. The proposed method SSRA-DC-iCL (Section 4.4) supported by an iterative algorithm with the feedback of the Markov parameters matrix provided a relevant improvement of the Fit Rate index to MIMO systems originated from 50 and 100 degrees of freedom models compared to the SSRA-DC algorithm. The comparison showing the improvement was verified by statistical analysis from 100 simulations of each algorithm's settings. Beyond considering the output devices to measure the displacements in most of the systems considered in this research, a system with accelerometers as outputs was also used in

⁶ Some parts presented in this chapter were published in the papers ([Soares Jr; Serpa, 2021](#); [Soares Jr; Serpa, 2022](#)).

the identification process.

The third phase of the research counted on a comparative analysis (Section 7.8) of the new iterative SSRA-DC-iCL method and the classical SSRA-DC compared with the well-known methods available in the SI Toolbox of the Matlab. In this task, the Matlab methods were used under the same number of samples applied to simulations with the State-Space identification methods. The algorithm settings determining the size of the identified system was also considered to assure the same systems size for all the methods. The comparison considered the computational processing time (CPT) of each algorithm as one of the indicators, besides the maximum and median Validated Fit Rate ($\overline{\text{VFR}}$) index for portraying the SI performance along 100 simulations accomplished.

The fourth phase, regarding the simulations of a nonlinear Cart-Pendulum system of one excitation input (force) and two outputs (cart displacement and pendulum rod angle), followed a similar analysis performed in the third phase, although here, comparing the novel method only with the N4SID and ARMAX algorithms from the SI Toolbox of the Matlab.

8.2 Highlights from the results

The time response analysis of the SSRA for the M5DOF model summarized in Table 6.1 and Table 6.3 depicts the influence and how each algorithm parameter determines the $\overline{\text{VFR}}$ result. It could be seen that increasing the number of samples q helps to improve the results. Still, the parameter p should increase either, preferably following the specific ration q/p if this has been previously adjusted properly. The time response analysis to the SSRA also shows what is expected when the system order is closer to the true system order, leading the SI result to a better $\overline{\text{VFR}}$. In several of the algorithm settings, $\overline{\text{VFR}} = 100\%$ was achieved, indicating that an adjustment with lower parameter values should be considered in the way to minimize computational processing.

The reduction of the PRBS clock frequency ($\mathcal{C}_{\mathcal{F}}$) at the SSRA parameters analysis, revealed in Table 6.1, showed no impact on the Fit Rate results, evidencing that the persistently exciting characteristics of the excitation signal remain suitable for the identification process. In this situation, the displacement curves depicted a different delineation from the original one, which can be beneficial and more appropriate for some system characteristics that do not allow a high switching of a PRBS signal. Comparing the PRBS and GWN results for the M5DOF system simulated here (Table 6.4), the PRBS signal can be considered a feasible alternative in

system identification for structures like that used in this work. Thus, the PRBS signal arises as a non-usual excitation type to the SSRA, notably due to the signals properties, opening possibilities to the algorithm application in several areas of engineering beyond structural mechanics.

For the time response analysis, the three distinct sampling time values in the simulations of the M5DOF model did not make any substantial difference in the results at first glance, except for the need to increase the respective parameter values to obtain approximately the same $\overline{\text{VFR}}$ levels. For frequency response analysis, employing the Maximum Singular Values (MSV) diagrams, together with assessing the sampling frequencies appropriated to the system discretization, supported by the Nyquist Sampling theorem, the sampling time of $d_t = 0.02$ s was the only one suitable to be used for the SI process of the M5DOF system simulated.

The SSRA-DC-iCL method, which is supported by an iterative algorithm working with Markov parameters' feedback in a closed-loop, represents the main contribution of this research. The results described along the Chapter 7 show the benefits of the proposed SSRA-DC-iCL method when applied for MIMO systems in the presence of measurement noise. Analyzing the steps of SSRA-DC-iCL pictured in Figure 4.2 and detailed in the Algorithm 1, it can be realized the specific concepts of the algorithm that led to contributions concerning the traditional SSRA-DC algorithm. The boxplot graphs precisely portray the comparative statistical results between the novel and traditional method when submitted to 100 simulations for several algorithms settings and systems conditions.

In the comparative analysis phase for the M5DOF and M100DOF systems, both the iterative and non-iterative SSRA-DC method, mainly the new SSRA-DC-iCL, presented much better results for the MIMO systems tested than the well-known autoregressive methods from Matlabs SI toolbox. Despite having being close but not achieved the same $\overline{\text{VFR}}$ level of the N4SID method, the SSRA-DC-iCL was on average 13 times faster for the M5DOF system and more than 100 times faster for the M100DOF, which represents a relevant saving of CPT.

In the simulations of the mass-spring-damper systems, the SSRA-DC-iCL was configured with the gain K_p set as a variable value over the iterations; however, these M-DOF systems, except the M5DOF-a, could use the fixed K_p gain with equivalent performance. Contrarily, for the nonlinear C-PEN system, the application of a fixed K_p showed more smooth $\overline{\text{FR}}$ curves, achieving the expected improvement provided by the novel algorithm. When SSRA-DC-iCL was compared with N4SID for the simulations with C-PEN, an opposite result occurred due to a higher $\overline{\text{VFR}}$ now achieved by the iterative method, although the N4SID reached

a lower CPT value. In this case, the more pronounced CPT difference was less than four times, significantly less than the gap seen with the M100DOF system result. Despite the SSRA-DC-iCL having achieved better $\overline{\text{VFR}}$ results than the N4SID, both methods were overcome by the ARMAX with consistent results.

8.3 Concluding remarks

The first phase of this work proposed an approach to analyse the behavior and performance of the Eigensystem Realization Algorithm method for identifying a MIMO system of 5 degrees of freedom under different algorithm configurations. The Validated Fit Rate ($\overline{\text{VFR}}$) indicator applied to measure the adherence of the identified system reveals how the parameters of the algorithm influence the results and play an important role as a guide to indicate the best settings for the SSRA. The analysis of the simulation steps indicates that a more appropriate order of the identified system can be attained, working as a complementary tool to the already well-known methods to determine the system order.

The PRBS signal arises as a novelty for SSRA excitation, notably due to the properties of the signal, opening possibilities to the algorithm application in several areas of engineering beyond structural mechanics. Moreover, based on the PRBS specific characteristics, which are welcome as an useful and interesting excitation signal to the system identification process, it was proper to compare its application and the individual results to the SSRA with the other types of excitation signals. This task was performed with GWN and CHIRP signals' employment at some of the simulations presented in Section 6.5.

Even though it was not so evident for time response analysis, the results of the M5DOF system also indicated the expected effect of increasing the sampling frequency to improve the system identification in the frequency response analysis. Furthermore, it would avoid sampling frequencies that can cause the identified system to lose some of its natural frequencies. This aspect was verified using the Fit Rate indicator applied to the Maximum Singular Values, instead of having the FR calculated for the system outputs, which allowed a different and more suitable analysis perspective of MIMO systems identified by the SSRA. However, to get better FR results in the frequency response analysis, the sampling frequency increment commonly leads to an increase in the length of the Hankel matrix, which in turn induces the amplification of computational processing, especially for large MIMO systems.

The SSRA-DC-iCL method is the meaningful contribution of this work as an ap-

appropriate algorithm for working with MIMO systems and in the presence of measurement noise from the process. The choice of more appropriated weighting factor (parameter ℓ) or directly the gain K_p can take a crucial role in the algorithm settings, influencing the effectiveness of the results in terms of both the $\overline{\text{VFR}}$ achieved and the number of iterations required. For instance, while the employment of a higher gain can be interesting to obtain a better fit rate with fewer iterations, depending on the system's characteristics and input-output data set, the gain augmented can promote significant oscillations. This trouble can lead the fit rate values to drop abruptly, which underscores this iterative algorithm's core objective: to achieve the highest fit rate independently of its broad variability. Also, severe drops of $\overline{\text{VFR}}$ can occur, or even some iterations lost when $\overline{\text{VFR}} = 0$, which means the algorithm lost the convergence. An example is the good $\overline{\text{VFR}} = 99.04\%$ attained for the M100DOF system simulated with $S_N = 0.3\%$ (Table 7.3) despite the substantial number of 36% unstable *IS*. On the other hand, the employment of lower K_p values can lead to a smoother fit rate evolution curve, however with longer time to the attainment of better $\overline{\text{VFR}}$ results, which sometimes can not be possible or even feasible.

It could be realized, as stated at Section 7.5.2 (Table 7.3), that a combination of small number of samples with lower level of measurement noise ($S_N = 0.3\%$ in that case) can lead the algorithm to lose the convergence through the unbounded drop of the $\overline{\text{FR}}$. Given these conditions, in the respective simulations, it was seen that the increase of measurement noise minimized or even ceased the convergence loss in the iterative identification process, where the value dropped from 36% to only 3% in the $\overline{\text{VFR}}$ indicator. Another alternative would be the growth of the number of samples. Still, in this case, depending on the increased amount, it will go against the SSRA-DC-iCL algorithm assumptions for the systems simulated.

Notwithstanding the close performance of the iterative SSRA-DC-iCL algorithm concerning the N4SID for large linear MIMO systems in a noisy plant, demanding much less computational processing time, one drawback of the SSRA-DC-iCL is the number of algorithm's parameters required to be configured. The SSRA-DC-iCL algorithm needs to set the parameter p stem from the classical SSRA and define the gain through the adjustment of ℓ or K_p . Still, for the data correlation issue, it should also be considered the configuration of the parameters ξ and γ (Equation (4.52)). N4SID requires definition and adjustment of only d_t , q , and n , which is either part of the classical SSRA configuration and therefore they are also required for SSRA-DC-iCL. Except for the order n that can count on specific techniques to be met as mentioned in this work, the other two parameters are part of input-output data set definitions. It

should be pointed out that an appropriate knowledge about the iterative SSRA-DC-iCL method proposed in this research can lead the algorithm settings to be a more straightforward and brief task. With a proper understanding of the algorithm, one can make more assertive parameters choices with fewer trials of algorithm execution, making these methods an attractive algorithm for the SI process of large MIMO systems in a noisy plant.

The simulation results with the nonlinear C-PEN provided an additional assessment to the simulations performed with the linear M50DOF and M100DOF. Besides the inherent nonlinearities of the C-PEN model, another difference relates to the smaller size of the SIMO system C-PEN, which should be considered in the analysis of the results. The $\overline{\text{VFR}}$ values attained in the nonlinear SIMO system with a lower magnitude compared to the linear MIMO systems reflect the condition of a nonlinear system being identified by methods that generate the representation in state-space of linear systems. This statement can be supported when comparing, in Table 7.12, the nonlinear system results with the values attained in the simulations of the linearized C-PEN for the same configurations of algorithms and systems. Even so, the iterative SSRA-DC-iCL showed up identification effectiveness, measured by the $\overline{\text{VFR}}$, much better than the conventional SSRA-DC and a little better than the N4SID. Although, for this kind of MIMO system with a considerably smaller size, despite being a nonlinear system, the autoregressive method ARMAX presented $\overline{\text{VFR}}$ results significantly better than the state-space methods. Moreover, for complying with a suitable CPT value and not overdone in the SSRA-DC-iCL running when simulating the nonlinear C-PEN, the novel method strengthens its range of applications, covering linear and possibly nonlinear MIMO systems for wider sizes.

8.4 Possible future works

The K_p gain setting, determined by the variable ℓ , directly influences the perspective of enhancing the Markov matrix updating control. Another option of this updating comes from a fixed K_p value. When considered for improvement opportunities, both options can yield identified systems with higher fit rate values and reduce the possibilities of convergence loss along the iterative process, as well as reduce the number of iterations to the achievement of higher $\overline{\text{VFR}}$ levels awaited. A broad study about input-output data set (Markov parameters) updating control for the iterative SSRA-DC-iCL can be considered feasible and suitable for this objective.

The losing of convergence of the SSRA-DC-iCL algorithm, characterized by the

unbounded drop of the fit rate, which depends on the algorithm's input data set, can be better studied about its causes in detail. These occurrences showed that a combination of a small number of samples with a low level of measurement noise triggers the process of convergence loss of the algorithm. The conditions related to these causes point out that the trace of the diagonal matrix Σ_n (Equation (4.29)), coming from the SVD of the Hankel matrix, gets lower than a minimum value expected to avoid ill-conditioned of the matrices involved on the state-space realization. The Regularisation technique, as recently approached in the work of Ljung et al. (Ljung *et al.*, 2020b), could be suggested in this case to improve the conditioning of the respective matrices.

It is noteworthy that the SSRA-DC-iCL algorithm was not concerned with programming techniques that would lead to greater efficiency in terms of less computational processing time. The algorithm evolution for the advancement and optimization of computational processing can be an interesting development encompassing other improvement proposals mentioned in this section.

Based on research for the developments described, expanding the overall scope of the cases in applying the iterative method to larger MIMO systems and higher levels or different characteristics of additive noise would be an even more challenge, raising the algorithm's application outlook. Additionally, the methods' application in a real plant could complement this work evolution. This scenario would lead to takeaways and ascertain the algorithm's effectiveness under nonlinear conditions inherently to the process, which occurs and comes from instrumentation noises to some degree in mechanical structural systems (Juang, 1994). The simulations with a typical nonlinear system in its dynamical characteristics also came as an opportunity to expand the study of applications of the novel method for nonlinear MIMO systems with larger sizes and broader features.

BIBLIOGRAPHY

- Aguirre, L. A. **Enciclopédia de Automática - Controle & Automação, volume 3**. 1. ed. São Paulo: Editora Blucher, 2007. 469 p. ISBN 978-85-212-0410-7.
- Aguirre, L. A. **Introdução à Identificação de Sistemas**. 4. ed. Belo Horizonte: Editora UFMG, 2015. ISBN 978-85-423-0079-6.
- Albertos, P.; Sala, A.; Chadli, M. **Multivariable control systemsan engineering approach**. [S.l.: s.n.], 2005. v. 41. 1665–1666 p. ISSN 00051098.
- Alenany, A.; Westwick, D.; Shang, H. A modified observer/Kalman filter identification (OKID) algorithm employing output residuals. **International Journal of Dynamics and Control**, v. 7, n. 2, p. 636–643, 2019.
- Amari, S. I.; Cichocki, A. Adaptive blind signal processing - Neural network approaches. **Proceedings of the IEEE**, v. 86, n. 10, p. 2026–2048, 1998.
- Åström, K. **Lectures on the identification problem the least squares method**. [S.l.], 1968.
- Åström, K. J.; Eykhoff, P. System identification-A survey. **Automatica**, v. 7, n. 2, p. 123–162, 1971.
- Åström, K.-J.; Torsten, B. Numerical Identification of Linear Dynamic Systems from Normal Operating Records. **IFAC Proceedings Volumes**, v. 2, n. 2, p. 96–111, 1965.
- Balakrishnan, A. V.; Peterka, V. Identification in automatic control systems. **Automatica**, v. 5, n. 6, p. 817–829, 1969.
- Ben-Israel, Adi and Greville, T. N. **Generalized inverses: theory and applications**. Second. New York, USA: Springer Science & Business Media, 2003. ISBN 0-387-00293-6.
- Benesty, J.; Mohan Sondhi, M.; Huang, Y. **Handbook of Speech Processing**. [S.l.]: Springer Science & Business Media, 2008. 1043–1046 p. ISBN 9783540491255.
- Bluestein, L. I. A Linear Filtering Approach to the Computation of Discrete Fourier Transform. **IEEE Transactions on Audio and Electroacoustics**, v. 18, n. 4, p. 451–455, 1970.
- Boghani, H. C.; Kim, J. R.; Dinsdale, R. M.; Guwy, A. J.; Premier, G. C. Analysis of the dynamic performance of a microbial fuel cell using a system identification approach. **Journal of Power Sources**, v. 238, p. 218–226, 2013.
- Brecher, C.; Fey, M.; Brockmann, B.; Chavan, P. Multivariable control of active vibration compensation modules of a portal milling machine. **Journal of Vibration and Control**, v. 24, n. 1, p. 3–17, 2018.
- Briggs, P.; Godfrey, K. Pseudorandom signals for the dynamic analysis of multivariable systems. **Proceedings of the Institution of Electrical Engineers**, v. 113, n. 7, p. 1259–1267, 1966.

Butcher, M.; Giustiniani, A.; Masi, A. On the identification of Hammerstein systems in the presence of an input hysteretic nonlinearity with nonlocal memory: Piezoelectric actuators - An experimental case study. **Physica B: Condensed Matter**, v. 486, p. 101–105, 2016.

Caicedo, J. M. Practical guidelines for the natural excitation technique (NExT) and the eigensystem realization algorithm (ERA) for modal identification using ambient vibration. **Experimental Techniques**, v. 35, n. 4, p. 52–58, 2011.

Caicedo, J. M.; Dyke, S. J.; Johnson, E. A. Natural excitation technique and Eigensystem realization algorithm for phase I of the IASC-ASCE benchmark problem: Simulated data. **Journal of Engineering Mechanics**, v. 130, n. 1, p. 49–60, 2004.

Carter, B.; Mancini, R. **Op Amps for Everyone**. [S.l.: s.n.], 2003. 1–438 p. ISBN 9780750677011.

Chang, M.; Pakzad, S. N. Modified Natural Excitation Technique for Stochastic Modal Identification. **Journal of Structural Engineering**, v. 139, n. 10, p. 1753–1762, 2013.

Chen, C. T. **Linear System Theory and Design**. [S.l.]: Oxford University Press, 1984.

Chen, G. W.; Chen, X.; Omenzetter, P. Modal parameter identification of a multiple-span post-tensioned concrete bridge using hybrid vibration testing data. **Engineering Structures**, v. 219, n. December 2019, p. 110953, 2020.

Chen, T.; Ohlsson, H.; Ljung, L. On the estimation of transfer functions, regularizations and Gaussian processes-Revisited. **Automatica**, v. 48, n. 8, p. 1525–1535, 2012.

Chen, T.; Zhao, Y.; Ljung, L. **Impulse response estimation with binary measurements: A regularized FIR model approach**. IFAC, 2012. v. 16. 113–118 p. ISSN 14746670. ISBN 9783902823069.

Chen, X.; Zhao, S.; Liu, F. Identification of jump Markov autoregressive exogenous systems with missing measurements. **Journal of the Franklin Institute**, v. 357, n. 6, p. 3498–3523, 2020.

Chiang, D. Y.; Lin, C. S. Identification of modal parameters from ambient vibration data using eigensystem realization algorithm with correlation technique. **Journal of Mechanical Science and Technology**, v. 24, n. 12, p. 2377–2382, 2010.

Chiang, D. Y.; Lin, C. S.; Su, F. H. Identification of modal parameters from ambient vibration data by modified eigensystem realization algorithm. **Journal of Aeronautics, Astronautics and Aviation**, v. 42, n. 2, p. 79–86, 2010.

Choi, W. C.; Kim, N. W. Experimental study on active vibration control of a flexible cantilever using an artificial neural-network state predictor. **Smart Materials and Structures**, v. 5, n. 6, p. 751–758, 1996.

De Callafon, R. A.; Moaveni, B.; Ponte, J. P.; He, X.; Udd, E. General realization algorithm for modal identification of linear dynamic systems. **Journal of Engineering Mechanics**, v. 134, n. 9, p. 712–722, 2008.

Eykhoff, P. Process parameter and state estimation. **Automatica**, v. 4, n. 4, p. 205–233, 1968.

- Fairweather, A. J.; Foster, M. P.; Stone, D. A. Battery parameter identification with Pseudo Random Binary Sequence excitation (PRBS). **Journal of Power Sources**, v. 196, n. 22, p. 9398–9406, 2011.
- Fairweather, A. J.; Foster, M. P.; Stone, D. A. Modelling of VRLA batteries over operational temperature range using Pseudo Random Binary Sequences. **Journal of Power Sources**, v. 207, p. 56–59, 2012.
- Fisher, R. A. On an absolute criterion for fitting frequency curves. **Messenger of Mathematics**, v. 41, p. 155–156, 1912.
- Fuentes, R.; Nayek, R.; Gardner, P.; Dervilis, N.; Rogers, T.; Worden, K.; Cross, E. J. Equation discovery for nonlinear dynamical systems: A Bayesian viewpoint. **Mechanical Systems and Signal Processing**, v. 154, 2021.
- Gabano, J. D.; Poinot, T.; Kanoun, H. Identification of a thermal system using continuous linear parameter-varying fractional modelling. **IET Control Theory and Applications**, v. 5, n. 7, p. 889–899, 2011.
- Garrido, H.; Curadelli, O.; Ambrosini, D. A heuristic approach to output-only system identification under transient excitation. **Expert Systems with Applications**, v. 68, p. 11–20, 2017.
- Gawronski, W. **Advanced Structural Dynamics And Active Control Of Structures**. [S.l.: s.n.], 2005. v. 50. 419 p. ISSN 15582523. ISBN 0-387-40649-2.
- Ghee Koh, C.; Ming See, L.; Balendra, T. Damage Detection of Buildings: Numerical and Experimental Studies. **Journal of Structural Engineering**, v. 121, n. 8, p. 1155–1160, 1995.
- Giordano, G.; Sjöberg, J. Black- and white-box approaches for cascaded tanks benchmark system identification. **Mechanical Systems and Signal Processing**, v. 108, p. 387–397, 2018.
- Gopinath, B. On the Identification of Linear TimeInvariant Systems from InputOutput Data. **Bell System Technical Journal**, v. 48, n. 5, p. 1101–1113, 1969.
- Gu, Y.; Wei, H. L. A robust model structure selection method for small sample size and multiple datasets problems. **Information Sciences**, v. 451-452, p. 195–209, 2018.
- Han, S. Measuring displacement signal with an accelerometer. **Journal of Mechanical Science and Technology**, v. 24, n. 6, p. 1329–1335, 2010.
- Hazra, B., A. J. Roffel, S. Narasimhan; Pandey, M. D. Modified cross-correlation method for the blind identification of structures. 2009.
- Ho, B. L.; Kalman, R. E. Effective construction of linear state-variable models from input/output functions. **At-Automatisierungstechnik**, v. 14, n. 1-12, p. 545–548, 1966.
- Hou, D.; Hsu, C. S. State-space model identification with data correlation. **International Journal of Control**, v. 53, n. 1, p. 181–192, 1991.
- Inc., Q. **User's Manual: Pendulum Experiment**. [S.l.]: QUANSER, 2012.
- James, G.; Carne, T.; Lauffer, J. The natural excitation technique (NExT) for modal parameter extraction from operating structures. **Modal Analysis-the International Journal of Analytical and Experimental Modal Analysis**, v. 10, n. 4, p. 260, 1995.

Juang, J. N. **Applied System Identification**. Upper Saddle River, USA: Prentice Hall PTR, 1994. v. 3. 1051–1052 p. ISBN 0-13-079211-X.

Juang, J. N.; Cooper, J. E.; Wright, J. R. Eigensystem Realization Algorithm using data correlations (ERA/DC) for modal parameter identification. **Control, theory and advanced technology**, v. 4, n. 1, p. 5–14, 1988.

Juang, J. N.; Pappa, R. S. An eigensystem realization algorithm for modal parameter identification and model reduction. **Journal of Guidance, Control, and Dynamics**, v. 8, n. 5, p. 620–627, 1985.

Juang, J. N.; Pappa, R. S. Effects of noise on modal parameters identified by the eigensystem realization algorithm. **Journal of Guidance, Control, and Dynamics**, v. 9, n. 3, p. 294–303, 1986.

Juang, J. N.; Phan, M.; Horta, L. G.; Longman, R. W. Identification of observer/kalman filter markov parameters - theory and experiments. **Journal of Guidance, Control, and Dynamics**, v. 16, n. 2, p. 320–329, 1993.

Jer-Nan Juang, M. P. Identification of System, Observer, and Controller from Closed-Loop Experimental Data. **Journal of Guidance, Control, and Dynamics**, v. 17, n. 1, p. 91–96, 1994.

Kailath, T. **Linear Systems**. [S.l.]: Prentice-Hall Englewood Cliffs, 1980. ISBN 0-13-536961-4.

Karimshoushtari, M.; Novara, C. Design of experiments for nonlinear system identification: A set membership approach. **Automatica**, v. 119, 2020.

Katayama, T. **Subspace Methods for System Identification**. [S.l.]: Springer Science & Business Media, 2005. 1–392 p. ISSN 21977119.

Kerschen, G.; Poncelet, F.; Golinvall, J. C. Physical interpretation of independent component analysis in structural dynamics. **Mechanical Systems and Signal Processing**, v. 21, n. 4, p. 1561–1575, 2007.

Kramer, B.; Gorodetsky, A. A. System identification via cur-factored hankel approximation. **SIAM Journal on Scientific Computing**, v. 40, n. 2, p. A848—A866, 2018.

Kramer, B.; Gugercin, S. Tangential interpolation-based eigensystem realization algorithm for MIMO systems. **Mathematical and Computer Modelling of Dynamical Systems**, v. 22, n. 4, p. 282–306, 2016.

Kung, S. A New Identification and Model Reduction Algorithm via Singular Value Decomposition. **Twelfth Asilomar Conference on Circuits, Systems and Computers**, p. 705–714, 1978.

Lee, P. J.; Vítkovský, J. P.; Lambert, M. F.; Simpson, A. R.; Liggett, J. Leak location in pipelines using the impulse response function. **Journal of Hydraulic Research**, v. 45, n. 5, p. 643–652, 2007.

Li, P.; Hu, S. L.; Li, H. J. Noise issues of modal identification using eigensystem realization algorithm. **Procedia Engineering**, v. 14, p. 1681–1689, 2011.

Li, X.; Jiang, T.; Yuan, H.; Cui, H.; Li, F.; Li, G.; Jia, H. An eigensystem realization algorithm based data-driven approach for extracting electromechanical oscillation dynamic patterns from synchrophasor measurements in bulk power grids. **International Journal of Electrical Power and Energy Systems**, v. 116, p. 105549, 2020.

Liu, X.; Yang, X.; Yu, M. Identification of switched FIR systems with random missing outputs: A variational Bayesian approach. **Journal of the Franklin Institute**, v. 358, n. 1, p. 1136–1151, 2021.

Ljung and Soderstrom. **Theory and practice of recursive identification**. London: MIT press, 1983. v. 30. ISSN 0018-9286.

Ljung, L. **Characterization of the Concept of ‘Persistently Exciting’ in the Frequency Domain**. [S.l.], 1971.

Ljung, L. **On The Consistency of Prediction Error Identification Methods**. [S.l.], 1976. v. 126, n. C, 121–164 p.

Ljung, L. **System identification: Theory for the user**. 2nd edition. ed. Upper Saddle River, USA: Prentice Hall PTR, 1999. ISSN 09594388. ISBN 0136566952.

Ljung, L. Perspectives on system identification. **Annual Reviews in Control**, v. 34, n. 1, p. 1–12, 2010.

Ljung, L. **System identification**. [S.l.], 2010. 1275–1314 p. Disponível em: <<http://www.control.isy.liu.se/publications>>.

Ljung, L. On Convexification of System Identification Criteria. **Automation and Remote Control**, v. 80, n. 9, p. 1591–1606, 2019.

Ljung, L.; Andersson, C.; Tiels, K.; Schön, T. B. Deep learning and system identification. **IFAC-PapersOnLine**, v. 53, n. 2, p. 1175–1181, 2020.

Ljung, L.; Chen, T.; Mu, B. A shift in paradigm for system identification. **International Journal of Control**, v. 93, n. 2, p. 173–180, 2020.

Ljung, Lennart. **System Identification Toolbox User’s Guide**. Version 9. Natick, MA: The MathWorks, Inc., 2014.

Longman, R. W.; Juang, J. N. Recursive form of the eigensystem realization algorithm for system identification. **Journal of Guidance, Control, and Dynamics**, v. 12, n. 5, p. 647–652, 1989.

MacWilliams, F. J.; Sloane, N. J. Pseudo-Random Sequences and Arrays. **Proceedings of the IEEE**, v. 64, n. 12, p. 1715–1729, 1976.

Masti, D.; Bemporad, A. Learning nonlinear statespace models using autoencoders. **Automatica**, v. 129, 2021.

McConnell, K. G.; Cappa, P. Transducer inertia and stinger stiffness effects on FRF measurements. **Mechanical Systems and Signal Processing**, v. 14, n. 4, p. 625–636, 2000.

McNeill, S. I.; Zimmerman, D. C. A framework for blind modal identification using joint approximate diagonalization. **Mechanical Systems and Signal Processing**, v. 22, n. 7, p. 1526–1548, 2008.

- Miao, B.; Zane, R.; Maksimović, D. System identification of power converters with digital control through cross-correlation methods. **IEEE Transactions on Power Electronics**, v. 20, n. 5, p. 1093–1099, 2005.
- Moaveni, B.; Masoumi, Z. Modifying the ERA and fast ERA to improve operational performance for structural system identification. **Mechanical Systems and Signal Processing**, v. 120, p. 664–692, 2019.
- Mohanty, P.; Rixen, D. J. Modified ERA method for operational modal analysis in the presence of harmonic excitations. **Mechanical Systems and Signal Processing**, v. 20, n. 1, p. 114–130, 2006.
- Montonen, J. H.; Nevaranta, N.; Lindh, T.; Alho, J.; Immonen, P.; Pyrhonen, O. Experimental Identification and Parameter Estimation of the Mechanical Driveline of a Hybrid Bus. **IEEE Transactions on Industrial Electronics**, v. 65, n. 7, p. 5921–5930, 2018.
- Narazaki, Y.; Hoskere, V.; Spencer, B. F. Free vibration-based system identification using temporal cross-correlations. **Structural Control and Health Monitoring**, v. 25, n. 8, p. e2207, 2018.
- Nelles, O. **Nonlinear system identification: from classical approaches to neural networks and fuzzy models**. [S.l.: s.n.], 2001. 785 p. ISBN 978-3-642-08674-8.
- Nevaranta, N.; Derammelaere, S.; Parkkinen, J.; Vervisch, B.; Lindh, T.; Niemelä, M.; Pyrhönen, O. Online identification of a two-mass system in frequency domain using a Kalman filter. **Modeling, Identification and Control**, v. 37, n. 2, p. 133–147, 2016.
- Nguyen, S. T. N.; Gong, J.; Lambert, M. F.; Zecchin, A. C.; Simpson, A. R. Least squares deconvolution for leak detection with a pseudo random binary sequence excitation. **Mechanical Systems and Signal Processing**, v. 99, p. 846–858, 2018.
- Nikiforuk, P. N.; Gupta, M. M. A bibliography on the properties, generation and control system applications of shift-register sequences. **International Journal of Control**, v. 9, n. 2, p. 217–234, 1969.
- Ninness, B. Some system identification challenges and approaches. **IFAC Proceedings Volumes (IFAC-PapersOnline)**, v. 15, n. PART 1, p. 1–20, 2009.
- Phan, M.; Juang, J. N.; Horta, L. G.; Longman, R. W. System identification from closed-loop data with known output feedback dynamics. **Journal of Guidance, Control, and Dynamics**, v. 17, n. 4, p. 661–669, 1994.
- Phan, M.; Juang, J. N.; Longman, R. W. On Markov parameters in system identification. **Proceedings of the International Modal Analysis Conference - IMAC**, v. 2, n. October 1991, p. 1415–1421, 1991.
- Piga, D.; Cox, P.; Tóth, R.; Laurain, V. LPV system identification under noise corrupted scheduling and output signal observations. **Automatica**, v. 53, p. 329–338, 2015.
- Pillonetto, G.; Dinuzzo, F.; Chen, T.; De Nicolao, G.; Ljung, L. Kernel methods in system identification, machine learning and function estimation: A survey. **Automatica**, v. 50, n. 3, p. 657–682, 2014.

Pintelon, R.; Schoukens, J. **System Identification: A Frequency Domain Approach, Second Edition**. [S.l.]: John Wiley & Sons, 2012. ISBN 9780470640371.

Qin, S. J.; Lin, W.; Ljung, L. A novel subspace identification approach with enforced causal models. **Automatica**, v. 41, n. 12, p. 2043–2053, 2005.

Rehman, N. H.; Verma, N. Application of Modified Multi Model Predictive Control Algorithm to Fluid Catalytic Cracking Unit. **arXiv e-prints**, p. 1405, 2014.

Roll, J.; Nazin, A.; Ljung, L. Nonlinear system identification via direct weight optimization. **Automatica**, v. 41, n. 3, p. 475–490, 2005.

Rossen, R. H.; Lapidus, L. Minimum realizations and system modeling: II. Theoretical and numerical extensions. **AIChE Journal**, v. 18, n. 5, p. 881–892, 1972.

Roy, R.; Lowenschuss, O. Chirp waveform generation using digital samples. **IEEE Transactions on Aerospace and Electronic Systems**, n. 1, p. 10–16, 1974.

Sarvat Mushtaq Ahmad, b. B. **Modelling and Control of a Twin Rotor MIMO System**. 161 p. Thesis (Ph.D.) — The University of Sheffield, 2001.

Schoukens, M.; Noël, J. P. Three Benchmarks Addressing Open Challenges in Nonlinear System Identification. **IFAC-PapersOnLine**, v. 50, n. 1, p. 446–451, 2017.

Schragl, P.; Tkachenko, P.; Del Re, L. Iterative Model Identification of Nonlinear Systems of Unknown Structure: Systematic Data-Based Modeling Utilizing Design of Experiments. **IEEE Control Systems**, v. 40, n. 3, p. 26–48, 2020.

Shariff, H. M.; Fazalul Rahiman, M. H.; Tajjudin, M. Nonlinear system identification: Comparison between PRBS and Random Gaussian perturbation on steam distillation pilot plant. **Proceedings - 2013 IEEE 3rd International Conference on System Engineering and Technology, ICSET 2013**, p. 269–274, 2013.

Silverman, L. M. Realization of Linear Dynamical Systems. **IEEE Transactions on Automatic Control**, v. 16, n. 6, p. 554–567, 1971.

Soares Jr, D.; Serpa, A. L. An evaluation of the influence of eigensystem realization algorithm settings on multiple input multiple output system identification. **Journal of Vibration and Control**, v. 0, n. 0, p. to appear, 2021.

Soares Jr, D.; Serpa, A. L. An iterative state-space identification method with data correlation for MIMO systems with measurement noise. **Journal of the Franklin Institute**, v. 359, n. 11, p. 5682–5711, 2022.

Soderstrom; Stoica. **System Identification**. [S.l.]: Prentice Hall International, 1989. ISBN 0-13-881236-5.

Song, B. G.; Ritcey, J. A. Prefilter design using the singular value decomposition for MIMO equalization. **Conference Record of the Asilomar Conference on Signals, Systems and Computers**, v. 1, p. 34–38, 1997.

Stigler, S. M. Gauss and the Invention of Least Squares. **The Annals of Statistics**, v. 9, p. 465–474, 1981.

Tangirala, Arun K. **Principles of System Identification: Theory and Practice [Bookshelf]**. Boca Raton, FL, USA: [s.n.], 2017. v. 37. 181–184 p. ISSN 1066-033X.

Taylor, J.; Noble, B.; Daniel, J. W. **Applied Linear Algebra**. [S.l.]: Prentice-Hall, 1988. v. 72. 335 p. ISSN 00255572.

Tether. Construction of Minimal Linear State-Variable Models from Finite Input-Output Data. **IEEE Transactions on Automatic Control**, v. 17, n. 1, p. 173–175, 1970.

To, K. W.; David, A. K. On-line identification and control of an AC/DC power system. **International Journal of Electrical Power and Energy Systems**, v. 18, n. 4, p. 223–227, 1996.

Uyanlk, I.; Ankarall, M. M.; Cowan, N. J.; Saranll, U.; Morgül, Ö. Identification of a vertical hopping robot model via harmonic transfer functions. **Transactions of the Institute of Measurement and Control**, v. 38, n. 5, p. 501–511, 2015.

Van Overschee, P.; De Moor, B. N4SID: Subspace algorithms for the identification of combined deterministic-stochastic systems. **Automatica**, v. 30, n. 1, p. 75–93, 1994.

Van Overschee, P.; De Moor, B. **Subspace Identification for Linear Systems**. Boston/London/Dordrecht: KLUWER ACADEMIC PUBLISHERS, 1996. ISBN 9781461304654.

Viberg, M. Subspace methods in system identification. **IFAC Proceedings Volumes**, v. 27, n. 8, p. 1–12, 1994, iFAC Symposium on System Identification (SYSID'94), Copenhagen, Denmark, 4-6 July.

Viberg, M. Subspace-based methods for the identification of linear time-invariant systems. **Automatica**, v. 31, n. 12, p. 1835–1851, 1995.

Vicario, F.; Phan, M. Q.; Betti, R.; Longman, R. W. OKID via output residuals: A converter from stochastic to deterministic system identification. **Journal of Guidance, Control, and Dynamics**, v. 40, n. 12, p. 3226–3238, 2017.

Vuojolainen, J.; Nevaranta, N.; Jastrzebski, R.; Pyrhonen, O. Comparison of Excitation Signals in Active Magnetic Bearing System Identification. **Modeling, Identification and Control**, v. 38, n. 3, p. 123–133, 2017.

Yang, Y.; Nagarajaiah, S. Time-frequency blind source separation for output-only modal identification using independent component analysis. **Safety, Reliability, Risk and Life-Cycle Performance of Structures and Infrastructures - Proceedings of the 11th International Conference on Structural Safety and Reliability, ICOSSAR 2013**, p. 1977–1983, 2013.

Yao, X. J.; Yi, T. H.; Qu, C.; Li, H. N. Blind Modal Identification in Frequency Domain Using Independent Component Analysis for High Damping Structures with Classical Damping. **Computer-Aided Civil and Infrastructure Engineering**, v. 33, n. 1, p. 35–50, 2018.

Yi, T. H.; Yao, X. J.; Qu, C. X.; Li, H. N. Blind modal identification in frequency domain for high damping structures through independent component analysis. **9th International Conference on Structural Health Monitoring of Intelligent Infrastructure: Transferring Research into Practice, SHMII 2019 - Conference Proceedings**, v. 2, p. 1491–1499, 2019.

Yi, T.-H.; Yao, X.-J.; Qu, C.-X.; Li, H.-N. Clustering Number Determination for Sparse Component Analysis during Output-Only Modal Identification. **Journal of Engineering Mechanics**, v. 145, n. 1, p. 04018122, 2019.

Yin, Y.; Živanović, S.; Li, D. Displacement modal identification method of elastic system under operational condition. **Nonlinear Dynamics**, v. 70, n. 2, p. 1407–1420, 2012.

Yu, K.; Yang, K.; Bai, Y. Estimation of modal parameters using the sparse component analysis based underdetermined blind source separation. **Mechanical Systems and Signal Processing**, v. 45, n. 2, p. 302–316, 2014.

Zadeh, L. A. On the Identification Problem. **IRE Transactions on Circuit Theory**, v. 3, n. 4, p. 277–281, 1956.

Zhang, G.; Ma, J.; Chen, Z.; Wang, R. Automated eigensystem realisation algorithm for operational modal analysis. **Journal of Sound and Vibration**, v. 333, n. 15, p. 3550–3563, 2014.

APPENDIX A – MATHEMATICAL DEVELOPMENT OF THE SSRA WITH DATA CORRELATION

The concepts presented in this topic was supported by the reference (Juang, 1994). Firstly, repeating the Hankel matrix in the format as represented in Equation (4.51), it follows:

$$\mathbf{H}_0 = \begin{bmatrix} \mathbf{H}_v(1) & \mathbf{H}_v(2) & \dots & \mathbf{H}_v(\beta) \\ \mathbf{H}_v(2) & \mathbf{H}_v(3) & \dots & \mathbf{H}_v(\beta + 1) \\ \vdots & \vdots & \ddots & \vdots \\ \mathbf{H}_v(\alpha) & \mathbf{H}_v(\alpha + 1) & \dots & \mathbf{H}_v(\alpha + \beta - 1) \end{bmatrix}. \quad (\text{A.1})$$

It can be noted that Equation (A.1) represents the Hankel matrix from the classical SSRA, then, analogously, the following equation can be introduced:

$$\mathbf{H}_{k-1} = \mathbf{O}_\alpha \mathbf{A}^{k-1} \mathbf{W}_\alpha, \quad (\text{A.2})$$

with

$$\mathbf{O}_\alpha = \begin{bmatrix} \mathbf{C} \\ \mathbf{CA} \\ \mathbf{CA}^2 \\ \vdots \\ \mathbf{CA}^{\alpha-1} \end{bmatrix}, \text{ and } \mathbf{W}_\alpha = \begin{bmatrix} \mathbf{B} & \mathbf{AB} & \mathbf{A}^2\mathbf{B} & \dots & \mathbf{A}^{\alpha-1}\mathbf{B} \end{bmatrix},$$

where \mathbf{H}_{k-1} is a generalized Hankel matrix, thus the Hankel matrix is taken with $k = 1$ and the shift Hankel matrix when $k = 2$.

Substituting Equation (A.2) into Equation (4.50) yields

$$\mathcal{R}h_k = \mathbf{H}_k \mathbf{H}_0^T = \mathbf{O}_\alpha \mathbf{A}^k \mathbf{W}_\alpha \mathbf{W}_\alpha^T \mathbf{O}_\alpha^T = \mathbf{O}_\alpha \mathbf{A}^k \mathbf{W}_c, \quad (\text{A.3})$$

where $\mathbf{W}_c = \mathbf{W}_\alpha \mathbf{W}_\alpha^T \mathbf{O}_\alpha^T$.

From Equation (4.3), the Markov parameters are defined as follows:

$$\mathbf{H}_v(k) = \mathbf{CA}^{k-1}\mathbf{B}, \quad (\text{A.4})$$

and comparing this Markov parameters (Equation (A.4)) with Equation (A.3), which is related to the correlation matrix $\mathcal{R}h_k$, the block correlation Hankel matrix (Equation (4.52)) can be

decomposed as

$$\mathcal{H}_k = \begin{bmatrix} \mathcal{R}h(k) & \mathcal{R}h(k+\tau) & \dots & \mathcal{R}h(k+\gamma\tau) \\ \mathcal{R}h(k+\tau) & \mathcal{R}h(k+2\tau) & \dots & \mathcal{R}h(k+(\gamma+1)\tau) \\ \vdots & \vdots & \ddots & \vdots \\ \mathcal{R}h(k+\xi\tau) & \mathcal{R}h(k+(\xi+1)\tau) & \dots & \mathcal{R}h(k+(\xi+\gamma)\tau) \end{bmatrix}, \quad (\text{A.5})$$

$$\mathcal{H}_k = \begin{bmatrix} O_\alpha \\ O_\alpha A^\tau \\ \vdots \\ O_\alpha A^{\xi\tau} \end{bmatrix} A^k \begin{bmatrix} W_c & A^\tau W_c & \dots & A^{\gamma\tau} W_c \end{bmatrix} = O_\xi A^k W_\gamma, \quad (\text{A.6})$$

where the matrices O_ξ and W_γ can be called block correlation observability and controllability matrices, respectively.

Following the same way as the ERA, state-space matrices A, B, C are obtained based on the Hankel matrices H_0 and H_1 , and the block correlation matrices \mathcal{H}_0 and \mathcal{H}_1 can be employed to solve for A, W_c, O_α . Then, making $k = 0$ in Equation (A.5) and (A.6), it yields:

$$\mathcal{H}_0 = \begin{bmatrix} \mathcal{R}h(0) & \mathcal{R}h(\tau) & \dots & \mathcal{R}h(\gamma\tau) \\ \mathcal{R}h(\tau) & \mathcal{R}h(2\tau) & \dots & \mathcal{R}h((\gamma+1)\tau) \\ \vdots & \vdots & \ddots & \vdots \\ \mathcal{R}h(\xi\tau) & \mathcal{R}h((\xi+1)\tau) & \dots & \mathcal{R}h((\xi+\gamma)\tau) \end{bmatrix} = O_\xi W_\gamma. \quad (\text{A.7})$$

Repeating Equation (4.55), the Singular Value Decomposition for the first n singular values holds as follows:

$$\mathcal{H}_{n0} = \mathcal{H}_n(0) = \mathcal{U}_n \Sigma_n \mathcal{V}_n^T, \quad (\text{A.8})$$

where \mathcal{U}_n and \mathcal{V}_n are orthonormal matrices, which means $\mathcal{U}_n^T \mathcal{U}_n = \mathcal{V}_n^T \mathcal{V}_n = \mathbf{I}_n$.

Relying on the direct relation $\mathcal{H}_{n0} \mathcal{H}_{n0}^\dagger \mathcal{H}_{n0} = \mathcal{H}_{n0}$, and from Equation (A.8), the following expression holds

$$\mathcal{H}_{n0}^\dagger = \mathcal{V}_n \Sigma_n^{-1} \mathcal{U}_n^T. \quad (\text{A.9})$$

From Equation (A.7), the pseudoinverse of the matrix \mathcal{H}_{n0} can also be written as

$$\mathcal{H}_{n0}^\dagger = [O_\xi W_\gamma]^\dagger = W_\gamma^\dagger O_\xi^\dagger, \quad (\text{A.10})$$

thus, the following expression clearly holds:

$$W_\gamma \mathcal{H}_{n0}^\dagger O_\xi = \mathbf{I}_n, \quad (\text{A.11})$$

considering that both \mathbf{W}_γ and \mathbf{O}_ξ are of rank n .

Introducing $\mathbf{0}_\gamma$ and \mathbf{I}_γ as a null and an identity matrices of order γ , then it can be defined the matrix

$$\mathbf{E}_\gamma^T = [\mathbf{I}_\gamma \ \mathbf{0}_\gamma \ \dots \ \mathbf{0}_\gamma]. \quad (\text{A.12})$$

From Equation (A.12) and also using Equation (A.5), the following sequence can be described:

$$\begin{aligned} \mathcal{R}h(k) &= \mathbf{E}_\gamma^T \mathcal{H}_k \mathbf{E}_\gamma, \\ &= \mathbf{E}_\gamma^T \mathbf{O}_\xi [\mathbf{W}_\gamma \mathcal{H}_0^\dagger \mathbf{O}_\xi] \mathbf{A}^k [\mathbf{W}_\gamma \mathcal{H}_0^\dagger \mathbf{O}_\xi] \mathbf{W}_\gamma \mathbf{E}_\gamma, \\ &= \mathbf{E}_\gamma^T [\mathbf{O}_\xi \mathbf{W}_\gamma] \mathcal{H}_0^\dagger [\mathbf{O}_\xi \mathbf{A}^k \mathbf{W}_\gamma] \mathcal{H}_0^\dagger [\mathbf{O}_\xi \mathbf{W}_\gamma] \mathbf{E}_\gamma, \end{aligned} \quad (\text{A.13})$$

applying the relation from Equation (A.7), yields

$$\mathcal{R}h(k) = \mathbf{E}_\gamma^T \mathcal{H}_0 \mathcal{H}_0^\dagger [\mathbf{O}_\xi \mathbf{A}^k \mathbf{W}_\gamma] \mathcal{H}_0^\dagger \mathcal{H}_0 \mathbf{E}_\gamma, \quad (\text{A.14})$$

employing Equations (A.8) and (A.9):

$$\mathcal{R}h(k) = \mathbf{E}_\gamma^T [\mathcal{U}_n \Sigma_n \mathcal{V}_n^T] \mathcal{V}_n \Sigma_n^{-1} \mathcal{U}_n^T [\mathbf{O}_\xi \mathbf{A}^k \mathbf{W}_\gamma] \mathcal{V}_n \Sigma_n^{-1} \mathcal{U}_n^T [\mathcal{U}_n \Sigma_n \mathcal{V}_n^T] \mathbf{E}_\gamma, \quad (\text{A.15})$$

considering that the matrices \mathcal{U}_n and \mathcal{V}_n are orthonormal, then

$$\begin{aligned} \mathcal{R}h(k) &= \mathbf{E}_\gamma^T \mathcal{U}_n \Sigma_n^{\frac{1}{2}} [\Sigma_n^{-\frac{1}{2}} \mathcal{U}_n^T [\mathbf{O}_\xi \mathbf{A}^k \mathbf{W}_\gamma] \mathcal{V}_n \Sigma_n^{-\frac{1}{2}}] \Sigma_n^{\frac{1}{2}} \mathcal{V}_n^T \mathbf{E}_\gamma, \\ &= \mathbf{E}_\gamma^T \mathcal{U}_n \Sigma_n^{\frac{1}{2}} [\Sigma_n^{-\frac{1}{2}} \mathcal{U}_n^T \mathcal{H}_1 \mathcal{V}_n \Sigma_n^{-\frac{1}{2}}]^k \Sigma_n^{\frac{1}{2}} \mathcal{V}_n^T \mathbf{E}_\gamma. \end{aligned} \quad (\text{A.16})$$

Comparing the last expression of Equation (A.16) with Equation (A.3), it can be achieved the triplet as follows:

$$\begin{aligned} \mathbf{A} &= \Sigma_n^{-\frac{1}{2}} \mathcal{U}_n^T \mathcal{H}_1 \mathcal{V}_n \Sigma_n^{-\frac{1}{2}}, \\ \mathbf{W}_c &= \Sigma_n^{\frac{1}{2}} \mathcal{V}_n^T \mathbf{E}_\gamma, \\ \mathbf{O}_\alpha &= \mathbf{E}_\gamma^T \mathcal{U}_n \Sigma_n^{\frac{1}{2}}. \end{aligned} \quad (\text{A.17})$$

From Equation (A.2), making $k = 1$, \mathbf{H}_0 can be attainment as follows:

$$\mathbf{H}_0 = \mathbf{O}_\alpha \mathbf{W}_\alpha = \begin{bmatrix} \mathbf{C} \\ \mathbf{CA} \\ \mathbf{CA}^2 \\ \vdots \\ \mathbf{CA}^{\alpha-1} \end{bmatrix} \begin{bmatrix} \mathbf{B} & \mathbf{AB} & \mathbf{A}^2 \mathbf{B} & \dots & \mathbf{A}^{\alpha-1} \mathbf{B} \end{bmatrix}, \quad (\text{A.18})$$

where \mathbf{W}_α can be found as

$$\mathbf{W}_\alpha = \mathbf{O}_\alpha^\dagger \mathbf{H}_0 = [\mathbf{E}_\gamma^T \mathcal{U}_n \Sigma_n^{\frac{1}{2}}]^\dagger \mathbf{H}_0. \quad (\text{A.19})$$

From Equation (A.18), the input matrix \mathbf{B} and the output matrix \mathbf{C} can be determined from the first s columns of \mathbf{W}_α and first r rows of \mathbf{O}_α , respectively. Consequently, consistently with Equation (4.58), the realization $[\hat{\mathbf{A}}, \hat{\mathbf{B}}, \hat{\mathbf{C}}, \hat{\mathbf{D}}]$ is determined as follows:

$$\begin{aligned}\hat{\mathbf{A}} &= \Sigma_n^{-\frac{1}{2}} \mathbf{U}_n^T \mathcal{H}(1) \mathbf{V}_n \Sigma_n^{-\frac{1}{2}}, \\ \hat{\mathbf{B}} &= [\mathbf{E}_\gamma^T \mathbf{U}_n \Sigma_n^{\frac{1}{2}}]^\dagger \mathbf{H}_0 \mathbf{E}_s, \\ \hat{\mathbf{C}} &= \mathbf{E}_r^T \mathbf{U}_n \Sigma_n^{\frac{1}{2}}, \\ \hat{\mathbf{D}} &= \mathbf{H}_v(0),\end{aligned}\tag{A.20}$$

where the auxiliaries matrices \mathbf{E}_s and \mathbf{E}_r are composed as

$$\begin{aligned}\mathbf{E}_s^T &= [\mathbf{I}_s \quad \mathbf{0}_s \quad \dots \quad \mathbf{0}_s], \\ \mathbf{E}_r^T &= [\mathbf{I}_r \quad \mathbf{0}_r \quad \dots \quad \mathbf{0}_r].\end{aligned}\tag{A.21}$$

The expression regarding the matrix $\hat{\mathbf{D}}$ was taken for the condition when a mass-spring-damper system is configured with accelerations as outputs. In this case, the matrix $\hat{\mathbf{D}}$ was represented by the Markov parameters in the first sampling instant ($k = 0$ in the algorithm). If the system's outputs come from displacement sensors, it should be considered $\mathbf{D} = \mathbf{H}_v(0) = \mathbf{0}$.